

# DYNAMICS AND ORDER IN GRAPHENE-BASED SYSTEMS

Zur Erlangung des akademischen Grades eines

DOKTORS DER NATURWISSENSCHAFTEN

(Dr. rer. nat.)

von der KIT-Fakultät für Physik des

Karlsruher Instituts für Technologie (KIT)

angenommene

DISSERTATION

von

M.SC. MARKUS JOHANNES KLUG

Tag der mündlichen Prüfung: 7. Februar 2020

Referent: Jörg Schmalian

Korreferent: Markus Garst

# ABSTRACT

---

The dynamics of out-of-time order correlators is studied in strongly correlated electron systems. This certain type of correlation function is a measure for the process of quantum information scrambling which is linked to the fundamental processes of entanglement growth and thermalization in quantum systems. Particularly interesting are quantum chaotic systems where the scrambling rate specifies the exponential growth of out-of-time order correlators. Whereas the scrambling rate is well defined theoretically, its interpretation in a physical context is still under debate. Furthermore, its role for physical effects and quantities which can be measured in experiments is little understood and deserves further investigation. In the first part of this work, scrambling rates are determined analytically and are analyzed for interacting electrons in graphene and electrons in a disordered metal coupled to a dissipative bath of phonons. A resemblance between the scrambling rate and the single-particle scattering rates is observed. In addition, a proposed link between quantum chaotic dynamics of out-of-time order correlators and the dynamics of fluctuations of observables is investigated. This principle could be used to determine scrambling rates in experiments.

Subsequently, possible electron orders are investigated in the system of small-angle twisted-bilayer graphene in the second part of this work. Here, the interplay between the moiré interference pattern and the interlayer hybridization due to a finite interlayer tunneling of electrons causes the bandwidth of the so-called moiré bands to depend on the twist-angle. For twist-angles in the vicinity of the magic-angle, interaction effects are strongly enhanced and a series of strong correlation effects is expected. A minimal low-energy model of interacting electrons is derived where relevant electron-electron interaction processes are identified. This model is analyzed with respect to possible electronic ground states as a function of the twist-angle. A tendency towards a formation of nematic states is observed in a weak-coupling regime, whereas various Mott-insulating states are found for strong couplings.

*Rastlos vorwärts mußt du streben,  
Nie ermüdet stillestehn,  
Willst du die Vollendung sehn;*

*Mußt ins Breite dich entfalten,  
Soll sich dir die Welt gestalten;  
In die Tiefe mußt du steigen,  
Soll sich dir das Wesen zeigen.  
Nur Beharrung führt zum Ziel,  
Nur die Fülle führt zur Klarheit,  
Und im Abgrund wohnt die Wahrheit.*

Auszug aus: Friedrich Schiller, Sprüche des Konfuzius

# CONTENTS

---

INTRODUCTION	1
I QUANTUM CHAOS IN GRAPHENE-BASED SYSTEMS	7
1 INTRODUCTION TO QUANTUM CHAOS	8
1.1 Thermalization, scrambling and quantum chaos	9
1.2 Quantum information scrambling	10
1.3 Definition of out-of-time order correlators	12
1.4 Quantum chaotic operator growth	13
1.5 A bound on operator growth	16
1.6 Out-of-time order correlators in experiments	17
1.7 Operator growth in the semiclassical limit	18
1.7.1 Phase space representation of out-of-time order correlators	19
1.7.2 Quantum chaotic dynamics of a disordered metal	21
1.8 Conclusion and outlook	23
2 QUANTUM CHAOS IN GRAPHENE	25
2.1 Summary of results	26
2.2 Microscopic model	28
2.2.1 Interacting Dirac electrons in graphene	28
2.2.2 Effective low-energy theory	29
2.3 Fermionic out-of-time order correlator	30
2.4 Augmented Keldysh formalism	31
2.4.1 Augmented Keldysh contour	32
2.4.2 Augmented Keldysh action	34
2.4.3 Out-of-time order correlator	34
2.5 Diagrammatic Approach	35
2.5.1 Bethe-Salpeter equation	36
2.5.2 Determination of the scrambling rate	39
2.5.3 Determination of the Butterfly velocity	40
2.6 Information scrambling in graphene	42
2.7 Conclusion and outlook	44
3 CHAOTIC FLUCTUATION DYNAMICS	46
3.1 Information dynamics	47
3.2 Summary of results	49
3.3 Microscopic model of a dissipative, disordered metal	52
3.4 Total momentum out-of-time order correlator	53
3.4.1 Four-point correlator	53
3.4.2 Kinetic equation approach	54

Contents

3.4.3	Chaotic operator dynamics . . . . .	57
3.5	Total momentum information dynamics . . . . .	59
3.5.1	Localized excitations . . . . .	59
3.5.2	Dynamics of classical fluctuations . . . . .	61
3.6	Conclusion and outlook . . . . .	62
REFERENCES OF PART I		65
II ELECTRON ORDER IN SMALL-ANGLE TWISTED BILAYER GRAPHENE		70
4	INTRODUCTION	71
4.1	Summary of results . . . . .	72
4.2	Overview of experimental observations . . . . .	74
4.3	Outline . . . . .	75
5	MODEL OF INTERACTING MOIRÉ ELECTRONS	76
5.1	Emerging symmetries . . . . .	78
5.2	Moiré band structure . . . . .	79
5.3	Construction of the Wannier basis . . . . .	80
5.4	Interaction matrix elements . . . . .	82
5.5	Effective model . . . . .	84
6	GROUND STATE ANALYSIS	85
6.1	Weak-coupling regime . . . . .	85
6.2	Strong-coupling regime . . . . .	88
6.3	Conclusion and outlook . . . . .	90
REFERENCES OF PART II		91
CONCLUSION		93
ACKNOWLEDGEMENTS		96
APPENDICES		97
A	APPENDICES TO PART I	98
A.1	Classical impurity scattering . . . . .	98
A.2	Semiclassical operator dynamics . . . . .	102
A.3	Interloop Keldysh component . . . . .	106
A.4	Homogeneous Bethe-Salpeter equation . . . . .	108
A.5	Kinetic equation approach . . . . .	110
B	APPENDICES TO PART II	116
B.1	Moiré band structure . . . . .	116
B.2	Construction of the wannier basis . . . . .	120
B.3	Unrestricted Hartree-Fock analysis . . . . .	122
B.4	Mean field theory of the charge density wave order . . . . .	124
B.5	Strong coupling analysis . . . . .	127

# INTRODUCTION

---

Condensed matter physics is the opposite of scientific reductionism as the physical systems are not given by the sum of their constituent parts. By adding the constituents step by step, the characteristics of a many-particle system may change dramatically when a certain threshold level of complexity is reached, as if to say quantitative differences turn, at a certain point, into qualitative ones (Anderson, 1972). This principle of emergence can be clearly traced back to interactions between constituents which render dynamics single-particle non-reducible, and the full many-problem has to be taken into account in order to describe the observed emergent effects.

Emerging states of matter are non-perturbative effects which are not deducible from the “theory of everything” (Laughlin and Pines, 2000) unless it is solved exactly, which is already a rather hopeless task for a few particles. Their description therefore requires radically new approaches. Two of the most prominent ones are the Fermi liquid theory, a generic theory based on the concept of quasiparticles which are adiabatically connected to the single-particle states of the interaction-free theory but are “dressed” by interactions (Landau, 1956), or the Bardeen-Cooper-Schrieffer theory of superconductivity with Bogoliubov quasiparticles as low-energy excitations (Bardeen *et al.*, 1957).

Generally, one is concerned with the identification of the ground state and the relevant low-energy excitations. The low-energy theory is further aimed to be connected to a microscopic basis of “elementary” excitations with mutual interactions to relate effective parameters to microscopic quantities. In particular, understanding the role of interactions and identifying the relevant interaction channels in the formation of emergent phases and their dynamics is a central aspect. It is a rather hard task, though, as interaction processes are not directly accessible in experiments, which are generally limited to the determination of response functions or single-particle spectra.

There are numerous emergent phenomena that are ill-understood yet: For example, whereas the electronic single-particle structure is rather well established in the systems of iron-based superconductors, the role of interactions in establishing the pairing mechanism for superconductivity remains elusive (Chubukov, 2012). Another example is the absence of resistivity saturation at high temperatures which violates the Mott-Ioffe-Regel limit observed in strongly correlated electron systems known as “strange metals”. This indicates a breakdown of the quasiparticle picture (Emery and Kivelson, 1995). Both examples illustrate the faced conceptual difficulties in theoretically grasping the emergent states of matter. Hence, new concepts are desirable.

The present work deals with two recent topics which provide new forms of “characterizing” and “tuning” interactions in many-body systems. “Out-of-time order correlators” represent a theoretical tool to characterize the nature and strength of interactions. This certain type of correlation function is a quantitative measure for the process of quantum information scrambling that is linked to the fundamental processes of entanglement growth and thermalization in quantum systems. In addition, a van der Waals heterostructure called “twisted bilayer graphene” is considered where two layers of graphene are stacked on top of each other and twisted by a small angle. Due to the inter-layer hybridization of electronic states, a set of electron bands emerges whose bandwidth can be tuned by varying the twist-angle. For small bandwidths, interaction effects are strongly enhanced and a series of strong correlation effects are observed in experiments.

“Out-of-time order correlators” were first considered within a semi classical approach to superconductivity as a measure of the sensitivity of classical phase space trajectories to changes in initial conditions (Larkin and Ovchinnikov, 1969) and underwent recently a revival as a measure of a system’s ability to scramble quantum information (Shenker and Stanford, 2014; Roberts *et al.*, 2015). They are generally represented as a sequence of Heisenberg operators acting at different points in time which is evaluated with respect to a certain state of the considered system. This sequence is out-of-time ordered, i.e. the direction of time propagation is repeatedly reversed when moving from one end to the other. This fact causes not only technical complications in their theoretical evaluation but also renders them inaccessible in experiments. Straightforward approaches would require the existence of a global time reversal operation which is not available in generic physical systems. Strictly speaking, out-of-time order correlators are not observable when following the general principle of initially perturbing a system and subsequently measuring its response.

Particularly interesting are “quantum chaotic” systems where, by definition, out-of-time order correlators exhibit exponential growth in time which requires sufficiently strong interactions between the system’s degrees of freedom. This growth behavior implies quantum information scrambling. The associate growth rate is called the “scrambling rate” and is determined by the details of microscopic interactions. Recently, the scrambling rate was determined for a series of systems which are representative for condensed matter physics. Whereas the scrambling rate is well defined theoretically, its interpretation in a physical context is still under debate. As a link via quantum information scrambling and entanglement growth to thermalization is indicated, a link between the scrambling rate and time scales representative for thermalization is suggestive. However, its role for physical effects and quantities, which can be measured in experiments, is little understood and deserves further investigation. Furthermore, experimental approaches to determine the scrambling rate which do not rely on global time reversal operations are desirable.

In the first part of this work, I will focus on aspects which are related to the specific

role of the scrambling rate in systems of condensed matter physics and its determination in experiments. The questions will be addressed for the system of electrons in two-dimensional graphene which represents an interacting many-body system and which is accessible in experiments (Novoselov *et al.*, 2004). In particular, I will answer the following questions:

- Which microscopic processes determine the exponential growth of out-of-time order correlators? What can be inferred from the associated scrambling rate about other physical processes?
- Is it possible to determine the scrambling rate in experiments without relying on a global time reversal operation? Under which circumstances are quantum chaotic dynamics reflected in the dynamics of observables?

The electronic system of “twisted bilayer graphene” exhibits a series of strong correlation effects for twist-angles in the vicinity of the so-called “magic-angle”. The experimentally observed effects are assigned to the dynamics of certain electron states which are associated with a set of bands energetically located around the charge neutrality point. These so-called “moiré bands” emerge due to the hybridization of electron states of the two stacked graphene layers. Their bandwidth depends on the twist-angle and is strongly reduced to values as small as 10 millielectron-volts for magic-angles, which are of the order of  $1.1^\circ$  (Bistritzer and MacDonald, 2011), indicating an enhanced role of interaction processes.

Transport measurements conducted in the magic-angle regime for low temperatures and a partially filling of the moiré bands revealed an onset of superconductivity with a relatively high critical temperature given a low carrier density (Cao *et al.*, 2018a). This observation was complemented by correlated insulator states observed for commensurate band fillings indicating strong-coupling Mott physics (Cao *et al.*, 2018b). Furthermore, a tendency towards nematic electron orders was observed in scanning tunneling microscopy experiments (Kerelsky *et al.*, 2019).

A consistent explanation of the observed correlation effects in terms of microscopic degrees of freedom is lacking. In addition, whereas the interaction-free system of two coupled layer of graphene is well established, the way to incorporate interaction effects in order to obtain an efficient description of the low-energy electron modes is still under debate.

Electrons in small-angle twisted bilayer graphene represent an interacting many-body system where the effective strength of interactions can be tuned by varying the twist-angle. This unique property allows one to study strong correlations effects in regimes of varying interaction strength, both theoretically and experimentally, which could lead to further insights into strong-coupling phenomena such as unconventional superconductivity or strange metals. In this context, I will elaborate in the second part of this work on the following questions:

- How to efficiently model the low-energy dynamics of interacting moiré electrons in small-angle twisted bilayer graphene? How does the twist-angle affect the electronic ground state?

## OUTLINE

This work is divided into two parts: Whereas part **I** deals with out-of-time order correlators in quantum chaotic systems, part **II** is concerned with electron orders in twisted bilayer graphene.

In the first part, I begin with a general introduction to out-of-time order correlators and associated concepts in Ch. **1**. It includes their definition but specifies also their relation to quantum information scrambling, entanglement growth and thermalization. In what follows, I discuss aspects which will be important for the subsequent two chapters. In particular, I introduce the notion of quantum chaos and define the scrambling rate and the Butterfly velocity, which describe information scrambling in time and space, respectively. I comment on a proposed universal, upper bound on the scrambling rate and discuss the issue of measuring out-of-time order correlators in experiments. I furthermore argue that out-of-time order correlators evaluated in the semiclassical limit are proportional to the sensitivity of classical phase space trajectories to changes in initial conditions. This finding establishes a connection between quantum and classical chaos rendering the scrambling rate and the classical Lyapunov exponent equivalent.

The gained insight is applied in Ch. **2** where an out-of-time order correlator is evaluated for a low-energy theory of interacting electrons graphene. The analytic evaluation of out-of-time order correlators is highly involved and requires non-standard methods which I discuss in detail in this work. In particular, I determine the scrambling rate and the Butterfly velocity for various interaction strengths by employing a diagrammatic approach to evaluate the correlator perturbatively. The obtained rate is subsequently compared to the single-particle scattering or the single-particle rates of energy and transport relaxation. I find that the scrambling rate resembles the single-particle scattering rate, whereas it is parametrically larger than the rates related to thermalization and hydrodynamic processes. This indicates that information scrambling is not related to these processes in graphene.

In Ch. **3**, a link between the exponential out-of-time order correlator growth and the dynamics of externally induced, classical fluctuations of observables is proposed and investigated. The link could be used to design experiments in which the scrambling rate is measured. In particular, by studying electrons in a disordered metal coupled to a dissipative bath, I first analyze the robustness of chaotic dynamics specified by an out-of-time order correlator in the presence of a dissipative environment. In contrast to the previously outlined approach, I derive a kinetic equation approach to describe the dynamics of out-of-time order correlators and the dynamics of observables. Second, I validate the proposed link for the particular microscopic model of a dissipative, disordered metal. Although results are obtained for a concrete systems, it is expected that this link is generic and therefore represents a possible new way to determine the scrambling rate in systems of condensed matter physics.

In the second part, a low-energy model of interacting electrons in small-angle twisted bilayer graphene is presented and investigated with respect to possible ground states. In particular, I first introduce the microscopic system and point out the experimental observations in Ch. 4. Subsequently, I present a modeling approach in Ch. 5 which includes the construction of a single-particle Wannier basis using the relevant electronic degrees of freedom associated with the moiré bands. Electron-electron interaction processes are projected into this basis in order to obtain an effective model defined on the moiré superlattice describing weakly dispersing electrons with long-range interactions. Eventually, I determine possible electronic ground states in the weak- and strong-coupling regime in Ch. 6. In the weak-coupling regime, the ground state analysis reveals a formation of stripe-type charge density wave orders which break the translational and rotational symmetry. In the strong-coupling regime, Mott insulating ground states are found for commensurate moiré band fillings which break, besides the translational and rotational, the global spin and valley symmetry.

This work is summarized and concluded in the chapter “**Conclusion**”.

## LIST OF PUBLICATIONS

The present work is based on the following publications:

1. Markus J. Klug, Mathias S. Scheurer, and Jörg Schmalian, *Hierarchy of information scrambling, thermalization, and hydrodynamic flow in graphene*, *Phys. Rev. B* **98**, 045102 (2018).
2. Markus J. Klug and Sergey V. Syzranov, *Chaos and the dynamics of information in dissipative electronic systems*, *Phys. Rev. B* **100**, 094304 (2019).
3. Markus J. Klug, *Charge order and Mott insulating ground states in small-angle twisted bilayer graphene*, *New J. Phys.* (2020).

## REFERENCES

- P. W. Anderson, *More is different*, *Science* **177**, 393 (1972).
- J. Bardeen, L. N. Cooper, and J. R. Schrieffer, *Theory of superconductivity*, *Phys. Rev.* **108**, 1175 (1957).
- R. Bistritzer and A. H. MacDonald, *Moiré bands in twisted double-layer graphene*, *Proc. Natl. Acad. Sci.* **108**, 12233 (2011).
- Y. Cao, V. Fatemi, S. Fang, K. Watanabe, T. Taniguchi, E. Kaxiras, and P. Jarillo-Herrero, *Unconventional superconductivity in magic-angle graphene superlattices*, *Nature* **556**, 43 (2018a).
- Y. Cao, V. Fatemi, A. Demir, S. Fang, S. L. Tomarken, J. Y. Luo, J. D. Sanchez-Yamagishi, K. Watanabe, T. Taniguchi, E. Kaxiras, R. C. Ashoori, and P. Jarillo-Herrero, *Correlated insulator behaviour at half-filling in magic-angle graphene superlattices*, *Nature* **556**, 80 (2018b).
- A. Chubukov, *Pairing mechanism in fe-based superconductors*, *Annu. Rev. Condens. Matter Phys* **3**, 57 (2012).
- V. J. Emery and S. A. Kivelson, *Superconductivity in bad metals*, *Phys. Rev. Lett.* **74**, 3253 (1995).
- A. Kerelsky, L. J. McGilly, D. M. Kennes, L. Xian, M. Yankowitz, S. Chen, K. Watanabe, T. Taniguchi, J. Hone, C. Dean, A. Rubio, and A. N. Pasupathy, *Maximized electron interactions at the magic angle in twisted bilayer graphene*, *Nature* **572**, 95 (2019).
- L. D. Landau, *The theory of a fermi liquid*, *J. Exptl. Theoret. Phys.* **30**, 1058 (1956).
- A. I. Larkin and Y. N. Ovchinnikov, *Quasiclassical method in the theory of superconductivity*, *Zh. Eksp. Teor. Fiz.* **55**, 2262 (1969), [*JETP* 28, 1200 (1969)].
- R. B. Laughlin and D. Pines, *The theory of everything*, *Proc. Natl. Acad. Sci.* **97**, 28 (2000).
- K. S. Novoselov, A. K. Geim, S. V. Morozov, D. Jiang, Y. Zhang, S. V. Dubonos, I. V. Grigorieva, and A. A. Firsov, *Electric field effect in atomically thin carbon films*, *Science* **306**, 666 (2004).
- D. A. Roberts, D. Stanford, and L. Susskind, *Localized shocks*, *J. High Energy Phys.* **2015**, 51 (2015).
- S. H. Shenker and D. Stanford, *Stringy effects in scrambling*, [arXiv:1412.6087](https://arxiv.org/abs/1412.6087) [hep-th] (2014).

# PART I

## QUANTUM CHAOS IN GRAPHENE-BASED SYSTEMS

Out-of-time order correlators are a measure for the ability of a system to scramble quantum information. The process of quantum information scrambling is related to the dynamical process of entanglement growth which is a proposed mechanism to explain thermalization in closed quantum systems. It is characterized by an exponential growth of out-of-time order correlators. In return, quantum systems which exhibit exponential out-of-time order correlator growth are said to obey “quantum chaotic” behavior. The scrambling rate, which is defined as the exponential growth rate, represents the main focus of the present work.

This part elaborates on the concept of out-of-time order correlators and addresses their role and significance in condensed matter physics. Whereas the scrambling rate is well-defined theoretically, its interpretation in a physical context is still elusive. In this chapter, a general introduction to out-of-time order correlators and associated concepts is given which also includes an introduction and definition of quantum information scrambling. In addition, several aspects are discussed which are intended to convey a general understanding of out-of-time order correlators and are important for the understanding of the next two chapters: The scrambling rate is determined for interacting electrons in graphene in Ch. 2, which is followed by a presentation of a proposed link between out-of-time order correlator dynamics and fluctuations of observables in Ch. 3. The general introduction is considered appropriate as the topic of out-of-time order correlators originates from the fields of quantum information theory and string theory, and certain aspects need to be clarified for their usage in condensed matter physics.

The present chapter is structured as follows: The relation between thermalization, information scrambling and out-of-time order correlators is outlined in Sec. 1.1. Subsequently, the notion of information scrambling is introduced more thoroughly in Sec. 1.2. In Sec. 1.3, out-of-time order correlators are introduced and are argued to imply information scrambling. Quantum chaos, which is reflected in an exponential growth of out-of-time order correlators, is introduced in Sec. 1.4. In Sec. 1.5, a universal bound on the scrambling rate is discussed, whereas Sec. 1.6 comments on aspect of the accessibility of out-of-time order correlators in experiments. The semiclassical limit of out-of-time order correlators and their relation to the sensitivity of classical phase space trajectories to changes in initial conditions is discussed in Sec. 1.7.

### 1.1. THERMALIZATION, SCRAMBLING AND QUANTUM CHAOS

In this section, a short introduction to thermalization, entanglement growth, quantum information scrambling and their mutual relations as well as their connection to out-of-time order correlators is given. The following is rather considered an overview of different concepts, whereas it is referred to the cited literature for further details.

“Thermalization” refers to the observation that observables, which are initially determined by the system’s non-equilibrium initial state, approach their constant equilibrium values varying only slightly due to statistical fluctuations. Their constant mean values are independent of the initial conditions suggesting a unique state which emerges from the large set of possible initial states. This equilibrated state is described by a handful of macroscopic parameters such as the total energy, the particle number or the volume (Greiner *et al.*, 1995). For closed systems, the process of thermalization is paradoxical: Microscopic dynamics is reversible because its time evolution is governed by unitary dynamics described by the Schrödinger equation. In contrast, the “loss of memory” of the equilibrated state with respect to its initial conditions suggests irreversibility. This paradox is (partially) resolved by the “eigenstate thermalization hypothesis” (Deutsch, 1991; Srednicki, 1994, 1999), which introduces “typical observables” whose off diagonal matrix elements between energy eigenstate are exponentially small in the system size. This fact renders them indistinguishable when evaluated for pure or mixed states. However, the occurrence of thermalization in closed quantum systems in general is still a topic of current research (D’Alessio *et al.*, 2016).

Thermalization in closed quantum systems can also occur when the system is acting as its own bath which relies on the principle of “entanglement growth” (D’Alessio *et al.*, 2016). If a subsystem is initially prepared in a pure, disentangled state, interactions between the system’s degrees of freedom generate entanglement under time evolution. Its reduced density matrix eventually approaches a mixed form characteristic for equilibration even if the full system still resides in a pure state. To obtain a mixed reduced density matrix, the size of the subsystem can be even large as long as it contains less than half of the total system’s degrees of freedom provided that the system’s Hilbert space is large (Page, 1993). That local thermalization occurs due to entanglement growth was confirmed in experiments for systems of cold atoms with small system sizes (Islam *et al.*, 2015; Kaufman *et al.*, 2016; Neill *et al.*, 2016).

“Quantum information scrambling” refers to the dynamical process of entanglement growth (Shenker and Stanford, 2014a). It arose in the context of the maximum possible speed of quantum information processing in quantum circuits<sup>1</sup> (Hayden and Preskill, 2007) and can be defined by following Ref. Sekino and Susskind (2008) as follows: An isolated quantum system is bipartitioned and prepared in a state in which both subsys-

---

<sup>1</sup>i.e. how fast a black hole, which is considered a quantum circuit, processes an initially inserted bit of quantum information such that the information can be reconstructed by measuring its Hawking radiation.

tems are disentangled. The information associated with the initial state, which may be quantified by a measure of entropy, is scrambled if for any possible bipartition the two, time evolved subsystems have become fully entangled and have approached the maximal value of entanglement entropy. A possible measure of information refers to, e.g., the von Neumann entropy, which may also quantify the entanglement entropy by using the reduced density matrices (Preskill, 2018).

The process of information scrambling is a consequence of interactions and therefore represents an intrinsic property of the system which ought to be quantified. However, quantifying the time evolution of the bipartite entanglement entropy turns out to be rather impractical for generic systems of condensed matter physics and is restricted to systems with a high degree of symmetry, e.g. conformal symmetries (Morrison and Roberts, 2013; Asplund *et al.*, 2015) or integrable theories (Calabrese and Cardy, 2005). Instead, so-called “out-of-time order correlators” serve as a measure of information scrambling (Roberts *et al.*, 2015; Roberts and Stanford, 2015; Shenker and Stanford, 2014a). Their exponential growth in time *implies* information scrambling as indicated by analytical approaches (Hosur *et al.*, 2016; Huang *et al.*, 2017; Fan *et al.*, 2017) and numerical experiments (Shenker and Stanford, 2014b; Huang *et al.*, 2017; Lewis-Swan *et al.*, 2019; Luitz and Bar Lev, 2017) whereas an analytical approach which proofs this link rigorously has not been found yet.

The discussion outlined above indicates that the scrambling of quantum information is a prerequisite for thermalization as it implies a delocalization of initial states and, in return, the emergence of local equilibrium. However, as a rigorous relation between out-of-time order correlators and thermalization does not exist, this possible link has to be investigated more thoroughly. By studying out-of-time order correlator growth based on microscopic dynamics, one could shed light on its role for observable effects.

## 1.2. QUANTUM INFORMATION SCRAMBLING

This section presents a heuristic approach to illustrate the previously quoted definition of information scrambling and follows ideas presented in Ref. Shenker and Stanford (2014b). In addition, it introduces the quantity “scrambling time” which denotes the time scale after which information about the initial conditions of a system can only be obtained by performing global measurements. A particular situation is considered where a subsystem of an isolated, interacting quantum system is prepared in an initial state. Under time evolution, the entanglement of the bipartite system grows and the initial conditions are “spread” in the system. This process is quantified by the “mutual information” between the two subsystems.

The system is bipartitioned into the subsystems  $A$  and  $\bar{A}$  as depicted in Fig. 1.1. Initially, the smaller subsystem  $A$  is prepared in a definite state which is disentangled from  $\bar{A}$  described by the density matrix  $\rho_A(0)$  such that the state of the total system is represented initially by a direct product state

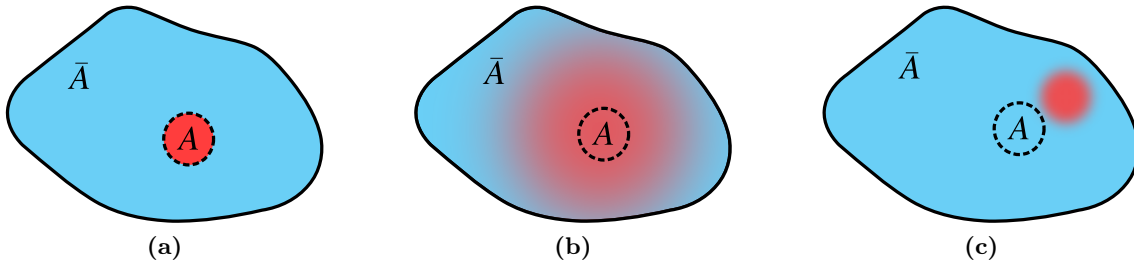


**Figure 1.1.:** Information spreading in a closed quantum system. (a) Subsystem  $A$  is initially prepared in a definite state. Red indicates high, blue zero amount of mutual information with respect to the initial conditions of  $A$ . (b) Under time evolution, the entanglement between subsystems  $A$  and  $\bar{A}$  grows and the initial conditions are spread over the system’s degrees of freedom. (c) In non-scrambling systems, information may disperse but still remains localized.

$$\rho(0) = \rho_A(0) \otimes \rho_{\bar{A}}(0). \quad (1.1)$$

The quantum information associated with the initial state can be quantified by using a measure of entropy, e.g. the von Neumann entropy  $S(\rho_A) = -\text{tr}[\rho_A \ln \rho_A]$  where the reduced density matrix is defined as  $\rho_A = \text{tr}_{\bar{A}}[\rho]$  (Preskill, 2018).

To quantify the process of information spreading, two concepts of quantum information theory are introduced. Mutual information quantifies the amount of information which can be deduced about  $A$  by measuring  $\bar{A}$ . It is defined as (Preskill, 2018)

$$I(A, \bar{A}) = S(\rho_A) + S(\rho_{\bar{A}}) - S(\rho). \quad (1.2)$$

As information scrambling relies on the mutual information between the initial state and the time evolved state at time  $t$ , a copy  $\mathcal{C}$  of the system, which is initially perfectly entangled with the original system  $\mathcal{O}$ , is introduced employing the “thermofield double” construction (Morrison and Roberts, 2013). Whereas  $\mathcal{O}$  is time evolved,  $\mathcal{C}$  remains in its initial state keeping track of the initial conditions. The doubling of the original Hilbert space,  $\mathcal{H} \rightarrow \mathcal{H}_{\mathcal{O}} \otimes \mathcal{H}_{\mathcal{C}}$ , allows one to encode the system’s (mixed) state in a thermofield double state,

$$|\rho\rangle\rangle = \sum_{i=1}^N \sqrt{p_i} |i\rangle_{\mathcal{O}} \otimes |i\rangle_{\mathcal{C}}, \quad (1.3)$$

with Hilbert space dimension  $N$  and  $p_i$  representing the statistical weights which constitute the original density matrix. It is obtained from the thermofield double state by tracing out the copy’s degrees of freedom,  $\rho = \sum_i p_i |i\rangle\langle i| = \text{tr}_{\mathcal{C}} [|\rho\rangle\rangle\langle\langle\rho|]$ . Within this representation, time evolution is described by the unitary operator  $\hat{U}(t)$  acting on  $\mathcal{O}$ , whereas  $\mathcal{C}$  is left unchanged. The time evolved thermofield double state is therefore given by

$$|\rho(t)\rangle\rangle = \hat{U}_{\mathcal{O}}(t) \otimes \hat{1}_{\mathcal{C}} |\rho\rangle\rangle. \quad (1.4)$$

After having established the concept of mutual information and thermofield double state representation, the notion of information scrambling is formalized by inspecting the mutual information between  $A$  or  $\bar{A}$  at time  $t$  and the initial conditions of  $A$ ,

$$I(A_{\mathcal{O}}, A_{\mathcal{C}}) = S(\rho_{A_{\mathcal{O}}}) + S(\rho_{A_{\mathcal{C}}}) - S(\rho_{A_{\mathcal{C}} \cup A_{\mathcal{O}}}), \quad (1.5)$$

where  $I(\bar{A}_{\mathcal{O}}, A_{\mathcal{C}})$  is given accordingly. The reduced density matrices are given by  $\rho_{A_{\mathcal{O}}} = \text{tr}_{\bar{A}_{\mathcal{O}} \cup \mathcal{C}} [|\rho(t)\rangle\rangle\langle\langle\rho(t)|]$  and  $\rho_{A_{\mathcal{C}}} = \text{tr}_{\mathcal{O} \cup \bar{A}_{\mathcal{C}}} [|\rho(t)\rangle\rangle\langle\langle\rho(t)|]$ .

Initially,  $A_{\mathcal{O}}$  and  $A_{\mathcal{C}}$  are perfectly entangled and  $I(A_{\mathcal{O}}, A_{\mathcal{C}})$  is maximum as the total system is in a pure state,  $S(\rho_{A_{\mathcal{C}} \cup A_{\mathcal{O}}}) = 0$ . In contrast,  $I(\bar{A}_{\mathcal{O}}, A_{\mathcal{C}}) = 0$  because  $A$  and  $\bar{A}$  are uncorrelated. For  $t > 0$ , the entanglement between  $A_{\mathcal{O}}$  and  $\bar{A}_{\mathcal{O}}$  increases, whereas the entanglement between  $A_{\mathcal{O}}$  and  $A_{\mathcal{C}}$  (and equally  $\bar{A}_{\mathcal{O}}$  and  $\bar{A}_{\mathcal{C}}$ ) decreases. Consequently, this causes  $I(A_{\mathcal{O}}, A_{\mathcal{C}})$  to decay and  $I(\bar{A}_{\mathcal{O}}, A_{\mathcal{C}})$  to grow. As  $A$  represents the smaller subsystem,  $I(A_{\mathcal{O}}, A_{\mathcal{C}})$  approaches zero asymptotically as the reduced density matrix  $\rho_{A_{\mathcal{O}}}$  ends up being fully mixed (Page, 1993). The process of decaying mutual information  $I(A_{\mathcal{C}}, A_{\mathcal{O}})$  is denoted information scrambling. The associated time scale which signals the onset of the decay of  $I(A_{\mathcal{C}}, A_{\mathcal{O}})$  for every possible partitioning  $A$  and  $\bar{A}$  for fixed initial conditions Eq. (1.1) is denoted ‘‘scrambling time’’ (Shenker and Stanford, 2014b).

As the scrambling time depends on the rate of entanglement growth, the nature of interactions between system’s degrees of freedom are crucial for information scrambling. It is expected that, e.g., integrable systems, which do not thermalize, also do not scramble quantum information. It may refer to a situation where initially localized information disperses but always remains localized in the system’s Hilbert space as depicted in Fig. 1.1c. This concept is similar to the concept of ergodicity of classical mechanics which represents a prerequisite for thermalization and refers to the ability of a system to reach all points in phase space equally likely independent of the initial conditions (D’Alessio *et al.*, 2016). As ergodic systems are characterized by chaotic classical dynamics, quantum systems which scramble quantum information obey quantum chaotic dynamics (Shenker and Stanford, 2014b; Hosur *et al.*, 2016). It is noted that this definition of quantum chaos and others, e.g. Wigner-Dyson level statistics (Haake, 2010), are indicated to be alike, however, a rigorous proof has not been given yet.

### 1.3. DEFINITION OF OUT-OF-TIME ORDER CORRELATORS

The time evolution of the mutual information introduced in Eq. (1.5) can be used to determine the scrambling time. Alternatively, one can also study operator dynamics quantified by out-of-time order correlators as their exponential growth implies information scrambling (Roberts *et al.*, 2015; Roberts and Stanford, 2015; Shenker and Stanford, 2014a; Hosur *et al.*, 2016). In the following section, out-of-time order correlators are introduced and defined as a measure of local operator growth.

Two types of hermitian operators  $\hat{V}$  and  $\hat{W}$  are considered which act ‘‘locally’’, i.e. on

## 1. Introduction to quantum chaos

one single among many degrees of freedom. These operators are separated such that their commutator vanishes,  $[\hat{V}, \hat{W}] \equiv \hat{V}\hat{W} - \hat{W}\hat{V} = 0$ . Dynamics is introduced by time evolving one operator  $\hat{V} \rightarrow \hat{V}(t) = \hat{U}^\dagger(t) \hat{V} \hat{U}(t)$  by using the time evolution operator<sup>2</sup>  $\hat{U}(t) = e^{-i\hat{H}t}$ , where Planck's constant is set to unity,  $\hbar = 1$ . This operator “grows” under time evolution as expanding the operator in powers of the time parameter yields

$$\hat{V}(t) = \hat{V} + it[\hat{H}, \hat{V}] + \frac{(it)^2}{2!}[\hat{H}, [\hat{H}, \hat{V}]] + \frac{(it)^3}{3!}[\hat{H}, [\hat{H}, [\hat{H}, \hat{V}]]] + \dots \quad (1.6)$$

If  $\hat{H}$  contains a “local” structure which connects “neighboring” degrees of freedom, every term represents an operator with a growing amount of local support due to the increasing number of nested commutators. Eventually, when the distance between  $\hat{V}$  and  $\hat{W}$  is bridged, the commutator ceases to vanish,  $[\hat{V}(t), \hat{W}] \neq 0$ . In this sense, the dynamics of  $\hat{V}(t)$  are tracked by  $\hat{W}$ .

An absolute measure of operator growth is given by the out-of-time order correlator (Roberts *et al.*, 2015)

$$C(t) = -\langle [\hat{V}(t), \hat{W}]^2 \rangle \quad (1.7)$$

which is defined for  $t \geq 0$  where  $\langle \dots \rangle = \text{tr}[\rho \dots]$  such that the dynamics of operators is evaluated with respect to certain state specified by the density matrix  $\rho$ . The minus sign assures positive definiteness of  $C(t)$ . As  $\hat{V}$  and  $\hat{W}$  commute initially,  $C(t)$  is expected to vanish for  $t \approx 0$  as  $\langle \hat{V}\hat{W}\hat{W}\hat{V} \rangle \approx \langle \hat{V}\hat{W}\hat{V}\hat{W} \rangle \approx \langle \hat{V}\hat{V} \rangle \langle \hat{W}\hat{W} \rangle$ . In contrast for  $t > 0$ ,  $C(t)$  is expected to grow. This behavior can be traced back to the decay of terms in Eq. (1.7) of the type

$$F(t) = \langle \hat{V}(t)\hat{W}\hat{V}(t)\hat{W} \rangle. \quad (1.8)$$

The remaining terms of the type  $\langle \hat{V}(t)\hat{W}\hat{W}\hat{V}(t) \rangle$  are slowly varying and are expected to saturate against the asymptotic long-time value  $\langle \hat{V}(t)\hat{W}\hat{W}\hat{V}(t) \rangle|_{t \rightarrow \infty} \approx \langle \hat{V}\hat{V} \rangle \langle \hat{W}\hat{W} \rangle$ , which represents also the asymptotic long-time value of  $C(t)$ . In the following,  $C(t)$  is called an “out-of-time order correlator”, whereas  $F(t)$  is called an “out-of-time order correlation function”.

$F(t)$  can be interpreted as a measure of the fidelity of two initially identical systems which exhibit different local perturbations. For this, a perfect copy  $\mathcal{C}$  of the considered system  $\mathcal{O}$  is generated by employing the thermofield double state representation as introduced in the previous sections in Eq. (1.3). Subsequently, the sequence of operators  $\hat{V}(t)\hat{W}$  is applied to  $\mathcal{O}$  whereas a reversed sequence  $[\hat{W}\hat{V}(t)]^*$  is applied to  $\mathcal{C}$ . The fidelity evaluates to an out-of-time order correlation function,

$$\langle\langle \rho | [\hat{V}(t)\hat{W}]_{\mathcal{O}} \otimes [\hat{W}\hat{V}(t)]_{\mathcal{C}}^* | \rho \rangle\rangle = \text{tr}[\sqrt{\rho}\hat{V}(t)\hat{W}\sqrt{\rho}\hat{V}(t)\hat{W}], \quad (1.9)$$

where, in contrast to Eq. (1.8), fractions of the density matrix  $\rho$  are placed between the

---

<sup>2</sup>Here, it is focused, for simplicity, on time-independent Hamilton operators which are represented by  $\hat{H}$ . A generalization to time-dependent Hamilton operators is straightforward.

sequences. Hence, the reversed order of operations applied to  $\mathcal{O}$  and  $\mathcal{C}$  renders the initial identical copies increasingly “incoherent” and the out-of-time order correlation function decays, similar to the decay of mutual information between a subsystem’s state at  $t$  and its initial state as discussed in Sec. 1.2. The special placement of the density matrices in Eq. (1.9) is the central focus of Sec. 1.5.

#### 1.4. QUANTUM CHAOTIC OPERATOR GROWTH

Similar to the dynamics of entanglement entropy discussed in Sec. 1.2, the growth of out-of-time order correlators depends on the nature of microscopic interactions. It is generally distinguished between three different classes: An exponential growth is obtained for strongly coupled systems with mutual interactions between all degrees of freedom, such as the Sachdev-Ye-Kitaev (SYK) model (Sachdev and Ye, 1993; Kitaev, 2015; Maldacena and Stanford, 2016), or large  $N$ -theories with  $N$  maximally coupled intrinsic degrees of freedom embedded in spatial space, see e.g. Refs. Roberts and Swingle (2016); Stanford (2016); Chowdhury and Swingle (2017); Patel and Sachdev (2017); Klug *et al.* (2018). Exponential growth is also observed for quantum systems which possess a semiclassical limit obeying classical chaotic behavior, e.g. Larkin and Ovchinnikov (1969); Rozenbaum *et al.* (2017); Syzranov *et al.* (2019); Klug and Syzranov (2019). These systems are denoted “quantum chaotic” (Maldacena *et al.*, 2016) implying the ability to scramble quantum information as discussed in Sec. 1.2. In contrast, slow polynomially growth is obtained, e.g., for many-body localized systems, see e.g. Refs. Swingle and Chowdhury (2017); Huang *et al.* (2017); Fan *et al.* (2017), which are expected to be non-ergodic. Furthermore, out-of-time order correlators evaluated for integrable systems are expected to oscillate with recurrence times polynomial in the number of degrees of freedom (Hosur *et al.*, 2016). This fact can be also deduced from Eq. (1.7) by employing its spectral representation.

This work focuses on quantum chaotic systems exhibiting exponential out-of-time order correlator growth. In this case, the leading order contribution to out-of-time order correlation functions decays exponentially,

$$F(t) \sim a - \epsilon e^{\lambda_L t}, \quad (1.10)$$

whereas the contribution to out-of-time order correlators grows exponentially,

$$C(t) \sim \epsilon e^{\lambda_L t}, \quad (1.11)$$

where  $\frac{\epsilon}{a} \ll 1$  represents a small parameter of the considered theory (e.g.  $\epsilon \sim \frac{1}{N}$  for large- $N$  theories) and the scrambling rate  $\lambda_L$  represents the largest rate of exponential growth. The existence of  $\epsilon$  is necessary to define  $\lambda_L$  and the corresponding quantum chaotic regime (Maldacena *et al.*, 2016). In analogy to classical chaotic systems, where initially close trajectories in phase space diverge exponentially with a rate given by the Lyapunov exponent (Lichtenberg and Lieberman, 1992),  $\lambda_L$  is also referred to as “Lyapunov

## 1. Introduction to quantum chaos

exponent” (Maldacena *et al.*, 2016). In the case of chaotic systems, this leading order behavior is expected to be independent of the particular choice of operators  $\hat{V}$  and  $\hat{W}$ . Here, certain operators, e.g., associated with conserved quantities are excluded.

The parameterization of the out-of-time order functions and correlators used in Eq. (1.10) and (1.11), respectively, is valid for times smaller than the cut-off time  $t^*$ , which is generally assumed to match the scrambling time defined in the context of information scrambling (Roberts *et al.*, 2015; Roberts and Stanford, 2015; Shenker and Stanford, 2014a; Hosur *et al.*, 2016) introduced earlier in Sec. 1.2. For  $t > t^*$ ,  $F(t)$  has decayed and  $C(t)$  has saturated to its constant asymptotic long-time value. Hence, the scrambling time defined by out-of-time order correlators is determined by  $C(t^*) \sim a$  yielding

$$t^* \sim \lambda_L^{-1} \log\left(\frac{a}{\epsilon}\right). \quad (1.12)$$

The exponential growth of type Eq. (1.11) of out-of-time order correlators evaluated for a strongly coupled system with all-to-all two-body interactions (see, e.g., the SYK model) can be understood by considering information scrambling as a step-wise process, where the characteristic time scale is given by the inverse scrambling rate  $\lambda_L^{-1}$ . Initially, a single degree of freedom (DoF) is brought into a definite state. At each time step, all DoFs interact where respective interaction partners are chosen by random. As the reference DoF gets correlated to a second DoF after the first time step, it is already correlated to four after the second, and so on. Hence,  $C(t) \sim \frac{1}{N} e^{\lambda_L^{-1} t}$ , and the growth stops when the initial DoF is correlated to all  $N$  degrees of freedom,  $C(t^*) \sim 1$ , yielding  $t^* \sim \lambda_L^{-1} \log N$ . This scrambling time saturates the conjectured lower bound on the scrambling time (Sekino and Susskind, 2008) which proposes a shortest possible time to scramble quantum information.

The discussion of operator growth can be extended to systems in  $d$  spatial dimensions. Besides the  $N$  strongly-coupled “intrinsic” degrees of freedom which guarantee a quantum chaotic regime, the system is extended to spatial space. Information scrambling now happens in two distinct entities, intrinsically and spatially. Quantum information scrambling in the intrinsic entity is described by an exponential growth of type Eq. (1.11), whereas information scrambling in real-space is described by a certain type of propagation. To probe the spatial spreading of quantum information, one considers out-of-time order correlators of the type

$$C(\mathbf{x}, t) = -\langle [\hat{V}(\mathbf{x}, t), \hat{W}(\mathbf{0})]^2 \rangle, \quad (1.13)$$

where the local operators are separated by a distance  $|\mathbf{x}|$ . In  $d \geq 2$ , the growth of  $C(\mathbf{x}, t)$  is diffusive, see e.g. Refs. Chowdhury and Swingle (2017); Patel *et al.* (2017); Patel and Sachdev (2017). It is quantified by a “chaos” diffusion coefficient which is parameterized by

$$D_L = \frac{v_B^2}{4\lambda_L}, \quad (1.14)$$

with the “butterfly velocity”  $v_B$  (Roberts *et al.*, 2015), which was found to represent the characteristic velocity of the interaction-free theory in, e.g., Refs. Chowdhury and Swingle

## 1. Introduction to quantum chaos

(2017); [Werman \*et al.\* \(2017\)](#), and the scrambling rate  $\lambda_L$ . Combined with the exponential growth due to “intrinsic” information scrambling, the out-of-time order correlator obeys the partial differential equation ([Chowdhury and Swingle, 2017](#); [Klug \*et al.\*, 2018](#))

$$\frac{\partial}{\partial t} C = D_L \Delta_{\mathbf{x}} C + \lambda_L C, \quad (1.15)$$

for long distances associated with the length scale  $\ell \sim \frac{v_B}{\lambda_L}$ . The growth is initiated by appropriate initial conditions or by adding a perturbing term of the form  $C_0 \delta(t) \delta(\mathbf{x})$  as discussed in Ref. [Klug \*et al.\* \(2018\)](#). A possible solution to Eq. (1.15) and a perturbing term mimicking the initial conditions is obtained by Fourier transform and is given by ([Klug \*et al.\*, 2018](#))

$$C(\mathbf{x}, t) \sim e^{\lambda_L t - \frac{|\mathbf{x}|^2}{4D_L t}} \approx e^{2(\lambda_L t - \frac{|\mathbf{x}|}{v_B})}, \quad (1.16)$$

where the approximate solution is obtained by expanding the spatial coordinate around the wave front  $|\mathbf{x}| \approx v_B t$ . Hence, quantum information, although indicated in Eq. (1.15) to propagate diffusively in space, spreads ballistically if combined with the intrinsic exponential growth which suggest the term “quasiballistic” propagation referring to a conventional diffusion boosted by a local exponential growth. Due to the spatial extension of the system, the scrambling time is delayed and is given by

$$t^* \sim \lambda_L^{-1} \log\left(\frac{a}{\epsilon}\right) + \frac{V^{1/d}}{v_B}, \quad (1.17)$$

where  $V$  represents the volume of the system.

### 1.5. A BOUND ON OPERATOR GROWTH

In conformal field theories with holographic duals, the scrambling rate is given by the universal constant  $\lambda_{L,\max} = \frac{2\pi k_B T}{\hbar}$  ([Kitaev, 2015](#); [Roberts and Stanford, 2015](#); [Roberts \*et al.\*, 2015](#); [Roberts and Swingle, 2016](#)). This is remarkable as the inverse of this scrambling rate relates to the Planckian dissipation time  $\lambda_{L,\max}^{-1} \sim \tau_P \sim \frac{\hbar}{k_B T}$  which is postulated as the shortest possible dissipation time ([Zaanen, 2004](#)) and is considered as a candidate for the dissipation time scale governing the phenomenon of linear-in-temperature resistivity observed for strange metals ([Bruin \*et al.\*, 2013](#)). Indeed, it was shown in Refs. [Maldacena \*et al.\* \(2016\)](#); [Tsuji \*et al.\* \(2018\)](#) that the scrambling rate determined for a system in thermal equilibrium is bounded from above by

$$\lambda_L \leq \lambda_{L,\max}. \quad (1.18)$$

This bound could have consequences for other physical quantities and could, e.g., be reflected in a bound on transport coefficients measurable in experiments.

The proof of Eq. (1.18) relies on a special type of out-of-time order correlator with certain analytic properties requiring the density matrix to be split into two fractions, which are

## 1. Introduction to quantum chaos

placed between the two correlators, respectively. Instead of Eq. (1.11), one considers a “regularized” out-of-time order correlator

$$C_{\text{reg}}(t) = \text{tr}\{\sqrt{\rho_{\text{th}}}[\hat{V}(t), \hat{W}]\sqrt{\rho_{\text{th}}}[\hat{V}(t), \hat{W}]\}, \quad (1.19)$$

where  $\rho_{\text{th}} = Z^{-1}e^{-\hat{H}/k_B T}$  denotes the thermal density matrix. This scheme regularizes ultra-violet divergences which arise in low-energy field theories and suppresses contributions to information scrambling from excitations with energies larger than the temperature  $k_B T$  as discussed in the Appendix A.3. The choice of placements of density matrices has consequences for the scrambling rate  $\lambda_L$ . In Ref. Klug *et al.* (2018), it was found that  $\lambda_L$  determined for interacting electrons in graphene depends on the regularization scheme: The scrambling rate  $\lambda_{L,\text{non-reg}}$  obtained with Eq. (1.11) with  $\rho = \rho_{\text{th}}$  differs from  $\lambda_{L,\text{reg}}$  obtained with Eq. (1.19). In particular, the “regularized” scrambling rate is determined to  $\lambda_{L,\text{reg}} < \frac{2\pi k_B T}{\hbar}$  (see Ch. 2 for details), whereas the bound Eq. (1.18) is violated by the “non-regularized” scrambling rate  $\lambda_{L,\text{non-reg}} \propto \Lambda$  as the scrambling rate depends linearly on the ultra-violet cut-off  $\Lambda$  of the low-energy theory. A violation of the bound for non-regularized out-of-time order correlators was also observed for electrons in a disordered interacting metal discussed in Ref. Liao and Galitski (2018).

An explanation for this observation is given by the representation of the out-of-time order correlators in terms of two copies of a systems which are initially perfectly entangled and “dephase” in the course of time due to quantum chaotic dynamics as argued in Sec. 1.3. The thermal density matrix  $\rho_{\text{th}}$  exponentially suppresses excitations with energies  $E \gg k_B T$ . When considering Eq. (1.19), both copies exhibit low-energy excitations for low temperatures, however with halved “physical” temperature  $\frac{T}{2}$ . In contrast, when considering the non-regularized out-of-time order correlator Eq. (1.11), one copy of the system is evaluated with respect to an infinite temperature state allowing excitations up to the ultra-violet cut-off scale in line with results obtained in Ref. Klug *et al.* (2018). Hence, Eq. (1.19) is regarded as a low-energy measure to characterize information scrambling in the case of thermally excited systems for low temperatures.

### 1.6. OUT-OF-TIME ORDER CORRELATORS IN EXPERIMENTS

The central characteristic of out-of-time order correlation functions is the non-monotonicity of its time arguments in the sequence of operators in Eq. (1.8), i.e. time does neither monotonically in- nor decrease when moving from one end to the other. This property renders out-of-time order correlators “non-observables”, in contrast to conventional correlation functions where the sequence of operators is always time-ordered because of the underlying principle of first perturbing and subsequently measuring the response of the system (Mahan, 2000). This has implications for the accessibility of out-of-time order correlators in experiments aiming to extract quantities such as the scrambling time, the scrambling rate and the butterfly velocity from physical systems.

## 1. Introduction to quantum chaos

In general, common experimental concepts are either based on the existence of a global time reversal operation, which allows one to realize arbitrary sequences of operators, or the generation of a perfect copy of the original system, which resemble the thermofield double state representation introduced in Eq. (1.9). Out-of-time order correlators are measured, e.g., for one dimensional Ising chains which are simulated using trapped ions (Gärttner *et al.*, 2017) or liquid-state nucleon magnetic resonance (Li *et al.*, 2017). The measurement protocols contain an effective time reversal operations which is achieved by inverting the sign of the Hamilton operator resembling spin echo techniques (Hahn, 1950). An interferometric approach is proposed in Ref. Bohrdt *et al.* (2017) which is applicable to cold atom systems. Their protocol is based on the existence of two copies of the same system, which are initially perfectly entangled, and the existence of an effective time reversal operation, which can be realized by using a Feshbach resonance and by tuning the optical lattice. There are also several approaches relying on the existence of control and ancilla qubits which effectively create a second copy of the system (Yao *et al.*, 2016; Zhu *et al.*, 2016; Swingle *et al.*, 2016; Zhang *et al.*, 2019).

However, these approaches are restricted to small system sizes and require a high degree of controllability over the microscopic degrees of freedom of a system. An application to generic systems of condensed matter physics is not possible yet.

### 1.7. OPERATOR GROWTH IN THE SEMICLASSICAL LIMIT

When evaluated in the semiclassical limit, out-of-time order correlators are proportional to the sensitivity of classical phase space trajectories to changes in initial conditions whose dynamics are determined by the classical counterpart of the considered quantum system. This connection is complementary to the picture of information spreading presented earlier in Sec. 1.2 and bears conceptually important aspects to understand the underlying mechanism of out-of-time order correlator growth.

The semiclassical limit of a quantum theory refers to the case where Planck's constant is small compared to a characteristic classical action scale  $s_{\text{cl}}$  which suggests to introduce an effective, dimensionless constant  $\hbar_{\text{eff}} = \frac{\hbar}{s_{\text{cl}}} \ll 1$ . In this limit, the dynamics of the quantum system is determined predominantly by classical dynamics which minimizes the classical action integral representing the so-called saddle point contributions (Gutzwiller, 1990). This link indicates that if the semiclassical limit of a quantum system exist, possible quantum chaotic behavior, which is signaled by an exponentially growing out-of-time order correlator, is connected to the chaotic dynamics of the corresponding classical system.

To illustrate the link between quantum and classical chaotic dynamics, an out-of-time order correlator of momentum operators is considered which is evaluated for a disordered metal where electrons move in static disorder potentials of randomly located impurities as presented first in Ref. Larkin and Ovchinnikov (1969). This quantum system, which possesses a classical chaotic semiclassical limit, obeys quantum chaotic dynamics. The operators in Eq. (1.11) are chosen to one component of the momentum operator,  $\hat{V} =$

## 1. Introduction to quantum chaos

$\hat{W} = \hat{p}_z$ . For  $\hbar_{\text{eff}} \ll 1$ , the out-of-time order correlator is approximated to (Larkin and Ovchinnikov, 1969)

$$-\langle [\hat{p}_z(t), \hat{p}_z]^2 \rangle \approx \hbar^2 \left\langle \left( \frac{\partial p_z(t)}{\partial z_0} \right)^2 \right\rangle_{\text{PS}}, \quad (1.20)$$

where  $p_z(t) = p_z(t, \mathbf{r}_0, \mathbf{p}_0)$  represents one component of a classical phase space trajectory depending on initial conditions  $(\mathbf{r}_0, \mathbf{p}_0)$ ,  $\langle \dots \rangle$  quantum mechanical averaging specified by a density matrix  $\rho$  and  $\langle \dots \rangle_{\text{PS}}$  refers to a phase space average specified by a classical distribution function  $\rho(\mathbf{r}, \mathbf{p})$ . As classical chaotic dynamics are characterized by an exponentially growing distance between initially close trajectories implying  $|\frac{\partial p_z(t)}{\partial z_0}| \sim e^{\lambda_{\text{cl}} t}$  with the classical Lyapunov exponent  $\lambda_{\text{cl}}$  (Lichtenberg and Lieberman, 1992), the out-of-time order correlator is expected to grow exponentially. This connection indicates an equivalence of the scrambling rate  $\lambda_L$  and the classical Lyapunov exponent  $\lambda_{\text{cl}}$ , which was, e.g., explicitly shown to exist for the quantum kicked rotor in Ref. Rozenbaum *et al.* (2017).

Similar to the saturation of out-of-time order correlators at the scrambling time  $t^*$ , the validity of Eq. (1.20) is expected to hold for  $t < t_E$  with the Ehrenfest time

$$t_E = \lambda_{\text{cl}}^{-1} \log \hbar_{\text{eff}}^{-1}, \quad (1.21)$$

which signals the crossover from classical to quantum dynamics (Ehrenfest, 1927; Aleiner and Larkin, 1996). It resembles the expression for the scrambling time Eq. (1.12) when assuming the correspondence  $\lambda_L \leftrightarrow \lambda_{\text{cl}}$  and  $\hbar_{\text{eff}} \leftrightarrow \frac{\epsilon}{a}$ . At  $t_E$ , the classical description is expected to break down and quantum effects are significant causing the exponential growth to saturate.

The connection Eq. (1.20) is readily made plausible by postulating the applicability of the correspondence principle of quantum mechanics. In particular, by referring to the correspondence between Ehrenfest's and Liouville's theorem, the commutators of quantum mechanical operators  $\hat{p}_z$  may be replaced by Poisson brackets of classical phase space variables  $p_z(t) = p_z(t, \mathbf{r}_0, \mathbf{p}_0)$ ,

$$[\hat{p}_z(t), \hat{p}_z] \xrightarrow{\hbar_{\text{eff}} \ll 1} i\hbar \{p_z(t), p_{0,z}\} = \frac{\partial p(t)}{\partial z_0}, \quad (1.22)$$

where  $\{f, g\} \equiv \frac{\partial f}{\partial z_0} \frac{\partial g}{\partial p_{0,z}} - \frac{\partial g}{\partial z_0} \frac{\partial f}{\partial p_{0,z}}$  for components of the phase space trajectories  $f = f(t, \mathbf{r}_0, \mathbf{p}_0)$  and  $g = g(t, \mathbf{r}_0, \mathbf{p}_0)$ . Additionally, by replacing the quantum mechanical average by a phase space average, identity Eq. (1.20) is obtained.

Instead of relying on the indicative reasoning outlined above, it is desirable to use more advanced methods which are tailored to evaluate quantum mechanical expectation values in the semiclassical limit to verify relation Eq. (1.20) based on microscopic grounds. In what follows, the link Eq. (1.20) is derived in Sec. 1.7.1 for a minimal model of two-degrees of freedom which illustrates its underlying principle where and an extension to many degrees of freedom is straightforward. Eventually, the out-of-time order correlator in the classical limit is qualitatively discussed for the electronic model of a disorder metal in Sec. 1.7.2.

### 1.7.1. PHASE SPACE REPRESENTATION OF OUT-OF-TIME ORDER CORRELATORS

Links of type Eq. (1.20) suggest a connection between quantum chaotic dynamics defined by out-of-time order correlators and classical chaotic dynamics defined by diverging phase space trajectories. As this connection is indicated by the correspondence principle Eq. (1.22), its underlying mechanism is elusive and an derivation based on microscopic grounds is desirable. In this section, a relation of type Eq. (1.20) is derived explicitly for a minimal model of two degrees of freedom by using semiclassical approximation methods. An extension to many degrees of freedom is straightforward. Similar approaches are presented in Ref. [Kurchan \(2018\)](#); [Rammensee \*et al.\* \(2018\)](#); [Jalabert \*et al.\* \(2018\)](#).

The relation of type Eq. (1.20) relies on the principal of fluctuating trajectories: In the semiclassical limit, the out-of-time order correlator corresponds to four classical phase space trajectories as it contains four time evolution operators (two for each time-evolved Heisenberg operator). The trajectories form a connected path as depicted in Fig. 1.2, where the operators constituting the out-of-time order correlator act at the end points, respectively. In the purely classical limit  $\hbar_{\text{eff}} = 0$ , the out-of-time order correlator vanishes as contributions cancels perfectly. However, when taking small fluctuations of order of  $\hbar_{\text{eff}} \ll 1$  around the endpoints into account, contributions interfere constructively and probe the sensitivity of the classical trajectories to changes in their endpoints, i.e. initial conditions.

In what follows, the relation

$$-\langle \psi_0 | [\hat{q}(t), \hat{q}]^2 | \psi_0 \rangle = \hbar^2 \left\langle \left( \frac{\partial q(t)}{\partial p_0} \right)^2 \right\rangle_{\text{PS}}, \quad (1.23)$$

is derived. Here, position  $\hat{q}$  and momentum  $\hat{p}$  operators obey the usual commutation relation,  $[\hat{p}, \hat{q}] = i\hbar$ , and are time-evolved by  $\hat{p}(t) = \hat{U}^\dagger(t) \hat{p} \hat{U}(t)$  with the time evolution operator  $\hat{U}(t)$ . Classical phase space trajectories  $q(t) = q(t, q_0, p_0)$  and  $p(t) = p(t, q_0, p_0)$  obey the Hamilton equations of motion and depend on the initial conditions  $(q_0, p_0)$ .  $|\psi_0\rangle$  denotes an initial pure quantum state, but, in principle, also ensemble averages can be considered. The connection of Eq. (1.23) to Eq. (1.20) is straightforward by using the Fourier representation of operators. In the following derivation, only the main steps are presented whereas details are found in the Appendix A.2.

To connect quantum and classical mechanics, the quantum mechanical time evolution operator is approximated in the limit  $\hbar_{\text{eff}} \ll 1$  by the so-called van Vleck propagator ([Gutzwiller, 1990](#); [Haake, 2010](#); [Altland and Simons, 2010](#)). It approximates the transition amplitude from the initial state  $|q_I\rangle$  to the final state  $|q_F\rangle$  by the sum over all classical trajectories connecting these end points in time  $t$ . Classical trajectories are obtained as saddle-point contributions which minimize the classical action integral, whereas quantum contributions are negligible due to rapid phase fluctuations. Expressed in the position basis, the quantum mechanical propagator is given by ([Haake, 2010](#))

## 1. Introduction to quantum chaos

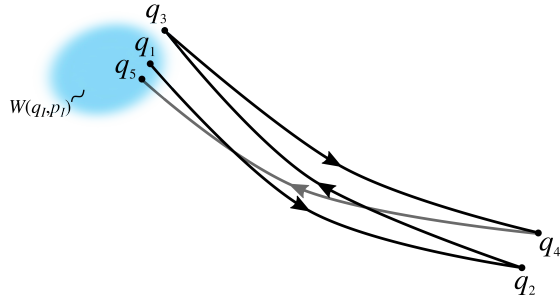


**Figure 1.2.:** Representation of the out-of-time order correlation function in classical phase space which constitutes the out-of-time order correlator Eq. (1.23). Straight lines with endpoints  $q_i$  denote classical trajectories which form a connected path with endpoints  $q_1$  and  $q_5$  related to the initial conditions.  $W(q_I, p_I)$  denotes the phase space distribution function representing the set of initial conditions  $(q_I, p_I)$  which is used for the phase space average.

$$\langle q_F | \hat{U}(t) | q_I \rangle \approx \sum_{\alpha} \mathcal{A}_{\alpha}(t, q_I, q_F) e^{iS_{\alpha}(t, q_I, q_F)/\hbar}, \quad (1.24)$$

where each possible classical trajectory  $\alpha$  with boundary conditions  $q_{\alpha}(0) = q_I$  and  $q_{\alpha}(t) = q_F$  is weighted by a phase factor given by the classical action  $S_{\alpha}(t, q_I, q_F)$ . The amplitude  $\mathcal{A}_{\alpha}(q_I, q_F)$  arises due to leading order quantum fluctuations around the classical trajectories and is kept as normalization constant (Altland and Simons, 2010). In the following, the existence of only one definite classical trajectory connecting  $q_I$  and  $q_F$  is assumed rendering the index  $\alpha$  superfluous. Furthermore, by inserting complete sets of states and replacing sections of time evolution by Eq. (1.24), the out-of-time order correlator is given by

$$\int \left( \prod_{i=1}^5 dq_i \right) \psi_0^*(q_5) \psi_0(q_1) \mathcal{A}^*(t, q_5, q_4) \mathcal{A}(t, q_3, q_4) \mathcal{A}^*(t, q_3, q_2) \mathcal{A}(t, q_1, q_2) \quad (1.25)$$

$$\times \exp \left[ \frac{i}{\hbar} \{ S(t, q_1, q_2) - S(t, q_3, q_2) + S(t, q_3, q_4) - S(t, q_5, q_4) \} \right] q_2(q_1 - q_3)q_4(q_5 - q_3),$$

where  $q_1, q_3, q_5$  denote initial and  $q_2, q_4$  final positions. The out-of-time order correlator is hence represented by four connected trajectories whose initial and final endpoints  $q_1$  and  $q_5$  are determined by initial conditions as depicted in Fig. 1.2. Contributions to the out-of-time order correlator are weighted by the phase factor and are possibly penalized by rapid phase fluctuations. Therefore, configurations of trajectories which contribute obey

$$S(t, q_1, q_2) - S(t, q_3, q_2) + S(t, q_3, q_4) - S(t, q_5, q_4) \sim \hbar, \quad (1.26)$$

where the purely classical case,  $S(t, q_1, q_2) - S(t, q_3, q_2) + S(t, q_3, q_4) - S(t, q_5, q_4) = 0$ , refers to coinciding endpoints  $q_1 = q_3 = q_5$  and  $q_2 = q_4$ . However, for this particular configuration, the out-of-time order correlator vanishes because of a vanishing integrand in Eq. (1.25). Thus, leading order contributions are given by constructively interfering trajectories. These contributions are necessarily small in  $\hbar$  and are captured by expand-

ing the position of endpoints in small deviations from their classical configuration. By introducing the Wigner function of the initial system's state,  $\int \frac{dp_0}{2\pi\hbar} W(q_0, p_0) e^{-ip_0x/\hbar} = \psi_0^*(q_0 + \frac{x}{2})\psi_0(q_0 - \frac{x}{2})$ , where  $W(q_0, p_0)$  can be interpreted as quasiprobability distribution function in phase space, and by integrating out fluctuations, the out-of-time correlator is given by

$$- \langle \psi_0 | [\hat{q}_z(t), \hat{q}_z]^2 | \psi_0 \rangle = \frac{\hbar^2}{4} \int \frac{dq_0 dp_0}{2\pi\hbar} W(q_0, p_0) \left( \frac{\partial q(t)}{\partial p_0} \right)^2, \quad (1.27)$$

which equates to the left-hand side of Eq. (1.23) with the phase space average specified by  $W(q_0, p_0)$ .

In the derivation conducted above, the existence of the small parameter  $\hbar_{\text{eff}} \ll 1$  was essential to relate quantum operator dynamics and classical phase space dynamics. This picture may even be extended to certain quantum chaotic theories which do not possess a strict classical counterpart: If the small parameter, which ensures the exponential growth of out-of-time order correlator growth as discussed in Sec. 1.4, can be used to obtain an effective quasiclassical theory, quantum chaotic behavior may be traced back to chaotic dynamics of the classical theory. This idea is expanded in the outlook Sec. 2.7 of the next chapter.

### 1.7.2. QUANTUM CHAOTIC DYNAMICS OF A DISORDERED METAL

Out-of-time order correlators evaluated in the semiclassical limit are connected to the sensitivity of classical phase space trajectories to changes in initial conditions. This connection and the notion of the Ehrenfest time  $t_E$  is illustrated for electrons in a disordered metal where particles move in a static disorder potential due to elastic impurity scattering. In the limit of hard sphere impurity potentials, this model maps to the so-called Sinai billiard which represents a toy model for classical chaotic dynamics (Chirikov, 1979). The presented model represents the microscopic basis for the work presented in Ref. Klug and Syzranov (2019) and the work which is discussed later in Ch. 3.

The system of electrons in a disordered metal is considered, where conduction electrons are described by wave packets which are localized in space on order of the Fermi wave length  $\lambda_F = \frac{\hbar}{p_F}$  and which propagate with the Fermi velocity  $v_F = \frac{p_F}{m}$ . The disorder is described by static scattering centers with impurity potentials varying on length scale  $a$  which are separated by the mean-free path  $l_{\text{tr}} = v_F \tau_0$ , where  $\tau_0$  denotes the elastic scattering time of electrons. To observe quantum chaotic dynamics, the electrons have to propagate quasiclassically for times  $t \gg \tau_0$  which requires scattering centers to be sufficiently large, short-ranged and separated (Aleiner and Larkin, 1996): As electron wave packets are localized on length scales of order of  $\lambda_F$ , the uncertainty in scattering angle is  $\delta\theta \sim \frac{\lambda_F}{a}$ . During ballistic propagation, the uncertainty increases to  $\delta r \sim l_{\text{tr}} \delta\theta$  before the particle hits the next scatterer. For classical propagation to continue, this requires  $\delta r \ll a$  which yields a condition on the scatterer's size and the elastic scattering time,  $a \gg \sqrt{\lambda_F v_F \tau_0}$ . Apparently, the uncertainty increases exponentially with  $\delta r(t) \sim \lambda_F e^{\lambda_{\text{cl}} t}$

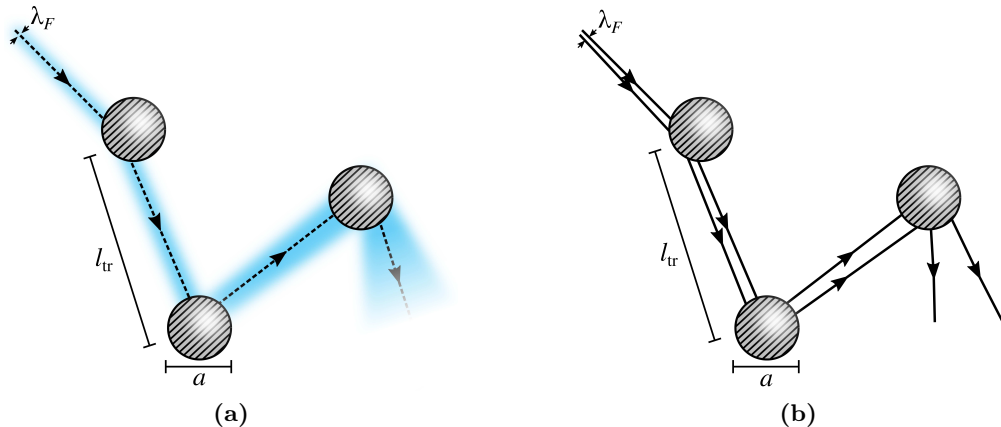


**Figure 1.3.:** Quantum chaotic dynamics in a disordered metal. Grey spots represents impurity potentials with size  $a$  which are separated by the mean-free path  $l_{\text{tr}} = v_F \tau_0$  with the elastic scattering time  $\tau_0$ . Solid lines denote classical trajectories of electrons. (a) Increasing uncertainty represented by the bluish trace associated with an electron wave packet which is initially confined to lengths  $\lambda_F$ . (b) Diverging mismatch of two trajectories which are initially close on order of  $\lambda_F$ .

with the classical Lyapunov exponent  $\lambda_{\text{cl}}$  as it relates to the fastest growing mismatch between two classical trajectories.  $\lambda_{\text{cl}}$  can be read off from the previous discussion to  $\lambda_{\text{cl}} \sim \tau_0^{-1} \log \frac{l_{\text{tr}}}{a}$  and is of order of the elastic scattering time. If the uncertainty is of order of the impurity size,  $\delta r(t_E) \sim a$ , further propagation relies on wave mechanics and the classical approximation breaks down. The Ehrenfest time is therefore defined by  $t_E = \lambda_{\text{cl}}^{-1} \log \hbar_{\text{eff}}^{-1}$  with  $\hbar_{\text{eff}} = \frac{\lambda_F}{a} = \frac{\hbar}{p_F a} \ll 1$ . Whereas the electron propagator is determined by classical trajectories for  $t < t_E$ , diffusive propagation is present for  $t > t_E$ .

Applied to the momentum out-of-time order correlator Eq. (1.20), the right-hand side, which contains only classical quantities, can readily be evaluated: At each scattering event the momentum mismatch of two classical trajectories increases by  $\delta p \sim p_F \delta \theta \sim \frac{p_F}{l_{\text{tr}}} \delta r$  yielding a time-dependent momentum mismatch of  $\delta p(t) \sim \frac{p_F \lambda_F}{l_{\text{tr}}} e^{\lambda_{\text{cl}} t}$ . By approximating  $|\frac{\partial p(t)}{\partial z_0}| \approx \frac{\delta p(t)}{\lambda_F}$ , the out-of-time order correlator increases exponentially,

$$- \langle [\hat{p}_z(t), \hat{p}_z]^2 \rangle \sim e^{2\lambda_{\text{cl}} t}, \quad (1.28)$$

where the growth persists for times  $\tau_0 < t < t_E$ . For  $t > t_E$ , diffusive propagation sets in and the out-of-time order correlator is expected to saturate.

This example of quantum chaotic behavior connected to classical chaotic behavior relies on the smallness of the parameter  $\hbar_{\text{eff}} = \frac{\lambda_F}{a} \ll 1$  and illustrates the equivalence of  $\lambda_{\text{cl}}$  and  $\lambda_L$  for out-of-time order correlators evaluated in the semiclassical limit. The process of impurity scattering as well as the equivalence of a growing uncertainty and the diverging mismatch between two trajectories is depicted in Fig. 1.3. Details on the computation of two diverging classical trajectories is found in Appendix A.1, whereas an explicit evaluation of the out-of-time order correlator Eq. (1.28) is presented in Ch. 3.

## 1.8. CONCLUSION AND OUTLOOK

In this chapter, the concept of out-of-time order correlators was introduced and a relation to entanglement growth as well as the fundamental process of thermalization was indicated. This special type of correlators was characterized by an out-of-time ordered sequence of operators which renders them non-observable in conventional experiments. In the semiclassical limit, it was argued that out-of-time order correlators are proportional to the sensitivity of classical phase space trajectories to initial conditions underlining the resemblance between classical chaotic and quantum chaotic behavior.

It was pointed out that the exponential growth of out-of-time order correlators is fundamentally connected to the existence of a small parameter  $\epsilon$  characterizing the quantum chaotic regime and rendering the scrambling rate  $\lambda_L$  and scrambling time  $t^*$  well-defined quantities. In contrast, systems exhibiting slow (polynomial) out-of-time order correlator growth are expected to be non-ergodic and hence non-scrambling. In other systems,  $\epsilon$  does not exist and  $\lambda_L$  and  $t^*$  are hence ill-defined objects. This, however, does not imply that the system is non-scrambling, but rather information scrambling may not be characterized by out-of-time order correlators.

The dynamics of out-of-time order correlators may further depend on the choice of operators. Generally, it is expected that the leading order exponential growth, and hence  $\lambda_L$ , are independent of the particular choice as generic operators are expected to have a finite overlap with those operators exhibiting the most rapid growth. Obviously, it does not hold for conserved quantities  $\hat{X}$  which obey  $[\hat{H}, \hat{X}] = 0$ . Therefore, physical insight is necessary to make a “meaningful” choice of operators which are susceptible to quantum chaotic dynamics.

To further gain insight into the role of out-of-time order correlators in condensed matter physics, the scrambling rate  $\lambda_L$  is determined in Ch. 2 for interacting electrons in graphene and compared to other physical scales, e.g. representative for thermalization. The aspect of a possible experimental determination of  $\lambda_L$  is addressed in Ch. 3 which is based on a proposed link between exponential operator growth and fluctuation dynamics of observables.

Out-of-time order correlators characterize the ability of a system to scramble quantum information. In the case of quantum chaotic systems, out-of-time order correlators grow exponentially specified by the scrambling rate  $\lambda_L$  and the Butterfly velocity  $v_B$ . Whereas  $\lambda_L$  is well-defined theoretically, its role for observable effects or observable quantities is little understood and deserves further investigation as discussed in Ch. 1.

To gain further insight, information scrambling is investigated for the model of electrons in graphene which interact via long-range Coulomb interaction. For this, an out-of-time order correlator is evaluated and  $\lambda_L$  is determined in a controlled large- $N$  perturbation series where the total number of electron flavors in graphene is given by  $N = 4$  because of the electronic spin and valley degrees of freedom. The presence of a small parameter  $N^{-1} \ll 1$  indicates the existence of a quantum chaotic regime and an exponential growth of out-of-time order correlators is expected.

Subsequently,  $\lambda_L$  is compared to single-particle rates which are, among others, representative for the processes of thermalization to shed light on the microscopic mechanism which determines the rate of information scrambling. In particular,  $\lambda_L$  is compared to certain single-particle rates which are generally functions of the single-particle excitation's energy  $\epsilon$ : the quantum dephasing rate  $\tau_q^{-1}(\epsilon)$  which is representative for the inelastic electron-electron scattering rate, the energy relaxation rate  $\tau_E^{-1}(\epsilon)$  which is characteristic for thermalization processes when evaluated for  $\epsilon \sim k_B T$ , and the transport relaxation rate  $\tau_{tr}^{-1}(\epsilon)$  which is representative for hydrodynamic relaxation processes when evaluated for  $\epsilon \sim k_B T$ .

Similar approaches revealed that the chaos diffusion coefficient  $D_L = \frac{v_B^2}{4\lambda_L}$ , which was introduced in Eq. (1.14), resembles the transport coefficients of charge and energy diffusion in strongly coupled, holographic theories (Blake, 2016a,b), whereas it relates to the energy diffusion coefficient in electronic systems which are strongly coupled to phonons (Werman *et al.*, 2017) or gauge bosons (Patel and Sachdev, 2017). Furthermore, the scrambling rate was determined to match the inelastic electron-electron scattering rate in a weakly interacting diffusive metal (Patel *et al.*, 2017) and is given for a Fermi liquid by  $\lambda_L \sim \frac{k_B^2 T^2}{\hbar c_F}$  (Banerjee and Altman, 2017; Aleiner *et al.*, 2016) resembling the Fermi liquid relaxation rate (Baym and Pethick, 1991).

### 2.1. SUMMARY OF RESULTS

In what follows, a diagrammatic approach is presented to determine  $\lambda_L$  for Dirac electrons in graphene which interact via long-range Coulomb interaction. The presented results are based on work which was published in Ref. Klug *et al.* (2018). In addition, an estimate for the Butterfly velocity  $v_B$  is given. As these quantities are determined in a perturbative manner controlled by the small parameter  $N^{-1} \ll 1$ , the electron-electron interaction strength, which is determined by the dimensionless effective fine structure constant

$$\alpha = \frac{Ne^2}{\hbar v_F \epsilon}, \quad (2.1)$$

with electron charge  $e$ , electric permittivity  $\epsilon$  and the Fermi velocity  $v_F$ , is considered variable. This allows one to study a weak ( $\alpha \ll 1$ ) and a strong-coupling regime ( $\alpha \gg 1$ ). Although  $\alpha \approx 1$  in realistic experimental settings (Novoselov *et al.*, 2005), a variable  $\alpha$  allows one to discriminate between the physical scales introduced earlier, which are characterized by different powers of  $\alpha$ , and to compare them with  $\lambda_L$ .

In the strong-coupling regime, the scrambling rate is determined to (Klug *et al.*, 2018)

$$\lambda_L(\alpha \gg 1) \simeq 0.80 \frac{4}{N} \frac{2\pi k_B T}{\hbar}, \quad (2.2)$$

which is similar to results obtained for other large- $N$  theories (Chowdhury and Swingle, 2017). As  $N^{-1} \ll 1$ , the rate is parametrically smaller than the bound on out-of-time order correlator growth rates as discussed in Sec. 1.5, even if extrapolated to  $N = 4$  which is representative for electrons graphene. It furthermore resembles the transport relaxation time  $\tau_{tr}^{-1}(\epsilon \sim k_B T) \sim \frac{k_B T}{\hbar N}$  which was determined in Ref. Link *et al.* (2018) in the same limit. However, as the temperature is the only energy scale present, similar results are also expected for the other rates introduced earlier and a clear assignment is hardly possible.

In the weak-coupling limit, the scrambling rate is determined to (Klug *et al.*, 2018)

$$\lambda_L(\alpha \ll 1) \gtrsim 0.37 \alpha \frac{4}{N} \frac{2\pi k_B T}{\hbar}, \quad (2.3)$$

which is parametrically small in  $\alpha$ . The result  $\lambda_L \propto \alpha$  is surprising as a naive power counting of interaction vertices suggests a quadratic dependence on the coupling strength. The finding is traced back to the dynamical screening of electron charge due to particle-hole fluctuations opening up a window for small momentum transfers which is independent on  $\alpha$  but limited by the inverse thermal screening length  $l_s^{-1} \sim \alpha \ln 2 \frac{k_B T}{v_F \hbar}$ . The very same screening length was also found in Ref. Schütt *et al.* (2011) in the determination of single-particle relaxation rates in graphene.

Compared to the previously introduced single-particle scales, the rate of information scrambling is parametrically larger than the transport relaxation rate  $\tau_{tr}^{-1}(\epsilon \sim k_B T) \sim \alpha^2 \frac{k_B T}{\hbar N}$  (Schütt *et al.*, 2011) which is representative for hydrodynamic transport coefficients such as dc conductivity (Fritz *et al.*, 2008) and viscosity (Müller *et al.*, 2009). It is

## 2. Quantum chaos in graphene

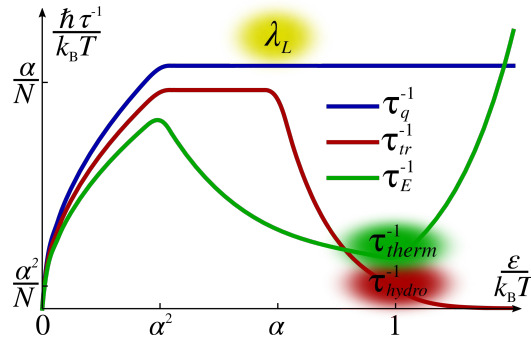


**Figure 2.1.:** The scrambling rate  $\lambda_L$  determined for electrons in graphene in the presence of long-range Coulomb interaction in the weak-coupling limit  $\alpha \ll 1$  and compared to single-particle rates obtained in Ref. Schütt *et al.* (2011). The obtained results indicate that  $\lambda_L$  rather resembles the single-particle quantum dephasing rate  $\tau_q^{-1}$  which is parametrically larger than rates representative for thermalization  $\tau_{therm}^{-1} = \tau_E^{-1}(\epsilon \sim k_B T)$  and hydrodynamic  $\tau_{hydro}^{-1} = \tau_{tr}^{-1}(\epsilon \sim k_B T)$  transport. Reprinted figure with permission from [M.J. Klug, M.S. Scheurer, and J. Schmalian, Phys. Rev. **B** 98, 045102] Copyright (2018) by the American Physical Society. The original work is found under <https://dx.doi.org/10.1103/PhysRevB.98.045102>.

also parametrically larger than the energy relaxation rate  $\tau_E^{-1}(\epsilon \sim k_B T) \sim \alpha^2 \log \alpha^{-1} \frac{k_B T}{\hbar N}$  (Schütt *et al.*, 2011) which is representative for single-particle thermalization processes. It rather resembles the quantum dephasing rate evaluated for energies determined by the inverse screening length,  $\tau_q^{-1}(\epsilon \sim v_F \hbar l_s^{-1}) \sim \alpha \frac{k_B T}{\hbar N}$  (Schütt *et al.*, 2011). The results indicate that information scrambling in graphene is not related to processes which determine thermalization or establish hydrodynamic transport but is rather connected to single-particle scattering processes. The results for the scrambling rate and the comparison to the discussed single-particle rates are illustrated in Fig. 2.1.

Furthermore, the Butterfly velocity specifying the spreading of information in space is estimated for both coupling regimes to the Fermi velocity,  $v_B \propto v_F$  which is in line with previous studies presented in Refs. Chowdhury and Swingle (2017); Werman *et al.* (2017).

In what follows, the evaluation of an out-of-time order correlator to determine the scrambling rate for interacting electrons in graphene is presented in detail. The microscopic model for interacting electrons in graphene is introduced in Sec. 2.2. Subsequently, the out-of-time order correlator, which is used to study information scrambling, is defined in Sec. 2.3. The technical aspects of the evaluation of out-of-time order correlators are discussed within the derived “augmented Keldysh formalism” in Sec. 2.4 which allows the evaluation of out-of-time order correlators for quantum field theories. This discussion is followed by the presentation of the diagrammatic approach to determine the scrambling rate  $\lambda_L$  and the Butterfly velocity  $v_B$  in Sec. 2.5. In Sec. 2.6, microscopic details of information scrambling for interacting electrons in graphene are discussed. This chapter concludes in Sec. 2.7.

## 2.2. MICROSCOPIC MODEL

In neutral graphene, electronic low-energy excitations, so-called “Dirac electrons”, are confined to a two-dimensional, hexagonal lattice of carbon atoms and are characterized by an ultrarelativistic, linear dispersion relation. In the presence of Coulomb interaction, the interacting electronic system resembles high-energy electrons which interact via photon exchange and is described within quantum electrodynamics, however, with a much smaller velocity  $v_F$  in comparison to the speed of light  $\frac{v_F}{c} \approx \frac{1}{300}$  (Novoselov *et al.*, 2005). This renders the effective electron-electron interactions quasi instantaneous. In contrast to quantum electrodynamics, where the coupling constant is small  $\alpha_{\text{QED}} \approx \frac{1}{137} \ll 1$  justifying a perturbative treatment of interaction effects,  $\alpha \approx 1$  in graphene and interactions are not negligible. Actually, interaction effects are relevant and result, e.g., in a strongly renormalized ultrarelativistic single-particle spectrum (Elias *et al.*, 2011).

### 2.2.1. INTERACTING DIRAC ELECTRONS IN GRAPHENE

On the single-particle level, the relevant electronic excitations at low energies and low temperatures are described by a linear dispersion relation with the conduction and valence bands touching at the two non-equivalent  $K$ -points of the hexagonal Brillouin zone (Castro Neto *et al.*, 2009). As these two points are separated by a large momentum of order of the inverse lattice constant, these two types of electrons effectively decouple which generating an emergent “valley symmetry” which can be associated with a binary quantum number. The valley degree of freedom combined with the electron spin gives rise to  $N = 4$  fermionic flavors labeled by the index  $i$ . The interaction-free Hamilton operator is described by (setting  $\hbar = 1$  in the following)

$$\hat{H}_0 = v_F \sum_{i=1}^N \sum_{\alpha\beta} \int d^2\mathbf{x} \hat{\psi}_i^\dagger(\mathbf{x}) (-i\nabla \cdot \vec{\sigma}) \hat{\psi}_i(\mathbf{x}), \quad (2.4)$$

with the Fermi velocity  $v_F$  and the two-component fermionic field operator  $\hat{\psi}_i = (\hat{\psi}_A, \hat{\psi}_B)_i^T$  representing the two-dimensional crystalline sublattice basis, also called “pseudospin” in the following. The field operators obey the usual anticommutation relation,  $\{\hat{\psi}_{i\alpha}^\dagger(\mathbf{x}), \hat{\psi}_{j\beta}(\mathbf{x}')\} = \delta_{ij} \delta_{\alpha\beta} \delta(\mathbf{x} - \mathbf{x}')$ , and the Pauli matrices  $\vec{\sigma}_{\alpha\beta} = (\sigma_x, \sigma_y)_{\alpha\beta}$  act in the pseudospin basis.

Long-range Coulomb interaction is described by

$$\hat{H}_{\text{int}} = \frac{e^2}{2\epsilon} \sum_{i,j=1}^N \int d^2\mathbf{x} d^2\mathbf{x}' \frac{\hat{\rho}_i(\mathbf{x}) \hat{\rho}_j(\mathbf{x}')}{|\mathbf{x} - \mathbf{x}'|}, \quad (2.5)$$

with the charge density operator  $\hat{\rho}_i(\mathbf{x}) = \hat{\psi}_i^\dagger(\mathbf{x}) \hat{\psi}_i(\mathbf{x})$ , the electron charge  $e$  and the electrical permittivity  $\epsilon$ , which is determined by the substrate.

Whereas the kinetic energy contributions dominate for high densities over potential energy contributions in the case of quadratic dispersion relations (and vice versa for low

## 2. Quantum chaos in graphene

densities), the relative interaction strength of Dirac electrons represented by  $\alpha$  is independent of the electron density rendering the contributions from interactions ubiquitous and marginally relevant in the sense of the renormalization group approach (Sheehy and Schmalian, 2007). The quantities  $\alpha$  and  $v_F$  are therefore considered quantities which are renormalized by interaction processes.

### 2.2.2. EFFECTIVE LOW-ENERGY THEORY

In what follows, the number of fermion flavors is kept as a larger parameter,  $N \gg 1$ , to control the perturbative expansion of the out-of-time order correlator in orders of  $N^{-1}$ . This approach follows established large- $N$  approaches to interacting electrons in graphene (Son, 2007; Foster and Aleiner, 2008) as the renormalization group approach assisted with large- $N$  perturbation theory is consistent with experiments probing interaction effects in graphene (Elias *et al.*, 2011; Siegel *et al.*, 2011; Yu *et al.*, 2013). In the large- $N$  limit, fermionic self-energy corrections which are of order  $N^{-1}$  are suppressed, whereas screening effects due to particle-hole fluctuations in the charge channel are of order unity. This suggest to decouple the interaction term Eq. (2.5) in the charge channel by introducing a real plasmon field.

The effective theory, which is considered in the following, is first represented in the imaginary time domain to specify the microscopic details and is later extended to the augmented Keldysh formalism to evaluate out-of-time order correlators. Its effective action is given by

$$S_\tau[\psi, \bar{\psi}, \phi] = - \sum_{i=1}^N \int_{xx'} \bar{\psi}_i^\dagger(x) \mathbf{G}^{-1}(x, x') \psi_i(x') + \frac{i}{\sqrt{N}} \sum_{i=1}^N \int_x \psi_i^\dagger(x) \psi_i(x) \phi(x) - \frac{1}{2} \int_{xx'} \phi(x) D^{-1}(x, x') \phi(x'), \quad (2.6)$$

with the two-component Grassmann fields  $\psi(x), \bar{\psi}(x)$  representing Dirac electrons and the real-valued field  $\phi(x)$  representing plasmon excitations with  $x = (\mathbf{x}, \tau)$ , imaginary time  $\tau$  and  $\int_x = \int d^2\mathbf{x} d\tau$ . The coupling vertex of plasmons and fermion densities is suppressed by a factor of  $N^{-1/2}$ . Components of the fermionic propagator are given after Fourier transform by

$$G_{\alpha\beta}(\mathbf{k}, i\epsilon) = [i\epsilon \boldsymbol{\sigma}_0 - v_F \mathbf{k} \cdot \vec{\boldsymbol{\sigma}}]_{\alpha\beta}^{-1}, \quad (2.7)$$

with the imaginary frequency  $i\epsilon$ . For later purposes, it is convenient to express Eq. (2.7) in the diagonal band basis. By introducing the projection operator

$$P_{\alpha\beta, \mathbf{k}}^\pm = \frac{1}{2} \left( \delta_{\alpha\beta} \pm \frac{\vec{\sigma}_{\alpha\beta} \cdot \mathbf{k}}{|\mathbf{k}|} \right), \quad (2.8)$$

with the properties  $\mathbf{P}_{\mathbf{k}}^a \mathbf{P}_{\mathbf{k}}^b = \delta_{ab} \mathbf{P}_{\mathbf{k}}^a$  and  $\text{tr}[\mathbf{P}^a(\mathbf{k}) \mathbf{P}^b(\mathbf{k}')] = \frac{1}{2} \left( 1 + ab \frac{\mathbf{k} \cdot \mathbf{k}'}{|\mathbf{k}| |\mathbf{k}'|} \right)$  and the band

## 2. Quantum chaos in graphene

indices  $a, b = \pm 1$ , the electronic Green's functions is expressed in the band basis by

$$G_a(\mathbf{k}, i\epsilon) = \text{tr} [\mathcal{P}_{\mathbf{k}}^a \mathbf{G}(\mathbf{k}, i\epsilon)] = \frac{1}{i\epsilon - av_F |\mathbf{k}|}. \quad (2.9)$$

The bosonic propagator is dressed by particle-hole fluctuations as the closed fermion loop provides a factor of  $N$  canceling the factor of  $N^{-1}$  of the two coupling vertices. By a resummation of an infinite bubble series, the dressed propagator is given by

$$D(\mathbf{q}, i\omega) = [D_0^{-1}(\mathbf{q}) + \Pi(\mathbf{q}, i\omega)]^{-1}, \quad (2.10)$$

where the bare plasmon propagator is given by  $D_0(\mathbf{q}) = \frac{2\pi e^2}{\epsilon |\mathbf{q}|}$  and the polarization operator by

$$\Pi(\mathbf{q}, i\omega) = k_B T \sum_n \int \frac{d^2 k}{(2\pi)^2} \text{tr} [\mathbf{G}(\mathbf{q} + \mathbf{k}, i\omega + i\epsilon_n) \mathbf{G}(\mathbf{k}, i\epsilon_n)]. \quad (2.11)$$

Here,  $k_B T \sum_n$  denotes the sum over Matsubara frequencies. The evaluation of  $\Pi(\mathbf{q}, i\omega)$  is standard and an explicit expression is found in the Appendix A.4, whereas it is referred to Ref. Schütt *et al.* (2011) for a detailed derivation.

In the following, the effective action Eq. (2.6) represented in the imaginary time domain is recast within the augmented Keldysh formalism, which is derived in Sec. 2.4. This framework is necessary to evaluate out-of-time order correlators because of the out-of-time order sequence of operators. However, the diagrammatic rules, which are useful in the perturbative treatment of expectation values, are already deduced by inspecting the effective action Eq. (2.6): Every interaction vertex is suppressed by a factor of  $N^{-1/2}$ , whereas each closed fermionic loop contributes a factor of  $N$ . This allows one to determine the leading order diagrams which contribute to information scrambling straightforwardly by power counting.

### 2.3. FERMIONIC OUT-OF-TIME ORDER CORRELATOR

The scrambling rate is determined by considering an out-of-time order correlator of fermionic field operators. As the Dirac electrons represent the relevant dynamical modes causing information to scramble, the fermionic operators  $\hat{\psi}, \hat{\psi}^\dagger$  are considered a meaningful choice of operators. As the electron-electron interaction is mediated by plasmon excitations, an out-of-time order correlator of “plasmon operators” is expected to yield equivalent results. In the case of fermionic field operators, it is reasonable to replace the commutators in the original definition Eq. (1.7) by anticommutators,  $\{\hat{V}, \hat{W}\} \equiv \hat{V}\hat{W} + \hat{W}\hat{V}$ , which ensures an initial vanishing of the out-of-time order correlator. The considered out-of-time order correlator is given by (Klug *et al.*, 2018)

$$C(t) = \theta(t) \int d^2 \mathbf{x} \sum_{\alpha\beta} f_{\alpha\beta}^{\alpha\beta}(x, 0, x, 0) \quad (2.12)$$



## 2. Quantum chaos in graphene

By introducing the contour of time integration  $\mathcal{C}$  as depicted in Fig. 2.2 and the contour evolution operator  $\hat{U}_{\mathcal{C}} = \hat{\mathcal{T}}_{\mathcal{C}} \exp[-\frac{i}{\hbar} \int_{\mathcal{C}} dt \hat{H}(t)] \rho_0$  with contour ordering operator  $\hat{\mathcal{T}}_{\mathcal{C}}$ , the out-of-time order correlation function is written as

$$\langle \hat{V}(t) \hat{W}(0) \hat{V}(t) \hat{W}(0) \rangle = \text{tr}[\hat{U}_{\mathcal{C}} \hat{V}_t^{l-} \hat{W}_0^{l+} \hat{V}_t^{u-} \hat{W}_0^{u+}], \quad (2.15)$$

where the position of operators on the contour is specified, besides the time argument  $\{0, t\}$ , by the index  $\{u, l\}$  denoting the upper and lower loop, and by the indices  $\{+, -\}$  denoting the forward and backward in time propagating branches. This principle constitutes the basis of the augmented Keldysh formalism presented in the following.

### 2.4.1. AUGMENTED KELDYSH CONTOUR

Representing out-of-time order correlators by means of contour ordered expectation values requires the introduction of a second loop of time integration. Additionally, fractions of the thermal density matrix  $\sqrt{\rho} = Z^{-1/2} \exp[-\frac{\hat{H}}{2k_B T}]$  are placed at the two left endpoints of the integration contour as a “regularized” out-of-time order correlator (see Sec. 1.5 for details) is considered. The resulting contour is depicted in Fig. 2.3. As a result, an additional component of the single-particle correlation function connecting the upper and lower loop emerges which resembles the Keldysh component (or the greater and lesser component) of the conventional “single-loop” Keldysh formalism (Mahan, 2000; Kamenev, 2011).

The presented derivation of the augmented Keldysh formalism uses the basic concepts and conventions established in the context of the conventional Keldysh formalism presented, e.g., in Ref. Kamenev (2011). It is derived for fermionic and bosonic degrees of freedom represented by the Grassmann fields  $\psi, \bar{\psi}$  and the real-valued field  $\phi$ , respectively. Details which are specific for electron and plasmon dynamics in graphene are dropped at first but are restored later when necessary.

The augmented Keldysh contour contains four branches labeled by the indices  $\sigma \in \{u, l\}$  denoting the upper and lower Keldysh loop and the indices  $\{+, -\}$  representing the branches which propagate forward and backward in time, respectively. For each branch, a field component is introduced yielding the four component fields (dropping the time argument in the following)

$$\psi = [\psi^{u+}, \psi^{u-}, \psi^{l+}, \psi^{l-}], \quad (2.16a)$$

$$\bar{\psi} = [\bar{\psi}^{u+}, \bar{\psi}^{u-}, \bar{\psi}^{l+}, \bar{\psi}^{l-}], \quad (2.16b)$$

$$\phi = [\phi^{u+}, \phi^{u-}, \phi^{l+}, \phi^{l-}]. \quad (2.16c)$$

Single-particle propagators are conveniently expressed in the space of “classical” and “quantum” field components. By applying the so-called Keldysh rotation (Kamenev, 2011), these components are given in the case of Grassmann fields by

## 2. Quantum chaos in graphene

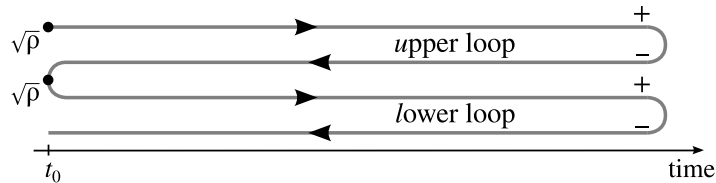


**Figure 2.3.:** Augmented Keldysh contour required to compute the regularized out-of-time order correlator Eq. (2.13), where fractions of the thermal density matrix  $\sqrt{\rho}$  are placed at  $t_0 \rightarrow -\infty$  to account for the equilibrium state of the system. Reprinted figure with permission from [M.J. Klug, M.S. Scheurer, and J. Schmalian, Phys. Rev. **B** 98, 045102] Copyright (2018) by the American Physical Society. The original work is found under <https://dx.doi.org/10.1103/PhysRevB.98.045102>.

$$\psi^{\sigma\text{cl}} = \frac{1}{\sqrt{2}}(\psi^{\sigma+} + \psi^{\sigma-}), \quad \psi^{\sigma\text{q}} = \frac{1}{\sqrt{2}}(\psi^{\sigma+} - \psi^{\sigma-}), \quad (2.17\text{a})$$

$$\bar{\psi}^{\sigma\text{cl}} = \frac{1}{\sqrt{2}}(\bar{\psi}^{\sigma+} - \bar{\psi}^{\sigma-}), \quad \bar{\psi}^{\sigma\text{q}} = \frac{1}{\sqrt{2}}(\bar{\psi}^{\sigma+} + \bar{\psi}^{\sigma-}), \quad (2.17\text{b})$$

whereas in the case of real fields by

$$\phi^{\sigma\text{cl}} = \frac{1}{2}(\phi^{\sigma+} + \phi^{\sigma-}), \quad \phi^{\sigma\text{q}} = \frac{1}{2}(\phi^{\sigma+} - \phi^{\sigma-}), \quad (2.18)$$

assigning a specific causality structure to single-particle correlation functions. The single-particle correlation functions are defined as

$$G_{\sigma's',\sigma s}(t,t') = -i\langle\psi^{\sigma's'}(t)\bar{\psi}^{\sigma s}(t')\rangle, \quad (2.19\text{a})$$

$$D_{\sigma's',\sigma s}(t,t') = -i\langle\phi^{\sigma's'}(t)\phi^{\sigma s}(t')\rangle, \quad (2.19\text{b})$$

with the field component index  $s \in \{\text{cl}, \text{q}\}$ . In the case of intraloop correlations,  $\sigma = \sigma'$ , the correlators are identical to those of the conventional Keldysh formalism and are given by (Kamenev, 2011)

$$G_{\sigma\sigma,ss'} = \begin{pmatrix} G^R & G^K \\ 0 & G^A \end{pmatrix}_{ss'} \quad \text{and} \quad D_{\sigma\sigma,ss'} = \begin{pmatrix} D^K & D^R \\ D^A & 0 \end{pmatrix}_{ss'}, \quad (2.20)$$

where the retarded ( $R$ ) and advanced ( $A$ ) components are analytic in the lower and upper half plane of complex frequencies, respectively, whereas the intra-loop Keldysh ( $K$ ) component contains information about the system's single-particle distribution function and is given in thermal equilibrium by

$$G^K(\mathbf{k}, \epsilon) = 2i \tanh\left(\frac{\epsilon}{2k_B T}\right) \text{Im}G^R(\mathbf{k}, \epsilon). \quad (2.21)$$

In the case of interloop correlations,  $\sigma \neq \sigma' \equiv \bar{\sigma}$ , the notion of retarded and advanced correlations is superfluous and the respective components vanish exactly. The interloop

## 2. Quantum chaos in graphene

components are therefore given by (Klug *et al.*, 2018)

$$G_{\sigma\bar{\sigma},ss'} = \begin{pmatrix} 0 & G_{\sigma\bar{\sigma}}^K \\ 0 & 0 \end{pmatrix}_{ss'} \quad \text{and} \quad D_{\sigma\bar{\sigma},ss'} = \begin{pmatrix} D_{\sigma\bar{\sigma}}^K & 0 \\ 0 & 0 \end{pmatrix}_{ss'}, \quad (2.22)$$

where the Keldysh components expressed in their spectral representation are given in thermal equilibrium by

$$G_{lu}^K(\mathbf{k}, \epsilon) = \frac{2i\text{Im}G^R(\mathbf{k}, \epsilon)}{\cosh\left(\frac{\epsilon}{2k_B T}\right)} \quad \text{and} \quad D_{lu}^K(\mathbf{q}, \omega) = \frac{2i\text{Im}D^R(\mathbf{q}, \omega)}{\sinh\left(\frac{\epsilon}{2k_B T}\right)}. \quad (2.23)$$

suppressing excitations with excitation energies  $|\epsilon| > k_B T$ . This characteristic is traced back to the regularization scheme, i.e. on the placement of fractions of the density matrix, and is discussed in detail in the derivation of Eq. (2.23) presented in the Appendix A.3.

### 2.4.2. AUGMENTED KELDYSH ACTION

By having established the central building blocks of the augmented Keldysh formalism in the previous section, the effective action describing electron and plasmon dynamics in graphene as introduced in Eq. (2.6) in the imaginary time domain is rewritten to obtain the augmented Keldysh action. The interaction-free part is given by (Klug *et al.*, 2018)

$$S_0[\psi, \bar{\psi}, \phi] = \sum_{\sigma(\prime)s(\prime)} \left[ \sum_{i=1}^N \int_{\mathbf{k}, \epsilon} \bar{\psi}_{i,\mathbf{k}}^{\sigma s}(\epsilon) \mathbf{G}_{\sigma\sigma',ss'}^{-1}(\mathbf{k}, \epsilon) \psi_{i,\mathbf{k}}^{\sigma' s'}(\epsilon) + \int_{\mathbf{q}, \omega} \phi_{-\mathbf{q}}^{\sigma s}(-\omega) D_{\sigma\sigma',ss'}^{-1}(\mathbf{q}, \omega) \phi_{\mathbf{q}}^{\sigma' s'}(\omega) \right], \quad (2.24)$$

with real frequencies  $\epsilon, \omega$  and  $\int_{\mathbf{k}, \epsilon} \equiv \int \frac{d^2\mathbf{k}}{(2\pi)^2} \int \frac{d\epsilon}{2\pi}$ . The single-particle propagators  $\mathbf{G}$  and  $D$  are specified in Eqs. (2.20) and (2.22), where retarded and advanced components are obtained by analytic continuation from Eqs. (2.7) and (2.10). The Keldysh components are given by employing their spectral representations Eqs. (2.21) and (2.23).

The interaction between electron and plasmon fields, which is diagonal in Keldysh loop indices, is obtained to (Klug *et al.*, 2018)

$$S_{\text{int}}[\psi, \bar{\psi}, \phi] = \frac{1}{\sqrt{N}} \sum_{\sigma s(\prime), \sigma' s'} \int_{\mathbf{k}, \epsilon} \int_{\mathbf{q}, \omega} \gamma_{ss'}^{\sigma' s'} \bar{\psi}_{i,\mathbf{k}+\mathbf{q}}^{\sigma s}(\epsilon + \omega) \psi_{i,\mathbf{k}}^{\sigma' s'}(\epsilon) \phi_{\mathbf{q}}^{\sigma s'}(\omega). \quad (2.25)$$

The interaction vertices  $\gamma$ , which are specific to the Keldysh representation are given by  $\gamma_{ss'}^{\text{cl}} = \delta_{ss'}$  and  $\gamma_{ss'}^{\text{q}} = (\sigma_1)_{ss'}$  with the first Pauli matrix  $\sigma_1$ , are identical to the interaction vertices of the single-loop Keldysh formalism (Kamenev, 2011).

### 2.4.3. OUT-OF-TIME ORDER CORRELATOR

Within the augmented Keldysh formalism introduced above, the fermionic out-of-time order correlator which was introduced in Eq. (2.13) is represented in terms of classical and

## 2. Quantum chaos in graphene

quantum field components by

$$f_{\gamma\delta}^{\alpha\beta}(x_1, x_2, x_3, x_4) = \frac{1}{N^2} \sum_{i,j=1}^N \langle \psi_{i\alpha}^{\text{cl}}(x_1) \bar{\psi}_{j\beta}^{\text{cl}}(x_2) \bar{\psi}_{i\gamma}^{\text{uq}}(x_3) \psi_{j\delta}^{\text{uq}}(x_4) \rangle_{\mathcal{K}}, \quad (2.26)$$

where  $\psi, \bar{\psi}$  denote Grassmann field components and  $x = (\mathbf{x}, t)$ . The expectation value is evaluated with respect to the augmented Keldysh action

$$\langle \dots \rangle_{\mathcal{K}} = \int \mathcal{D}(\bar{\psi}, \psi, \phi) \dots e^{iS_{\mathcal{K}}[\bar{\psi}, \psi, \phi]} \quad (2.27)$$

with  $S_{\mathcal{K}} = S_0 + S_{\text{int}}$  given in Eq. (2.24) and (2.25). Expression Eq. (2.26) may now be evaluated perturbatively by expanding  $e^{iS_{\text{int}}}$  in orders of  $N^{-1}$  and contracting the generated expectation values with respect to the quadratic action  $S_0$ . This approach is presented in the next section.

### 2.5. DIAGRAMMATIC APPROACH

Exponential out-of-time order correlator growth is caused by interactions. The scrambling rate is therefore expected to depend on the small parameter,  $\lambda_L \sim N^{-1}$ . Hence, the out-of-time order correlator  $C(t) \sim \frac{1}{N} e^{\lambda_L t}$  is represented by an infinite series when expanded in powers of  $N^{-1}$ . In reverse, an infinite series of terms has to be resummed to capture the exponential growth behavior of  $C(t)$  when evaluating out-of-time order correlators perturbatively.

In what follows, a diagrammatic approach is presented to determine the exponential growth of the out-of-time order correlators controlled by the small parameter  $N^{-1} \ll 1$ . It follows approaches presented in Refs. Patel and Sachdev (2017); Stanford (2016); Chowdhury and Swingle (2017), but is here applied to interacting electrons in graphene. This approach is complementary to approaches which are based on non-equilibrium techniques deriving a kinetic equation as presented later in Ch. 3, or in in Refs. Klug *et al.* (2018); Klug and Syzranov (2019), which resemble the well-known Boltzmann equation but derived within the augmented Keldysh formalism. However, as the scrambling rate and the Butterfly velocity represent the central focus of the present work, it is restricted to the diagrammatic approach for concreteness.

The approach is summarized as follows: Let  $f_L$  represent the out-of-time order correlator contribution of Eq. (2.13) which determines the leading order exponential growth of  $C(t)$ , and  $f_L^{(i)} \sim N^{-i}$  for  $i \in \mathbb{N}$  contributions thereof. By introducing the irreducible two-particle, interloop interaction vertex  $\Gamma$ ,  $f_L$  is written as

$$\begin{aligned} f_L &= f_L^{(1)} + f_L^{(2)} + f_L^{(3)} + \dots \\ &= f_L^{(1)} + f_L \circ \Gamma, \end{aligned} \quad (2.28)$$

where  $\circ$  represents a matrix product over internal indices. The interaction vertex itself

## 2. Quantum chaos in graphene

may be represented as a series  $\Gamma = \Gamma^{(1)} + \Gamma^{(2)} + \dots$ , where  $\Gamma^{(1)} \sim N^{-1}$  is expected to determine the leading order contribution to  $\lambda_L$ . In what follows, a so-called ‘‘Bethe-Salpeter equation’’<sup>1</sup> of type Eq. (2.28), which self-consistently determines  $f_L$ , is derived in Sec. 2.5.1. Subsequently, the scrambling rate  $\lambda_L$  is extracted in Sec. 2.5.2 and the Butterfly velocity in Sec. 2.5.3.

### 2.5.1. BETHE-SALPETER EQUATION

To construct a minimal Bethe-Salpeter equation which contains the relevant free variables to set up an self-consistency equation for  $f_L$ , half of the external variables of  $f$  are traced out. After Laplace and Fourier transform, one obtains (Klug *et al.*, 2018)

$$f_{\beta}^{\alpha}(\omega; \mathbf{k}, \epsilon) \equiv \int_{\epsilon' \mathbf{k}'} \int_{\mathbf{x}_1 t_1} \int_{\mathbf{x}_2 t_2} \int_{\mathbf{x}_3 t_3} \sum_{\gamma} f_{\beta\gamma}^{\alpha\gamma}(x_1, x_2, x_3, 0) \times e^{i(\omega+\epsilon')t_1 - i(\omega+\epsilon)t_2 - i\epsilon t_3 - i\mathbf{k}\cdot(\mathbf{x}_1 - \mathbf{x}_3) + i\mathbf{k}'\cdot\mathbf{x}_2} \quad (2.29)$$

$$\equiv \begin{array}{c} \text{---} \alpha, (\epsilon + \omega, \mathbf{k}) \\ \text{---} \text{---} \text{---} \\ \text{---} \text{---} \text{---} \\ \text{---} \beta, (\epsilon, \mathbf{k}) \end{array},$$

with  $\int_{\mathbf{x}t} = \int_0^{\infty} dt \int d^2\mathbf{x}$ , where the second line depicts its diagrammatic representation.  $f$  is labeled by the external  $\omega$ , the internal frequency  $\epsilon$  and the internal momentum  $\mathbf{k}$ , as well as the pseudo spin indices  $\alpha, \beta$ . It is connected to the Laplace transformed out-of-time order correlator Eq. (2.12) by

$$C(\omega) = \sum_{\alpha} \int_{\mathbf{k}\epsilon} f_{\alpha}^{\alpha}(\omega; \mathbf{k}, \epsilon). \quad (2.30)$$

Upper and lower arrows, which carry frequency  $\omega + \epsilon$  and  $\epsilon$  and pseudo spin  $\alpha$  and  $\beta$ , reside on the lower and upper Keldysh loop Fig. 2.3, respectively.

In a next step,  $f$  is dressed by interactions where the contributions are generated by expanding the exponential Eq. (2.27) in powers of  $S_{\text{int}}$ . By rearranging terms as indicated in Eq. (2.28), one obtains a Bethe-Salpeter equation as depicted diagrammatically in Fig. 2.4 where the two-particle vertex  $\Gamma$  incorporates the irreducible interaction processes. In particular, only interloop interaction processes containing at least one interloop correlation function Eq. (2.23) which connects the upper and lower lines in the diagrammatic representation, contribute to the out-of-time order correlator growth. In leading order, intraloop contributions are compensated in the single-particle self-energy corrections and are therefore dropped from consideration.

The leading order diagrams constituting  $\Gamma$  are depicted in Fig. 2.5. Straight lines denote fermionic propagators, wavy double lines plasmon propagators which are dressed by particle-hole fluctuations. Propagators are of the order  $N^0$  whereas interaction vertices

<sup>1</sup>Normally, Bethe-Salpeter equations arise in the context of two-particle vertices which are dressed by interaction corrections. See e.g. Ref. Altland and Simons (2010).

## 2. Quantum chaos in graphene

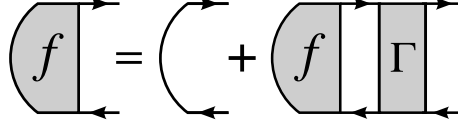


**Figure 2.4.:** Diagrammatic representation of the Bethe-Salpeter equation used to determine the growth of the out-of-time order correlator  $f$  introduced in Eq. (2.29). Reprinted figure with permission from [M.J. Klug, M.S. Scheurer, and J. Schmalian, Phys. Rev. **B** 98, 045102] Copyright (2018) by the American Physical Society. The original work is found under <https://dx.doi.org/10.1103/PhysRevB.98.045102>.

are suppressed by a factor of  $N^{-1/2}$ . The irreducible interaction vertex  $\Gamma$  (Fig. 2.5a) is given to leading order by the “one-rung” diagram (Fig. 2.5b) and the “two-rung” diagram (Fig. 2.5c) which are both of order  $N^{-1}$ . Though possessing twice as many interaction vertices, the latter contains an extra closed fermionic loop when connecting to the out-of-time order correlator  $C(\omega)$  which gives an additional factor of  $N$ . Diagram Fig. 2.5d vanishes as plasmon interloop correlators are necessarily of retarded and advanced type which vanish exactly as indicated in Eq. (2.23)

Expressed in terms of single-particle propagators, the Bethe-Salpeter equation depicted in Fig. 2.4 is given by (Klug *et al.*, 2018)

$$f_{\beta}^{\alpha}(\omega; \mathbf{k}, \epsilon) = \frac{1}{N} \sum_{\gamma} G_{\alpha\gamma}^R(\mathbf{k}, \omega + \epsilon) G_{\gamma\beta}^A(\mathbf{k}, \epsilon) + \frac{1}{N} \int_{\mathbf{k}'\epsilon'} \sum_{\gamma'\delta'} f_{\delta'}^{\gamma'}(\omega; \mathbf{k}', \epsilon') \Gamma_{\delta\delta'}^{\gamma\gamma'}(\omega; \mathbf{k}, \epsilon, \mathbf{k}', \epsilon') G_{\alpha\gamma}^R(\mathbf{k}, \omega + \epsilon) G_{\delta\beta}^A(\mathbf{k}, \epsilon), \quad (2.31)$$

where the irreducible two-particle vertex is given by

$$\Gamma_{\gamma\delta}^{\alpha\beta}(\omega; \mathbf{k}, \epsilon, \mathbf{k}', \epsilon') = i\delta_{\alpha\beta}\delta_{\gamma\delta}D_{ul}^K(\mathbf{k} - \mathbf{k}', \epsilon - \epsilon') + \int_{\tilde{\mathbf{k}}\tilde{\epsilon}} G_{\alpha\gamma}^{lu}(\mathbf{k} - \tilde{\mathbf{k}}, \epsilon - \tilde{\epsilon}) G_{\delta\beta}^{ul}(\mathbf{k}' - \tilde{\mathbf{k}}, \epsilon' - \tilde{\epsilon}) D^R(\tilde{\mathbf{k}}, \omega + \tilde{\epsilon}) D^A(\tilde{\mathbf{k}}, \tilde{\epsilon}). \quad (2.32)$$

Here, the  $N$ -dependence was made explicit. In what follows, the contribution of Eq. (2.31),

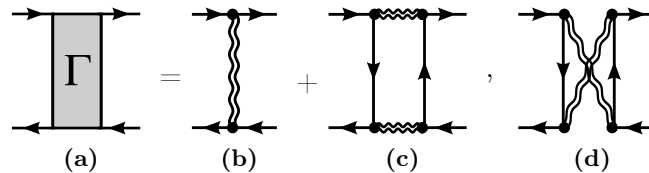


**Figure 2.5.:** Rung diagrams contributing in leading order in  $N^{-1}$  to the two-particle vertex  $\Gamma$  entering the Bethe-Salpeter equation depicted in Fig. 2.4. Reprinted figure with permission from [M.J. Klug, M.S. Scheurer, and J. Schmalian, Phys. Rev. **B** 98, 045102] Copyright (2018) by the American Physical Society. The original work is found under <https://dx.doi.org/10.1103/PhysRevB.98.045102>.

## 2. Quantum chaos in graphene

which yield the most rapid, exponential growth to Eq. (2.30) is extracted to determine the scrambling rate  $\lambda_L$  and the Butterfly velocity  $v_B$ .

Solving the integral equation Eq. (2.31) is highly involved. Therefore, a series of approximation is conducted relying on the smallness of  $N^{-1} \ll 1$  and the fact that information scrambling is determined by the most rapidly growing contribution to the out-of-time order correlator. The product of Green's functions occurring in both terms of Eq. (2.31) is strongly peaked at their single-particle poles. Therefore, a so-called ‘‘mass-shell’’ approximation is conducted where the electronic excitations are assumed well defined quasiparticles which represent the leading contribution of the  $\epsilon$ -integration. By using the band projector Eq. (2.8), the product of electronic propagators is expressed as (Klug *et al.*, 2018)

$$G_{\alpha\gamma}^R(\omega + \epsilon, \mathbf{k}) G_{\delta\beta}^A(\epsilon, \mathbf{k}) \approx 2\pi i \frac{\mathcal{P}_{\alpha\gamma}^a(\mathbf{k}) \mathcal{P}_{\delta\beta}^b(\mathbf{k}) \delta(\epsilon - v_F b |\mathbf{k}|)}{\omega - v_F (a - b) |\mathbf{k}| + i0^+}, \quad (2.33)$$

with band indices  $a, b = \pm 1$ . Here, the most rapidly growing contribution is traced back to electronic excitations of the same band,  $a = b$ . The same holds true for  $f_\beta^\alpha(\omega; \mathbf{k}, \epsilon)$ , which, projected into the band basis, is specified to leading order by one band index only (Klug *et al.*, 2018)

$$f_\beta^\alpha(\omega; \mathbf{k}, \epsilon) = \sum_{a=\pm 1} f_a(\omega, \mathbf{k}) \mathcal{P}_{\alpha\beta}^a(\mathbf{k}) 2\pi \delta(\epsilon - a v_F |\mathbf{k}|). \quad (2.34)$$

Additionally, the vertex Eq. (2.32) is assumed a smooth function of  $\omega$  which allows one to set the frequency to zero to extract the most rapid growth,  $\Gamma_{\gamma\delta}^{\alpha\beta}(\omega; \mathbf{k}, \epsilon, \mathbf{k}', \epsilon')|_{\omega=0}$ . By Applying both approximations and performing the  $\epsilon$ -integration as well as the trace over pseudo spin indices as specified in Eq. (2.30), the Bethe-Salpeter equation reduces to

$$\sum_{a=\pm 1} f_a(\omega; \mathbf{k}) = \frac{i}{\omega} \frac{1}{N} \left[ 1 + \sum_{b=\pm 1} \int_{\mathbf{k}'} M_{ab}(\mathbf{k}, \mathbf{k}') f_b(\omega; \mathbf{k}') \right], \quad (2.35)$$

where it is discriminated between band preserving ( $+ \equiv \{ab | a = b\}$ ) and band changing ( $- \equiv \{ab | a \neq b\}$ ) processes with

$$M_\pm(\mathbf{k}, \mathbf{k}') = i K_{\pm\pm}(\mathbf{k}, \mathbf{k}') D_{ul}^K(v_F |\mathbf{k}'| \mp v_F |\mathbf{k}|, \mathbf{k}' \mp \mathbf{k}) + \sum_{a'b'} \int_{\tilde{\mathbf{k}}} K_{+b'}(\mathbf{k}', \mathbf{k}' - \tilde{\mathbf{k}}) K_{\pm a'}(\mathbf{k}, \mathbf{k} - \tilde{\mathbf{k}}) \\ \times G_{a'}^{ul}(\pm v_F a' |\mathbf{k}| - \tilde{\epsilon}, \mathbf{k} - \tilde{\mathbf{k}}) G_{b'}^{lu}(v_F b' |\mathbf{k}'| - \tilde{\epsilon}, \mathbf{k}' - \tilde{\mathbf{k}}) D^R(\tilde{\epsilon}, \tilde{\mathbf{k}}) D^A(\tilde{\epsilon}, \tilde{\mathbf{k}}), \quad (2.36)$$

where  $K_{ab}(\mathbf{k}, \mathbf{k}') \equiv \frac{1}{2}(1 + ab \frac{\mathbf{k} \cdot \mathbf{k}'}{|\mathbf{k}| |\mathbf{k}'|})$ . Furthermore, by exploiting particle-hole symmetry,  $M_{-a-b}(\omega, \mathbf{k}, \mathbf{k}') = M_{ab}(\omega, \mathbf{k}, \mathbf{k}')$ , the solving of Eq. (2.31) is reduced to solving the integral equation (Klug *et al.*, 2018)

$$f(\omega; \mathbf{k}) = \frac{i}{\omega} \frac{1}{N} \left[ 1 + \int_{\mathbf{k}'} M(\mathbf{k}, \mathbf{k}') f(\omega; \mathbf{k}') \right], \quad (2.37)$$

where  $f(\omega, \mathbf{k}) = \sum_{a=\pm 1} f_a(\omega; \mathbf{k})$  with the symmetric kernel  $M = M_+ + M_-$ .

## 2.5.2. DETERMINATION OF THE SCRAMBLING RATE

The scrambling rate is eventually determined by the eigensystem of the homogeneous part of the integral equation (2.37) as argued in the following. The term rendering the integral equation inhomogeneous takes the initial conditions into account. By means of an orthonormal transformation  $V(\mathbf{k}, \mathbf{k}')$ , the real and symmetric kernel is brought into a diagonal form,

$$M'(\mathbf{k}, \mathbf{k}') = \int_{\mathbf{q}\mathbf{q}'} V(\mathbf{k}, \mathbf{q})M(\mathbf{q}, \mathbf{q}')V^T(\mathbf{q}', \mathbf{k}') \quad (2.38a)$$

$$\equiv N\lambda_{\mathbf{k}}\delta(\mathbf{k} - \mathbf{k}'), \quad (2.38b)$$

where  $\{\lambda_{\mathbf{k}}\} \sim N^{-1}$  denotes the set of corresponding eigenvalues. Applied to the integral equation (2.37), one obtains for the Bethe-Salpeter equation

$$\tilde{f}(\omega; \mathbf{k}) = \frac{i}{\omega} \frac{1}{N} \left[ e_{\mathbf{k}} + N\lambda_{\mathbf{k}}\tilde{f}(\omega; \mathbf{k}) \right], \quad (2.39)$$

with corresponding eigenfunctions  $\tilde{f}(\omega; \mathbf{k}) = \int_{\mathbf{q}} V(\mathbf{k}, \mathbf{q})f(\omega; \mathbf{q})$  and  $e_{\mathbf{k}} = \int_{\mathbf{q}} V(\mathbf{k}, \mathbf{q})$ , which yields

$$\tilde{f}(\omega; \mathbf{k}) = \frac{i}{N} \frac{e_{\mathbf{k}}}{\omega - i\lambda_{\mathbf{k}}}. \quad (2.40)$$

By applying the inverse Laplace transform where the contour of integration is shifted in the complex plane to generate a non-vanishing result for  $t \geq 0$  in accordance with the definition of the Laplace transform introduced earlier,  $\int_{-\infty+i\Omega}^{\infty+i\Omega} \frac{d\omega}{2\pi} \dots e^{-i\omega t}$  with  $\Omega > \lambda_{\mathbf{k}}$ , one obtains

$$\tilde{f}(t; \mathbf{k}) = \theta(t) \frac{e_{\mathbf{k}}}{N} e^{\lambda_{\mathbf{k}} t} \quad (2.41)$$

with the Heaviside step function  $\theta(t)$ . Hence, the exponential growth behavior is specified by the spectrum of eigenvalues  $\{\lambda_{\mathbf{k}}\}$ . The scrambling rate is given by  $\lambda_L = \max[\{\lambda_{\mathbf{k}}\}]$ , whereas the corresponding eigenfunction is denoted  $f_L$ . Instead of solving the inhomogeneous integral equation (2.37), the scrambling rate is therefore efficiently determined as the largest eigenvalue of the homogeneous integral equation (Klug *et al.*, 2018)

$$\lambda f(\omega; \mathbf{k}) = \frac{1}{N} \int_{\mathbf{k}'} M(\mathbf{k}, \mathbf{k}')f(\omega; \mathbf{k}'). \quad (2.42)$$

By inspecting the units of the kernel,  $[M] = \frac{k_B T}{\hbar}$ , one infers  $\lambda_L = c g(\alpha) \frac{k_B T}{\hbar N}$  with a numerical constant  $c$  and the function  $g(\alpha)$ , which takes the dependence on the coupling constant into account and discriminates between the weak- and strong-coupling regime.  $c$  has to be determined numerically. Explicit expressions for  $M(\mathbf{k}, \mathbf{k}')$  and details about the numerical solution procedure are presented in the Appendix A.4.

### 2.5.3. DETERMINATION OF THE BUTTERFLY VELOCITY

In this section, the Butterfly velocity for interacting Dirac electrons, which quantifies the spatial spreading of quantum information as introduced in Sec. (1.4), is argued to match the Fermi velocity,  $v_B \propto v_F$ . Instead of the “integrated” out-of-time order correlator Eq. (2.12), one considers a correlator with a spatial dependence

$$C(\mathbf{x}, t) = \theta(t) \sum_{\alpha\beta} f_{\alpha\beta}^{\alpha\beta}(x, 0, x, 0), \quad (2.43)$$

with  $x = (\mathbf{x}, t)$ , which is expected to grow exponentially combined with a quasiballistic propagation in space as discussed in Sec. (1.4). Eq. (2.43) suggests to introduce the Laplace and Fourier transform of  $f$  similar to Eq. (2.29), but with an additional external momentum  $\mathbf{q}$ ,

$$f_{\beta}^{\alpha}(\mathbf{q}, \omega; \mathbf{k}, \epsilon) \equiv \left( \begin{array}{c} \xrightarrow{\alpha, (\epsilon + \omega, \mathbf{k} + \mathbf{q})} \\ \boxed{f} \\ \xleftarrow{\beta, (\epsilon, \mathbf{k})} \end{array} \right), \quad (2.44)$$

which is connected to the previously introduced out-of-time order correlator by

$$C(\mathbf{q}, \omega) = \sum_{\alpha} \int_{\mathbf{k}\epsilon} f_{\alpha}^{\alpha}(\mathbf{q}, \omega; \mathbf{k}, \epsilon). \quad (2.45)$$

Therefore, the Bethe-Salpeter equation (2.31) has to be generalized to external momentum  $\mathbf{q}$  in addition to external frequency  $\omega$ .

The evolution in time and space of the most rapidly contribution of  $C(\mathbf{x}, t)$  is expected to be governed by a kinetic equation introduced in the last chapter in Eq. (1.15) where information scrambling and the spatial propagation of carriers introduce a characteristic length scale,  $\ell \sim v_F \lambda_L^{-1}$ . As  $\lambda_L \propto g(\alpha) \frac{k_B T}{\hbar N}$ , it is introduced as

$$\ell = g(\alpha) \frac{v_F \hbar N}{k_B T}. \quad (2.46)$$

Changes on length scale  $\ell$  are expected to be small justifying a gradient expansion of type Eq. (1.15) and suggesting to determine the largest eigenvalue of the generalized Bethe-Salpeter equation in powers of dimensionless external momentum  $\mathbf{Q} = \ell \mathbf{q} \ll 1$ .

The  $\mathbf{q}$ -dependence of the Bethe-Salpeter equation enters predominantly in the section of free electron propagation represented by the products of two fermion Green’s functions in Eq. (2.31) where the “upper” propagator carries an additional momentum  $\mathbf{q}$ , i.e.  $G_{\alpha\gamma}^R(\mathbf{k} + \mathbf{q}, \omega + \epsilon) G_{\delta\beta}^A(\mathbf{k}, \epsilon)$ . In contrast, the external momentum in the vertex functions is set to zero,  $\Gamma_{\gamma\delta}^{\alpha\beta}(\mathbf{q}, \omega; \mathbf{k}, \epsilon, \mathbf{k}', \epsilon') \big|_{\omega=0, \mathbf{q}=0}$ , to obtain the leading order contribution. By introducing the band basis and performing the series of approximation discussed earlier which are assumed to hold also for finite  $\mathbf{q}$ , the pole in Eq. (2.35) at  $\omega' = 0$  is modified to  $\omega' = av_F \hat{\mathbf{k}} \cdot \mathbf{q}$ . The Bethe-Salpeter equation for a single band component is given by

## 2. Quantum chaos in graphene

$$f_a(\mathbf{q}, \omega; \mathbf{k}) = \frac{i}{\omega - av_F \hat{\mathbf{k}} \cdot \mathbf{q}} \frac{1}{N} \left[ 1 + \sum_b \int_{\mathbf{k}'} M_{ab}(\mathbf{k}, \mathbf{k}') f_b(\mathbf{q}, \omega; \mathbf{k}') \right], \quad (2.47)$$

where it was used that  $|\mathbf{k} + \mathbf{q}| - |\mathbf{k}| \approx \hat{\mathbf{k}} \cdot \mathbf{q}$  with  $\hat{\mathbf{k}} = \frac{\mathbf{k}}{|\mathbf{k}|}$ .

For simplicity, only band preserving processes are considered,  $b = a$ , which, as shown in the following section, represent the predominant contribution to quantum information scrambling. Furthermore, the discussion is restricted to one particular band only, without loss of generality  $a = +1$ , yielding the generalized Bethe-Salepter equation

$$[\omega - v_F \hat{\mathbf{k}} \cdot \mathbf{q}] f_+(\mathbf{q}, \omega; \mathbf{k}) = \frac{i}{N} \left[ 1 + \int_{\mathbf{k}'} M_+(\mathbf{k}, \mathbf{k}') f_+(\mathbf{q}, \omega; \mathbf{k}') \right], \quad (2.48)$$

where the spectrum of eigenvalues of the homogeneous part determines the  $\mathbf{q}$ -dependent exponential growth exponent.

Introducing dimensionless momenta  $\mathbf{Q} = \ell \mathbf{q}$  and a dimensionless integration kernel  $\mathcal{M} = \frac{\hbar}{k_B T} M$ , the following eigenvalue problem has to be solved,

$$\lambda f(\mathbf{Q}, \omega; \mathbf{K}) = \frac{k_B T}{N \hbar} \left[ g^{-1}(\alpha) \hat{\mathbf{K}} \cdot \mathbf{Q} + \int_{\mathbf{k}'} \mathcal{M}(\mathbf{k}, \mathbf{k}') f(\mathbf{q}, \omega; \mathbf{k}') \right], \quad (2.49)$$

where the first term on the right-hand side is considered as a small perturbation. Thus, expanding the largest eigenvalue relevant for information scrambling in powers of external momenta  $\mathbf{Q}$  is assumed justified. In the unperturbed case,  $\mathbf{Q} = 0$ , the largest eigenvalue coincides with the scrambling rate  $\lambda_L$  of the previous section. Furthermore, as the unperturbed eigensystem is rotationally invariant, the first order contribution is expected to vanish. Thus, the largest eigenvalue up to second order perturbation theory is given by (Chowdhury and Swingle, 2017)

$$\lambda(\mathbf{Q}) = \lambda_L - \lambda_B |\mathbf{Q}|^2, \quad (2.50)$$

where it is expected  $\lambda_B \sim g^{-2}(\alpha) \lambda_L$ . Hence, the most-rapidly growing contribution to the out-of-time order correlator is given by

$$\tilde{f}(\mathbf{q}, \omega; \mathbf{k}) = \frac{i}{N} \frac{e_L}{\omega - i(\lambda_L - D_L |\mathbf{q}|^2)}, \quad (2.51)$$

where  $D_L = \lambda_B \ell^2$  and  $v_B = v_F \sqrt{\lambda_B \lambda_L} \frac{\hbar N}{k_B T} \sim v_F$ . After inverse Laplace and Fourier transform, this yields (Sec. 1.4)

$$C(\mathbf{x}, t) = \frac{e_L}{N} e^{\lambda_L t - \frac{|\mathbf{x}|^2}{4D_L t}} \approx \frac{e_L}{N} e^{2\lambda_L(t - \frac{|\mathbf{x}|}{v_B})}, \quad (2.52)$$

which is valid for distances  $|\mathbf{x}| > \ell$  representing the characteristic exponential growth time and quasiballistic spreading in space as discussed in Sec. (1.4).

In conclusion, it was demonstrated that the Butterfly velocity for interacting Dirac electrons in graphene is directly linked to the Fermi velocity,  $v_B = c v_F$ , where the constant

## 2. Quantum chaos in graphene

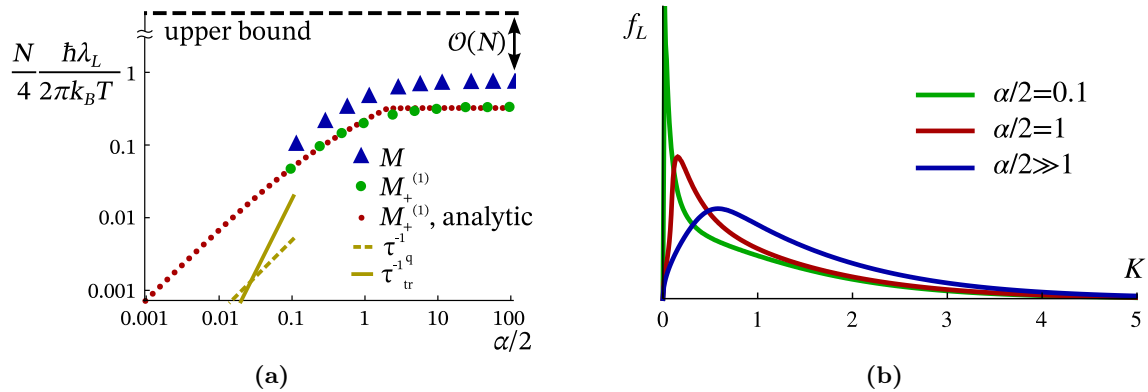


**Figure 2.6.:** Scrambling rate  $\lambda_L$  for interacting Dirac electrons in graphene. (a) Numerical results for  $\lambda_L$  as function of coupling strength  $\alpha$ . Obtained values differ in the number of considered scrambling processes, where  $M$  indicates the full kernel and  $M_+^{(1)}$  the one-rung, band preserving contribution (Fig. 2.5b). Additionally, numerical values for the quantum dephasing  $\tau_q^{-1}$  and the transport rate  $\tau_{tr}^{-1}$  taken from Ref. Schütt *et al.* (2011) are presented. (b) Eigenfunctions  $f_L$  as function of dimensionless momentum  $K = \frac{\hbar v_F |\mathbf{k}|}{2k_B T}$  for various coupling strengths. Reprinted figures with permission from [M.J. Klug, M.S. Scheurer, and J. Schmalian, Phys. Rev. **B** 98, 045102] Copyright (2018) by the American Physical Society. The original work is found under <https://dx.doi.org/10.1103/PhysRevB.98.045102>.

$c$  has to be determined numerically but is expected to be of order unity. This result is in line with similar studies, e.g., presented in Refs. Chowdhury and Swingle (2017); Werman *et al.* (2017), where the Butterfly velocity matches the characteristic velocity of carriers responsible for information scrambling.

### 2.6. INFORMATION SCRAMBLING IN GRAPHENE

The scrambling rate for electrons in graphene is determined by the largest eigenvalue of the homogeneous Bethe–Salpeter equation (2.42) whose explicit expression is given in the Appendix A.4. This equation is solved numerically for a discrete momentum grid. Additionally, the Bethe-Salpeter equation is solved by considering the one-rung contribution (Fig. 2.5b) only where the integral kernel can be expressed analytically and more efficient numerical methods apply. This contribution represent a lower bound on the scrambling rate which is particularly important for weak couplings. The obtained scrambling rate  $\lambda_L$  as function of the coupling strength  $\alpha$  is depicted in Fig. 2.6a. For strong couplings ( $\alpha \gg 1$ ), a saturation to a constant value is observed whereas for weak couplings ( $\alpha \ll 1$ ), the scrambling rate vanishes linearly as discussed in Sec. 2.1.

The eigenfunctions  $f_L$  corresponding to  $\lambda_L$  are depicted for different coupling strengths in Fig. 2.6b. For strong couplings ( $\alpha \gg 1$ ),  $f_L$  is peaked for momenta  $|\mathbf{k}| \approx \frac{k_B T}{\hbar v_F}$  suggesting that scrambling is determined by modes with excitation energies  $\epsilon \sim k_B T$ . This is reasonable as in the strong-coupling limit no energy scale except temperature exist. This changes in the weak-coupling limit ( $\alpha \ll 1$ ) where the peak shifts to momenta  $|\mathbf{k}| \approx \alpha \frac{k_B T}{\hbar v_F}$

## 2. Quantum chaos in graphene

indicating that scrambling is determined by excitations with excitation energies  $\epsilon \sim \alpha k_B T$ . This observation is explained by inspecting the explicit expression for the Bethe-Salpeter equation where only the predominant band preserving, one-rung process  $M_{\pm}^{(1)}$  is taken into account. It yields for the homogeneous Bethe-Salpeter equation (Klug *et al.*, 2018)

$$\lambda f(\omega, K) = \frac{2\pi k_B T}{\hbar} \frac{4}{N} \frac{2}{K} \int_0^{\infty} \frac{dK'}{2\pi} \int_{|K-K'|}^{|K+K'|} \frac{Q dQ}{2\pi} \frac{\sqrt{(K+K')^2 - Q^2}}{\sqrt{Q^2 - (K-K')^2}} \frac{\text{Im}\mathcal{D}^R(|K-K'|, Q)}{\sinh(|K-K'|)} f(\omega, K'), \quad (2.53)$$

where dimensionless momenta  $K^{(\prime)} = \frac{\hbar v_F |\mathbf{k}^{(\prime)}|}{2k_B T}$  are introduced and  $Q$  accordingly. The kernel, which is largest for diagonal elements  $K = K'$ , is (up to a prefactor) given by (Klug *et al.*, 2018)

$$\frac{2Q \text{Im}\mathcal{D}_{ul}^R(|K-K'|, Q)}{\sinh(|K-K'|)} \stackrel{K \rightarrow K'}{=} \frac{\alpha^2 \ln 2}{(Q + \alpha \ln 2)^2}. \quad (2.54)$$

One observes that in the limit of small transferred momenta,  $Q < \alpha \ln 2$ , the kernel becomes independent of the coupling constant  $\alpha$ . The associated length scale is given by the interaction induced thermal screening length

$$l_{\text{th}}^{-1} = \ln 2 \alpha \frac{k_B T}{\hbar v_F}, \quad (2.55)$$

which screens the long-range Coulomb interaction. This screening length was also determined in the context of transport coefficients in Ref. Schütt *et al.* (2011). These scattering processes determine  $\lambda_L$  predominantly and the linear-in- $\alpha$  dependence is traced back to the fact that for small momenta,  $Q < \alpha \ln 2$ , interactions are of order  $\alpha^0$  resulting in  $\lambda_L \sim \alpha \frac{k_B T}{\hbar N}$ .

The obtained scrambling rate in the weak-coupling limit is compared to the single-particle rates, the quantum dephasing rate  $\tau_q^{-1}(\epsilon)$ , the energy relaxation rate  $\tau_E^{-1}(\epsilon)$  and the transport relaxation rate  $\tau_{tr}^{-1}(\epsilon)$  which are presented in Ref. (Schütt *et al.*, 2011). The rates were obtained for the same microscopic model of interacting electrons in graphene as presented in Sec. 2.2 and scale differently with coupling constant and temperature due to the characteristic infrared-singular collision kernel which allows a clear distinction between different types of microscopic processes. The rates are determined in Ref. Schütt *et al.* (2011) by evaluating the following expression (Klug *et al.*, 2018)

$$\tau_i^{-1}(\epsilon) = \pi \int_{\omega} [\coth \frac{\omega}{2k_B T} + f(\epsilon - \omega)] \int_{\mathbf{q}} \text{Im}D^R(\omega, \mathbf{q}) \times \mathcal{K}_i(\mathbf{p} \cdot \mathbf{q}, \omega) \sum_{a=\pm} \delta(\epsilon - \omega - \hbar v_F |\mathbf{p} - \mathbf{q}|), \quad (2.56)$$

where  $\mathcal{K}_i(\mathbf{p} \cdot \mathbf{q}, \omega)$  represents different kernels specific for the different rates. The external momentum is set on “mass-shell” with respect to the external frequency,  $|\mathbf{p}| \approx \frac{\epsilon}{\hbar v_F}$ , and the Fermi distribution function is given by  $f(\epsilon) = [1 + e^{\epsilon/k_B T}]^{-1}$ . The kernel for the

## 2. Quantum chaos in graphene

dephasing rate is given by  $\mathcal{K}_q(\mathbf{p} \cdot \mathbf{q}, \omega) = 1$  yielding the single-particle scattering rate  $\tau_q^{-1}(\epsilon) = -2\text{Im}\Sigma^R(\epsilon, \mathbf{p})|_{|\mathbf{p}| \approx \frac{\epsilon}{\hbar v_F}}$ . In the case of energy relaxation,  $\mathcal{K}_E(\mathbf{p} \cdot \mathbf{q}, \omega) = (\frac{\omega}{k_B T})^2$  which is relevant in the determination of the energy diffusion coefficient. In the case of transport processes,  $\mathcal{K}_{tr}(\mathbf{p} \cdot \mathbf{q}, \omega) = \sin^2 \theta_{\mathbf{p}, \mathbf{q}}$  suppressing forward scattering processes which generally enters, e.g., in the determination of the electrical conductivity.

First, by comparing the integration kernels Eq. (2.53) and Eq. (2.56), scrambling is similar to scattering processes determining  $\tau_q^{-1}(\epsilon)$ . As scrambling is determined by excitations with energies  $\epsilon \sim \alpha k_B T$ ,  $\lambda_L$  resembles indeed the quantum dephasing rate which, evaluated at the same excitation energies, is given by  $\tau_q^{-1}(\epsilon = \alpha k_B T) \approx 0.58 \alpha \frac{k_B T}{\hbar N}$  (Schütt *et al.*, 2011). This rate is, however, numerically by a factor of 16 smaller than  $\lambda_L$  which indicates that scrambling processes are the fastest processes. In particular, when assuming that typical thermalization and hydrodynamic processes are governed by excitations with excitation energies  $\epsilon \sim k_B T$ , the rate of thermalization is  $\tau_E^{-1}(\epsilon = k_B T) \sim \alpha \log \alpha^{-1} \frac{k_B T}{\hbar N}$  and the rate of hydrodynamic processes is  $\tau_{tr}^{-1}(\epsilon = k_B T) \sim \alpha^2 \frac{k_B T}{\hbar N}$  – both parametrically smaller than  $\lambda_L$ .

### 2.7. CONCLUSION AND OUTLOOK

In this chapter, an out-of-time order correlator was evaluated for interacting Dirac electrons in graphene in the presence of Coulomb interaction to determine the scrambling rate  $\lambda_L$  and the Butterfly velocity  $v_B$ . For this, the augmented Keldysh formalism was derived and a perturbative, diagrammatic approach was employed to extract the leading order contribution to the out-of-time order correlator.

In the strong-coupling limit ( $\alpha \gg 1$ ),  $\lambda_L$  was determined to depend solely on the temperature as no other energy scale exist. In the weak-coupling limit ( $\alpha \ll 1$ ),  $\lambda_L$  was found to resemble the single-particle scattering rate,  $\tau_q^{-1} < \lambda_L$ , though numerically larger, probing the microscopic system at excitations energies  $\epsilon \sim \alpha k_B T$ . This finding is similar to results obtained in Refs. Aleiner *et al.* (2016); Swingle and Chowdhury (2017); Banerjee and Altman (2017). In contrast,  $\lambda_L$  was found parametrically larger than the energy relaxation rate,  $\tau_E^{-1} \ll \lambda_L$ , or transport relaxation rate,  $\tau_{tr}^{-1} \ll \lambda_L$ , evaluated at excitation energies  $\epsilon \sim k_B T$ , which are representative for thermalization or transport processes. This indicates that these processes are not relevant for information scrambling in graphene. As information scrambling is not directly related to thermalization or hydrodynamics, associated characteristics cannot be extracted from  $\lambda_L$ . However, if considering information scrambling as a prerequisite for the applicability of the concept of thermalization or hydrodynamic descriptions, this is found justified for interacting electrons in graphene.

As the rate of information scrambling was found to represent the fastest rate for interacting electrons in graphene, the spreading of quantum information could be interpreted as an effective, causality constraining “light-cone”, which bounds, combined with the Butterfly velocity, any other physical process. It may indicate that processes which are representative for, e.g., thermalization or hydrodynamics cannot happen faster than specified by

## 2. Quantum chaos in graphene

$\lambda_L$  and  $v_B$ . This principal is similar to the Lieb-Robinson bound which predicts a finite upper bound on the group-velocity of non-relativistic systems in the case of finite ranged interactions (Lieb and Robinson, 1972). Out-of-time order correlator growth could also provide a maximum speed of information spreading but here determined for a particular low-energy and low-temperature state (Roberts and Swingle, 2016). An appropriate bound could be formulated in terms of diffusion coefficients, which is independent on the existence of a quasiparticle picture (Hartnoll, 2014) similar to Ref. Blake (2016a,b). In particular,

$$D \gtrsim D_L \sim \frac{v_B^2}{\lambda_L}, \quad (2.57)$$

where  $D$  represents the coefficient of diffusive transport for late times and long distances of conserved quantities (Kadanoff and Martin, 1963) such as charge or energy. In the strong-coupling limit, the bound is expected to be saturated. Interestingly, combined with the bound on the scrambling rate  $\lambda_L \lesssim \frac{k_B T}{\hbar}$  discussed in Sec. 1.5, the ‘‘Planckian’’ time scale enters naturally. The validity and applicability of the possible bound Eq. (2.57) has to be investigated more thoroughly for the system of interacting electrons in graphene. In addition, an application to other systems of condensed matter physics could be examined.

The presented analysis relied on the ‘‘largeness’’ of the number of fermion flavors,  $N \gg 1$ , which guaranteed a quantum chaotic regime for times smaller than the scrambling time  $t^* \sim \lambda_L^{-1} \log N$ . Similar to the semiclassical approach presented previously in Sec. 1.7, one may argue that the quantum chaotic behavior of the considered quantum field theory, which manifests in the exponential growth of out-of-time order correlators, can be traced back to classical chaotic behavior of the corresponding classical theory. A possible approach to validate this insight for the case of interacting electrons in graphene involves a determination of a classical field theory, which is obtained by integrating out the fermionic degrees of freedom of the action introduced in Eq. (2.6). This yields an effective action in terms of the real-valued field  $\phi(\mathbf{x}, t)$  describing the dynamics of plasmon excitations. In this case, the time evolution from an initial state  $\phi_i(\mathbf{x})$  to a final state  $\phi_f(\mathbf{x})$  in the time interval  $t$  is determined by

$$\langle \phi_f | \hat{U}(t) | \phi_i \rangle \propto \int_{\phi(0, \mathbf{x}) = \phi_i(\mathbf{x})}^{\phi(t, \mathbf{x}) = \phi_f(\mathbf{x})} \mathcal{D}\phi e^{iNS[\phi]}, \quad (2.58)$$

where the effective action is independent of  $N$ , i.e.  $S[\phi] \sim N^0$ . For large  $N \gg 1$ , the dynamics of  $\phi$  are solely determined by classical contributions which are governed by the classical equations of motion determined by the saddle point,  $\frac{\delta S}{\delta \phi} = 0$ . Following the semiclassical approach discussed in Sec. 1.7.1, one could examine the classical dynamics of fields with respect to possible chaotic behavior, i.e. its sensitivity to changes in the initial conditions. Exponentially diverging trajectories in phase space then provide a classical Lyapunov exponent  $\lambda_{cl}$  which could be compared to the scrambling rate  $\lambda_L$ .

Exponential growth of out-of-time order correlators signals the ability of a system to scramble quantum information. The associated exponential growth rate, the scrambling rate  $\lambda_L$ , is determined by the strength and the nature of microscopic interactions as demonstrated in the previous Ch. 2 for the system of interacting Dirac electrons in graphene. There,  $\lambda_L$  was identified with the fastest rate resembling the inelastic electron-electron scattering rate. It was further argued in Sec. 1.7 and supported by the analysis presented in Ch. 2 that the exponential growth of out-of-time order correlators can be traced back to classical chaotic dynamics which are exponentially sensitive to changes in the initial conditions.

In this chapter, the aspect of determining the dynamics of out-of-time order correlators in experiments is discussed. Until now, these are merely a theoretical tool and their experimental realization requires the existence of a global time reversal operation or the ability to generate a perfect copy of the system which is impossible by means of “conventional” experimental techniques as discussed in Sec. 1.6. This constraint restricts proposed experimental approaches to systems of small sizes where a high degree of control over microscopic degrees of freedom can be achieved. This is not the case for generic condensed matter systems and approaches based on principles others than time reversal operations or creating copies are desirable.

In particular, a connection between out-of-time order correlators and the dynamics of classical fluctuations of certain observables is proposed. The fluctuations are initially induced by, e.g., inaccuracies in the experimental preparation procedure and their amplitude is subsequently monitored as a function of time. A possible measure of fluctuations is the amount of information associated with the considered observable which decreases with an increasing amplitude of fluctuations. Quantum chaotic dynamics could be reflected in the dynamics of fluctuations causing the associated amount of information to decay in time. As the observable and its fluctuations can be measured in experiments using conventional techniques, information about the system’s quantum chaotic behavior could be deduced.

In addition, the robustness of quantum chaotic dynamics against dissipative perturbations is examined in this chapter. As realistic systems cannot be perfectly isolated from their environment, the effect of dissipation on chaotic dynamics ought to be investigated.

In what follows, the proposed link between fluctuation dynamics and quantum chaotic dynamics as well as the role of dissipation is investigated for a microscopic model of electrons in a disordered metal coupled to a bath of phonons. In the absence of phonons, the system obeys quantum chaotic dynamics as argued previously in Sec. 1.7.2. To evaluate

the corresponding quantities, a kinetic equation approach is employed which complements the previously presented diagrammatic approach presented in Ch. 2. The following work is based on results presented in Ref. Klug and Syzranov (2019).

### 3.1. INFORMATION DYNAMICS

The proposed link between fluctuation dynamics of observables and quantum chaotic dynamics specified by out-of-time order correlators is further specified in this section. It is based on a series of steps which could be realized in experiments used to extract characteristics of quantum chaotic dynamics.

The considered equilibrated system is locally excited at the beginning of the experiment where the excitation is associated with the hermitian operator  $\hat{B}$ . Subsequently, the observable  $A(t) = \langle \hat{A}(t) \rangle$  associated with the hermitian operator  $\hat{A}$  is measured at time  $t$  where  $\langle \dots \rangle$  denotes quantum mechanical averaging. Within this approach, it is essential to determine  $A(t)$  in a time series to extract the time evolution of the fluctuation's amplitude. As the dynamics of the system is required to be unaffected by the measurement,  $A(t)$  is measured by performing weak measurements. Weak measurements are not projective, i.e. all possible outcomes are assumed to result in small, negligible changes to the system's state (Oreshkov and Brun, 2005). In the limit of a continuous monitoring, the evolution of  $A$  can hence be thought of as a trajectory in the space of possible outcomes.

Subsequently, the experiment is repeated several times where initial excitations vary from experiment to experiment, e.g., because of inaccuracies in the initial preparation procedure. These externally induced fluctuations, which are neither of thermal nor quantum nature and are therefore termed "classical" in the following, render the weakly measured quantity  $A(t)$  a fluctuating random variable,

$$A(t) = \overline{A}(t) + \delta A(t) \tag{3.1}$$

with fluctuations  $\delta A(t)$  with respect to the mean trajectory  $\overline{A}(t)$ , where  $\overline{\dots}$  denotes the average over experimental realizations. It is expected that the chaotic dynamics of the considered system, which causes out-of-time order correlators to grow exponentially, is reflected in the fluctuations  $\delta A(t)$ . This link could be used to probe the sensitivity of the trajectory  $A(t)$  to changes in initial conditions. The presented principle resembles the picture of out-of-time order correlators in the semiclassical limit where the trajectory's sensitivity is probed by means of fluctuations around its endpoints as discussed in Sec. 1.7. The described approach is summarized graphically in Fig. 3.1.

A possible measure which can be used to extract chaotic quantities from fluctuation dynamics is the information associated with the quantity  $A(t)$ . By introducing the probability density  $\rho(A, t)$  which describes the fluctuations of  $A(t)$  such that, e.g.,  $\overline{A}(t) =$

### 3. Chaotic fluctuation dynamics

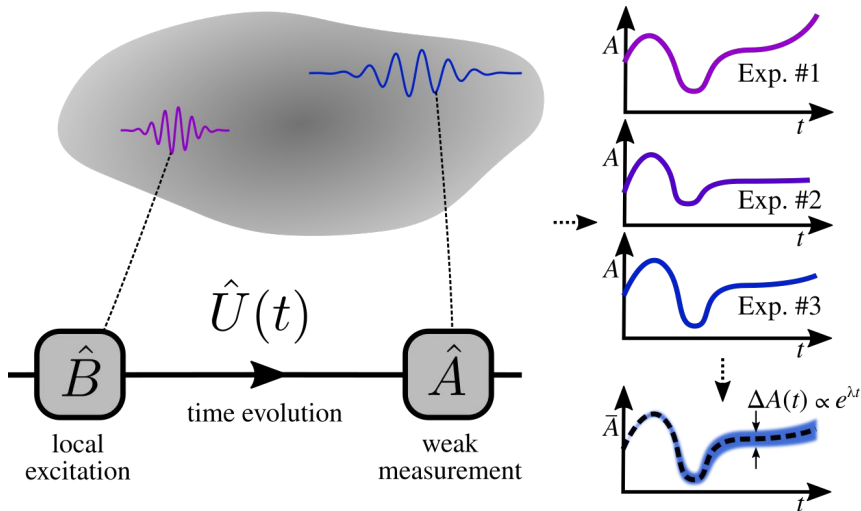


**Figure 3.1.:** Proposed approach to determine the time evolution of the amplitude of fluctuations of an observable  $A(t) = \langle \hat{A}(t) \rangle$ . The considered system is initially excited where the local excitations is associated with the operator  $\hat{B}$ . Consequently, the observable  $A(t)$  is determined in a time series by performing weak measurements which do not affect the time evolution of the state of the system. The experiment is repeated several times with varying initial conditions to determine the amplitude of fluctuations around the mean value  $\bar{A}(t)$ . In the case of chaotic dynamics, the amplitude is expected to grow exponentially,  $\Delta A(t) \propto e^{\lambda t}$ .

$\int dA \rho(A, t) A$ , it is defined as (Klug and Syzranov, 2019)

$$I_A(t) \equiv I_0 + \int dA \rho(A, t) \ln \rho(A, t), \quad (3.2)$$

which is also known (up to a sign) as Shannon entropy (Preskill, 2018). The information (in units  $\frac{1}{\ln 2}$ -th of bit) associated with  $A$  is maximal,  $I_A = I_0$ , if  $A(t)$  does not fluctuate at all and, hence, its distribution function is sharply peaked,  $\rho(A) = \delta(A - \bar{A})$ . In contrast, no information can be deduced if  $A$  fluctuates strongly and the distribution is without any feature,  $\rho(A) = \text{const.}$ , resulting in  $I_A = 0$  by definition.

In what follows, an observable  $A$  is considered which is sensitive to the system's chaotic dynamics. In this case,  $I_A(t)$  is expected to decay. This principal of chaotic dynamics manifesting in the dynamics of information is made plausible by considering the following argument: While the amplitude of fluctuations,  $\Delta A(t) = \sqrt{\overline{\delta A(t)^2}}$ , is initially determined by the excitation procedure, it is expected to grow for sufficiently small  $\Delta A(0)$  exponentially,  $\Delta A(t) \sim \Delta A(0)e^{\lambda t}$ , with a growth exponent  $\lambda$ . By approximating the probability density by a constant value,  $\rho(A, t) = [\Delta A(t)]^{-1}$ , for  $\bar{A} - \frac{\Delta A}{2} < A < \bar{A} + \frac{\Delta A}{2}$  else 0, the information is readily determined and found to decay linearly with the exponential growth rate,  $\frac{d}{dt} I_A(t) \propto -\lambda$ .

For this reason, information dynamics is contrasted to chaotic dynamics characterized by the exponential growth of out-of-time order correlators. In particular, for hermitian operators  $\hat{A}$  and  $\hat{B}$  acting as probe and perturbation, respectively, the out-of-time order

### 3. Chaotic fluctuation dynamics

correlator given by

$$C_A(t) = -\langle [\hat{A}(t), \hat{B}]^2 \rangle \quad (3.3)$$

is expected to obey chaotic dynamics,  $C_A(t) \propto e^{2\lambda_L t}$ , providing the scrambling rate  $\lambda_L$ . It is expected that the decay of  $I_A(t)$  and the growth of  $C_A(t)$  is determined by the same microscopic processes resulting in the matching of associated rates,  $\lambda \sim \lambda_L$  (Klug and Syzranov, 2019). Therefore,  $\lambda_L$  can be determined by extracting the decay of information from the classical fluctuations associated with an observable. An illustrative overview of the proposed link between dynamics of information and out-of-time order correlators is depicted in Fig. 3.1.

In the following, the proposed link between  $\lambda$  and  $\lambda_L$  is investigated for an exemplary quantum system of a disordered metal coupled to a dissipative bath of phonons. Although this work rather represents a proof of principle, the proposed link is expected to be more generic and also applicable to other systems of condensed matter physics.

#### 3.2. SUMMARY OF RESULTS

In this chapter, quantum chaotic dynamics and information dynamics are investigated for a disordered metal coupled to a bath of phonons. The systems of a disordered metal in the absence of phonons obeys chaotic dynamics for short Fermi wave length and large impurities,  $\lambda_F \ll a$ , with the Fermi wave length  $\lambda_F$  and the impurity size  $a$ , and sufficiently short distances between impurities,  $l_{\text{tr}} \ll \frac{a^2}{\lambda_F}$ , with mean-free path  $l_{\text{tr}}$  as discussed in Sec. 1.7.2. This model also represents the microscopic basis for a series of studies on chaotic dynamic, see e.g. Refs. Larkin and Ovchinnikov (1969); Aleiner and Larkin (1996); Syzranov *et al.* (2019).

In contrast to the work presented in Ch. 2 where chaotic dynamics arose due to electron-electron interactions, chaotic dynamics in the disordered metal arises due to electron-impurity scattering and is therefore already present on the single-particle level. Electron-phonon scattering processes are merely of dissipative nature and tend to slow down or even suppresses chaotic behavior similar to results obtained for systems coupled to dissipative environments presented in Ref. Syzranov *et al.* (2018). The bath of phonons is considered weakly coupled to the electronic degrees of freedom and the neutral excitations are furthermore characterized by a short correlation length  $\xi_{\text{ph}}$ . These are integral properties for the presented approach to apply. The presented approach is also expected to apply in the case of other types of neutral excitations, e.g. systems with magnon or plasmon excitations, as long as these conditions are met.

In the following, operator and information dynamics are investigated for one component of the system's total momentum. In particular, operators constituting the out-of-time order correlator Eq. (3.3) are chosen to  $\hat{A} = \hat{B} = \hat{P}_z$ . This choice is meaningful as it gives rise to chaotic out-of-time order correlator growth in the absence of the dissipative bath as argued in Sec. 1.7.2 and demonstrated in Ref. Syzranov *et al.* (2019). By recalling

### 3. Chaotic fluctuation dynamics

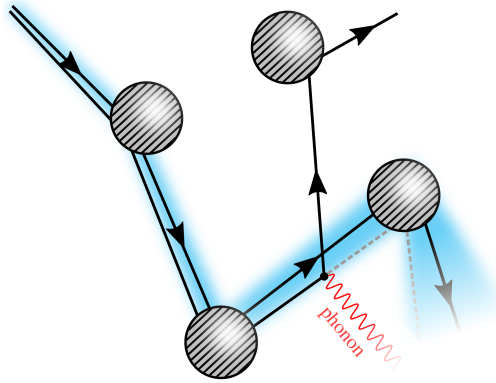


**Figure 3.2.:** Time evolution of classical trajectories (solid black lines) and the uncertainty associated with an electron (bluish trace) initially localized on lengths of order  $\lambda_F$  in the presence of electron-phonon scattering. As the transferred momentum in the phonon scattering process is large,  $p_{\text{ph}} \sim \xi_{\text{ph}}^{-1} \gg \frac{a}{l_{\text{tr}}} p_F$ , the scattered electron does not contribute to the out-of-time order correlator growth anymore. Reprinted figure with permission from [M.J. Klug, and S.V. Syzranov, Phys. Rev. **B** 100, 094304] Copyright (2019) by the American Physical Society. The original work is found under <https://dx.doi.org/10.1103/PhysRevB.100.094304>.

Sec. 1.7.2, the out-of-time order correlator in the semiclassical limit can be interpreted as two classical phase space trajectories which are initially separated by  $\lambda_F$  and diverge due to chaotic dynamics caused by impurity collisions. Therefore, quantum chaotic behavior in a disorder metal requires large impurities of size  $a$  compared to small Fermi wave length  $\lambda_F$  such that the propagation is classical for times  $t < t_E$  where the Ehrenfest time is given by

$$t_E = \lambda_{\text{cl}}^{-1} \ln \hbar_{\text{eff}}^{-1}, \quad (3.4)$$

with the classical Lyapunov exponent,  $\lambda_{\text{cl}} \sim \tau_0^{-1}$ , being of order of the elastic scattering time  $\tau_0$ , and  $\hbar_{\text{eff}} = \frac{\lambda_F}{a} \ll 1$  terminating the growth of out-of-time order correlators when the mismatch of trajectories has reached the order of the impurity size  $a$ . Furthermore, to observe chaotic dynamics in a significant time interval with many impurity collisions,  $a \gg \sqrt{\lambda_F l_{\text{tr}}}$  with the mean free path  $l_{\text{tr}} = v_F \tau_0$  and the Fermi velocity  $v_F$ .

The coupling of electrons to phonons introduces a second time scale related to the phonon correlation length  $\xi_{\text{ph}}$  (Klug and Syzranov, 2019)

$$t_{\text{ph}} = \lambda_{\text{cl}}^{-1} \ln \frac{\xi_{\text{ph}}}{\lambda_F}, \quad (3.5)$$

which defines two different regimes relevant for out-of-time order correlator growth: For  $t \ll t_{\text{ph}}$ , the distance between the classical trajectories is smaller than  $\xi_{\text{ph}}$  and their dynamics is strongly affected by phonon excitations. Here, analytic results are hardly achievable. For  $t \gg t_{\text{ph}}$ , the distance between the trajectories exceeds  $\xi_{\text{ph}}$  and phonons interact effectively short-ranged acting merely as source of dissipation: Once scattered by a phonon, electrons cease to contribute to the out-of-time order correlator growth as illustrated in Fig. 3.2. As the time scale for electron-phonon scattering is given by the

### 3. Chaotic fluctuation dynamics

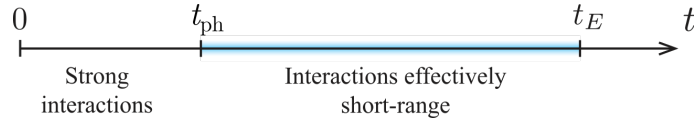


**Figure 3.3.:** In the regime of quantum chaotic dynamics considered in this work,  $t_{\text{ph}} \ll t \ll t_E$ , phonon interactions are effectively short-ranged reducing the scrambling rate by the inelastic electron-phonon scattering rate. Reprinted figure with permission from [M.J. Klug, and S.V. Syzranov, Phys. Rev. **B** 100, 094304] Copyright (2019) by the American Physical Society. The original work is found under <https://dx.doi.org/10.1103/PhysRevB.100.094304>.

inelastic scattering time  $\tau$ , the scrambling rate in the presence of the phonon bath is shown to be reduced to (Klug and Syzranov, 2019)

$$\lambda_L = \lambda_{\text{cl}} - \frac{1}{\tau}, \quad (3.6)$$

indicating that the chaotic dynamics is slowed down and is even suppressed if  $\tau^{-1} > \lambda_L$  in the presence of strong dissipative effects. As the correlation length of phonons is considered small,  $\xi_{\text{ph}} \ll a$ , the regime of quantum chaotic dynamics determined by  $\lambda_L$  in the interval  $t_{\text{ph}} \ll t \ll t_E$  is parametrically large and significant for out-of-time order correlators and the dynamics of information. It therefore represents the main focus of this work. The two regimes are illustrated in Fig. 3.3.

In this chapter, the dynamics of information associated with one component of the total momentum

$$P_z(t) = \langle \hat{P}_z(t) \rangle \quad (3.7)$$

is studied where quantum averaging is performed with respect to the initially excited many-body state. As the initial perturbation is considered classically fluctuating,  $P_z(t)$  is rendered a random variable varying from experiment to experiment where the amplitude of fluctuations is expected to increase in the case of chaotic dynamics. However, the initial excitation has to be sufficiently localized in real space and momentum space for chaotic dynamics to reflect in the decay of information. For this, one considers a “beam” of electrons which may contain several electrons and is localized on characteristic length  $\ell_{\text{ex}}$  and momentum scale  $p_{\text{ex}}$ , respectively. Similar to the discussion conducted above, these parameters represent the initial “uncertainty” of the excitation which will grow in the course of time. Quantum chaotic dynamics is therefore expected to be observed for  $\ell_{\text{ex}} \ll a^2/l_{\text{tr}}$  and  $p_{\text{ex}} \ll \frac{a}{l_{\text{tr}}} p_F$  in the modified time interval  $t'_{\text{ph}} \ll t \ll t'_E$  with  $t'_{\text{ph}} \sim \lambda_{\text{cl}}^{-1} \ln \frac{\xi_{\text{ph}}}{\ell_{\text{ex}}}$  and  $t'_E \sim \lambda_{\text{cl}}^{-1} \ln \frac{a}{\ell_{\text{ex}}}$ . The measured total momentum  $P_z(t)$  fluctuates from experiment to experiment giving rise to non-trivial dynamics of the associated information. For this particular setting, it is found that the information decays linearly in time (Klug and Syzranov, 2019)

$$\frac{d}{dt} I_P(t) = -\lambda_L, \quad (3.8)$$

with the scrambling rate  $\lambda_L$  given in Eq. (3.6).

### 3. Chaotic fluctuation dynamics

In what follows, the obtained results Eq. (3.6) and (3.8) are derived in microscopic detail. In particular, the microscopic model of a disordered metal coupled to a dissipative bath is presented Sec. 3.3. The out-of-time order correlator of momentum operators is evaluated and the scrambling rate is determined in Sec. 3.4 by employing a kinetic equation approach. Subsequently, information dynamics are discussed in Sec. 3.5. This chapter concludes in Sec. 3.6 with comments on a possible realization of the approach presented in Sec. 3.1 in experiments.

#### 3.3. MICROSCOPIC MODEL OF A DISSIPATIVE, DISORDERED METAL

The considered microscopic model describes electrons propagating in a quenched disorder potential. The randomly located impurities are characterized by the scattering length  $a$  and the elastic scattering time  $\tau_0$ . Additionally, the electrons are weakly coupled to a bath of neutral excitation characterized by short correlation length  $\xi_{\text{ph}}$ , here termed “phonons”. Independent of the exact nature of interactions and disorder, the system is assumed to be in a many-body delocalized phase.

The Hamilton operator of the systems is given by (Klug and Syzranov, 2019)

$$\hat{H} = \hat{H}_{\text{el}} + \hat{H}_{\text{el-ph}} + \hat{H}_{\text{ph}}, \quad (3.9)$$

with the interaction-free electron part  $\hat{H}_{\text{el}}$ , the phonon bath  $\hat{H}_{\text{ph}}$  and a coupling of electrons to phonons described by  $\hat{H}_{\text{el-ph}}$ . Electrons in three spatial dimensions are described by

$$\hat{H}_{\text{el}} = \int d^3\mathbf{r} \hat{\psi}^\dagger(\mathbf{r}) [\epsilon_{\hat{\mathbf{k}}} + U_{\text{imp}}(\mathbf{r})] \hat{\psi}(\mathbf{r}), \quad (3.10)$$

with fermionic creation and annihilation operators  $\hat{\psi}(\mathbf{r})$  and  $\hat{\psi}^\dagger(\mathbf{r})$  obeying the usual the anticommutation relation  $\{\hat{\psi}^\dagger(\mathbf{r}), \hat{\psi}(\mathbf{r}')\} = \delta(\mathbf{r} - \mathbf{r}')$ , and the electron dispersion  $\epsilon_{\hat{\mathbf{k}}}$  measured from the chemical potential with the momentum operator  $\hat{\mathbf{k}} = -i\frac{\partial}{\partial\mathbf{r}}$ . Here and in the following, Planck’s constant is set to unity,  $\hbar = 1$ , but is recovered if necessary. The spin index is generally suppressed as it does not affect the subsequent discussion. The static disorder potential is represented by  $U_{\text{imp}}(\mathbf{r}) = \sum_i U(\mathbf{r} - \mathbf{R}_i)$  with the randomly located, uncorrelated impurity positions  $\{\mathbf{R}_i\}$ . The single-impurity potential  $U(\mathbf{r})$  is considered short-ranged compared to the mean free path  $l_{\text{tr}}$  such that each scattering event can be considered uncorrelated from preceding collisions. In the following, one particular disorder realization is considered. However, as the scattering events are mutually uncorrelated and phonons short-range correlated, the determined quantities are considered self-averaged such that results do not depend on the disorder realization. It is commented on the aspect of disorder averaging when necessary.

The interaction between phonons and electrons is described by

$$\hat{H}_{\text{el-ph}} = g_{\text{el-ph}} \int d^3\mathbf{r} \hat{\phi}(\mathbf{r}) \hat{\psi}^\dagger(\mathbf{r}) \hat{\psi}(\mathbf{r}), \quad (3.11)$$

### 3. Chaotic fluctuation dynamics

with the bosonic phonon field operators  $\hat{\phi}(\mathbf{r})$  corresponding to a real-valued displacement field and a constant coupling strength which is small compared to the Fermi energy,  $g_{\text{el-ph}} \ll \epsilon_F$ . The following analysis is conducted within a weak-coupling limit where interaction effects can be controlled perturbatively in powers of  $g_{\text{el-ph}}$ . The dynamics of the phonon bath is further specified by  $\hat{H}_{\text{ph}}$ . However, as the microscopic details are not important in the following (except for the inelastic scattering time  $\tau$  and correlation length  $\xi_{\text{ph}}$  which are introduced phenomenologically) and the phonon spectrum is considered non-renormalized by electron dynamics,  $\hat{H}_{\text{ph}}$  is further left unspecified.

#### 3.4. TOTAL MOMENTUM OUT-OF-TIME ORDER CORRELATOR

In this section, the out-of-time order correlator of total momentum operators,

$$C_P(t) = -\langle [\hat{P}_z(t), \hat{P}_z]^2 \rangle, \quad (3.12)$$

is evaluated with respect to the thermal equilibrium state  $\langle \dots \rangle = Z^{-1} \text{tr}[e^{-\hat{H}/k_B T} \dots]$  with the partition function  $Z = \text{tr}[e^{-\hat{H}/k_B T}]$  and specified by the temperature  $T$ . One component of the total momentum operator is given by

$$\hat{P}_z(t) = \int d^3\mathbf{r} \hat{\psi}^\dagger(\mathbf{r}, t) \hat{p}_z \hat{\psi}(\mathbf{r}, t), \quad (3.13)$$

where  $\hat{p}_z = -i\nabla_z$  is the single-particle momentum operator and  $z$  one of the coordinates of  $\mathbf{r}$ . The time evolution of fermionic field operators is realized as usual, e.g.  $\hat{\psi}(\mathbf{r}, t) = \hat{U}^\dagger(t) \hat{\psi}(\mathbf{r}) \hat{U}(t)$ , with the time evolution operator  $\hat{U}(t) = e^{-i\hat{H}t}$ .

In what follows, a kinetic equation is derived which determines the time evolution of Eq. (3.12) in the time interval  $t_{\text{ph}} \ll t \ll t_E$  where quantum chaotic dynamics is expected. The approach, whose derivation is rather lengthy and therefore presented in the Appendix A.5, resembles kinetic equation approaches for single-particle distribution functions (see e.g. Refs. Mahan (2000); Kamenev (2011)) resulting in the celebrated Boltzmann equation. Here, the usual approach is extended to the augmented Keldysh formalism introduced in Sec. 2.4 to treat out-of-time ordered sequences of operators as well as to four point correlation functions as illustrated in the following section. In particular, a certain correlation function is introduced in Sec. 3.4.1 which represents the central object of the kinetic equation approach. Subsequently, the kinetic equation is presented and discussed in Sec. 3.4.2. The out-of-time order correlator is eventually evaluated in Sec. 3.4.3 to determine the scrambling rate.

##### 3.4.1. FOUR-POINT CORRELATOR

To derive a kinetic equation which governs the dynamics of the out-of-time order correlator introduced in Eq. (3.12), the following correlation function is introduced,

### 3. Chaotic fluctuation dynamics

$$K(\mathbf{R}\mathbf{r}\tau, \mathbf{R}'\mathbf{r}'\tau', t) = \langle [\hat{\psi}^\dagger(\mathbf{R} - \frac{\mathbf{r}}{2}, t - \frac{\tau}{2})\hat{\psi}(\mathbf{R} + \frac{\mathbf{r}}{2}, t + \frac{\tau}{2}), \hat{P}_z(0)] \times [\hat{\psi}^\dagger(\mathbf{R}' - \frac{\mathbf{r}'}{2}, t - \frac{\tau'}{2})\hat{\psi}(\mathbf{R}' + \frac{\mathbf{r}'}{2}, t + \frac{\tau'}{2}), \hat{P}_z(0)] \rangle, \quad (3.14)$$

where  $\mathbf{R}^{(l)}$  and  $t^{(l)}$  are ‘‘center-of-mass’’ coordinates and times (Kamenev, 2011) of the respective pairs of the fermionic operators whereas  $\mathbf{r}^{(l)}$  and  $\tau^{(l)}$  the difference coordinates, respectively.  $K(\mathbf{R}\mathbf{r}\tau, \mathbf{R}'\mathbf{r}'\tau', t)$  can be generally used to express out-of-time order correlators of type  $\langle [\hat{A}(t), \hat{P}_z(0)]^2 \rangle$ . In particular, by introducing its Wigner transform (Kamenev, 2011),

$$K(\mathbf{R}\mathbf{p}, \mathbf{R}'\mathbf{p}', t) = \int_{\mathbf{r}\omega\tau} \int_{\mathbf{r}'\omega'\tau'} e^{i(\omega\tau - \mathbf{r}\mathbf{p}) + i(\omega'\tau' - \mathbf{r}'\mathbf{p}')} K(\mathbf{R}\mathbf{r}\tau, \mathbf{R}'\mathbf{r}'\tau', t), \quad (3.15)$$

where  $\int_{\mathbf{r}\omega\tau} \equiv \int d^3\mathbf{r}d\tau \frac{d\omega}{2\pi}$ , the out-of-time order correlator of momentum operators Eq. (3.12) is given by

$$C_P(t) = \int_{\mathbf{p}\mathbf{R}} \int_{\mathbf{p}'\mathbf{R}'} p_z p'_z K(\mathbf{R}\mathbf{p}, \mathbf{R}'\mathbf{p}', t), \quad (3.16)$$

with  $\int_{\mathbf{p}} \equiv \int \frac{d^3\mathbf{p}}{(2\pi)^3}$ .

The form of Eq. (3.16) suggests that  $K(\mathbf{R}\mathbf{p}, \mathbf{R}'\mathbf{p}', t)$  can be interpreted as distribution function of two systems centered at  $\mathbf{R}$  and  $\mathbf{R}'$  carrying momentum  $\mathbf{p}$  and  $\mathbf{p}'$ , respectively. This representation resembles the thermal double state representation discussed in Sec. 1.2 where the total system is interpreted as two identical copies which are initially perfectly entangled. As shown in the next section, the initial condition  $K(\mathbf{R}\mathbf{p}, \mathbf{R}'\mathbf{p}', 0)$  is indeed a sharply peaked function of  $|\mathbf{p} - \mathbf{p}'|$  and  $|\mathbf{R} - \mathbf{R}'|$ , the latter with a finite width of order  $\lambda_F$ .  $K(\mathbf{R}\mathbf{p}, \mathbf{R}'\mathbf{p}', t)$  is therefore interpreted as sharp wave packet which broadens under chaotic dynamics as discussed in Sec. 1.7.2 until the Ehrenfest time  $t_E$  is reached where its characteristic length scale is of order of the impurity size.

#### 3.4.2. KINETIC EQUATION APPROACH

To describe the time evolution of  $K(\mathbf{R}\mathbf{p}, \mathbf{R}'\mathbf{p}', t)$ , a kinetic equation approach is employed. Its derivation follows the usual one for ‘‘greater’’ and ‘‘lesser’’ components of single particle propagators, see e.g. Ref. Mahan (2000) for details, but requires an extension to the augmented Keldysh formalism introduced in Sec. 2.4 to represent out-of-time order correlation functions. As the derivation is rather technical, the result is quoted whereas its derivation is presented in the Appendix A.5.

For weak electron-phonon coupling and a separation of scales between center-of-mass and difference coordinates (Mahan, 2000), the kinetic equation is determined to (Klug and Syzranov, 2019)

### 3. Chaotic fluctuation dynamics

$$(\partial_t + i\hat{L}_{\mathbf{r},\mathbf{p}} + i\hat{L}_{\mathbf{r}',\mathbf{p}'})K(\mathbf{R}\mathbf{p}, \mathbf{R}'\mathbf{p}', t) = I_{\text{ph}}[K], \quad (3.17)$$

where the left-hand side is given in terms of the Liouville operator

$$i\hat{L}_{\mathbf{R},\mathbf{p}} = \mathbf{v}_{\mathbf{p}} \cdot \nabla_{\mathbf{R}} - \nabla_{\mathbf{R}} U_{\text{imp}}(\mathbf{R}) \cdot \nabla_{\mathbf{p}} \quad (3.18)$$

which describes “free” propagation of electrons with the phonon renormalized velocity  $\mathbf{v}_{\mathbf{p}} \equiv \nabla_{\mathbf{p}} \epsilon(\mathbf{p}) \approx v_F \frac{\mathbf{p}}{|\mathbf{p}|}$  in the impurity potential  $U_{\text{imp}}$ . If the initial condition  $K(\mathbf{R}\mathbf{p}, \mathbf{R}'\mathbf{p}', 0)$  is sufficiently peaked on scales introduced earlier in Sec. 3.2 and if phonons are absent, it describes propagation determined by classical trajectories for  $t < t_E$ .

The inelastic scattering of electrons with phonons is represented by the collision integral  $I_{\text{ph}}[K]$  on the right-hand side of Eq. (3.17). Initially for  $0 < t \ll t_{\text{ph}}$  when the distance between the systems is shorter than the phonon correlation length,  $|\mathbf{R} - \mathbf{R}'| \ll \xi_{\text{ph}}$ , phonon interactions generate correlations between the two copies centered at  $\mathbf{R}$  and  $\mathbf{R}'$  and the evolution of  $K(\mathbf{R}\mathbf{p}, \mathbf{R}'\mathbf{p}', t)$  is significantly determined by phonon dynamics. Instead for  $t \gg t_{\text{ph}}$ , the distance between systems exceeds the phonon correlation length  $|\mathbf{R} - \mathbf{R}'| \gg \xi_{\text{ph}}$  and scattering processes connecting subsystems at  $\mathbf{R}$  and  $\mathbf{R}'$  can be neglected. See the Appendix (A.5) for a detailed discussion. In this case, the collision integral is given by

$$I_{\text{ph}}[K] = - \left[ \int_{\mathbf{k}} (\Gamma_{\mathbf{p} \rightarrow \mathbf{k}} + \Gamma_{\mathbf{p}' \rightarrow \mathbf{k}}) \right] K(\mathbf{R}\mathbf{p}, \mathbf{R}'\mathbf{p}', t) \\ + \int_{\mathbf{k}} \Gamma_{\mathbf{k} \rightarrow \mathbf{p}} K(\mathbf{R}\mathbf{k}, \mathbf{R}'\mathbf{p}', t) + \int_{\mathbf{k}} \Gamma_{\mathbf{k} \rightarrow \mathbf{p}'} K(\mathbf{R}\mathbf{p}, \mathbf{R}'\mathbf{k}, t), \quad (3.19)$$

where the first line contains scattering process out of the reference state, which is specified by the left-hand side of Eq. (3.17), and the second line scattering processes into the reference state. The phonon-assisted scattering rate is obtained to

$$\Gamma_{\mathbf{p} \rightarrow \mathbf{k}} = ig_{\text{el-ph}}^2 \{ D^<(\mathbf{p} - \mathbf{k}, \epsilon_{\mathbf{p}} - \epsilon_{\mathbf{k}}) f_0(\epsilon_{\mathbf{k}}) + D^>(\mathbf{p} - \mathbf{k}, \epsilon_{\mathbf{p}} - \epsilon_{\mathbf{k}}) [1 - f_0(\epsilon_{\mathbf{k}})] \}, \quad (3.20)$$

where  $g_{\text{el-ph}}$  is the electron-phonon coupling constant defined by Eq. (3.11).  $D^<$  and  $D^>$  are the lesser and greater phonon propagators which are defined in the Appendix A.5.  $f_0(\epsilon) = [e^{\frac{\epsilon}{k_B T}} + 1]^{-1}$  refers to the Fermi distribution function.

The kinetic equation is complemented by initial conditions. At  $t = 0$ , the correlator Eq. (3.14) can be evaluated explicitly by using the anticommutation relations of fermionic field operators. The result reads (Klug and Syzranov, 2019)

$$K_0(\mathbf{R}\mathbf{p}, \mathbf{R}'\mathbf{p}') = (4\pi)^3 \delta(\mathbf{p} - \mathbf{p}') \partial_Z \partial_{Z'} \int_{\mathbf{q}} e^{2iq(\mathbf{R} - \mathbf{R}')} f_0(\epsilon_{\mathbf{p}-\mathbf{q}}) [1 - f_0(\epsilon_{\mathbf{p}+\mathbf{q}})]. \quad (3.21)$$

For  $|\mathbf{R} - \mathbf{R}'|$  exceeding  $\lambda_F$ , it is approximated to

$$K_0(\mathbf{R}\mathbf{p}, \mathbf{R}'\mathbf{p}') \approx (2\pi)^6 f_0(\epsilon_{\mathbf{p}}) [1 - f_0(\epsilon_{\mathbf{p}})] \delta(\mathbf{p} - \mathbf{p}') \partial_Z \partial_{Z'} \delta(\mathbf{R} - \mathbf{R}'), \quad (3.22)$$

### 3. Chaotic fluctuation dynamics

which is a sharply peaked function of  $|\mathbf{p} - \mathbf{p}'|$  and  $|\mathbf{R} - \mathbf{R}'|$  with partial derivatives with respect to the  $z$ -components of  $\mathbf{R}$  and  $\mathbf{R}'$ , respectively. The factors including Fermi functions restrict contributions to the out-of-time order correlator to quasiparticle excitation on the Fermi surface with energies  $\epsilon_{\mathbf{p}} \approx \epsilon_F$ . In the following, it is assumed that  $K(\mathbf{R}\mathbf{p}, \mathbf{R}'\mathbf{p}', t_{\text{ph}}) \approx K_0(\mathbf{R}\mathbf{p}, \mathbf{R}'\mathbf{p}')$ . This assumption is valid for short-range correlations which render  $t_{\text{ph}}$  sufficiently short, and may even be correct for the case of insufficiently short-range correlations as long as  $K$  is still peaked for  $t \sim t_{\text{ph}}$ .

By making use of the characteristic peaked form of  $K_0$ , the kinetic equation may be simplified considerably (Klug and Syzranov, 2019). It is first noted that the kinetic equation (3.17) is norm preserving, i.e. the correlation function is globally conserved,

$$\int_{\mathbf{R}\mathbf{p}} \int_{\mathbf{R}'\mathbf{p}'} K(\mathbf{R}\mathbf{p}, \mathbf{R}'\mathbf{p}', t) \equiv N_K = \text{const.} \quad (3.23)$$

This suggest to split up the correlation function into a “peaked” ( $p$ ) and “smooth” ( $s$ ) part,

$$K(\mathbf{R}\mathbf{p}, \mathbf{R}'\mathbf{p}', t) = K^{(s)}(\mathbf{R}\mathbf{p}, \mathbf{R}'\mathbf{p}', t) + K^{(p)}(\mathbf{R}\mathbf{p}, \mathbf{R}'\mathbf{p}', t), \quad (3.24)$$

where the characteristic scales of  $K^{(p)}$  associated with the length  $|\mathbf{R} - \mathbf{R}'|$  and the momentum  $|\mathbf{p} - \mathbf{p}'|$  are considerably shorter than the chaotic cut-off scales,

$$a_{\text{ch}} = \frac{a^2}{l_{\text{tr}}} \quad \text{and} \quad p_{\text{ch}} = \frac{a}{l_{\text{tr}}} p_F, \quad (3.25)$$

which terminates the chaotic growth at  $t \sim t_E$ . While  $K^{(p)}$  contributes to the growth of the out-of-time order correlator,  $K^{(s)}$  represents an “incoherent” background which does not contribute as momenta  $\mathbf{p}$  and  $\mathbf{p}'$  are uncorrelated. Hence,

$$F^{(s)} = \int_{\mathbf{R}\mathbf{p}} \int_{\mathbf{R}'\mathbf{p}'} p_z p'_z K^{(s)}(\mathbf{R}\mathbf{p}, \mathbf{R}'\mathbf{p}', t) = 0. \quad (3.26)$$

Whereas the time evolution of  $K^{(p)}$  for  $t < t_E$  is determined in the absence of phonons by classical trajectories,  $K^{(s)}$  spreads diffusively but is of no significant for the subsequent discussion and therefore not pursued further.

Initially, the full weight  $N_K$  is contained in  $K^{(p)}$  which broadens under time evolution because of classical chaotic dynamics. If an electron is scattered by a phonon, the typical momentum transfer is  $p_{\text{ph}} \sim \xi_{\text{ph}}^{-1}$  exceeding the cut-off scale  $p_{\text{ph}} \gg p_{\text{ch}}$  as depicted in Fig. 3.2. Thus, the electron does not contribute to the out-of-time order correlator growth anymore and increases the weight of  $K^{(s)}$  while lowering the weight of  $K^{(p)}$  as depicted in Fig. 3.4.

This fact simplifies the kinetic equation considerably as “in-scattering” processes in Eq. (3.19) can be neglected,  $\int_{\mathbf{k}} \Gamma_{\mathbf{k} \rightarrow \mathbf{p}} K^{(s)}(\mathbf{R}\mathbf{k}, \mathbf{R}'\mathbf{p}', t) \approx \int_{\mathbf{k}} \Gamma_{\mathbf{k} \rightarrow \mathbf{p}} K^{(p)}(\mathbf{R}\mathbf{k}, \mathbf{R}'\mathbf{p}', t) \approx 0$ , and “out-scattering” processes are independent of the direction of reference momenta. The simplified kinetic equation is consequently given by

### 3. Chaotic fluctuation dynamics

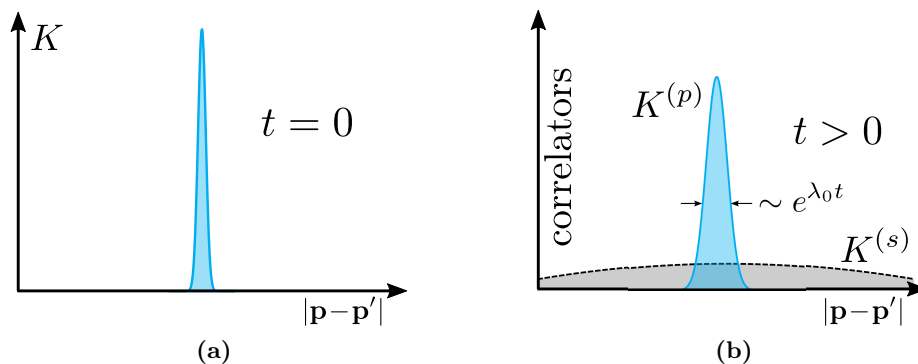


**Figure 3.4.:** The correlation function Eq. (3.15) is split into a “smooth” (s) and a “peaked” (p) part  $K = K^{(s)} + K^{(p)}$ . (a) Initially, the total weight is contained in  $K^{(p)}$  which is a sharply peaked function of  $|\mathbf{p} - \mathbf{p}'|$  and  $|\mathbf{R} - \mathbf{R}'|$  dictated by initial conditions  $K_0$ . (b) For  $t_{\text{ph}} < t < t_E$ ,  $K^{(p)}$  broadens due to impurity scattering. Furthermore, weight is transferred from  $K^{(p)}$  to  $K^{(s)}$  due to inelastic phonon scattering. As  $K^{(s)}$  accumulates “incoherent” particle excitations, it does not contribute to the out-of-time order correlator growth. Reprinted figures with permission from [M.J. Klug, and S.V. Syzranov, Phys. Rev. B 100, 094304] Copyright (2019) by the American Physical Society. The original work is found under <https://dx.doi.org/10.1103/PhysRevB.100.094304>.

$$(\partial_t + i\hat{L}_{\mathbf{r},\mathbf{p}} + i\hat{L}_{\mathbf{r}',\mathbf{p}'} - \frac{2}{\tau})K^{(p)}(\mathbf{R}\mathbf{p}, \mathbf{R}'\mathbf{p}', t) = 0, \quad (3.27)$$

where the inelastic scattering rate  $\tau^{-1}$  due to phonon scattering is independent on impurity scattering processes. This holds for regimes with a separation of elastic and inelastic scattering events but breaks down for long-ranged interactions or short elastic scattering times where  $\tau^{-1}$  is significantly renormalized (Klug and Syzranov, 2019). The inelastic phonon scattering rate is given by

$$\begin{aligned} \tau^{-1} &= \int_{\mathbf{k}} \Gamma_{\mathbf{p} \rightarrow \mathbf{k}} \Big|_{|\mathbf{p}|=p_F} \\ &= -2g_{\text{el-ph}}^2 \int_{\mathbf{k}} \text{Im} D_{\mathbf{p}-\mathbf{k}}^R(\epsilon_{\mathbf{p}} - \epsilon_{\mathbf{q}}) [n_B(\epsilon_{\mathbf{p}} - \epsilon_{\mathbf{q}}) + 1 - f_0(\epsilon_{\mathbf{k}})] \Big|_{|\mathbf{p}|=p_F}, \end{aligned} \quad (3.28)$$

which matches the relaxation rate of electrons due to phonons in a metal (Mahan, 2000). Here,  $n_B(\omega) = [e^{\frac{\omega}{k_B T}} - 1]^{-1}$  is the equilibrium Bose distribution function and  $|\mathbf{p}| \approx |\mathbf{p}'| \approx p_F$  are close to the Fermi surface. The retarded phonon propagator is given in terms of phonon field operators  $\hat{\phi}(\mathbf{r}, t)$  by  $D^R(\mathbf{r}-\mathbf{r}', t-t') = -i\theta(t-t')\langle \hat{\phi}(\mathbf{r}, t)\hat{\phi}(\mathbf{r}', t') \rangle$  with  $\langle \dots \rangle = Z_{\text{ph}}^{-1} \text{tr}[e^{-\hat{H}_{\text{ph}}/k_B T} \dots]$ .

#### 3.4.3. CHAOTIC OPERATOR DYNAMICS

The simplified kinetic equation (3.27) is now solved for given initial condition  $K_0$  specified in Eq. (3.22). For  $t < t_E$ , the ballistic motion of electrons and the scattering on phonons can be separated by introducing

### 3. Chaotic fluctuation dynamics

$$K^{(p)}(\mathbf{R}\mathbf{p}, \mathbf{R}'\mathbf{p}', t) = e^{-2t/\tau} \tilde{K}(\mathbf{R}\mathbf{p}, \mathbf{R}'\mathbf{p}', t), \quad (3.29)$$

where  $\tilde{K}$  obeys the kinetic equation

$$(\partial_t + i\hat{L}_{\mathbf{r},\mathbf{p}} + i\hat{L}_{\mathbf{r}',\mathbf{p}'})\tilde{K}(\mathbf{R}\mathbf{p}, \mathbf{R}'\mathbf{p}', t) = 0, \quad (3.30)$$

which describes the evolution of a correlation function in the absence of phonons. This problem was solved in Ref. [Syzranov \*et al.\* \(2019\)](#) but is discussed here for completeness. By introducing the classical, ballistic propagator,

$$G(\mathbf{R}\mathbf{p}; \mathbf{R}_0\mathbf{p}_0, t) = (2\pi)^3 \delta[\mathbf{p} - \tilde{\mathbf{p}}] \delta[\mathbf{R} - \tilde{\mathbf{R}}], \quad (3.31)$$

with classical trajectories  $\tilde{\mathbf{R}} = \tilde{\mathbf{R}}(t, \mathbf{R}_0, \mathbf{p}_0)$  and  $\tilde{\mathbf{p}} = \tilde{\mathbf{p}}(t, \mathbf{R}_0, \mathbf{p}_0)$  depending on initial conditions  $\mathbf{R}_0$  and  $\mathbf{p}_0$  and describing the classical motion of electrons in the disorder potential, the time evolved correlation function is determined to

$$\tilde{K}(\mathbf{R}\mathbf{p}, \mathbf{R}'\mathbf{p}', t) = \int_{\mathbf{R}_0\mathbf{p}_0} \int_{\mathbf{R}'_0\mathbf{p}'_0} G(t, \mathbf{R}\mathbf{p}; \mathbf{R}_0\mathbf{p}_0) G(t, \mathbf{R}'\mathbf{p}'; \mathbf{R}'_0\mathbf{p}'_0) K_0(\mathbf{R}_0\mathbf{p}_0, \mathbf{R}'_0\mathbf{p}'_0). \quad (3.32)$$

By inserting the expression for  $K_0$ , Eq. (3.22), and using Eq. (3.29) to incorporate phonon scattering, the out-of-time order correlator Eq. (3.16) is given by

$$C_P(t) = e^{2t/\tau} \left\langle \left\langle \left| \frac{\partial \tilde{p}_z(t)}{\partial Z_0} \right|^2 \right\rangle \right\rangle, \quad (3.33)$$

where the average runs over all thermally activated states near the Fermi surface  $\langle \dots \rangle \equiv \int_{\mathbf{R}_0\mathbf{p}_0} \dots f_0(\epsilon_{\mathbf{p}_0}) [1 - f_0(\epsilon_{\mathbf{p}_0})]$ .

To determine the sensitivity of classical trajectories to changes in initial conditions for one particular disorder realization, it is legitimate to consider self-averaged quantities as the dynamics of sufficiently short-ranged correlated ([Klug and Syzranov, 2019](#)). This allows one to consider the disorder averaged sensitivity of classical trajectories. It is found in Refs. [Larkin and Ovchinnikov \(1969\)](#); [Syzranov \*et al.\* \(2019\)](#), but also within a detailed derivation presented in the Appendix A.1, that

$$\left\langle \left| \frac{\partial \tilde{p}_z(t)}{\partial Z_0} \right| \right\rangle_{\text{dis}} \propto e^{\lambda_{\text{cl}} t}, \quad (3.34)$$

with the classical Lyapunov exponent (see Appendix A.1)

$$\lambda_{\text{cl}} = \frac{1}{\tau_0} \left\{ \int_0^{l_{\text{tr}}} \frac{\rho}{8} \left[ \frac{\sin^2 \theta}{\rho^2} + \left( \frac{d\theta}{d\rho} \right)^2 \right] d\rho \right\}^{1/3}, \quad (3.35)$$

with the scattering angle  $\theta = \theta(\rho)$  and the impact parameter  $\rho$  which is of order as the elastic scattering rate  $\tau_0^{-1}$ . Hence, the out-of-time order correlator of momentum operators Eq. (3.12) grows exponentially,  $C_P(t) \propto e^{2\lambda_L t}$ , with the scrambling rate given by  $\lambda_L = \lambda_{\text{cl}} - \frac{1}{\tau}$ .

### 3.5. TOTAL MOMENTUM INFORMATION DYNAMICS

The scrambling rate  $\lambda_L$  determined in the previous section is compared to the decay rate of information associated with one component of the total momentum  $P_z(t)$  as introduced in Eq. (3.7). In this section, the microscopic details of information dynamics for the model of a disordered metal coupled to a dissipative phonon bath are discussed. As the decay rate is supposed to reflect characteristics of quantum chaotic dynamics, certain requirements on the initial excitation of the system are presented. In particular, first, the dynamics of localized excitations is discussed in Sec. 3.5.1 and second, the aspect of classical induced fluctuations is discussed in Sec. 3.5.2.

#### 3.5.1. LOCALIZED EXCITATIONS

To extract information dynamics, the system is initially excited and brought into a state with finite total momentum. Subsequently, the total momentum observable  $P_z(t)$  introduced in Eq. (3.7) is monitored in weak measurements in several experimental realizations to determine the decay rate of the associated information. Under the same assumption which justifies the applicability of the kinetic equation approach for out-of-time order correlators presented in Sec. 3.4, the total momentum is expressed by introducing the quasiclassical distribution function  $f(\mathbf{R}, \mathbf{q}, t)$  whose dynamics are determined by a conventional Boltzmann equation. For this, the perturbation with respect to the equilibrated ground state due to the initial excitation of the system is parameterized by

$$g(\mathbf{R}, \mathbf{p}, t) = f(\mathbf{R}, \mathbf{p}, t) - f_0(\epsilon_{\mathbf{p}}) \quad (3.36)$$

with the Fermi distribution function  $f_0$ . As the total momentum of the equilibrated system is zero, the total momentum is given by

$$P_z(t) = \int_{\mathbf{R}\mathbf{p}} p_z g(\mathbf{R}, \mathbf{p}, t). \quad (3.37)$$

To observe quantum chaotic behavior based on classical, ballistic propagation of electrons, the initial excitations have to be sufficiently localized in momentum and real space, otherwise their dynamics is diffusive. These local excitations may contain several electrons and are therefore termed “beams” in the following. In particular, the initial perturbation  $g(\mathbf{R}, \mathbf{p}, 0) = g_0(\mathbf{R}, \mathbf{p})$  has to be short-range correlated such that

$$\int_{\mathbf{p}\mathbf{R}} g_0(\mathbf{R}, \mathbf{p}) g_0(\mathbf{R} - \Delta\mathbf{R}, \mathbf{p} - \Delta\mathbf{p}) = \mathcal{F}\left(\frac{|\Delta\mathbf{R}|}{\ell_{\text{ex}}}, \frac{|\Delta\mathbf{p}|}{p_{\text{ex}}}\right), \quad (3.38)$$

where  $\mathcal{F}(x, y)$  represents a rapidly decaying function if its arguments are of order one and larger. The quantities  $\ell_{\text{ex}}$  and  $p_{\text{ex}}$  denote the initial excitation scales in spatial and momentum space, respectively. To observe quantum chaotic behavior, these scales have to be contrasted to the chaotic cut-off scales  $a_{\text{ch}}$  and  $p_{\text{ch}}$  introduced in Eq. (3.25). As  $\ell_{\text{ex}}$  and

### 3. Chaotic fluctuation dynamics

$p_{\text{ex}}$  are associated with the initial uncertainty of the beam,

$$\ell_{\text{ex}} \ll a, a_{\text{ch}} \quad \text{and} \quad p_{\text{ex}} \ll p_{\text{ch}}, \quad (3.39)$$

and a similar setting as presented in the previous section is obtained. Hence, the beam is sufficiently localized to obey classical chaotic instead of diffusive dynamics rendering  $g(\mathbf{R}, \mathbf{p}, t)$  a sharply peaked function of  $\mathbf{R}$  and  $\mathbf{p}$  which evolves under quantum chaotic dynamics in the interval  $t'_{\text{ph}} \ll t \ll t'_E$  as discussed in Sec. 3.2.

Similar to the discussion presented in Sec. 3.4.2, the distribution function is split into a “peaked” (p) and “smooth” (s) part,

$$g(\mathbf{R}, \mathbf{p}, t) = g^{(s)}(\mathbf{R}, \mathbf{p}, t) + g^{(p)}(\mathbf{R}, \mathbf{p}, t), \quad (3.40)$$

which allows several simplifications. As the transferred momentum in electron-phonon collisions is large,  $p_{\text{ph}} \gg p_{\text{ch}}$ , and the beams of electrons are sufficiently localized, particles once scattered by a phonon move from  $g^{(p)}$  to  $g^{(s)}$ , which can be interpreted as “incoherent” background and does not contribute to  $P(t)$  as the momenta of excitations in  $g^{(s)}$  are uncorrelated. Similar to the discussion leading to the kinetic equation (3.27), the Boltzmann equation governing the time evolution of  $g^{(p)}$  is given by (Klug and Syzranov, 2019)

$$(\partial_t + i\hat{L}_{\mathbf{R}, \mathbf{p}} - \frac{1}{\tau})g^{(p)}(\mathbf{R}, \mathbf{p}, t) = 0, \quad (3.41)$$

with the inelastic phonon scattering rate  $\tau^{-1}$  introduced in Eq. (3.28). Again, contributions from ballistic propagation in the disorder potential and inelastic phonon scattering separate suggesting the ansatz

$$g^{(p)}(\mathbf{R}, \mathbf{p}, t) = e^{-t/\tau} \tilde{g}(\mathbf{R}, \mathbf{p}, t), \quad (3.42)$$

where the distribution function in the absence of phonon coupling obeys

$$(\partial_t + i\hat{L}_{\mathbf{R}, \mathbf{p}})\tilde{g}(\mathbf{R}, \mathbf{p}, t) = 0 \quad (3.43)$$

and  $\tilde{g}(\mathbf{R}, \mathbf{p}, t)$  evolves under classical chaotic dynamics for  $t < t'_E$ . Hence, the beams move on average on a classical trajectory determined by the classical equations of motion. Additionally, their width grows exponentially as it resembles the evolution of  $K(\mathbf{p}\mathbf{R}, \mathbf{p}'\mathbf{R}', t)$  discussed in the previous section or the growing uncertainty of the position and momentum of a constantly scattered single electron as discussed in Sec. (1.7.2). The solution to Eq. (3.43) with initial conditions obeying Eq. (3.38) is given by means of the classical propagators  $G(t, \mathbf{R}\mathbf{p}; \mathbf{R}_0\mathbf{p}_0)$  introduced in Eq. (3.31),

$$\tilde{g}(\mathbf{R}, \mathbf{p}, t) = \int_{\mathbf{R}_0\mathbf{p}_0} G(t, \mathbf{R}\mathbf{p}; \mathbf{R}_0\mathbf{p}_0)g_0(\mathbf{R}_0, \mathbf{p}_0).$$

Similar to the previous discussion on the time evolution of  $K$ , the beams of electrons described by the peaked distribution function  $g^{(p)}(\mathbf{R}, \mathbf{p}, t)$  broadens under time evolution

### 3. Chaotic fluctuation dynamics

due to chaotic dynamics and additionally loses weight due to electron-phonon scattering.

#### 3.5.2. DYNAMICS OF CLASSICAL FLUCTUATIONS

By having established the dynamics of the localized beams, varying initial conditions due to small uncertainties in the initial experimental preparation procedure are introduced. The initial perturbation from equilibrium is considered to fluctuate which is modeled by

$$g_0(\mathbf{R}, \mathbf{p}, t) = \bar{g}_0(\mathbf{R}, \mathbf{p}, t) + \delta g_0(\mathbf{R}, \mathbf{p}, t), \quad (3.44)$$

where  $\overline{\dots}$  denotes averaging over experimental realization and  $\delta g_0$  represents the fluctuating part of each experimental realization with respect to their mean value. The experiments are considered mutually correlated on scales  $l_{\text{ex}}$  and  $p_{\text{ex}}$ , which were introduced in the context of Eq. (3.38), such that  $\overline{\delta g_0(\mathbf{R}', \mathbf{p}') \delta g_0(\mathbf{R}, \mathbf{p})} = (2\pi)^3 \delta(\mathbf{R} - \mathbf{R}') \delta(\mathbf{p} - \mathbf{p}')$  where the  $\delta$ -functions are of finite width of order  $l_{\text{ex}}$  and  $p_{\text{ex}}$ , respectively. This renders  $P_z(t)$  a random variable whose fluctuations may be modeled by the probability density  $\rho(P_z, t)$  such that, e.g., its mean value as function of time is determined by  $\bar{P}(t) = \int dP_z \rho(P_z, t) P_z$ .

In the quantum chaotic regime where many impurity collisions of a beam are possible before  $t'_E$  is reached, the variance  $\overline{\delta P_z^2(t)}$  with

$$\delta P_z(t) = P_z(t) - \bar{P}_z(t) \quad (3.45)$$

also determines the probability density  $\rho(P_z, t)$ : In the case of many impurity collisions or in the case of many beams,  $\rho(P_z, t)$  can be approximated by a Gaussian form. This assumption is justified with either the central limit theorem, or it holds anyway if the initial distribution is already of Gaussian form (Klug and Syzranov, 2019). The probability density is therefore parameterized by

$$\rho(P_z, t) = [2\pi \overline{\delta P_z^2(t)}]^{-1/2} \exp \left\{ -\frac{[P_z - \bar{P}_z(t)]^2}{2 \overline{\delta P_z^2(t)}} \right\}, \quad (3.46)$$

and information dynamics are traced back to the dynamics of  $\overline{\delta P_z^2(t)}$  as indicated in the introductory section 3.1.

To determine the time evolution of the magnitude of fluctuations, first ballistic propagation and inelastic electron-phonon scattering processes are separated as introduced in Eq. (3.42) yielding

$$\overline{\delta P_z^2(t)} = e^{-2t/\tau} \overline{\delta \tilde{P}_z^2(t)}, \quad (3.47)$$

where  $\overline{\delta \tilde{P}_z^2(t)}$  evolves under classical dynamics in the absence of phonons. By using the

### 3. Chaotic fluctuation dynamics

single-particle propagators introduced in Eq. (3.31) which are valid for  $t < t_E$ ,

$$\overline{\delta\tilde{P}_z^2(t)} = \int_{\mathbf{R}^{(i)}\mathbf{p}^{(i)}} \int_{\mathbf{R}_0^{(i)}\mathbf{p}_0^{(i)}} p_z p'_z \times G(t, \mathbf{R}_\mathbf{p}; \mathbf{R}_0\mathbf{p}_0) G(t, \mathbf{R}'\mathbf{p}'; \mathbf{R}'_0\mathbf{p}'_0) \overline{\delta g_0(\mathbf{R}_0, \mathbf{p}_0) \delta g_0(\mathbf{R}'_0, \mathbf{p}'_0)}, \quad (3.48)$$

resembling the time evolved correlation function Eq. (3.32) constituting the out-of-time order correlator. To obtain an explicit expression for  $\overline{\delta\tilde{P}_z^2(t)}$ , this quantity is considered self-averaged: Although only one particular disorder realization is considered, the average over experimental realization is assumed to equate to the disorder average (Klug and Syzranov, 2019)

$$\overline{\delta\tilde{P}_z^2(t)} = \langle \delta\tilde{P}_z^2(t) \rangle_{\text{dis}}. \quad (3.49)$$

Hence, the results obtained in the Appendix A.1 are applicable to the present setting: By introducing the beams' total momentum  $\tilde{\mathbf{P}} = (\tilde{P}_x, \tilde{P}_y, \tilde{P}_z)$ , the time evolution of its variance for  $t < t'_E$  is therefore determined by the set of coupled differential equations (Klug and Syzranov, 2019)

$$\frac{d}{dt} \overline{\delta\tilde{\mathbf{P}}^2(t)} = \lambda_{\text{cl}}^3 \frac{4v_F^2}{p_F^2} \overline{\tilde{\zeta}^2(t)}, \quad (3.50a)$$

$$\frac{d}{dt} \overline{\tilde{\zeta}^2(t)} = \frac{2v_F}{p_F} \overline{\tilde{\zeta} \cdot \delta\tilde{\mathbf{P}}(t)}, \quad (3.50b)$$

$$\frac{d}{dt} \overline{\tilde{\zeta} \cdot \delta\tilde{\mathbf{P}}(t)} = \frac{v_F}{p_F} \overline{\delta\tilde{\mathbf{P}}^2(t)}, \quad (3.50c)$$

with the classical Lyapunov exponent  $\lambda_{\text{cl}}$  given in Eq. (3.35) and the position deviation  $\tilde{\zeta}(t)$  of the beam with respect to its mean trajectory. This set of equation is solved for appropriate initial conditions associated with scales  $\ell_{\text{ex}}$  and  $p_{\text{ex}}$  representing a finite total momentum or spatial mismatch and the time evolution of the magnitude of fluctuations is determined to  $\overline{\delta\tilde{P}^2(t)} \propto e^{2\lambda_{\text{cl}}t}$  where only the most rapid growing contribution is considered. Thus, the variance in the presence of a coupling to phonons is determined by using Eq. (3.47) to  $\overline{\delta\tilde{P}_z^2(t)} \propto e^{2(\lambda_{\text{cl}} - \frac{1}{\tau})t}$ . The time evolution of the amount of information associated with one component of the total momentum is therefore given by

$$I_P(t) = \text{const.} - \frac{1}{2} \int dP_z \rho(P_z, t) \ln[2\pi\overline{\delta\tilde{P}^2(t)}] \quad (3.51a)$$

$$= \text{const.} - \lambda_L t, \quad (3.51b)$$

with the scrambling rate  $\lambda_L = \lambda_{\text{cl}} - \frac{1}{\tau}$  as introduced in Eq. (3.6) which is identified as the decay rate of the information associated with one component of the total momentum operator.

### 3.6. CONCLUSION AND OUTLOOK

In this chapter, the scrambling rate was determined for electrons in a disordered metal coupled to a dissipative bath of phonons by evaluating the out-of-time order correlator of total momentum operators. Here, a kinetic equation was derived to determine the exponential growth contribution to the out-of-time order correlator. In addition, the decay rate of information associated with the total momentum of the system was shown to match the scrambling rate.

It was found that the scrambling rate,  $\lambda_L = \lambda_{cl} - \tau^{-1}$ , is of the order of the elastic impurity scattering rate  $\tau_0^{-1}$  but reduced by the inelastic phonon scattering rate  $\tau^{-1}$ . Hence, two possible regimes of electron dynamics are possible: For a sufficiently weak electron-phonon coupling,  $\lambda_L > 0$ , the system obeys quantum chaotic behavior. In contrast, for a sufficiently strong electron-phonon coupling,  $\lambda_L < 0$ , dissipative effects dominate preventing the system to develop chaotic dynamics. The transition from dissipative to chaotic dynamics could be realized, e.g., by tuning the temperature  $T$  as  $\tau^{-1}(T)$  depends on the number of thermally activated phonons whereas  $\lambda_{cl}$  remains constant (Klug and Syzranov, 2019).

A principle that chaotic dynamics are reflected in the fluctuations of certain observable was proposed in Sec. 3.1. It was explicitly shown to hold for the system of a dissipative, disordered metal, where the monitored observables were chosen to the total momentum of the system. To realize this principle in an experiment, certain requirements have to be fulfilled: The considered microscopic system generally has to obey chaotic dynamics, the excitations have to be sufficiently “localized” to evolve under chaotic dynamics and they need to be monitored appropriately. Recent advances in the fabrication of quantum dots could provide a system which is representative for the microscopic system discussed above. In particular, graphene quantum dots can be carved into a form resembling a chaotic Billiard as depicted in Fig. 3.5, which maps to the chaotic system of ballistic particle motion in a disordered hard sphere potential. Arbitrary shapes can be fabricated by quantum confinement based on  $p$ - $n$  junctions using electrostatic gating as presented in Refs. Lee *et al.* (2016); Velasco *et al.* (2016). Furthermore, due to the ultrarelativistic spectrum of Dirac electrons, the effect of Klein-tunneling allows electrons to leave the quantum dot if approaching the  $p$ - $n$  interface almost perpendicularly (Cheianov and Fal’ko, 2006). For a beam containing several electrons, the effect renders the interface partially traversable mimicking the effect of dissipation caused by inelastic electron-phonon scattering.

By assuming a quantum dot device as depicted in Fig. 3.5, a pulsed current of electrons is injected through a narrow lead into the system. The beam is reflected steadily by the walls of the quantum dot representing the scattering off impurities. Whereas the beam follows a classical trajectory on average, its width grows exponentially with the classical Lyapunov exponent  $\lambda_{cl}$ . Additionally, Klein tunneling renders the confining barriers semitransparent considered to be quantified by the tunneling rate  $\tau^{-1}$  resulting in a steady loss of the beam’s weight. To monitor fluctuations in the beam’s total momentum, the magnetic noise, which

### 3. Chaotic fluctuation dynamics

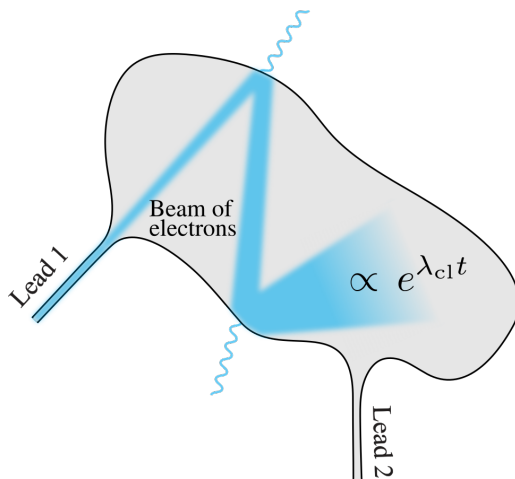


**Figure 3.5.:** Chaotic quantum dot with semi transparent walls mimicking the dissipative coupling to phonons. Reprinted figure with permission from [M.J. Klug, and S.V. Syzranov, Phys. Rev. **B** 100, 094304] Copyright (2019) by the American Physical Society. The original work is found under <https://dx.doi.org/10.1103/PhysRevB.100.094304>.

is radiated, may be measured. In particular, by measuring one component of the magnetic field  $B_z(t) \propto P_z(t)$  away from the quantum dot, the scrambling rate  $\lambda_L = \lambda_{cl} - \frac{1}{\tau}$  is then determined as average over experimental realizations,

$$\overline{[B_z(t) - \overline{B_z}(t)]^2} \propto e^{2\lambda_L t}. \quad (3.52)$$

As the evolution of the total momentum is intrinsically chaotic, other methods of chaos theory are applicable to obtain the scrambling rate. By analyzing the time series of one observable, information about the Lyapunov exponent can be extracted using the method of phase space portrait reconstruction based on delay coordinates (Wolf *et al.*, 1985; Rosenstein *et al.*, 1993). By considering the distance between observables separated by time  $\tau$  as functions of time,

$$|B_z(t) - B_z(t + \tau)| \propto e^{\lambda_L(t-t_0)}$$

where  $\tau$  and  $t_0$  are chosen such that the initial distance is small,  $|B_z(t_0) - B_z(t_0 + \tau)| \ll \epsilon$ , the scrambling rate can be determined.

The proposed approach assumed that electron-electron interactions between Dirac electrons are negligible. However, as interaction effects are marginally relevant for long-range Coulomb interaction as discussed in the previous chapter, the robustness of the presented findings has to be investigated in further details. Generally, it remains to be seen whether this approach applies to other systems of condensed matter physics. As this concept was applied to a system where chaotic dynamics is already present on the single-particle level, it is not clear yet how this concept is transferred to systems where chaotic dynamics is traced back to many-body interaction effects, e.g., as in the case of interacting electrons in graphene discussed previously in Ch. 2. This aspect has to be investigated more thoroughly in future works.

## REFERENCES OF PART I

- I. L. Aleiner and A. I. Larkin, *Divergence of classical trajectories and weak localization*, *Phys. Rev. B* **54**, 14423 (1996).
- I. L. Aleiner, L. Faoro, and L. B. Ioffe, *Microscopic model of quantum butterfly effect: Out-of-time-order correlators and traveling combustion waves*, *Ann. Phys.* **375**, 378 (2016).
- A. Altland and B. D. Simons, *Condensed Matter Field Theory*, 2nd ed. (Cambridge University Press, 2010).
- C. T. Asplund, A. Bernamonti, F. Galli, and T. Hartman, *Entanglement scrambling in 2d conformal field theory*, *J. High Energy Phys.* **2015**, 110 (2015).
- S. Banerjee and E. Altman, *Solvable model for a dynamical quantum phase transition from fast to slow scrambling*, *Phys. Rev. B* **95**, 134302 (2017).
- G. A. Baym and C. J. Pethick, *Landau Fermi-liquid theory: concepts and applications*, 1st ed., A Wiley-Interscience publication (Wiley, New York [u.a.], 1991).
- M. Blake, *Universal charge diffusion and the butterfly effect in holographic theories*, *Phys. Rev. Lett.* **117**, 091601 (2016a).
- M. Blake, *Universal diffusion in incoherent black holes*, *Phys. Rev. D* **94**, 086014 (2016b).
- A. Bohrdt, C. B. Mendl, M. Endres, and M. Knap, *Scrambling and thermalization in a diffusive quantum many-body system*, *New J. Phys.* **19**, 063001 (2017).
- J. A. N. Bruin, H. Sakai, R. S. Perry, and A. P. Mackenzie, *Similarity of scattering rates in metals showing  $t$ -linear resistivity*, *Science* **339**, 804 (2013).
- P. Calabrese and J. Cardy, *Evolution of entanglement entropy in one-dimensional systems*, *J. High Energy Phys.* **2005**, P04010 (2005).
- A. H. Castro Neto, F. Guinea, N. M. R. Peres, K. S. Novoselov, and A. K. Geim, *The electronic properties of graphene*, *Rev. Mod. Phys.* **81**, 109 (2009).
- V. V. Cheianov and V. I. Fal'ko, *Selective transmission of dirac electrons and ballistic magnetoresistance of  $n$ - $p$  junctions in graphene*, *Phys. Rev. B* **74**, 041403 (2006).
- B. V. Chirikov, *A universal instability of many-dimensional oscillator systems*, *Physics Reports* **52**, 263 (1979).
- D. Chowdhury and B. Swingle, *Onset of many-body chaos in the  $O(N)$  model*, *Phys. Rev. D* **96**, 065005 (2017).
- L. D'Alessio, Y. Kafri, A. Polkovnikov, and M. Rigol, *From quantum chaos and eigenstate thermalization to statistical mechanics and thermodynamics*, *Advances in Physics* **65**, 239 (2016).
- J. M. Deutsch, *Quantum statistical mechanics in a closed system*, *Phys. Rev. A* **43**, 2046 (1991).
- P. Ehrenfest, *Bemerkung über die angenäherte Gültigkeit der klassischen Mechanik innerhalb der Quantenmechanik*, *Z. Physik* **45**, 455 (1927).

- D. C. Elias, R. V. Gorbachev, A. S. Mayorov, S. V. Morozov, A. A. Zhukov, P. Blake, L. A. Ponomarenko, I. V. Grigorieva, K. S. Novoselov, F. Guinea, and A. K. Geim, *Dirac cones reshaped by interaction effects in suspended graphene*, [Nature Physics](#) **7**, 701 (2011).
- R. Fan, P. Zhang, H. Shen, and H. Zhai, *Out-of-time-order correlation for many-body localization*, [Sci. Bull.](#) **62**, 707 (2017).
- M. S. Foster and I. L. Aleiner, *Graphene via large  $n$ : A renormalization group study*, [Phys. Rev. B](#) **77**, 195413 (2008).
- L. Fritz, J. Schmalian, M. Müller, and S. Sachdev, *Quantum critical transport in clean graphene*, [Phys. Rev. B](#) **78**, 085416 (2008).
- M. Gärttner, J. G. Bohnet, A. Safavi-Naini, M. L. Wall, J. J. Bollinger, and A. M. Rey, *Measuring out-of-time-order correlations and multiple quantum spectra in a trapped-ion quantum magnet*, [Nat. Phys.](#) **13**, 781 EP (2017).
- W. Greiner, L. Neise, and H. Stöcker, *Thermodynamics and Statistical Mechanics* (Springer, New York, NY, 1995).
- M. C. Gutzwiller, *Chaos in Classical and Quantum Mechanics* (Springer, New York, NY, 1990).
- F. Haake, *Quantum Signatures of Chaos*, 3rd ed. (Springer, Berlin, Heidelberg, 2010).
- E. L. Hahn, *Spin echoes*, [Phys. Rev.](#) **80**, 580 (1950).
- S. A. Hartnoll, *Theory of universal incoherent metallic transport*, [Nat. Phys.](#) **11**, 54 (2014).
- P. Hayden and J. Preskill, *Black holes as mirrors: quantum information in random subsystems*, [J. High Energy Phys.](#) **2007**, 120 (2007).
- P. Hosur, X.-L. Qi, D. A. Roberts, and B. Yoshida, *Chaos in quantum channels*, [J. High Energy Phys.](#) **2016**, 4 (2016).
- Y. Huang, Y.-L. Zhang, and X. Chen, *Out-of-time-ordered correlators in many-body localized systems*, [Ann. Phys.](#) **529**, 1600318 (2017).
- R. Islam, R. Ma, P. M. Preiss, M. Eric Tai, A. Lukin, M. Rispoli, and M. Greiner, *Measuring entanglement entropy in a quantum many-body system*, [Nature](#) **528**, 77 (2015).
- R. A. Jalabert, I. García-Mata, and D. A. Wisniacki, *Semiclassical theory of out-of-time-order correlators for low-dimensional classically chaotic systems*, [Phys. Rev. E](#) **98**, 062218 (2018).
- L. P. Kadanoff and P. C. Martin, *Hydrodynamic equations and correlation functions*, [Ann. Phys.](#) **24**, 419 (1963).
- A. Kamenev, *Field Theory of Non-Equilibrium Systems*, 1st ed. (Cambridge University Press, 2011).
- A. M. Kaufman, M. E. Tai, A. Lukin, M. Rispoli, R. Schittko, P. M. Preiss, and M. Greiner, *Quantum thermalization through entanglement in an isolated many-body system*, [Science](#) **353**, 794 (2016).
- A. Kitaev, *A simple model of quantum holography 1 & 2*, [Talks at KITP](#) (2015), unpublished.

- M. J. Klug and S. V. Syzranov, *Chaos and the dynamics of information in dissipative electronic systems*, *Phys. Rev. B* **100**, 094304 (2019).
- M. J. Klug, M. S. Scheurer, and J. Schmalian, *Hierarchy of information scrambling, thermalization, and hydrodynamic flow in graphene*, *Phys. Rev. B* **98**, 045102 (2018).
- J. Kurchan, *Quantum bound to chaos and the semiclassical limit*, *J. Stat. Phys.* **171**, 965 (2018).
- A. I. Larkin and Y. N. Ovchinnikov, *Quasiclassical method in the theory of superconductivity*, *Zh. Eksp. Teor. Fiz.* **55**, 2262 (1969), [*JETP* 28, 1200 (1969)].
- J. Lee, D. Wong, J. Velasco Jr, J. F. Rodriguez-Nieva, S. Kahn, H.-Z. Tsai, T. Taniguchi, K. Watanabe, A. Zettl, F. Wang, L. S. Levitov, and M. F. Crommie, *Imaging electrostatically confined dirac fermions in graphene quantum dots*, *Nat. Phys.* **12**, 1032 (2016).
- R. J. Lewis-Swan, A. Safavi-Naini, J. J. Bollinger, and A. M. Rey, *Unifying scrambling, thermalization and entanglement through measurement of fidelity out-of-time-order correlators in the Dicke model*, *Nat. Commun.* **10**, 1581 (2019).
- J. Li, R. Fan, H. Wang, B. Ye, B. Zeng, H. Zhai, X. Peng, and J. Du, *Measuring out-of-time-order correlators on a nuclear magnetic resonance quantum simulator*, *Phys. Rev. X* **7**, 031011 (2017).
- Y. Liao and V. Galitski, *Nonlinear sigma model approach to many-body quantum chaos: Regularized and unregularized out-of-time-ordered correlators*, *Phys. Rev. B* **98**, 205124 (2018).
- A. J. Lichtenberg and M. A. Leiberman, *Regular and Chaotic Dynamics*, 2nd ed. (Springer, New York, NY, 1992).
- E. H. Lieb and D. W. Robinson, *The finite group velocity of quantum spin systems*, *Commun. Math. Phys.* **28**, 251 (1972).
- J. M. Link, B. N. Narozhny, E. I. Kiselev, and J. Schmalian, *Out-of-bounds hydrodynamics in anisotropic dirac fluids*, *Phys. Rev. Lett.* **120**, 196801 (2018).
- D. J. Luitz and Y. Bar Lev, *Information propagation in isolated quantum systems*, *Phys. Rev. B* **96**, 020406 (2017).
- G. D. Mahan, *Many-particle physics*, 3rd ed., Physics of solids and liquids (Kluwer Acad./Plenum Publ., New York, NY, 2000).
- J. Maldacena and D. Stanford, *Remarks on the sachdev-ye-kitaev model*, *Phys. Rev. D* **94**, 106002 (2016).
- J. Maldacena, S. Shenker, and D. J. Stanford, *A bound on chaos*, *J. High Energy Phys.* **7**, 106 (2016).
- I. A. Morrison and M. M. Roberts, *Mutual information between thermo-field doubles and disconnected holographic boundaries*, *J. High Energy Phys.* **2013**, 81 (2013).
- M. Müller, J. Schmalian, and L. Fritz, *Graphene: A nearly perfect fluid*, *Phys. Rev. Lett.* **103**, 025301 (2009).

- C. Neill, P. Roushan, M. Fang, Y. Chen, M. Kolodrubetz, Z. Chen, A. Megrant, R. Barends, B. Campbell, B. Chiaro, A. Dunsworth, E. Jeffrey, J. Kelly, J. Mutus, P. J. J. O'Malley, C. Quintana, D. Sank, A. Vainsencher, J. Wenner, T. C. White, A. Polkovnikov, and J. M. Martinis, *Ergodic dynamics and thermalization in an isolated quantum system*, *Nat. Phys.* **12**, 1037 (2016).
- K. S. Novoselov, A. K. Geim, S. V. Morozov, D. Jiang, M. I. Katsnelson, I. V. Grigorieva, S. V. Dubonos, and A. A. Firsov, *Two-dimensional gas of massless dirac fermions in graphene*, *Nature* **438**, 197 (2005).
- O. Oreshkov and T. A. Brun, *Weak measurements are universal*, *Phys. Rev. Lett.* **95**, 110409 (2005).
- D. N. Page, *Average entropy of a subsystem*, *Phys. Rev. Lett.* **71**, 1291 (1993).
- A. A. Patel and S. Sachdev, *Quantum chaos on a critical fermi surface*, *Proc. Natl. Acad. Sci.* **114**, 1844 (2017).
- A. A. Patel, D. Chowdhury, S. Sachdev, and B. Swingle, *Quantum butterfly effect in weakly interacting diffusive metals*, *Phys. Rev. X* **7**, 031047 (2017).
- J. Preskill, *Quantum Information - Quantum Shannon Theory*, lecture notes (2018).
- J. Rammensee, J. D. Urbina, and K. Richter, *Many-body quantum interference and the saturation of out-of-time-order correlators*, *Phys. Rev. Lett.* **121**, 124101 (2018).
- D. A. Roberts and D. Stanford, *Diagnosing chaos using four-point functions in two-dimensional conformal field theory*, *Phys. Rev. Lett.* **115**, 131603 (2015).
- D. A. Roberts and B. Swingle, *Lieb-robinson bound and the butterfly effect in quantum field theories*, *Phys. Rev. Lett.* **117**, 091602 (2016).
- D. A. Roberts, D. Stanford, and L. Susskind, *Localized shocks*, *J. High Energy Phys.* **2015**, 51 (2015).
- M. T. Rosenstein, J. J. Collins, and C. J. D. Luca, *A practical method for calculating largest lyapunov exponents from small data sets*, *Physica D* **65**, 117 (1993).
- E. B. Rozenbaum, S. Ganeshan, and V. Galitski, *Lyapunov exponent and out-of-time-ordered correlator's growth rate in a chaotic system*, *Phys. Rev. Lett.* **118**, 086801 (2017).
- S. Sachdev and J. Ye, *Gapless spin-fluid ground state in a random quantum heisenberg magnet*, *Phys. Rev. Lett.* **70**, 3339 (1993).
- M. Schütt, P. M. Ostrovsky, I. V. Gornyi, and A. D. Mirlin, *Coulomb interaction in graphene: Relaxation rates and transport*, *Phys. Rev. B* **83**, 155441 (2011).
- Y. Sekino and L. Susskind, *Fast scramblers*, *J. High Energy Phys.* **2008**, 065 (2008).
- D. E. Sheehy and J. Schmalian, *Quantum critical scaling in graphene*, *Phys. Rev. Lett.* **99**, 226803 (2007).
- S. H. Shenker and D. Stanford, *Stringy effects in scrambling*, [arXiv:1412.6087 \[hep-th\]](https://arxiv.org/abs/1412.6087) (2014a).
- S. H. Shenker and D. Stanford, *Black holes and the butterfly effect*, *J. High Energy Phys.* **2014**, 67 (2014b).

- D. A. Siegel, C.-H. Park, C. Hwang, J. Deslippe, A. V. Fedorov, S. G. Louie, and A. Lanzara, *Many-body interactions in quasi-freestanding graphene*, *Proc. Natl. Acad. Sci.* **108**, 11365 (2011).
- D. T. Son, *Quantum critical point in graphene approached in the limit of infinitely strong coulomb interaction*, *Phys. Rev. B* **75**, 235423 (2007).
- M. Srednicki, *Chaos and quantum thermalization*, *Phys. Rev. E* **50**, 888 (1994).
- M. Srednicki, *The approach to thermal equilibrium in quantized chaotic systems*, *J. Phys. A: Math. Gen.* **32**, 1163 (1999).
- D. Stanford, *Many-body chaos at weak coupling*, *J. High Energy Phys.* **2016**, 9 (2016).
- B. Swingle and D. Chowdhury, *Slow scrambling in disordered quantum systems*, *Phys. Rev. B* **95**, 060201 (2017).
- B. Swingle, G. Bentsen, M. Schleier-Smith, and P. Hayden, *Measuring the scrambling of quantum information*, *Phys. Rev. A* **94**, 040302 (2016).
- S. V. Syzranov, A. V. Gorshkov, and V. Galitski, *Out-of-time-order correlators in finite open systems*, *Phys. Rev. B* **97**, 161114 (2018).
- S. Syzranov, A. Gorshkov, and V. Galitski, *Interaction-induced transition in the quantum chaotic dynamics of a disordered metal*, *Annals of Physics* **405**, 1 (2019).
- N. Tsuji, T. Shitara, and M. Ueda, *Bound on the exponential growth rate of out-of-time-ordered correlators*, *Phys. Rev. E* **98**, 012216 (2018).
- J. Velasco, L. Ju, D. Wong, S. Kahn, J. Lee, H.-Z. Tsai, C. Germany, S. Wickenburg, J. Lu, T. Taniguchi, K. Watanabe, A. Zettl, F. Wang, and M. F. Crommie, *Nanoscale control of rewriteable doping patterns in pristine graphene/boron nitride heterostructures*, *Nano Lett.* **16**, 1620 (2016).
- Y. Werman, S. A. Kivelson, and E. Berg, *Quantum chaos in an electron-phonon bad metal*, [arXiv:1705.07895 \[cond-mat.str-el\]](https://arxiv.org/abs/1705.07895) (2017).
- A. Wolf, J. B. Swift, H. L. Swinney, and J. A. Vastano, *Determining lyapunov exponents from a time series*, *Physica D* **16**, 285 (1985).
- N. Y. Yao, F. Grusdt, B. Swingle, M. D. Lukin, D. M. Stamper-Kurn, J. E. Moore, and E. A. Demler, *Interferometric approach to probing fast scrambling*, [arXiv:1607.01801 \[quant-ph\]](https://arxiv.org/abs/1607.01801) (2016).
- G. L. Yu, R. Jalil, B. Belle, A. S. Mayorov, P. Blake, F. Schedin, S. V. Morozov, L. A. Ponomarenko, F. Chiappini, S. Wiedmann, U. Zeitler, M. I. Katsnelson, A. K. Geim, K. S. Novoselov, and D. C. Elias, *Interaction phenomena in graphene seen through quantum capacitance*, *Proceedings of the National Academy of Sciences* **110**, 3282 (2013).
- J. Zaanen, *Why the temperature is high*, *Nature* **430**, 512 EP (2004).
- Y.-L. Zhang, Y. Huang, and X. Chen, *Information scrambling in chaotic systems with dissipation*, *Phys. Rev. B* **99**, 014303 (2019).
- G. Zhu, M. Hafezi, and T. Grover, *Measurement of many-body chaos using a quantum clock*, *Phys. Rev. A* **94**, 062329 (2016).

## PART II

### ELECTRON ORDER IN SMALL-ANGLE TWISTED BILAYER GRAPHENE

Previously, out-of-time order correlators were introduced to characterize interaction effects in strongly correlated electron systems. In this part, an interacting electronic many-body system is investigated where the effective strength of electron-electron interactions can be tuned by varying an external tuning parameter. In twisted bilayer graphene, the interplay between the long length scale moiré interference pattern, which is depicted in Fig. 4.1a, and the interlayer hybridization of electronic states due to a finite interlayer tunneling of electrons causes the bandwidth of the so-called “moiré bands” to depend on the twist-angle. For certain “magic-angles”, the bandwidth of the moiré bands is as small as a few milli-electron volts and a strong enhancement of interaction effects can be expected. Modeling these electronic degrees of freedom and investigating the effect of band tuning on the electronic ground state is the central focus of this part.

In experiments, a series of strong correlation effects were observed for low temperatures and partial fillings of the weakly dispersing moiré bands. The phase diagram of temperature and gate voltage is characterized by correlated insulator states as seen in transport experiments (Cao *et al.*, 2018a,b; Yankowitz *et al.*, 2019; Lu *et al.*, 2019). Their regular pattern of occurrences at commensurate band fillings indicate strong-coupling Mott physics which is, among others, complemented by superconductivity for incommensurate band fillings (Lu *et al.*, 2019; Cao *et al.*, 2018b; Yankowitz *et al.*, 2019). Besides, correlated electron states were also observed in scanning tunneling microscopy and spectroscopy measurements where an onset of a rotational symmetry breaking order was determined for commensurate and incommensurate moiré band fillings around the charge neutrality point (Kerelsky *et al.*, 2019; Choi *et al.*, 2019; Jiang *et al.*, 2019; Xie *et al.*, 2019). Though vast theoretical efforts were made to model the electronic structure, see e.g. Refs. Yuan and Fu (2018); Kang and Vafeek (2018); Po *et al.* (2018), and the insulating states, see e.g. Refs. Ochi *et al.* (2018); Po *et al.* (2018); Kang and Vafeek (2019), a comprehensive understanding of the correlated electron states and their underlying microscopic mechanism for variable carrier concentrations is still lacking.

As the bandwidth of the moiré bands and hence the relative strength of interactions can be tuned by varying the twist-angle, this system of small-angle twisted bilayer graphene suggests to study the role of interactions for a variable interaction strength. In particular in this part, two regimes are considered, a weak- and a strong-regime, which are both possibly realized in experiments. To this end, the electronic structure of the moiré electrons including electron-electron interaction effects are modeled to conduct, subsequently,

## 4. Introduction

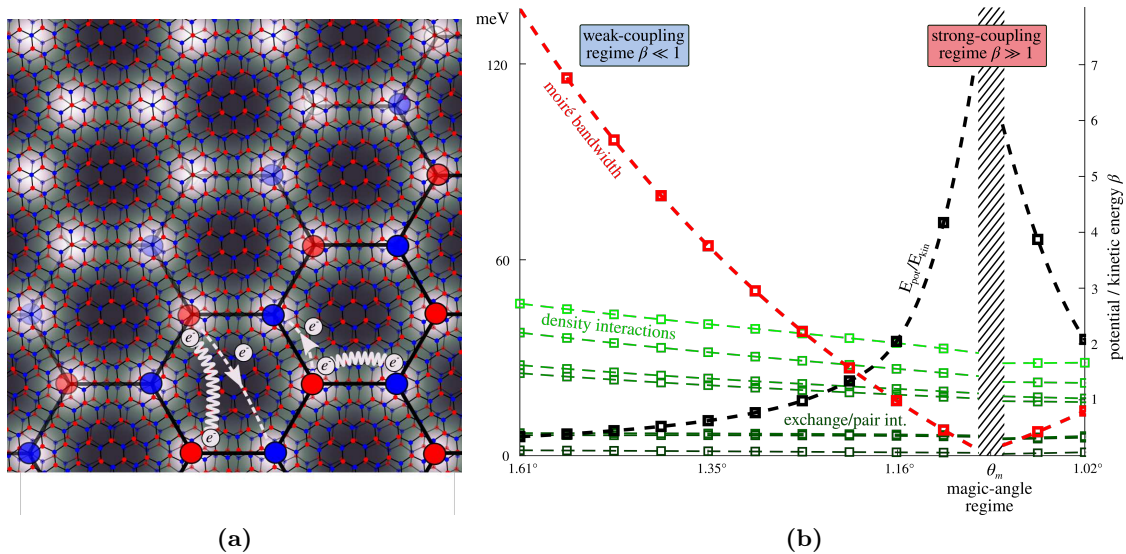


**Figure 4.1.:** (a) Moiré interference pattern of two twisted graphene lattices for a commensurate twist-angle with exact translational and rotational symmetry. The hexagonal superlattice (bottom right) serves as crystalline basis to construct an effective electron model with long-range hopping (striped arrows) and long-range interaction (wiggly lines) processes. (b) Evolution of the kinetic and potential energy scales as function of the twist-angle. The moiré bandwidth (red) represents the kinetic energy scale, whereas the amplitudes of the interaction matrix elements (green) the potential energy scale. Their ratio (black) in units of  $\beta$  increases when tuning the system towards the magic-angle regime signaling a crossover from weak to strong couplings. Reprinted figure from Ref. Klug (2020). The original work is found under <https://dx.doi.org/10.1088/1367-2630/ab950c>.

an electronic ground states analysis. The obtained results are eventually related to the previously mentioned experimental observations. The topic discussed in this part is based on work presented in Ref. Klug (2020).

### 4.1. SUMMARY OF RESULTS

Within this part, the electronic structure of twisted bilayer graphene is modeled by following a two-orbital approach (Koshino *et al.*, 2018) where localized electron states centered at the high symmetry points of the moiré interference pattern of the bilayer lattice are constructed by means of Bloch states associated with the weakly dispersing moiré bands. Subsequently, electron-electron interactions are projected into the basis of localized states giving rise to an extended Hubbard model on a hexagonal superlattice with long-range hopping and long-range interaction processes as depicted in Fig. 4.1a. In this representation, relevant interaction processes are identified to obtain a tractable, minimal model of interacting “moiré electrons”. The symmetries of this effective model are an approximate translational symmetry  $T$ , which renders the crystal momentum of moiré electrons a “good” quantum number, and an approximate point group  $D_6$  symmetry, which includes a rotational  $C_3$  symmetry, constituting the corresponding space group of the superlattice.

#### 4. Introduction

Additionally, the presence of a spin-rotation  $SU(2)$  symmetry, which is justified in the limit of vanishing spin-orbit coupling (Castro Neto *et al.*, 2009), and a valley  $U_v(1)$  symmetry, which is inherited from the single-layer graphene systems in the limit of small twist-angles (Po *et al.*, 2018), is assumed.

The potential and kinetic energy scales of this model, which are represented by the moiré bandwidth and the interaction matrix elements of the interaction processes, respectively, as well as their ratio are determined in Ch. 5 and are depicted as a function of twist-angle in Fig. 4.1b. In the magic-angle regime, the bandwidth is minimal and as small as 10 millielectron-volts. In contrast, the interaction matrix elements vary approximately linearly with the twist-angle. Their ratio, which represents the relative interaction strength, significantly increases in the vicinity of the magic angle  $\theta_m$  indicating a transition from a weak to a strong-coupling regime.

In the subsequent analysis it is found that within this modeling approach the role of interactions is determined by the dimensionless quantity

$$\beta \equiv \frac{e^2}{\epsilon L_M \Lambda}, \quad (4.1)$$

with the electron charge  $e$ , the relative permittivity  $\epsilon$ , the effective length scale of the superlattice  $L_M$  and the moiré bandwidth  $\Lambda$ . Here, the potential energy scale is represented by  $e^2/\epsilon L_M$ , which represent the natural units of the interaction matrix elements, whereas the kinetic energy scale is represented by  $\Lambda$ . As  $\Lambda = \Lambda(\theta, t_\perp)$  and  $L_M = L_M(\theta)$  scale differently with the twist-angle  $\theta$  (and the interlayer tunneling amplitude  $t_\perp$ ), the relative strength of interactions can be tuned by varying the twist-angle.

Based on the constructed effective model, the effect of electron-electron interactions on the electronic ground state is investigated in Ch. 6 in two limiting regimes: A weak-coupling regime representative for twist-angles  $\theta \gg \theta_m$  where  $\beta \ll 1$  and a strong-coupling regime representative for twist-angles  $\theta \approx \theta_m$  where  $\beta \gg 1$ .

In the weak-coupling regime, where interaction effects can be treated perturbatively, a mean-field analysis reveals as leading electronic instability a stripe charge density wave order with commensurate ordering vectors of half of the reciprocal lattice vector of the moiré Brillouin zone, which breaks translational  $T$  and rotational  $C_3$  symmetry. The onset of the order is determined by a critical interaction strength and a critical moiré band filling.

In the strong-coupling regime, an infinite coupling approximation is performed where the kinetic part of the theory is dropped and only interaction processes are considered. Furthermore, it is focused on interaction processes in the density-density channel only which renders the model solvable. This approach would be ineffective in the limit of local Hubbard interactions. However for the present model, the important role of long-range interactions combined with ferromagnetic and ferrovalley exchange interactions, which favor a general alignment of spin and valley degrees of freedom, allows one to determine the nature of ordered states even without kinetic energy contributions of electrons. For all commensurate moiré band fillings  $\nu = 0, \pm\frac{1}{4}, \pm\frac{1}{2}, \pm\frac{3}{4}$  with the band filling factor  $\nu$ , Mott-

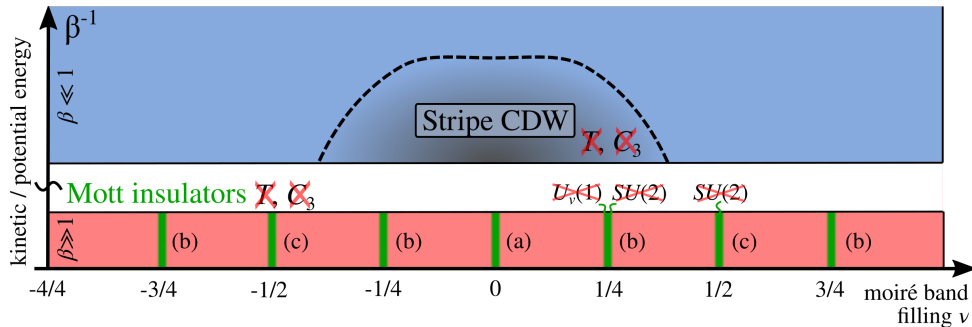


**Figure 4.2.:** In the weak-coupling regime, the conducted ground state analysis reveals a formation of stripe charge density wave orders which break translational  $T$  and  $C_3$ -rotational symmetries. In the strong-coupling regime, three types of Mott insulating ground states (a, b, c) for all commensurate moiré band fillings  $\nu = 0, \pm\frac{1}{4}, \pm\frac{1}{2}, \pm\frac{3}{4}$  are found, which resemble the stripe-type orders in the weak-coupling limit (a) but differ, in part, by the absence of the spin  $SU(2)$  (b) as well as the valley  $U_v(1)$  symmetry (c). Reprinted figure from Ref. Klug (2020). The original work is found under <https://dx.doi.org/10.1088/1367-2630/ab950c>.

insulating ground states are found which break the translational  $T$  and the  $C_3$ -rotational symmetry ( $\nu = 0$ ), as well as the spin  $SU(2)$  symmetry ( $\nu = \pm\frac{1}{4}, \pm\frac{1}{2}, \pm\frac{3}{4}$ ) and the valley  $U_v(1)$  symmetry ( $\nu = \pm\frac{1}{4}, \pm\frac{3}{4}$ ). Here,  $\nu = -1, 1$  represents completely empty and completely filled moiré bands, respectively. The results of the ground state analysis for the weak and strong-coupling regimes are summarized in Fig. 4.2.

#### 4.2. OVERVIEW OF EXPERIMENTAL OBSERVATIONS

Experimental observations related to electronic ground states in small-angle twisted bilayer graphene were obtained in transport and quantum oscillations measurements as well as scanning tunneling microscopy and scanning tunneling spectroscopy. In what follows, the most recent results are shortly discussed and interpreted.

Besides resistivity measurements, which revealed a series of correlated insulator states at commensurate moiré band fillings emerging at low temperatures, quantum oscillation measurements were used to extract information about the number of broken global symmetries of the correlated insulator states. Here, local minima in the longitudinal resistivity form straight lines in the plane of perpendicular magnetic field strength and carrier density, whose slope is antiproportional to the Landau Level filling factors from which the Landau level degeneracy can be obtained, see e.g. Ref. Novoselov *et al.* (2005) for details. In twisted bilayer graphene, these measurements showed that the insulating states differ in their Landau level degeneracy (Cao *et al.*, 2018b,a; Yankowitz *et al.*, 2019; Lu *et al.*, 2019). This implies the presence (or absence) of (global) symmetries which generate Kramer-like degeneracies of single-particle states. By assuming a global spin and valley symmetry of the interaction-free system, this might indicate for the insulator state at charge neutrality ( $\nu = 0$ ), which is found to be 4-fold degenerate, the presence of a combined spin- and valley-symmetry. In contrast for half electron- or hole-filling ( $\nu = \pm\frac{1}{2}$ ), the Landau levels

## 4. Introduction

are found to be two-fold degenerate implying that either the spin- or the valley-symmetry is broken, whereas for moiré band fillings  $\nu = \pm\frac{3}{4}$  being single degenerate that both the spin- and the valley-symmetry are absent. These observations put strong requirements on possible electronic ground states associated with the correlated insulator states.

In addition to transport experiments, which were performed on samples identified with the magic-angle regime accommodating, among others, Mott-like insulator states and superconductivity, scanning tunneling spectroscopy and microscopy experiments revealed correlated electron states for large ranges of electron- and hole-dopings around the point of charge neutrality (Kerelsky *et al.*, 2019; Choi *et al.*, 2019; Jiang *et al.*, 2019; Xie *et al.*, 2019). Here, interaction effects manifested as a significant redistribution of the single-particle spectral weight setting in at certain filling fractions of the moiré bands. Additionally, it was unanimously reported that the correlated states break  $C_3$ -rotational symmetry as seen in spatially resolved charge distribution measurements and that the effect is largest at charge neutrality. Those results were obtained for samples with moiré bandwidths significantly larger than 10 millielectron-volts perhaps placing them in a “close-to-magic-angle regime” where correlation effects are expected to be still present yet with interaction energies smaller than in the magic-angle regime justifying their perturbative treatment in theoretic modeling approaches.

### 4.3. OUTLINE

The current part is twofold as it includes the presentation of a modeling approach and an electronic ground state analysis.

First in Ch. 5, the system of electrons in twisted bilayer graphene is generally introduced and the underlying mechanism of the formation of moiré band is described. Subsequently, an effective model of interacting moiré electrons in twisted bilayer graphene is constructed. In particular, a discussion of the relevant emerging symmetries is given in Sec. 5.1. The moiré band structure is obtained in Sec. 5.2 by using a minimal model of two relatively twisted and coupled single-layer graphene systems. A two-orbital approach is employed in Sec. 5.3 to construct a Wannier basis where localized electron states are centered at the high symmetry points of the superlattice. Interaction effects are incorporated by determining the interaction matrix elements of the various interaction channels in Sec. 5.4.

Second, an analysis of possible electronic ground states in the presence of finite-range Coulomb interaction is conducted for various fillings of the moiré bands in Ch. 6. It is distinguished between two parameter regimes, a weak-coupling regime, where interaction effects are subleading (Sec. 6.1), and a strong-coupling regime, which is representative for angles in the vicinity of the magic-angle, where interaction effects dominate (Sec. 6.2).

In this chapter, an effective model of interacting electrons in small-angle twisted bilayer graphene is presented. As experiments indicate a link of correlation effects and electronic states associated with the moiré bands, these degrees of freedom are considered the relevant ones for the presented modeling approach. Thereby, one focuses on electron dynamics on scales of the effective superlattice providing a new set of emerging, approximate symmetries. These include symmetries which constitute the space group but also symmetries which are associated with the intrinsic properties of the moiré electrons. By deriving a low-energy description of the moiré electrons, light may be shed on the microscopic mechanism which underlies the strong correlation effects observed in experiments.

The emergence of the isolated moiré bands, which are centered around the charge neutrality point of the system, with small, twist-angle dependent bandwidths is traced back to the interplay of the moiré interference pattern and the hybridization of electronic states due to a finite interlayer tunneling. This can be understood by considering, for each layer, an “ultrarelativistic” theory of non-interacting electrons in graphene which is characterized by two distinct “Dirac cones” centered at the  $K$ -points of the Brillouin zone (Castro Neto *et al.*, 2009). By twisting the two-layers as depicted in Fig. 5.1a, an additional inverse length scale emerges which is given by the distance of the Dirac points in reciprocal space,

$$k_\theta = \frac{8\pi \sin \frac{\theta}{2}}{3a}, \quad (5.1)$$

with twist-angle  $\theta$  and graphene lattice constant  $a$ . The associated length scale  $L_M = \frac{4\pi}{3}k_\theta^{-1}$  represents the characteristic length scale of the superlattice (Bistritzer and MacDonald, 2011). Because of a finite interlayer tunneling represented by the energy scale  $t_\perp$ , electronic states at the intersection points of the cones of the two layers hybridize which causes an opening of a band gap. As the size of the band gap is of the order of  $t_\perp$  and the distance of the intersection points to the point of charge neutrality of the order of  $\frac{\hbar v_F k_\theta}{2}$ , the bandwidth of the moiré bands is smallest if their peaks are pushed towards the charge neutrality point, i.e. if  $t_\perp \sim \hbar v_F k_\theta$ . By introducing the dimensionless scale

$$\alpha \equiv \frac{t_\perp}{\hbar v_F k_\theta}, \quad (5.2)$$

the condition for the magic-angle regime can be made more precise and is determined to  $\alpha_m \approx \frac{1}{\sqrt{3}}$  (Bistritzer and MacDonald, 2011). Hence, the condition for the magic-angle  $\theta_m$

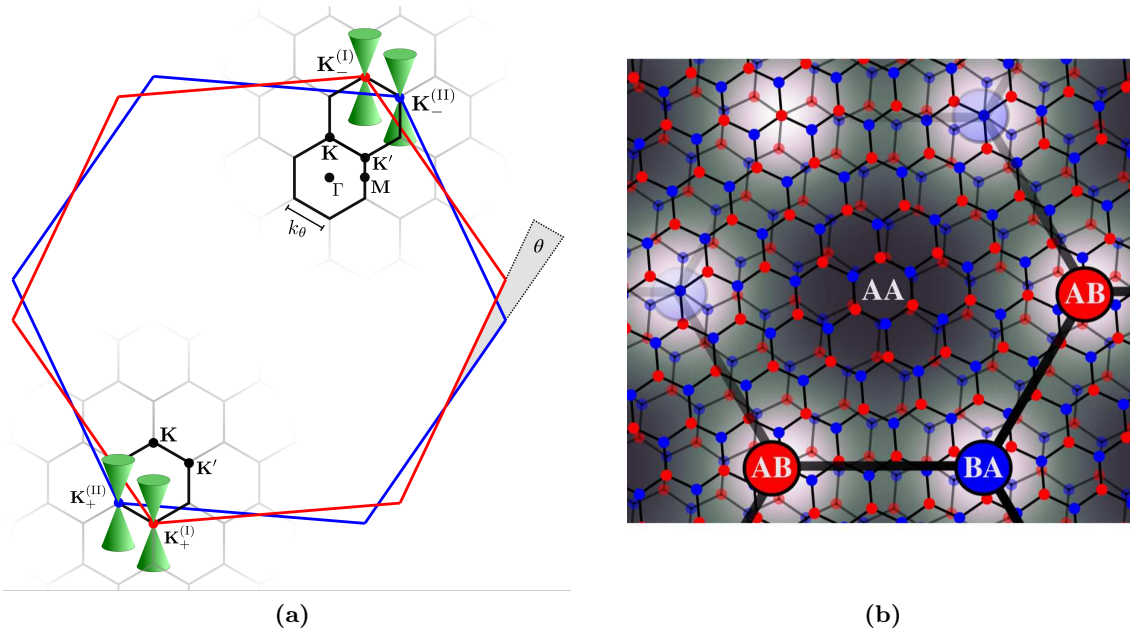


**Figure 5.1.:** (a) Twisted Brillouin zones with twist-angle  $\theta$  of graphene layer I (red) and graphene layer II (blue) with Dirac cones (green) centered at the corresponding  $K$ -points. The electronic states in the vicinity of  $\mathbf{K}_{\xi}^{(I,II)}$  fold to the  $K$ - and  $K'$ -points of the moiré Brillouin zone (black). (b) Bilayer lattice in real space. Small red and blue dots denote the crystalline sublattices  $A$  and  $B$  of the single-layer graphene layers, respectively, whereas big red and blue spots mark regions of AB- and BA- stacking which span the hexagonal superlattice. The center of a hexagon refers to regions of AA- and BB-stacking.

is determined not only by the twist-angle  $\theta$ , but depends also on the interlayer transition amplitude  $t_{\perp}$  which can also be tuned, e.g., by applying an external pressure (Yankowitz *et al.*, 2019).

After having established the moiré band structure, electron-electron interaction effects can be incorporated by constructing electronic states localized in real-space at the high symmetry points of the superlattice from the previously determined Bloch states constituting a complete Wannier basis. Here, a minimal two-orbital approach (Koshino *et al.*, 2018) is chosen where localized electron orbitals centered at AB- and BA-regions of the superlattice are obtained forming a hexagonal lattice as depicted in Fig. 5.1b. Relevant interaction processes due to electron-electron Coulomb interaction between localized electronic states are identified by determining the respective interaction matrix elements leading to a minimal model of interacting moiré electrons.

The approach to construct the effective model, which is outlined in the following, involves three steps: First, the moiré band structure is obtained by employing a continuum model approach presented in Sec. 5.2. Second, a maximally localized Wannier basis is constructed by using the moiré Bloch basis in Sec. 5.3. Eventually in Sec. 5.4, electron-electron interaction processes are projected into the Wannier basis leading to an effective model of interacting electrons in twisted bilayer graphene. However, before outlining the

details of the approach, a summary of the emerging symmetries is presented in Sec. 5.1 which are important for the construction of the effective model and are necessary for the interpretation of the experimental observations.

### 5.1. EMERGING SYMMETRIES

The symmetries characterizing moiré electrons, which are relevant for the construction of the effective model and emerge in the limit of small twist-angles, are introduced in this section, whereas it is referred to Refs. [Po \*et al.\* \(2018\)](#); [Zou \*et al.\* \(2018\)](#) for a thorough discussion.

In general, one can distinguish between two classes of symmetries: The first one related to the space group of the superlattice and the second one concerned with the intrinsic properties of the electronic degrees of freedom, i.e. the spin and the valley quantum number which are specific to Dirac electrons in graphene ([Castro Neto \*et al.\*, 2009](#)). The symmetries of the superlattice are determined by the moiré interference pattern which is specified by a twist-angle and a center of rotation. Exact translational symmetries are only present for commensurate twist-angles, whereas exact point group symmetries are obtained for centers of rotation coinciding with the high symmetry points of the graphene lattices ([Zou \*et al.\*, 2018](#)), e.g. carbon lattice sites or hexagon centers. This can also be inferred by inspecting [Fig. 5.1b](#). As these lattice configurations are not energetically favored, bilayer systems with exact space group symmetries require fine tuning. Furthermore, as the graphene lattices are dynamical objects, lattice relaxation effects as well as spatial variations in the twist-angle may occur, see e.g. Ref. [Choi \*et al.\* \(2019\)](#), rendering the superlattice structure “imperfect”. The robustness of the experimental observations therefore suggests to relax the demand for exact space group symmetries on the microscale  $a$  in favor of approximate symmetries on the macroscale  $L_M$ . In the following, these are represented by translational symmetries  $T$  and point group  $D_6$  symmetries ([Zou \*et al.\*, 2018](#)) governing the relevant electronic degrees of freedom and justifying the continuum model approach presented in the next section.

Additionally, there are symmetries connected to the intrinsic properties of the moiré electrons. For small twist-angles, scattering processes of electrons between Dirac cones located at the non-equivalent  $K$ -points of the hexagonal Brillouin zone require a large momentum transfer and are therefore suppressed (see [Fig. 5.1a](#) for an illustration and the microscopic details presented in [Appendix B.1](#)). Hence, the two valley sectors of the original single-layer graphene theories decouple leading to an emerging valley symmetry  $U_v(1)$  which conserves the “valley charge”. Additionally, a spin rotational  $SU(2)$  symmetry of the bilayer electrons is assumed as the spin-orbit coupling of electrons in graphene can be neglected ([Castro Neto \*et al.\*, 2009](#)).

In the following section, an effective single-particle model with the set of previously introduced approximate symmetries is constructed.

## 5.2. MOIRÉ BAND STRUCTURE

The weakly dispersing moiré bands are obtained by employing a continuum model (Bistritzer and MacDonald, 2011; Weckbecker *et al.*, 2016) where states near the slightly twisted Dirac cones of the two graphene layers hybridize due to a finite interlayer coupling. It relies on the existence of the approximate translational symmetries and is hence applicable to commensurate and incommensurate twist-angles. The approach has to be contrasted to real-space tight-binding approaches, e.g. Refs. Moon and Koshino (2012); Kang and Vafeek (2018), which rely on exact translational symmetries and are limited by the large size of superlattice unit cells for small twist-angles, but which yield consistent results.

The emerging moiré Brillouin zone is spanned by the Dirac points of the two twisted graphene systems where states near the two rotated  $K$ -points fold to the  $K$ - and  $K'$ -point of the moiré Brillouin zone as depicted in Fig. 5.1a. Because of the large separation in momentum space, the states near the non-equivalent Dirac cones, in the following labeled by the valley quantum number  $\xi = \pm$ , are assumed to be effectively decoupled generating an emergent  $U_v(1)$  valley symmetry. Within this approach, the band structure is specified by the Fermi velocity  $v_F$  of the Dirac electrons, the twist-angle  $\theta$  and the interlayer transition amplitude  $t_\perp$  which determine the magic-angle regime in form of  $\alpha$  as specified in Eq. (5.2).

The single-particle Hamilton operator of the bilayer system is expressed in the basis of the graphene layers,

$$\hat{\Phi}_{\mathbf{K}\xi\sigma} = (\hat{\phi}_A^{(I)}, \hat{\phi}_B^{(I)}, \hat{\phi}_A^{(II)}, \hat{\phi}_B^{(II)})_{\mathbf{K}\xi\sigma} \quad (5.3)$$

with the fermionic operator  $\hat{\phi}_\gamma^{(n)}$  of the graphene layer  $n \in \{I, II\}$  and the crystalline sublattice basis  $\gamma \in \{A, B\}$ , and is given by

$$\hat{H}_{\text{TBG}} = \sum_{\mathbf{K}\sigma\xi} \hat{\Phi}_{\mathbf{K}\xi\sigma}^\dagger \begin{pmatrix} H_{\xi, \theta/2} - \mu & T(t_\perp) \\ T^\dagger(t_\perp) & H_{\xi, -\theta/2} - \mu \end{pmatrix}_{\mathbf{K}\mathbf{K}'} \hat{\Phi}_{\mathbf{K}\xi\sigma}, \quad (5.4)$$

where  $H_{\xi, \varphi}$  represents the Hamiltonian of the Dirac electrons near valley  $\xi$  rotated by angle  $\varphi$ .  $\mathbf{K}$  denotes the crystal momentum in the rotated single-layer graphene Brillouin zones and  $\sigma$  the electron spin. The interlayer coupling is described by the tunneling matrix element  $T(t_\perp)$  which assumes local tunneling processes with an associated energy scale  $t_\perp$ . An explicit expression of this matrix is derived in the Appendix B.1.

By diagonalizing Eq. (5.4), the moiré band structure is obtained as the set of bands centered at the charge neutrality point and is separated by considerable band gaps from a continuum of bands at higher and lower energies, respectively. Free moiré electrons are eventually described by (Klug, 2020)

$$\hat{H}_M = \sum_{\lambda\mathbf{k}\sigma\xi} \hat{\psi}_{\lambda\mathbf{k}\xi\sigma}^\dagger (\epsilon_{\lambda\mathbf{k}\xi} - \mu) \hat{\psi}_{\lambda\mathbf{k}\xi\sigma}, \quad (5.5)$$

where the band index  $\lambda$ , spin index  $\sigma$ , valley index  $\xi$  and crystal momentum  $\mathbf{k}$ , which is element of the moiré Brillouin zone, label the superlattice Bloch states  $\hat{\psi}_{\lambda\mathbf{k}\xi\sigma}$ . The

## 5. Model of interacting moiré electrons

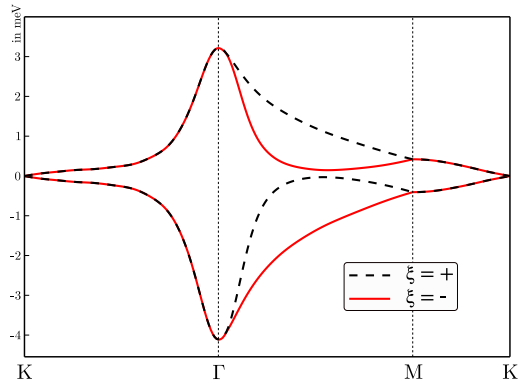


**Figure 5.2.:** Moiré band structure which is obtained by diagonalizing the effective tight-binding model Eq. (5.6) for a twist-angle  $\theta = 1.05^\circ$  and  $\alpha = 0.59$ . The dashed-black and red lines depict the bands with valley number  $\xi = +$  and  $\xi = -$ , respectively. Reprinted figure from Ref. Klug (2020). The original work is found under <https://dx.doi.org/10.1088/1367-2630/ab950c>.

dispersion relation  $\epsilon_{\lambda\mathbf{k}\xi}$  with  $\lambda \in \{1, 2\}$  describes two bands per valley and is depicted in Fig. 5.2 for cuts along the high symmetry lines of the hexagonal moiré Brillouin zone. The characteristics are the Dirac cones centered at the  $K$ - and  $K'$ -points of the moiré Brillouin zone with strongly renormalized Fermi velocities and the van Hove points at the  $M$ -points. The bands of the different valleys are related by a mirror symmetry exchanging the  $K_+$  and  $K_-$ -points of the graphene Brillouin zones. The moiré Brillouin zone and the position of high symmetry points are depicted in Fig. 5.2. Combined with the spin degree of freedom, each superlattice unit cell therefore contains 8 single-electron states.

### 5.3. CONSTRUCTION OF THE WANNIER BASIS

In this section, a real-space localized single-electron basis is constructed by employing the method of maximally localized Wannier functions. Here, the Wannier basis is connected to the Bloch basis by a unitary transformation. This transformation is determined by the constraint that the Wannier functions centered at certain high symmetry points of the underlying lattice are exponentially localized (Marzari and Vanderbilt, 1997; Marzari *et al.*, 2012).

In the case of moiré electrons in twisted bilayer graphene, the Wannier basis is constructed by using the Bloch states of the associated moiré bands representing the basis states of Eq. (5.5). Single orbital approaches, which restrict themselves to a set of orbitals localized at the hexagon's centers of the superlattice, can be ruled out because a touching of the valence and conduction bands at the  $\Gamma$ -point results due to symmetry reasons (Po *et al.*, 2018), which is incompatible with the moiré band structure. Therefore, a two orbital approach is employed by following Ref. Koshino *et al.* (2018) which is capable of reproducing the band structure correctly. Here, two orbitals per superlattice unit cell are centered at the AB- and BA-stacked regions of the superlattice (see Fig. 5.1b for an illustration). Additionally, an exact valley symmetry is assumed a-priori. This approach is expected

## 5. Model of interacting moiré electrons

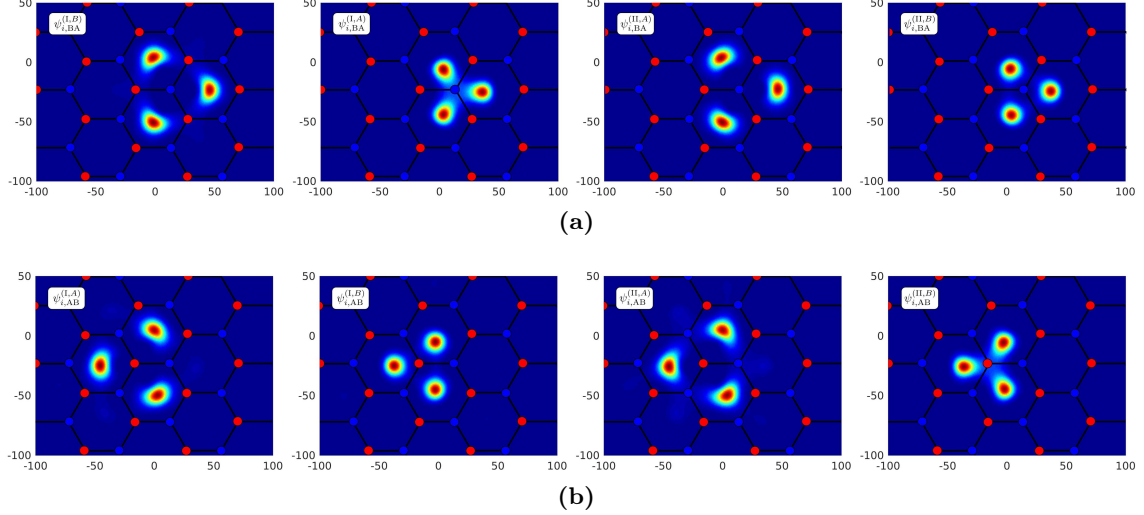


**Figure 5.3.:** Constructed Wannier functions  $\psi_{i\alpha}(\mathbf{r})$  projected on the single-layer graphene sites labeled by the lattice index  $j = \text{I, II}$  and the crystalline sublattice index  $\gamma = A, B$  as introduced in Eq. 5.3. In the upper panel (a)  $\alpha = \text{BA}$ , in the lower panel (b)  $\alpha = \text{AB}$ . Reprinted figure from Ref. Klug (2020). The original work is found under <https://dx.doi.org/10.1088/1367-2630/ab950c>.

to be equivalent to other two-orbital approaches (Kang and Vafeek, 2018; Po *et al.*, 2018) which drop this assumption first, but recover an approximate valley symmetry later. However, also within this two-orbital approach, a Wannier obstruction occurs which renders certain exact symmetries non-local as not all symmetries of the bilayer lattice introduced in Sec. 5.1 can be represented by two orbitals only (Po *et al.*, 2018; Zou *et al.*, 2018). In principal, this issue can be resolved by incorporating additional auxiliary bands (Carr *et al.*, 2019; Po *et al.*, 2019) which introduce, in return, many degrees of freedom. However, it is assumed in this work that the relevant physics of the conducted ground state analysis is captured by the two-orbital approach introduced above.

The procedure to construct maximally localized Wannier functions is standard and can be found, e.g., in Refs. Marzari and Vanderbilt (1997); Marzari *et al.* (2012), whereas its application to the present problem is outlined in detail in the Appendix B.2. As a result, orthogonal and exponentially localized Wannier functions  $\psi_{a\sigma}(\mathbf{r})$  are obtained representing the orbital states labeled by the single-particle quantum numbers  $a = (i, \alpha, \xi)$  and the spin  $\sigma$ . They are centered at the  $\alpha \in \{\text{AB, BA}\}$ -stacked regions of the  $i$ th unit cell of the superlattice, however, possessing highest weight at the AA-stacked regions. Their projection onto the graphene sublattices  $A$  and  $B$  of the graphene layer I and II, respectively, is depicted in Fig. 5.3. As shown in the next section, this characteristic shape of the Wannier functions results in long-range interaction processes between neighboring localized electron states as a direct overlap of wave functions is given.

Eventually, the single-particle moiré electron Hamilton operator Eq. (5.5) is projected

## 5. Model of interacting moiré electrons

into the Wannier basis yielding the effective tight-binding model (Klug, 2020)

$$\hat{H}_0 = \sum_{ab\sigma} (t_{ab} - \mu\delta_{ab}) \hat{\psi}_{a\sigma}^\dagger \hat{\psi}_{b\sigma} \quad (5.6)$$

which is defined on the hexagonal superlattice with the transition amplitudes  $t_{aa'} = t_{i\alpha, i'\alpha'} \delta_{\xi\xi'}$ , which are, by construction, diagonal in the valley index. An explicit expression of  $t_{i\alpha, i'\alpha'}$  is given in the Appendix B.2.

### 5.4. INTERACTION MATRIX ELEMENTS

In a next step, electron-electron interaction effects are incorporated within the established Wannier basis derived previously in Sec. 5.3 to identify the relevant processes. The interaction part of the effective model is given in its most general form by (Mahan, 2000)

$$\hat{H}_{\text{int}} = \frac{1}{2} \sum_{\sigma\sigma'} \sum_{abcd} U_{abcd} \hat{\psi}_{a\sigma}^\dagger \hat{\psi}_{b\sigma'}^\dagger \hat{\psi}_{c\sigma'} \hat{\psi}_{d\sigma}, \quad (5.7)$$

which represents interaction processes between orbital states labeled by the single-particle quantum numbers  $a = (i, \alpha, \xi)$  and the spin index  $\sigma$ . Here, the position of the states on the superlattice is specified by the unit cell index  $i$ , the basis index  $\alpha$ , and the valley number  $\xi$ .  $U_{abcd}$  represents the interaction matrix elements which are determined numerically in the present section to identify the relevant interaction processes.

By means of the corresponding Wannier functions  $\psi_{a\sigma}(\mathbf{r})$ , the interaction matrix elements are expressed as

$$U_{abcd} = \int_{\mathbf{r}\mathbf{r}'} \psi_{a\sigma}^\dagger(\mathbf{r}) \psi_{b\sigma'}^\dagger(\mathbf{r}') V(\mathbf{r} - \mathbf{r}') \psi_{c\sigma'}(\mathbf{r}') \psi_{d\sigma}(\mathbf{r}), \quad (5.8)$$

with an interaction potential  $V(\mathbf{r})$ . Here, the interaction between electrons is modeled by an unscreened Coulomb potential

$$V(\mathbf{r}) = \frac{1}{4\pi\epsilon} \frac{e^2}{|\mathbf{r}|} \quad (5.9)$$

with electron charge  $e$  and relative permittivity  $\epsilon \approx 7$  for hexagonal boron nitride (Cao *et al.*, 2018a). The aspect of screening, which might possibly occur, is neglected by now and will be discussed later in this section.

In the evaluation of Eq. (5.8), it is distinguished between the density ( $a = d$  and  $b = c$  introducing  $U = U_{abba}$ ), the exchange ( $a = c \neq b = d$  introducing  $J = U_{abab}$ ), and the pair-hopping ( $a = b \neq c = d$  introducing  $X = U_{aabb}$ ) channel. In principle, also charge-bond interaction processes ( $a \neq d \neq b = c$ ) are possible. However, the corresponding interaction matrix elements are found to be one order of magnitude smaller than comparable processes and are therefore neglected. Furthermore, the interaction channels are separated into intravalley processes, where the valley indices in  $a$  and  $b$  are identical, and intervalley

## 5. Model of interacting moiré electrons

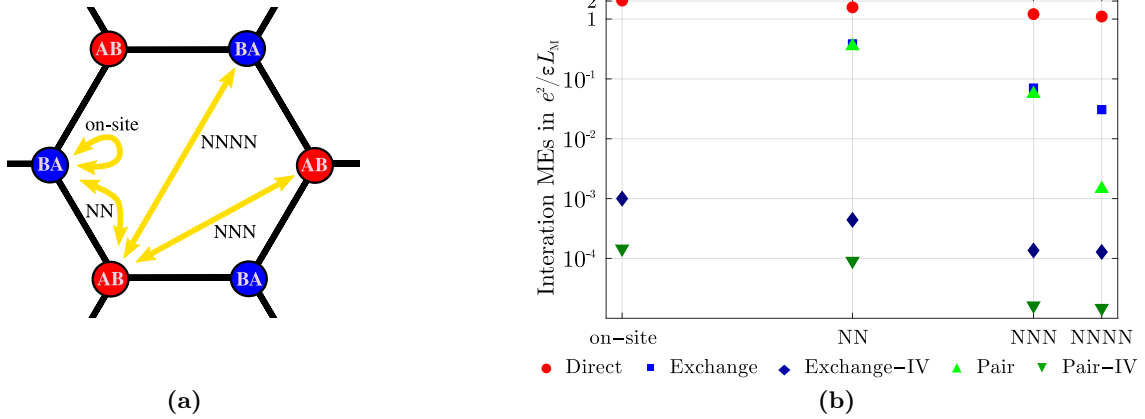


**Figure 5.4.:** Interaction processes and corresponding matrix elements in the constructed Wannier basis. (a) Interaction processes connecting all sites belonging to the same hexagon are identified to be relevant. This include on-site, nearest neighbor (NN), next-to-nearest neighbor (NNN) and next-to-next-to-nearest neighbor (NNNN) interactions. (b) Amplitudes of the interaction matrix elements in units of  $\frac{e^2}{\epsilon L_M}$  for  $\theta = 1.05^\circ$  and  $\alpha = 0.59$  as the function of distance between the interacting orbitals. Reprinted figure from Ref. Klug (2020). The original work is found under <https://dx.doi.org/10.1088/1367-2630/ab950c>.

processes, where the valley indices in  $a$  and  $b$  differ. The latter are labeled by the subscript IV in the following.

The results of the numerical evaluation of Eq. (5.8) are presented in Fig. 5.4. It is found that the amplitude of the interaction matrix elements drops with the distance between the interacting orbitals, but remains significant for processes connecting all orbitals which belong to one hexagon formed by the AB- and BA-stacked regions of the superlattice as depicted in Fig. 5.4a. This is traced back to the fact that the shape of the orbitals is highly non-local (see Fig. 5.3 for an illustration) with highest weight at the AA-stacked regions and substantial overlap between neighboring orbitals. In contrast, longer-distance interactions are numerically small and are dropped from the ongoing discussion. Screening effects even enhance this trend: As the distance to the gating voltage is of the order of the superlattice unit cell (Cao *et al.*, 2018b), screening effects suppress longer-ranged interaction effects. However, as orbitals belonging to one hexagon have a finite direct overlap, the corresponding matrix elements are only affected by screening effects in minor order. This insight is obtained by replacing the interaction potential Eq. (5.9) by a Yukawa-type potential, which is exponentially suppressed for distances larger than the screening length which is of order of  $L_M$ , and by analyzing the resulting interaction matrix elements as a function of distance as discussed in detail in Ref. Klug (2020).

When comparing different types of interaction channels, it is found that direct interaction processes clearly dominate as their matrix elements are at least one order of magnitude larger (see Fig. 5.4b). Since this type of interaction is insensitive to local valley or spin configurations, possible charge modulations are expected to be determined by  $U$ . Although

## 5. Model of interacting moiré electrons

at least one order of magnitude smaller but sensitive to the valley and spin quantum numbers, intra- and intervalley exchange  $J$  and  $J_{IV}$  as well as intra- and intervalley pair-hopping  $X$  and  $X_{IV}$  processes are expected to be relevant. Due to rapid phase fluctuations, intervalley processes are much smaller. However, because of the coupling of otherwise decoupled valley sectors, they are considered relevant to determine the exact ground state. For both the intra- and intervalley case, all matrix elements are found to be positive  $J, J_{IV} > 0$  causing neighboring spin- and orbital-degrees of freedom to align.

As the shape of the Wannier functions changes only little with the twist-angle, the twist-angle dependence of interaction matrix element is found to be rather weak and approximately determined by the superlattice length scale  $U_{abcd} \propto L_M^{-1} \propto \sin(\frac{\theta}{2})$ . This observation is depicted in Fig. 4.1b. The relative amplitudes of the interaction matrix elements presented in Fig. 5.4b are therefore representative for both the weak- and strong-coupling regime.

In conclusion, the weak angle dependence of interaction matrix elements combined with the weak dependence on screening effects indicates that the relative total strength of the interaction processes in twisted bilayer graphene is reasonably well specified, at least within the presented modeling approach, by the dimensionless parameter  $\beta$  (Klug, 2020) introduced in Eq. (4.1). Additionally, the hierarchy of amplitudes of interaction matrix elements for small twist-angles  $\theta \sim \theta_m$  (Klug, 2020),

$$U \gg J > |X| \gg J_{IV} > |X_{IV}|, \quad (5.10)$$

is found to be characteristic for interacting electrons in small-angle twisted bilayer graphene.

### 5.5. EFFECTIVE MODEL

In this chapter, an effective model describing interacting electrons in small-angle twisted bilayer graphene was derived. By combining the kinetic (Eq. (5.6)) and the interaction part (Eq. (5.7)), the total Hamilton operator is given by (Klug, 2020)

$$\hat{H}_{\text{TBG}} = \sum_{ab\sigma} (t_{ab} - \mu\delta_{ab}) \hat{\psi}_{a\sigma}^\dagger \hat{\psi}_{b\sigma} + \frac{1}{2} \sum_{\sigma\sigma'} \sum_{abcd \in \square} U_{abcd} \hat{\psi}_{a\sigma}^\dagger \hat{\psi}_{b\sigma'}^\dagger \hat{\psi}_{c\sigma'} \hat{\psi}_{d\sigma}, \quad (5.11)$$

with transition matrix elements  $t_{ab}$  representing the moiré band structure and the interaction matrix elements  $U_{abcd}$  which are finite for processes connecting all localized electronic states belonging to a same hexagon of the superlattice.

Whereas the relative total strength of interactions was found to be specified by the dimensionless parameter  $\beta$  (Eq. (4.1)), a characteristic hierarchy of interaction processes (Eq. (5.10)) determines the strength of the various interaction channels. Here, it was found that direct interaction processes dominate. They are followed by intra- and intervalley exchange interaction processes which are at least one order of magnitude smaller but always positive. This model constitutes the basis for the electronic ground state analysis.

In the previous chapter, an effective two-orbital model was constructed. In this chapter, this model is investigated regarding possible electronic ground states. Here, two limiting regimes are investigated: First, a weak-coupling regime where  $\beta \ll 1$  and the moiré bandwidth strongly exceeds the energy scale associated with the electron-electron interaction processes representative for small twist-angles away from the magic angle  $|\alpha - \alpha_m| > 0$ , and second, a strong-coupling regime where  $\beta \gg 1$  and the interaction effects dominate representative for twist-angles in the vicinity of the magic angle  $\alpha \approx \alpha_m$ . Here,  $\alpha$ , which is defined in Eq. (5.2), specifies the distance of the considered realization of twisted bilayer graphene to the magic-angle regime. A possible crossover regime where  $\beta \sim 1$  is not considered in this work as its analysis is highly involved and first the limiting cases ought to be understood thoroughly. It is furthermore noted that the following ground state analysis does not depend on the actual twist-angle  $\theta$  or the interlayer transition amplitude  $t_\perp$  as it is based on the smallness or largeness of the dimensionless parameter  $\beta$ . This is justified as tuning the twist-angle causes, to leading order, quantitative but no qualitative changes to the electronic band structure and the interaction matrix elements as discussed previously in Sec. 5.4.

### 6.1. WEAK-COUPLING REGIME

In the limit of weak couplings where  $\beta \ll 1$ , it is possible to treat the interactions on mean field level suggesting a mean field analysis to determine the electronic ground state. In particular, it is intended to identify the interaction channel which first develops an instability. Subsequently, fluctuations can be incorporated to investigate the stability of the determined ground state towards fluctuations which is however beyond the scope of this work. As fluctuations, which are particularly strong in two-dimensional systems, may prevent long-range order to establish, the mean-field analysis provides, nonetheless, information about the interaction channels where strong fluctuations can be expected.

As the number of types of relevant interaction processes is large and the number of possible interaction channels even larger, an unrestricted Hartree-Fock approach is employed to identify the leading electron instability. Interaction terms Eq. (5.7) are therefore locally decoupled by introducing static, local mean fields in all possible interaction channels (Klug, 2020):

## 6. Ground state analysis

$$\begin{aligned} \hat{\psi}_{a\sigma}^\dagger \hat{\psi}_{b\sigma'}^\dagger \hat{\psi}_{c\sigma'} \hat{\psi}_{d\sigma} &\approx \langle \hat{\psi}_{b\sigma'}^\dagger \hat{\psi}_{c\sigma'} \rangle \hat{\psi}_{a\sigma}^\dagger \hat{\psi}_{d\sigma} + \langle \hat{\psi}_{a\sigma}^\dagger \hat{\psi}_{d\sigma} \rangle \hat{\psi}_{b\sigma'}^\dagger \hat{\psi}_{c\sigma'} \\ &\quad - \langle \hat{\psi}_{a\sigma}^\dagger \hat{\psi}_{c\sigma'} \rangle \hat{\psi}_{b\sigma'}^\dagger \hat{\psi}_{d\sigma} - \langle \hat{\psi}_{a\sigma}^\dagger \hat{\psi}_{c\sigma'} \rangle \hat{\psi}_{b\sigma'}^\dagger \hat{\psi}_{d\sigma} + \text{const.}, \end{aligned} \quad (6.1)$$

where  $\langle \dots \rangle$  denotes averaging with respect to the electronic ground state. This yields the quadratic mean field Hamilton operator

$$\begin{aligned} \hat{H}_{\text{MF}} = \sum_{ab\sigma\sigma'} &\left\{ (t_{ab} - \mu\delta_{ab} + \sum_{cd\sigma''} [U_{adcb} \langle \hat{\psi}_{d\sigma''}^\dagger \hat{\psi}_{c\sigma''} \rangle + U_{cabd} \langle \hat{\psi}_{c\sigma''}^\dagger \hat{\psi}_{d\sigma''} \rangle]) \delta_{\sigma\sigma'} \right. \\ &\quad \left. - \sum_{cd} [U_{dacb} \langle \hat{\psi}_{d\sigma'}^\dagger \hat{\psi}_{c\sigma} \rangle + U_{dbca} \langle \hat{\psi}_{d\sigma'}^\dagger \hat{\psi}_{c\sigma} \rangle] \right\} \hat{\psi}_{a\sigma}^\dagger \hat{\psi}_{b\sigma'} \end{aligned} \quad (6.2)$$

with the local mean fields  $\langle \hat{\psi}_{a\sigma}^\dagger \hat{\psi}_{b\sigma'} \rangle$  as variational parameters. This approach ensures that the analysis is susceptible to various kinds of electron instabilities (excluding superconductivity). The energy spectrum is readily determined for the quadratic Hamilton operators given a configuration of local mean-fields. The mean-field configuration of the ground state is determined by minimizing the ground state energy functional  $E[\langle \hat{\psi}^\dagger \hat{\psi} \rangle] = \langle \hat{H}_{\text{MF}} \rangle$ . The numerical simulation is performed on a finite lattice of  $30 \times 30$  unit cells of the superlattice. Details about the the computational scheme are presented in the Appendix B.3.

The interaction channel which first develops an instability for a finite interaction strength  $\beta \gtrsim 0.04$  is a stripe charge density wave order which breaks translational  $T$  and  $C_3$ -rotational symmetry while preserving the spin  $SU(2)$  and the valley  $U_v(1)$  symmetry (Klug, 2020). An onset of this order does also depend on the filling of the moiré bands. For a large amount of electron- or hole-doping, no electronic order is observed and the characteristic van-Hove singularities as well as the linear dispersion relation near the charge neutrality point is observed in the density of states as depicted in Fig. 6.1. In contrast for a finite doping range around the charge neutrality point, the formation of a stripe charge density wave order causes a significant redistribution of spectral weight and suppresses the van-Hove peaks.

Additionally, a representation of this order in real space is depicted in Fig. 6.1. Here, the local electron density is parametrized by (Klug, 2020)

$$\langle \hat{n}_{a\sigma} \rangle = \frac{n}{8} + \frac{\Delta_{\mathbf{Q}}}{8N} \cos(\mathbf{Q} \cdot \mathbf{R}_a), \quad (6.3)$$

where the order parameter is given by

$$\Delta_{\mathbf{Q}} = \sum_{\mathbf{k}\alpha\xi\sigma} \langle \hat{\psi}_{\mathbf{k}+\mathbf{Q}\alpha\xi\sigma}^\dagger \hat{\psi}_{\mathbf{k}\alpha\xi\sigma} \rangle, \quad (6.4)$$

with the electron density  $n = \frac{1}{N} \sum_{a\sigma} \langle \hat{n}_{a\sigma} \rangle$  and the number of superlattice unit cells  $N$ , the particle number operator  $\hat{n}_{a\sigma} = \hat{\psi}_{a\sigma}^\dagger \hat{\psi}_{a\sigma}$  and the lattice site vectors  $\mathbf{R}_a$ . Possible ordering vectors are  $\mathbf{Q} \in \{\mathbf{G}_1/2, \mathbf{G}_2/2, (\mathbf{G}_1 + \mathbf{G}_2)/2\}$  with  $\mathbf{G}_i$  a basis reciprocal superlattice vector

## 6. Ground state analysis

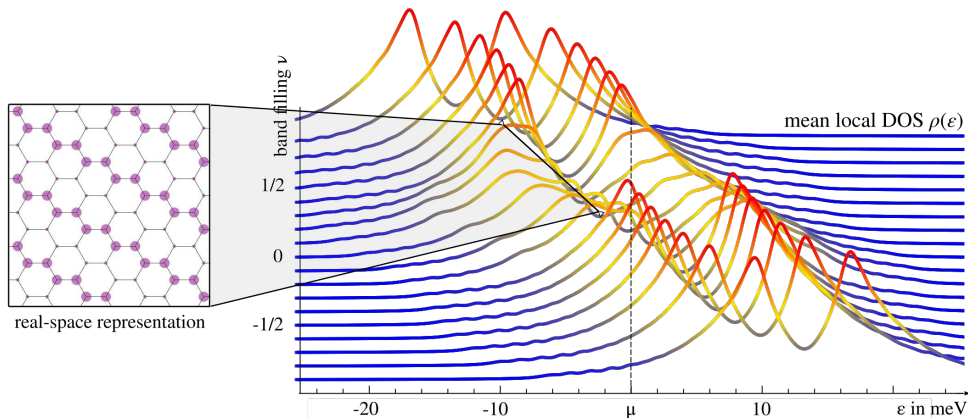


**Figure 6.1.:** Mean local density of states as function of frequency ( $x$ -axis) for various moiré band fillings ( $y$ -axis) for a fixed twist-angle in the weak-coupling regime. The local density of states is averaged over all lattice site and is given by  $\rho(\epsilon) = -\frac{1}{\pi N} \sum_{a,\sigma} \text{Im}G_{aa,\sigma\sigma}^R(\epsilon)$  where the retarded Green’s function is obtained from the mean field Hamiltonian as discussed in the Appendix B.3. A possible real space representation of the order with  $\frac{\Delta_{\mathbf{Q}}}{n} \approx 0.126$  is depicted in the inset where the hexagon’s vertices represent the AB- and BA-stacked regions of the superlattice. The purple dot’s diameter scales with the local occupation of orbitals  $\bullet \propto \sum_{\xi\sigma} \langle \hat{n}_{i\alpha\xi\sigma} \rangle$ . Reprinted figure from Ref. Klug (2020). The original work is found under <https://dx.doi.org/10.1088/1367-2630/ab950c>.

(see Eq. (B.7) in the Appendix B.1 for its definition).

The observations are understood by setting up a corresponding mean field theory using the interaction channel specified by the order parameter  $\Delta_{\mathbf{Q}}$  where the details of the approach are presented in the Appendix B.5. As charge modulations are predominantly determined by direct interaction processes with numerically large interaction matrix elements, exchange and pair-hopping processes are here neglected and the effective interaction in the corresponding channel is determined to (Klug, 2020)

$$U_{\text{CDW}} = U_{\text{on-site}} + U_{\text{NN}} - 4U_{\text{NNN}} - 3U_{\text{NNNN}}, \quad (6.5)$$

which can be negative for sufficiently large  $U_{\text{NNN}}$ ,  $U_{\text{NNNN}}$  and small  $U_{\text{on-site}}$ ,  $U_{\text{NN}}$  interaction matrix elements. This is made plausible by inspecting a possible real space representation of the charge density wave order depicted in the inset of Fig. 6.1: At the mean field level, this charge configuration minimizes the interaction contributions from NNN and NNNN direct interaction processes. In particular for the numerical values determined in Sec. 5.4,  $U_{\text{CDW}}/U_{\text{on-site}} \approx -2.2$  and the effective interaction is attractive. This finding is complemented by results for the static charge susceptibility with finite momentum transfer. It is peaked for doping levels around charge neutrality but does not diverge due to the absence of nesting conditions linked to the momentum  $\mathbf{Q}$ . An onset of this order therefore requires an finite, attractive interaction strength and follows the qualitative illustration depicted in Fig. 4.2.

A possible real space representation of the stripe density charge order is depicted in the inset of Fig. 6.1. Note that the corresponding real-space charge distribution, which is acces-

sible, e.g., in scanning tunneling microscopy measurements, differs qualitatively because of the highly non-local shape of Wannier orbitals with highest localization probability at the center of hexagons of the superlattice. The local charge distribution would rather resemble a distorted,  $C_3$ -rotational symmetry breaking version of the disordered state.

## 6.2. STRONG-COUPLING REGIME

In the magic-angle regime, kinetic energy contributions of the electrons are expected to be much smaller than the contributions from interaction processes and hence  $\beta \gg 1$ . Therefore, kinetic energy contributions are assumed to be negligible and only interaction processes in the density-density channels are considered. As  $[\hat{H}_{\text{SC}}, \hat{n}_{a\sigma}] = 0$ , this approximation renders the local occupation number a good quantum number and the theory classical. Later, kinetic contributions could be incorporated perturbatively in orders of  $\sim t/U$ , which is however not part of this work. In this limit of “infinite couplings”, the Hamiltonian contains only contributions from direct and exchange interaction processes and is given by (Klug, 2020)

$$\hat{H}_{\text{SC}} = \frac{1}{2} \sum_{\sigma\sigma'} \sum_{ab \in \square} (U_{ab} - J_{ab} \delta_{\sigma\sigma'}) (\hat{n}_{a\sigma} - \frac{1}{2}) (\hat{n}_{b\sigma'} - \frac{1}{2}), \quad (6.6)$$

where  $\hat{n}_{\alpha\sigma}$  represents the local occupation number operator. This model is particle-hole symmetric, i.e. invariant under  $\hat{n}_{a\sigma} \rightarrow 1 - \hat{n}_{a\sigma}$ , which allows one to study either hole or electron doping. Since electronic single-particle states are either occupied or empty,  $\langle \hat{n}_{\alpha\sigma} \rangle = 0, 1$ , the ground state is determined by minimizing the energy functional  $E[\langle \hat{n} \rangle] = \langle \hat{H}_{\text{SC}} \rangle$  with the local occupation numbers as variational parameters. The optimization problem is solved by using the conventional Monte Carlo based simulated-annealing-algorithm (Kirkpatrick *et al.*, 1983). Details about the numerical procedure are found in the Appendix B.5.

For all commensurate moiré band fillings  $\nu = 0, \pm\frac{1}{4}, \pm\frac{1}{2}, \pm\frac{3}{4}$ , Mott-insulating ground states are found (Klug, 2020): When adding or removing electrons, it is expected that these insulating states turn into conducting states where single electrons move in a landscape of potential barriers generated by electrons and holes constituting the nearest insulating state. The resulting ground states for the hole-doped side are depicted in Fig. 6.2.

For moiré band fillings  $\nu = 0, \pm\frac{1}{4}$ , stripe-type orders are observed which resemble the findings of the weak-coupling approach (Sec. 6.1) with charge inhomogeneities described by ordering vectors as given in Eq. (6.4). It indicates, that this particular density configuration minimizes the potential energy costs generated by the dominant direct interaction processes irrespective of kinetic energy contributions. It supports the earlier presumption that the formation of density inhomogeneities in the weak-coupling regime is not linked to features of the single-particle spectrum, e.g. nesting conditions. For  $\nu = \pm\frac{1}{2}, \pm\frac{3}{4}$ , charge configurations are found which maximize the distance between charges similar to the principle of Wigner crystallization.

## 6. Ground state analysis

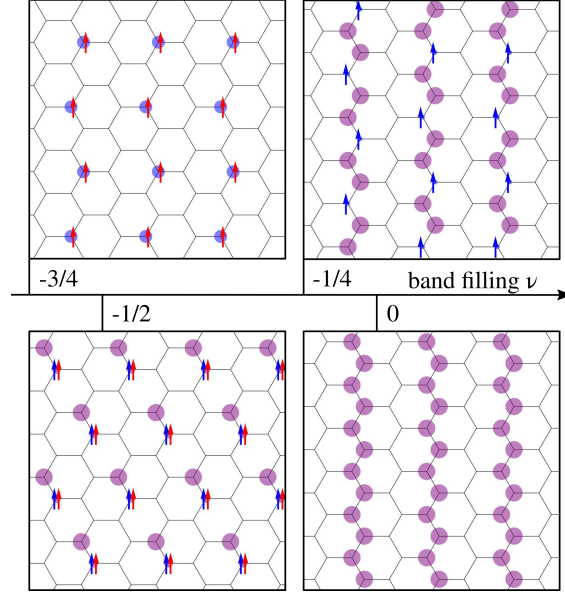


**Figure 6.2.:** Real-space representations of possible ground states in the strong-coupling regime which exhibit Mott-insulating behavior. The occupation number at one particular lattice site, which accommodates in total 4 electronic states, is indicated by symbols as follows (arrows represent spin up / down state, color red / blue valley  $\xi = \pm 1$  state):  $\frac{4}{4}$  occupation  $\bullet$ ,  $\frac{3}{4}$  occupation  $\color{red}\uparrow$ ,  $\color{blue}\uparrow$ ,  $\frac{3}{4}$  occupation  $\color{red}\uparrow$ ,  $\color{red}\downarrow$ ,  $\color{blue}\uparrow$ ,  $\frac{1}{2}$  occupation  $\color{red}\uparrow$ ,  $\color{red}\downarrow$ ,  $\color{blue}\uparrow$ ,  $\frac{1}{4}$  occupation  $\uparrow$ ,  $-\uparrow$ , else empty. Reprinted figure from Ref. Klug (2020). The original work is found under <https://dx.doi.org/10.1088/1367-2630/ab950c>.

It is concluded that the charge distribution is decisively determined by direct interaction processes  $U$  which are characterized by a significant coupling of all sites belonging to one hexagon. It is determined solely by the ratio of direct interaction terms, which was determined to  $(U_{\text{on-site}}:U_{\text{NN}}:U_{\text{NNN}}:U_{\text{NNNN}})/U_{\text{on-site}} = (1:0.79:0.63:0.58)$ , where the exact numerical values matter. Simple ratios of type  $(1:\frac{2}{3}:\frac{1}{3}:\frac{1}{3})$  which are suggestive when counting the direct overlap of Wannier orbitals as, e.g., discussed in Ref. Ochi *et al.* (2018) lead to qualitatively different results. Furthermore, since the local single-particle states are either empty or occupied, the particular ground state is required, unless occupied lattice sites are always fully occupied, to additionally break the spin- and/ or valley-symmetry. Since direct interaction processes do not discriminate between spin and charge degrees-of-freedom, the energetically most favorable configuration is here determined by exchange interactions. Their matrix elements, for both the intra- and intervalley channel, are always found to be positive and therefore favor an alignment of spins non-locally (because of intravalley exchange) and locally (because of intervalley exchange). This results for  $\nu = \pm\frac{1}{4}, \pm\frac{3}{4}$  in a condensation of local degrees of freedom of partially occupied sites in one particular spin and valley sector, whereas for  $\nu = \pm\frac{1}{2}$  in one particular spin sector because on-site intravalley exchange interaction is absent, as depicted in Fig. 6.2.

### 6.3. CONCLUSION AND OUTLOOK

In this chapter, an electronic ground states analysis in the limit of weak and strong couplings was conducted. By using the effective model of interacting moiré electron constructed in Ch. 5, a tendency towards the formation of a charge density wave order specified by the order parameter  $\Delta_{\mathbf{Q}}$  introduced in Eq. (6.4) was observed for both coupling regimes. The robustness of this finding is traced back to direct interaction processes which connect all sites on the superlattice belonging to the same hexagon and whose matrix elements are numerically largest.

However, a possible formation of a long-range charge density wave order has to be investigated more thoroughly as strong fluctuations may render the correlation length finite preventing a long-range order to develop. Instead, a nematic state may develop as a fluctuation-induced composite order (Fernandes *et al.*, 2019). Applied to the present case, a possible nematic order is described by the condensation of one component of the two-component field

$$\phi = \begin{pmatrix} \frac{1}{\sqrt{3}}[2|\rho_3|^2 - |\rho_1|^2 - |\rho_2|^2] \\ |\rho_1|^2 - |\rho_2|^2 \end{pmatrix}, \quad (6.7)$$

which transforms as the two-dimensional irreducible  $E_g$ -representation. Here,  $\rho_1 = \rho_{\frac{\mathbf{G}_1}{2}}$ ,  $\rho_2 = \rho_{\frac{\mathbf{G}_2}{2}}$  and  $\rho_3 = \rho_{\frac{\mathbf{G}_1 + \mathbf{G}_2}{2}}$  are the density fields  $\rho_{\mathbf{Q}}$  with finite momentum  $\mathbf{Q}$  associated with the density operator constituting the order parameter  $\Delta_{\mathbf{Q}} = \langle \hat{\rho}_{\mathbf{Q}} \rangle$ . The nematic order emerges in a second order phase transition with well defined transition temperature, which only breaks discrete rotational but no translational symmetry. This finding is consistent with the results obtained in scanning tunneling microscopy measurements (Kerelsky *et al.*, 2019; Choi *et al.*, 2019; Jiang *et al.*, 2019; Xie *et al.*, 2019). Besides, fluctuations in the nematic channel may also induce and amplify superconductivity as discussed in Refs. Lederer *et al.* (2015, 2017); Kozii *et al.* (2019).

In addition to the nematic state, an onset of spin- and valley-polarized orders for strong couplings was found implying a reduced degeneracy of Landau levels which is consistent with the observations obtained in magneto transport measurements (Cao *et al.*, 2018b; Yankowitz *et al.*, 2019; Lu *et al.*, 2019). This effect is due to the non-local, positive intravalley and intervalley exchange couplings suggesting modified Hund's rule, where first the spin and subsequently the valley number is maximized when filling up superlattice sites with electrons. This yields the observed degeneracy pattern of the observed insulating states as summarized in Fig. 4.2.

## REFERENCES OF PART II

- R. Bistritzer and A. H. MacDonald, *Moiré bands in twisted double-layer graphene*, *Proc. Natl. Acad. Sci.* **108**, 12233 (2011).
- Y. Cao, V. Fatemi, A. Demir, S. Fang, S. L. Tomarken, J. Y. Luo, J. D. Sanchez-Yamagishi, K. Watanabe, T. Taniguchi, E. Kaxiras, R. C. Ashoori, and P. Jarillo-Herrero, *Correlated insulator behaviour at half-filling in magic-angle graphene superlattices*, *Nature* **556**, 80 (2018a).
- Y. Cao, V. Fatemi, S. Fang, K. Watanabe, T. Taniguchi, E. Kaxiras, and P. Jarillo-Herrero, *Unconventional superconductivity in magic-angle graphene superlattices*, *Nature* **556**, 43 (2018b).
- S. Carr, S. Fang, Z. Zhu, and E. Kaxiras, *Exact continuum model for low-energy electronic states of twisted bilayer graphene*, *Phys. Rev. Research* **1**, 013001 (2019).
- A. H. Castro Neto, F. Guinea, N. M. R. Peres, K. S. Novoselov, and A. K. Geim, *The electronic properties of graphene*, *Rev. Mod. Phys.* **81**, 109 (2009).
- Y. Choi, J. Kemmer, Y. Peng, A. Thomson, H. Arora, R. Polski, Y. Zhang, H. Ren, J. Alicea, G. Refael, F. von Oppen, K. Watanabe, T. Taniguchi, and S. Nadj-Perge, *Electronic correlations in twisted bilayer graphene near the magic angle*, *Nature* **15**, 1174 (2019).
- R. M. Fernandes, P. P. Orth, and J. Schmalian, *Intertwined vestigial order in quantum materials: Nematicity and beyond*, *Annu. Rev. Condens. Matter Phys.* **10**, 133 (2019).
- Y. Jiang, X. Lai, K. Watanabe, T. Taniguchi, K. Haule, J. Mao, and E. Y. Andrei, *Charge-order and broken rotational symmetry in magic angle twisted bilayer graphene*, *Nature* **573**, 91 (2019).
- J. Kang and O. Vafek, *Symmetry, maximally localized wannier states, and a low-energy model for twisted bilayer graphene narrow bands*, *Phys. Rev. X* **8**, 031088 (2018).
- J. Kang and O. Vafek, *Strong coupling phases of partially filled twisted bilayer graphene narrow bands*, *Phys. Rev. Lett.* **122**, 246401 (2019).
- A. Kerelsky, L. J. McGilly, D. M. Kennes, L. Xian, M. Yankowitz, S. Chen, K. Watanabe, T. Taniguchi, J. Hone, C. Dean, A. Rubio, and A. N. Pasupathy, *Maximized electron interactions at the magic angle in twisted bilayer graphene*, *Nature* **572**, 95 (2019).
- S. Kirkpatrick, C. D. Gelatt, and M. P. Vecchi, *Optimization by simulated annealing*, *Science* **220**, 671 (1983).
- M. J. Klug, *Charge order and mott insulating ground states in small-angle twisted bilayer graphene*, *New J. Phys.* (2020).
- M. Koshino, N. F. Q. Yuan, T. Koretsune, M. Ochi, K. Kuroki, and L. Fu, *Maximally localized wannier orbitals and the extended hubbard model for twisted bilayer graphene*, *Phys. Rev. X* **8**, 031087 (2018).
- V. Kozii, H. Isobe, J. W. F. Venderbos, and L. Fu, *Nematic superconductivity stabilized by density wave fluctuations: Possible application to twisted bilayer graphene*, *Phys. Rev. B* **99**, 144507 (2019).

- S. Lederer, Y. Schattner, E. Berg, and S. A. Kivelson, *Enhancement of superconductivity near a nematic quantum critical point*, *Phys. Rev. Lett.* **114**, 097001 (2015).
- S. Lederer, Y. Schattner, E. Berg, and S. A. Kivelson, *Superconductivity and non-fermi liquid behavior near a nematic quantum critical point*, *Proc. Natl. Acad. Sci.* **114**, 4905 (2017).
- X. Lu, P. Stepanov, W. Yang, M. Xie, M. A. Aamir, I. Das, C. Urgell, K. Watanabe, T. Taniguchi, G. Zhang, A. Bachtold, A. H. MacDonald, and D. K. Efetov, *Superconductors, orbital magnets and correlated states in magic-angle bilayer graphene*, *Nature* **574**, 653 (2019).
- G. D. Mahan, *Many-particle physics*, 3rd ed., Physics of solids and liquids (Kluwer Acad./Plenum Publ., New York, NY, 2000).
- N. Marzari and D. Vanderbilt, *Maximally localized generalized wannier functions for composite energy bands*, *Phys. Rev. B* **56**, 12847 (1997).
- N. Marzari, A. A. Mostofi, J. R. Yates, I. Souza, and D. Vanderbilt, *Maximally localized wannier functions: Theory and applications*, *Rev. Mod. Phys.* **84**, 1419 (2012).
- P. Moon and M. Koshino, *Energy spectrum and quantum hall effect in twisted bilayer graphene*, *Phys. Rev. B* **85**, 195458 (2012).
- K. S. Novoselov, A. K. Geim, S. V. Morozov, D. Jiang, M. I. Katsnelson, I. V. Grigorieva, S. V. Dubonos, and A. A. Firsov, *Two-dimensional gas of massless dirac fermions in graphene*, *Nature* **438**, 197 (2005).
- M. Ochi, M. Koshino, and K. Kuroki, *Possible correlated insulating states in magic-angle twisted bilayer graphene under strongly competing interactions*, *Phys. Rev. B* **98**, 081102(R) (2018).
- H. C. Po, L. Zou, A. Vishwanath, and T. Senthil, *Origin of mott insulating behavior and superconductivity in twisted bilayer graphene*, *Phys. Rev. X* **8**, 031089 (2018).
- H. C. Po, L. Zou, T. Senthil, and A. Vishwanath, *Faithful tight-binding models and fragile topology of magic-angle bilayer graphene*, *Phys. Rev. B* **99**, 195455 (2019).
- D. Weckbecker, S. Shallcross, M. Fleischmann, N. Ray, S. Sharma, and O. Pankratov, *Low-energy theory for the graphene twist bilayer*, *Phys. Rev. B* **93**, 035452 (2016).
- Y. Xie, B. Lian, B. Jäck, X. Liu, C.-L. Chiu, K. Watanabe, T. Taniguchi, B. A. Bernevig, and A. Yazdani, *Spectroscopic signatures of many-body correlations in magic-angle twisted bilayer graphene*, *Nature* **572**, 101 (2019).
- M. Yankowitz, S. Chen, H. Polshyn, Y. Zhang, K. Watanabe, T. Taniguchi, D. Graf, A. F. Young, and C. R. Dean, *Tuning superconductivity in twisted bilayer graphene*, *Science* **363**, 1059 (2019).
- N. F. Q. Yuan and L. Fu, *Model for the metal-insulator transition in graphene superlattices and beyond*, *Phys. Rev. B* **98**, 045103 (2018).
- L. Zou, H. C. Po, A. Vishwanath, and T. Senthil, *Band structure of twisted bilayer graphene: Emergent symmetries, commensurate approximants, and wannier obstructions*, *Phys. Rev. B* **98**, 085435 (2018).

## CONCLUSION

---

The thesis was divided into two parts which dealt with out-of-time order correlators and electronic orders in small-angle twisted bilayer graphene united under the umbrella of “characterizing” and “tuning” interactions in graphene-based systems.

The first part dealt with out-of-time order correlators and associated scrambling rates in the context of condensed matter physics. In particular, the issues of microscopic processes determining quantum information scrambling and the deducible amount of information from scrambling rates about other physical processes were addressed. In addition, the question of measuring the scrambling rate in experiments was investigated, i.e. under which circumstances quantum chaotic dynamics are reflected in the dynamics of observables.

To determine the scrambling rates, the augmented Keldysh formalism was first developed to represent out-of-time order correlators as contour-ordered expectation values. Subsequently, two approaches were presented which are compatible, yet complementary: As the diagrammatic approach is suitable for determining the scrambling rate, the kinetic equation approach conveys a more physical picture of the process of information scrambling.

By recapitulating the presented discussion in Chs. 1-3, the dynamics of out-of-time order correlators is best pictured as a measure of fidelity of two copies of a considered system. The copies are initially perfectly entangled, but the fidelity diminishes because of small, initial perturbations which grow exponentially in time due to interaction-induced quantum chaotic dynamics rendering the two copies increasingly “incoherent”. This picture was initially indicated by the thermofield double representation of out-of-time order correlators (Ch. 1), whereas it corresponded to two classical phase space trajectories which diverge because of slightly different initial conditions in the case of electrons in a disordered metal (Ch. 3). In the system of interacting electrons in graphene (Ch. 2), two copies of graphene “dephased” because of mutual interaction processes between these copies.

The diminishing of fidelity is an interaction-driven effect specified by the scrambling rate (and the Butterfly velocity) which cannot be directly linked to a specific physical process in general: The two systems considered in this work suggested a connection of the scrambling rate with the interaction rate of elementary excitations, i.e. it resembled the inelastic electron-electron scattering rate in the case of graphene and the elastic electron-impurity scattering rate in the case of electrons in a disordered metal. However, there are systems where information scrambling is related to other physical processes, e.g. charge diffusion, energy diffusion, or transport processes. The mechanism causing information scrambling is hence determined by microscopic details and cannot be considered universal.

The scrambling rate determined for interacting electrons in graphene was further compared to other single-particle relaxation rates in Ch. 2. It was found parametrically larger

than rates representative for thermalization and hydrodynamic transport processes. This large hierarchy of rates may indicate that the process of information scrambling is generally the fastest and may provide upper bounds on rates of other physical processes. In particular, in combination with the Butterfly velocity, which was identified with the interaction-dressed Fermi velocity, the possibility of a bound on diffusion constants was discussed in Sec. 2.7 and is worth pursuing in future works.

In the first part, the exponential growth of out-of-time order correlators was argued to be fundamentally linked to the existence of a small parameter. On the one hand, it was necessary to define the exponential growth, on the other it rendered the system’s dynamics, which are in general of quantum nature, classically chaotic. This principle paves the way to a proposed link between fluctuations dynamics of observables and quantum chaotic dynamics defined by out-of-time order correlators. In Ch. 3, this link was explicitly shown to exist for electrons in a disordered metal coupled to a dissipative bath of phonons. Here, fluctuations in observables were initially induced by uncertainties in the experimental preparation procedure. The link was argued to provide access to the scrambling rate in experiments with settings which do not require a global time reversal operation or a generation of identical copies allowing applications to complex many-body systems as demonstrated on the example of a chaotic graphene quantum dot. However, it was pointed out that special care has to be taken in order to initially excite the chaotic “sector” of the dynamical system and measure the resulting dynamics with “appropriate” observables. The relevant operators and characteristic scales can be identified by studying the corresponding out-of-time order correlator.

The proposed link may also be generalized to systems which do not have a strict classical counterpart, e.g. to interacting electrons in graphene where the pseudoclassical low-energy theory is obtained in terms of plasmon excitations as discussed in Sec. 2.7. One would need to first derive the classical theory which provides classical equations of motions, and then evaluate the out-of-time order correlator in order to identify the relevant operators and scales to excite the quantum system in the classical chaotic sector. Then, the Lyapunov exponent, which equates to the scrambling rate, is determined by the sensitivity of trajectories to small changes in initial conditions and can be extracted from the time series of a weakly measured observable in Sec. 3.6. Using this principle, the complications of realizing out-of-time order correlators in experiments could be eliminated.

The presented results of the first part of the thesis provide starting points for future research. In particular, one could:

- Study the possibility of a bound imposed by the scrambling rate and the butterfly velocity. In particular, one could try to identify physical processes which overshoot the scrambling processes to possibly disprove this proposal.
- Generalize the proposed connection between fluctuation dynamics and out-of-time order correlators to field theories, e.g. the discussed Dirac electrons in graphene in order to propose approaches for measuring the scrambling rate in experiments.

In the second part of this work, the system of interacting electrons in small-angle twisted bilayer graphene was investigated. In particular, the issues of efficiently modeling the low-energy dynamics of interacting moiré electrons and the twist-angle dependence of electronic ground states were addressed in Chs. 4-6.

For this purpose after introducing the system of twisted bilayer graphene in general in Ch. 4, a single-particle Wannier basis was constructed defined on the moiré superlattice which allowed an efficient way of incorporating electron-electron interaction effects in Ch. 5. Within this representation, interaction processes are long-ranged and connect all superlattice sites belonging to one hexagon. This feature was traced back to the unusual shape of the maximally-localized Wannier functions with a direct overlap of neighboring wave functions. In addition, a characteristic hierarchy of interaction processes was identified rendering direct interaction processes predominant. These processes were complemented by ferromagnetic and ferrovalley exchanges processes which potentially lift ground state degeneracies. By including kinetic single-particle processes, they also constitute the effective low-energy model of interacting moiré electrons.

Based on this model, possible electronic ground states were determined for a weak- and a strong-coupling regime in Ch. 6. In the weak-coupling regime, a stripe-type charge density wave order was identified as leading electronic instability. As strong fluctuations were expected to render the correlation length of this order finite, the results indicated a tendency towards enhanced nematic fluctuations. These may condense to form a long-ranged nematic order as observed in experiments, or may further provide a possible pairing mechanism of superconductivity as discussed in Sec. 6.3. In contrast, in the strong-coupling regime, Mott states for all commensurate band fillings, which differed in the number of broken symmetries, were observed. This effect was traced back to the non-local, positive intravalley and intervalley exchange couplings suggesting modified Hund's rules.

As the effective model was able to produce results which are consistent with central experimental features, the correlated insulator states observed in transport measurements and the nematic states observed in scanning tunneling microscopy, it represents a promising starting point for further research. Based on these findings, one could:

- Study the effect of nematic fluctuations and their possible condensation forming a nematic state. Furthermore, one could investigate their possible role in mediating unconventional superconductivity.
- Study the robustness of Mott states with respect to fluctuations and the incorporation of further interaction- and single-particle transition processes.

This work addressed two new forms of “characterizing” and “tuning” interaction effects in graphene-based systems by means of out-of-time order correlators and small-angle twisted bilayer graphene. Further progress is expected from these promising concepts. This underlines their potential relevance for future research in strongly correlated condensed matter systems.

## ACKNOWLEDGEMENTS

---

This work would have not been possible without the support and guidance of a group of people.

First of all, I would like to express my sincere gratitude to Jörg Schmalian for his continuous support and trust, his encouragement and for making so many things possible.

I am also particularly grateful to my collaborators Mathias Scheurer and Sergey Syzranov who significantly contributed to the presented results. Additionally, I sincerely appreciate the support of Sergey Syzranov who made my research stay at the University of California, Santa Cruz, United States of America possible. This research stay has been supported financially by the Karlsruhe House of Young Scientists.

Besides, I also thank all my present and former colleagues of the Institute of Condensed Matter Physics at the Karlsruhe Institute of Technology for countless discussions on various topics and for making the recent years very cheerful ones.

I am also most thankful to my wife who supported me during all stages as a physicist and always gets me with a smile.

Last but not least, I would like to thank my family and friends who supported me for all the years and made this time an unforgettable period of my life.

## APPENDICES

### A.1. CLASSICAL IMPURITY SCATTERING

This section deals with the elastic scattering of classical particles in a static random disorder potential as discussed qualitatively in the context of wave packet spreading in Sec. 1.7.2 and in the context of fluctuations dynamics in Ch. 3. This dynamical system exhibits chaotic dynamics which manifest in an exponentially growing distance between initially close trajectories. The approach follows Ref. Syzranov *et al.* (2019) and is presented for completeness as it represents an integral part of this work.

In what follows, the distance between two trajectories as a function of time and averaged over impurity configuration is computed to extract the classical Lyapunov exponent  $\lambda_{\text{cl}}$ . As argued in the main text, the Lyapunov exponent is of order of the elastic scattering rate  $\tau_0^{-1}$ , where the exact relation is determined by the microscopic details of scattering processes. Other parameters are the mean free path,  $l_{\text{tr}} = v_F \tau_0$ , with the Fermi velocity  $v_F$  representing the particle's velocity and the scattering length  $a$ .

A single scattering event is characterized by its scattering angle  $\theta = \theta(\rho)$  which is assumed to depend solely on the impact parameter  $\rho$ . E.g. for the scattering of a charged particle on impurities described by unscreened long-range Coulomb potentials, the scattering angle is given by  $\theta(\rho) = 2 \tan^{-1}(\frac{a}{\rho})$ , whereas for scattering on hard spheres,  $\theta(\rho) = [\pi - 2 \sin^{-1}(\frac{\rho}{a})]$  for  $\rho \leq a$  else 0, which maps on the problem of a particle in a chaotic billiard (Chirikov, 1979). As both models represent limiting cases which are not applicable in generic condensed matter systems, the scattering angle is solely considered a function of the impact parameter  $\theta = \theta(\rho)$  and is further left unspecified.

In the following, the concentration of impurities is assumed dilute,  $a^3 n_{\text{imp}} \ll 1$  with the impurity density  $n_{\text{imp}}$ , such that the distance between impurities exceeds the scattering length and each scattering event can be considered separately. Furthermore, disorder averaging is treated as follows: First, a particular disorder realization is considered and the classical trajectories are determined. Second, the position of each impurity is considered random and independent from each other which allows one to average over impurity positions.

To determine the distance between trajectories, a reference trajectory with impact parameter  $\rho_1$  and resulting scattering angle  $\theta_1 = \theta(\rho_1)$  is introduced spanning the  $xy$ -plane as depicted in Fig. A.1. Here, the initial momentum is given by  $\mathbf{p}_1 = p_F \hat{\mathbf{e}}_x$ , whereas the scattered momentum is given by  $\mathbf{p}'_1 = p_F (\cos \theta_1 \hat{\mathbf{e}}_x + \sin \theta_1 \hat{\mathbf{e}}_y)$ . The second trajectory is parameterized by  $\mathbf{p}_2 = \mathbf{p}_1 + \mathbf{Q}$  and  $\rho_2 = \rho_1 + \zeta$ , where the momentum difference  $\mathbf{Q}$  and spatial

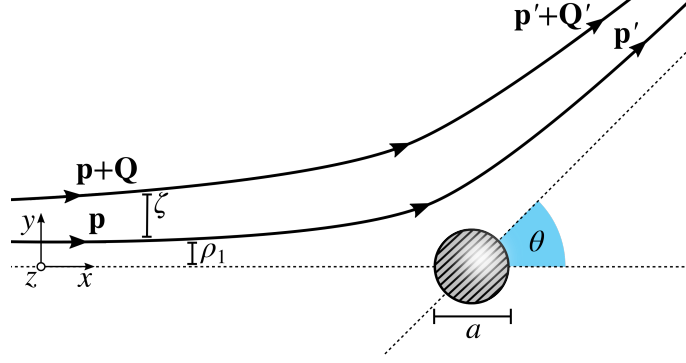


**Figure A.1.:** Two trajectories of particles with initial momentum  $\mathbf{p}$ , momentum difference  $\mathbf{Q}$  and spatial displacement  $\zeta$  scattered elastically by an impurity with scattering length  $a$ . Scattered quantities are denoted by primed variables. Scattering angles  $\theta = \theta(\rho)$  are considered functions of the impact parameter  $\rho$  and depend on the microscopic details of the scattering potential.

displacement  $\zeta$  cause the scattering angle  $\theta_2$  to deviate from  $\theta_1$ . Both displacements are considered orthogonal to the reference trajectory's momentum,  $\mathbf{Q} \cdot \mathbf{p}_1 = \zeta \cdot \mathbf{p}_1 = 0$ , and small,  $|\zeta| \ll \frac{a^2}{l_{\text{tr}}}$  and  $|\mathbf{Q}| \ll p_F \frac{a}{l_{\text{tr}}}$ , to observe chaotic growth as discussed in the main text. In the following, the time evolution of the distance between trajectories quantified by  $\zeta^2$  and  $\mathbf{Q}^2$  is separated into sections of ballistic propagation between impurity collisions and scattering events. While the momentum distance  $\mathbf{Q}^2$  changes in leading order in scattering events,  $\zeta^2$  changes predominately during ballistic propagation. Furthermore, the quantity  $\zeta \cdot \mathbf{Q}$  has to be introduced to obtain a closed set of differential equations.

For a given  $\zeta$ , the impact parameter of the second trajectory changes to

$$\rho_2 = \sqrt{(\rho_1 + \zeta_y)^2 + \zeta_z^2} \approx \rho_1 + |\zeta| \cos \varphi \quad (\text{A.1})$$

where  $\zeta = |\zeta|(0, \cos \varphi, \sin \varphi)^T$  and  $\varphi$  denoting the out-of-plane angle. The scattering angle is given by

$$\theta_2 = \theta(|\boldsymbol{\rho} + \zeta|) \approx \theta_1 + \left. \frac{d\theta}{d\rho} \right|_{\rho=\rho_1} |\zeta| \cos \varphi. \quad (\text{A.2})$$

Furthermore, the scattering plane is slightly tilted by angle  $\phi$  around the  $y$ -axis with  $\phi = \tan^{-1} \frac{|\zeta| \sin \varphi}{\rho_1}$ , such that the scattered momentum of the second trajectory reads

$$\mathbf{p}'_2 = \cos \theta_2 \hat{\mathbf{e}}_x + \sin \theta_2 \hat{\mathbf{e}}_Y, \quad (\text{A.3})$$

with an additional out-of-plane component given by

$$\hat{\mathbf{e}}_Y = \cos \phi \hat{\mathbf{e}}_y + \sin \phi \hat{\mathbf{e}}_z \quad (\text{A.4a})$$

$$\approx \left[ 1 - \frac{1}{2} \sin^2 \varphi \left( \frac{|\zeta|}{\rho_1} \right)^2 \right] \hat{\mathbf{e}}_y + \sin \varphi \frac{|\zeta|}{\rho_1} \hat{\mathbf{e}}_z. \quad (\text{A.4b})$$

## A. Appendices to Part I

Hence, the scattered momentum difference due to finite  $\zeta$  is given by

$$\mathbf{Q}' \approx \mathbf{Q} - \sin \theta_1 \frac{d\theta}{d\rho} \Big|_{\rho=\rho_1} |\zeta| \cos \varphi \hat{\mathbf{e}}_x + \cos \theta_1 \frac{d\theta}{d\rho} \Big|_{\rho=\rho_1} |\zeta| \cos \varphi \hat{\mathbf{e}}_y + \sin \theta_1 \sin \varphi \frac{|\zeta|}{\rho_1} \hat{\mathbf{e}}_z. \quad (\text{A.5})$$

In a next step, the rate of change of differences,  $\frac{d}{dt} \mathbf{Q}^2$ ,  $\frac{d}{dt} \zeta^2$  and  $\frac{d}{dt} (\zeta \cdot \mathbf{Q})$ , are determined and averaged over disorder realizations to obtain a closed set of three coupled differential equations. Here, the disorder averaging is performed by averaging over impurity positions. It effectively translates into averaging over the angle  $\varphi$  and the impact parameter  $\rho$ , which were introduced in parameterizing the scattering angle and the initial distance between trajectories. Both quantities are considered independent of each other. Averages are represented in the following by  $\langle \dots \rangle_\varphi = \frac{1}{2\pi} \int_0^{2\pi} \dots d\varphi$  and  $\langle \dots \rangle_\rho = \frac{2}{l_{\text{tr}}^2} \int_0^{l_{\text{tr}}} \rho \dots d\rho$ , where a cut-off of order  $l_{\text{tr}}$  is introduced. The total average is denoted by  $\langle \dots \rangle_{\text{dis}} \equiv \langle \dots \rangle_{\rho, \varphi}$ .

With the rate of scattering  $\tau_0^{-1} = v_F/l_{\text{tr}}$ , the change in momentum difference during collisions is determined to

$$\frac{d}{dt} \langle \mathbf{Q}^2 \rangle_{\text{dis}} = \tau_0^{-1} [\langle (\mathbf{Q}')^2 \rangle_{\text{dis}} - \mathbf{Q}^2] \quad (\text{A.6a})$$

$$= \frac{p_F^2 v_F}{2l_{\text{tr}}^3} \langle \zeta^2 \rangle_{\text{dis}} \int_0^{l_{\text{tr}}} \rho \left[ \frac{\sin^2 \theta}{\rho^2} + \left( \frac{d\theta}{d\rho} \right)^2 \right] d\rho. \quad (\text{A.6b})$$

While the change of  $\zeta^2$  during collisions is negligible, it changes during ballistic propagation by

$$\frac{d}{dt} \langle \zeta^2 \rangle_{\text{dis}} = \frac{2v_F}{p_F} \langle \zeta \cdot \mathbf{Q} \rangle_{\text{dis}}, \quad (\text{A.7})$$

where it was used that  $\frac{d}{dt} \zeta \approx \frac{v_F}{p_F} \mathbf{Q}$ . Next,  $\zeta \cdot \mathbf{Q}$  changes due to contributions from ballistic propagation and scattering events. The contribution from scattering is given by

$$\frac{d}{dt} \zeta \cdot \mathbf{Q} \Big|_{\text{col}} = \frac{\zeta' \cdot \mathbf{Q}' - \zeta \cdot \mathbf{Q}}{\tau_0}, \quad (\text{A.8})$$

where the second term vanishes in the disorder average as  $\mathbf{Q}$  and  $\zeta$  are uncorrelated. The scattered spatial displacement is tilted using Eq. (A.3) to

$$\zeta' \approx |\zeta| [\cos \varphi (\cos \theta_1 \hat{\mathbf{e}}_y - \sin \theta_1 \hat{\mathbf{e}}_x) + \sin \varphi \hat{\mathbf{e}}_z], \quad (\text{A.9})$$

yielding with the results for  $\mathbf{Q}'$  Eq. (A.5) and after disorder averaging

$$\frac{d}{dt} \langle \zeta \cdot \mathbf{Q} \rangle_{\text{dis}} \Big|_{\text{col}} = \frac{p_F v_F}{l_{\text{tr}}^3 2} \langle \zeta^2 \rangle \int_0^{l_{\text{tr}}} \rho \left[ \frac{\sin \theta}{\rho} + \frac{d\theta}{d\rho} \right] d\rho. \quad (\text{A.10})$$

The contribution from ballistic propagation is determined to

$$\frac{d}{dt} \langle \zeta \cdot \mathbf{Q} \rangle_{\text{dis}} \Big|_{\text{bal}} = \frac{v_F}{p_F} \langle \mathbf{Q}^2 \rangle_{\text{dis}}, \quad (\text{A.11})$$

yielding in total  $\frac{d}{dt} \langle \zeta \cdot \mathbf{Q} \rangle_{\text{dis}} = \frac{d}{dt} \langle \zeta \cdot \mathbf{Q} \rangle_{\text{dis}} \Big|_{\text{bal}} + \frac{d}{dt} \langle \zeta \cdot \mathbf{Q} \rangle_{\text{dis}} \Big|_{\text{col}}$ . However, for dilute disorder,

## A. Appendices to Part I

$a^3 n_{\text{imp}} \sim \frac{a^3}{l_{\text{tr}}^3} \ll 1$ , the rate of change due to collisions is subleading and is therefore neglected in the following (Syzranov *et al.*, 2019).

Eventually, one obtains a closed set of coupled differential equations,

$$\frac{d}{dt} \langle \mathbf{Q}^2 \rangle_{\text{dis}} = \frac{4p_F^2 \lambda_{\text{cl}}^3}{v_F^2} \langle \zeta^2 \rangle_{\text{dis}}, \quad (\text{A.12a})$$

$$\frac{d}{dt} \langle \zeta^2 \rangle_{\text{dis}} = \frac{2v_F}{p_F} \langle \zeta \cdot \mathbf{Q} \rangle_{\text{dis}}, \quad (\text{A.12b})$$

$$\frac{d}{dt} \langle \zeta \cdot \mathbf{Q} \rangle_{\text{dis}} = \frac{v_F}{p_F} \langle \mathbf{Q}^2 \rangle_{\text{dis}}, \quad (\text{A.12c})$$

where the classical Lyapunov exponent is read off from Eq. (A.6b) and is given by

$$\lambda_{\text{cl}} = \frac{1}{2\tau_0} \left\{ \int_0^{l_{\text{tr}}} \rho \left[ \frac{\sin^2 \theta}{\rho^2} + \left( \frac{d\theta}{d\rho} \right)^2 \right] d\rho \right\}^{1/3}. \quad (\text{A.13})$$

Homogeneous solutions are of type  $\langle \mathbf{Q}^2 \rangle_{\text{dis}}(t) = \sum_i c_i e^{\gamma_i t}$  with  $\gamma_1 = 2\lambda_{\text{cl}}$ ,  $\gamma_{2,3} = \lambda_{\text{cl}}(\pm i\sqrt{3} - 1)$ . Thus, for small initial displacements in spatial or momentum space specified by  $c_i$ , the distance between trajectories grows with  $e^{2\lambda_{\text{cl}} t}$ . The sensitivity of momentum mismatch to initial conditions as discussed in Sec. 1.7.2 and Sec. 3.5.2 with initial mismatch in space,  $\langle \zeta^2 \rangle_{\text{dis}}(0) = \zeta_0^2$  and  $\langle \mathbf{Q}^2 \rangle_{\text{dis}}(0) = \langle \zeta \cdot \mathbf{Q} \rangle_{\text{dis}}(0) = 0$ , is eventually determined to

$$\left\langle \left| \frac{\partial p_z(t)}{\partial z_0} \right|^2 \right\rangle_{\text{dis}} \sim \lim_{\zeta_0 \rightarrow 0} \frac{\langle \mathbf{Q}^2(t) \rangle_{\text{dis}}}{\zeta_0^2}, \quad (\text{A.14a})$$

$$\propto e^{2\lambda_{\text{cl}} t}. \quad (\text{A.14b})$$

## REFERENCES

- B. V. Chirikov, *A universal instability of many-dimensional oscillator systems*, *Physics Reports* **52**, 263 (1979).
- S. Syzranov, A. Gorshkov, and V. Galitski, *Interaction-induced transition in the quantum chaotic dynamics of a disordered metal*, *Annals of Physics* **405**, 1 (2019).

## A.2. SEMICLASSICAL OPERATOR DYNAMICS

In what follows, out-of-time order correlators are evaluated in the semiclassical limit  $\hbar_{\text{eff}} = \frac{\hbar}{s_{\text{cl}}} \ll 1$  with  $s_{\text{cl}}$  representing a classical action scale, where a link to the sensitivity of classical phase space trajectories to initial conditions of type Eq. (1.20) is expected. This relation is important for understanding the physical significance of chaotic operator dynamics discussed in the main text, Sec. 1.7, as its applicability may even go beyond the semiclassical limit. Here, the relation is derived microscopically for a minimal model with two-degrees of freedom which already illustrate the underlying principal. A generalization to many-degrees of freedom is straightforward.

In particular, the relation

$$C_q(t) \equiv -\langle [\hat{q}(t), \hat{q}]^2 \rangle \quad (\text{A.15a})$$

$$\stackrel{\hbar_{\text{eff}} \ll 1}{\equiv} \hbar^2 \left\langle \left( \frac{\partial q(t)}{\partial p_0} \right)^2 \right\rangle_{\text{PS}} \quad (\text{A.15b})$$

is derived, where  $\hat{q}, \hat{q}(t) = \hat{U}(t)^\dagger \hat{q} \hat{U}(t)$  represent position operators and  $q(t) = q(t, p_0, q_0, \dots)$  denotes a classical phase space trajectory which depends on initial conditions  $(p_0, q_0, \dots)$ . Quantum mechanical averaging on the right-hand side is denoted by  $\langle \dots \rangle$ , whereas  $\langle \dots \rangle_{\text{PS}}$  represents a phase space average. The presented approach, while referring explicitly to the out-of-time order correlator of position operators Eq. (A.15a), can also be generalized to out-of-time order correlators with more complex operators  $V(q, q') = \langle q | \hat{V} | q' \rangle$  and  $W(q, q') = \langle q | \hat{W} | q' \rangle$ .

In the following, the semiclassical limit of the considered quantum system is assumed to exist. In this limit, the two operators  $\hat{q}$  and  $\hat{p}$ , which obey the canonical commutation relation  $[\hat{p}, \hat{q}] = i\hbar$ , correspond to the canonical phase space variables  $(q, p)$ . Whereas the time evolution of quantum states and operators is determined by the time evolution operator  $\hat{U}(t) = e^{-i\hat{H}t/\hbar}$  with the Hamilton operator  $\hat{H}$ , classical phase space trajectories obey the classical equations of motion  $\frac{\partial q}{\partial t} = \frac{\partial H(q, p)}{\partial p}$  and  $\frac{\partial p}{\partial t} = -\frac{\partial H(q, p)}{\partial q}$  with the Hamilton function  $H(q, p)$ .

To connect quantum and classical mechanics, matrix elements of the quantum mechanical time evolution operator are approximated in the limit  $\hbar_{\text{eff}} \ll 1$  by the van Vleck propagator (Gutzwiller, 1990; Haake, 2010; Altland and Simons, 2010). It approximates the transition amplitude from the initial state  $|q_I\rangle$  to the final state  $|q_F\rangle$  by the sum over all classical trajectories connecting these end points in time  $t$ . These classical trajectories represent the saddle-point contributions which minimize the action integral. Non-classical contributions are negligible due to rapid phase fluctuations. The quantum mechanical propagator in the position basis is therefore given by (Haake, 2010)

$$\langle q_F | \hat{U}(t) | q_I \rangle \approx \sum_{\alpha} \mathcal{A}_{\alpha}(t, q_I, q_F) e^{iS_{\alpha}(t, q_I, q_F)/\hbar}. \quad (\text{A.16})$$

## A. Appendices to Part I

Here, each trajectory  $\alpha$  is weighted by a phase factor, where the classical action is given by

$$S_\alpha(t, q_I, q_F) = \int_0^t dt' [p_\alpha \dot{q}_\alpha - H(q_\alpha, p_\alpha)], \quad (\text{A.17})$$

with  $q_\alpha(0) = q_I$  and  $q_\alpha(t) = q_F$  as boundary conditions. The initial and final momenta are implicitly given by

$$\frac{\partial S_\alpha(t, q_I, q_F)}{\partial q_I} = -p_I \quad \text{and} \quad \frac{\partial S_\alpha(t, q_I, q_F)}{\partial q_F} = p_F, \quad (\text{A.18})$$

where  $p_\alpha(0) = p_I$  and  $p_\alpha(t) = p_F$ . Furthermore, the amplitude's absolute value is given by

$$|\mathcal{A}_\alpha(q_I, q_F)|^2 = \frac{1}{2\pi\hbar} \left| \frac{\partial^2 S_\alpha(t, q_I, q_F)}{\partial q_I \partial q_F} \right|, \quad (\text{A.19})$$

and arises due to leading order quantum fluctuations around the classical trajectories and is kept as normalization constant. The Morse factor (see e.g. Ref. [Haake \(2010\)](#)), which enters the phase factor Eq. (A.16), is of no significance for the following analysis and therefore compensated into the definition of  $\mathcal{A}_\alpha(t, q_I, q_F)$ .

In what follows, only one classical trajectory connecting  $q_I$  and  $q_F$  is assumed to exist and the index  $\alpha$  is dropped. By inserting complete sets of states and replacing sections of time evolution by Eq. (A.16), the out-of-time order correlator is given by

$$\begin{aligned} C_q(t) &= \int \left( \prod_{i=1}^5 dq_i \right) \psi_0^*(q_5) \psi_0(q_1) \mathcal{A}^*(t, q_5, q_4) \mathcal{A}(t, q_3, q_4) \mathcal{A}^*(t, q_3, q_2) \mathcal{A}(t, q_1, q_2) \\ &\times \exp \left[ \frac{i}{\hbar} \{ S(t, q_1, q_2) - S(t, q_3, q_2) + S(t, q_3, q_4) - S(t, q_5, q_4) \} \right] q_2(q_1 - q_3)q_4(q_5 - q_3). \end{aligned} \quad (\text{A.20})$$

where  $q_1, q_3, q_5$  denote initial and  $q_2, q_4$  final positions. The out-of-time order correlator is constituted by four connected trajectories whose two initial and final endpoints are confined to a certain region in phase space because of the system's initial conditions as depicted in Fig. 1.2. Contributions to the out-of-time order correlator are weighted by the phase factor and are possibly penalized by rapid phase fluctuations. Configurations of trajectories which contribute therefore obey

$$S(t, q_1, q_2) - S(t, q_3, q_2) + S(t, q_3, q_4) - S(t, q_5, q_4) \sim \hbar. \quad (\text{A.21})$$

The purely classical case refers to coinciding endpoints  $q_1 = q_3 = q_5$  and  $q_2 = q_4$ . However for this particular configuration, the out-of-time order correlator vanishes because of a vanishing integrand in Eq. (A.20). Hence, leading order contributions are due to constructively interfering trajectories. These contributions are small in  $\hbar$  and are captured by expanding the positions of endpoints in small deviations from their classical configuration.

Next, a series of simplifications is applied based on the assumption that the difference

## A. Appendices to Part I

between trajectories in phase space is small, which is justified for early times. Coordinates are parametrized around the initial and final endpoints  $q_I$  and  $q_F$ , respectively, by

$$q_1 = q_I - \frac{y}{2}, q_2 = q_F - \frac{x}{2}, q_3 = q_I + z, q_4 = q_F + \frac{x}{2}, q_5 = q_I + \frac{y}{2}, \quad (\text{A.22})$$

to expand the classical action expressions Eq. (A.17), which contribute to the phase of Eq. (A.20), up to quadratic order. The resulting phase factor reads

$$\exp \left[ \frac{i}{\hbar} \left\{ \frac{\partial S(t, q_I, q_F)}{\partial q_I \partial q_F} z x + p_I y \right\} \right]. \quad (\text{A.23})$$

The deviations entering the amplitudes in Eq. (A.16) are dropped yielding

$$\mathcal{A}^*(t, q_I + \frac{y}{2}, q_F + \frac{x}{2}) \mathcal{A}(t, q_I + z, q_F + \frac{x}{2}) \quad (\text{A.24a})$$

$$\approx \mathcal{A}^*(t, q_I + z, q_F - \frac{x}{2}) \mathcal{A}(t, q_I - \frac{y}{2}, q_F - \frac{x}{2}) \quad (\text{A.24b})$$

$$\approx |\mathcal{A}^*(t, q_I, q_F)|^2 = \frac{1}{2\pi\hbar} \left| \frac{\partial p_I}{\partial q_F} \right|, \quad (\text{A.24c})$$

which allows one to change the integration over final positions to an integration over initial momenta,  $(q_I, q_F) \rightarrow (q_I, p_I)$ , rendering the final position a function of initial position and momentum  $p_F = p_F(q_I, p_I)$ . By introducing

$$\psi_0^*(q_I + \frac{y}{2}) \psi_0(q_I - \frac{y}{2}) = \int \frac{dk}{2\pi\hbar} W(q_I, k) e^{-iky/\hbar}, \quad (\text{A.25})$$

where  $W(q, k)$  is interpreted as quasiprobability distribution function in phase space representing initial states, one obtains for the out-of-time order correlator

$$\begin{aligned} C_q(t) &= - \int \frac{dq_I dp_I}{2\pi\hbar} \int \frac{dk dy}{2\pi\hbar} W(q_I, k) e^{i(p_I - k)y/\hbar} \\ &\times \frac{1}{2\pi\hbar} \left| \frac{\partial p_I}{\partial q_F} \right| \int dx dz \exp \left[ \frac{i}{\hbar} \frac{\partial S(t, q_I, q_F)}{\partial q_I \partial q_F} z x \right] (q_F - \frac{x}{2}) (\frac{y}{2} + z) (q_F + \frac{x}{2}) (\frac{y}{2} - z). \end{aligned} \quad (\text{A.26})$$

The integral over fluctuations is regularized by introducing the generating functional

$$I[J] = \frac{1}{2\pi\hbar} \left| \frac{\partial p_I}{\partial q_F} \right| \int dx dz \exp \left[ \frac{i}{\hbar} \frac{\partial S(t, q_I, q_F)}{\partial q_I \partial q_F} z x + i(J_x x + J_z z) \right] \quad (\text{A.27a})$$

$$= \exp \left[ -i\hbar J_x \left\{ \frac{\partial S(t, q_I, q_F)}{\partial q_I \partial q_F} \right\}^{-1} J_z \right], \quad (\text{A.27b})$$

where  $\frac{\partial S(t, q_I, q_F)}{\partial q_I \partial q_F} = \frac{\partial p_I}{\partial q_F}$  such that terms constituting Eq. (A.26) are generated by partial differentials with respect to the generating fields  $J_x$  and  $J_z$ , which are finally set to zero.

There are two contributions which do not vanish: The term in Eq. (A.26)  $\propto y^2$  takes fluctuations of the initial conditions into account and yields

$$\frac{\hbar_{\text{eff}}^2}{4} \int \frac{dq_I dp_I}{2\pi\hbar_{\text{eff}}} \frac{\partial^2 W(q_I, p_I)}{\partial p_I^2} q_F^2. \quad (\text{A.28})$$

## A. Appendices to Part I

This contribution is not related to the sensitivity of trajectories and does not contribute to an exponential growth of out-of-time order correlators. In contrast, the term  $\propto z^2 x^2$  takes fluctuations around the trajectories' endpoints into account yielding

$$\frac{\hbar_{\text{eff}}^2}{4} \int \frac{dq_I dp_I}{2\pi\hbar_{\text{eff}}} W(q_I, p_I) \left( \frac{\partial q_F}{\partial p_I} \right)^2, \quad (\text{A.29})$$

which is proportional to the trajectories' sensitivity to changes in initial conditions. This contribution is expected to be predominant for systems obeying chaotic dynamics determining the growth of the out-of-time order correlator Eq. (A.15a), where phase space averaging is hence identified to

$$\langle \dots \rangle_{\text{PS}} = \frac{\hbar_{\text{eff}}^2}{4} \int \frac{dq_0 dp_0}{2\pi\hbar_{\text{eff}}} W(q_0, p_0) \dots \quad (\text{A.30})$$

### REFERENCES

- A. Altland and B. D. Simons, *Condensed Matter Field Theory*, 2nd ed. (Cambridge University Press, 2010).
- M. C. Gutzwiller, *Chaos in Classical and Quantum Mechanics* (Springer, New York, NY, 1990).
- F. Haake, *Quantum Signatures of Chaos*, 3rd ed. (Springer, Berlin, Heidelberg, 2010).

### A.3. INTERLOOP KELDYSH COMPONENT

Within the augmented Keldysh formalism, the evaluation of out-of-time correlators involves so-called interloop Keldysh components of single-particle propagators as introduced in Sec. 2.4. In this section, spectral representations of interloop Keldysh components, which quantify correlations between field components residing on different loops of the augmented Keldysh contour Fig. 2.3 and introduced in Eq. (2.23), are obtained for thermal equilibrium.

The regularization scheme which is used to evaluate out-of-time order correlators as introduced in Sec. 1.5 is reflected in the energy dependence of the interloop Keldysh components. Here, non-regularized and regularized out-of-time order correlation functions are given by

$$F_{\text{non-reg}}(t) = \text{tr}[\hat{V}(t)\hat{W}(0)\hat{V}(t)\hat{W}(0)\rho_0], \quad (\text{A.31a})$$

$$F_{\text{reg}}(t) = \text{tr}[\hat{V}(t)\hat{W}(0)\sqrt{\rho_0}\hat{V}(t)\hat{W}(0)\sqrt{\rho_0}]. \quad (\text{A.31b})$$

and differ in the placement of fractions of initial density matrices  $\rho_0$ . Using the notation introduced in Sec. 2.4, the interloop Keldysh components are given by

$$C_{\sigma s', \bar{\sigma} s}(t', t) = -i\langle \varphi^{\sigma s'}(t') \bar{\varphi}^{\bar{\sigma} s}(t) \rangle_{\mathcal{K}_0}, \quad (\text{A.32})$$

where  $\sigma = \{u, l\}$  and its complements  $\bar{\sigma}$  denote the loop index and  $s = \{\text{cl}, \text{q}\}$  “classical” or “quantum” field components. The Grassmann or complex fields obey the usual commutation relations  $[\bar{\varphi}(t), \varphi(t')]_{\zeta} = \bar{\varphi}(t)\varphi(t') + \zeta\varphi(t')\bar{\varphi}(t) = \delta(t - t')$  depending on their fermionic ( $\zeta = 1$ ) or bosonic ( $\zeta = -1$ ) character. As the two fields reside, per definition, on different loops, the retarded and advanced components are zero because the notion of (anti)time-ordered correlators (see e.g. Ref. Kamenev (2011)) does not exist. Instead, the Keldysh component is given by

$$C_{ul}^K(t', t) = 2C^<(t', t) \quad \text{and} \quad C_{lu}^K(t', t) = 2C^>(t', t), \quad (\text{A.33})$$

where the greater and lesser interloop components are defined, respectively, by

$$C^<(t', t) = -i\zeta \langle \bar{\varphi}(t')\varphi(t) \rangle_{\mathcal{K}_0} \quad \text{and} \quad C^>(t', t) = -i \langle \varphi(t)\bar{\varphi}(t') \rangle_{\mathcal{K}_0}. \quad (\text{A.34a})$$

Expressed in the operator representation, the correlation functions translate into

$$C_{\gamma}^<(t', t) = -i\zeta \text{tr} \left[ \hat{\varphi}^{\dagger}(t') \rho_0^{\gamma} \hat{\varphi}(t) \rho_0^{1-\gamma} \right] \quad (\text{A.35a})$$

$$C_{\gamma}^>(t', t) = -i \text{tr} \left[ \hat{\varphi}(t) \rho_0^{\gamma} \hat{\varphi}^{\dagger}(t') \rho_0^{1-\gamma} \right], \quad (\text{A.35b})$$

with Heisenberg operators  $\hat{\varphi}(t) = e^{i\hat{H}t}\hat{\varphi}e^{-i\hat{H}t}$  where Planck’s constant is set to unity,  $\hbar = 1$ . The introduced parameter  $\gamma$  is used to tune between the non-regularized ( $\gamma = 0$ ) and regularized ( $\gamma = \frac{1}{2}$ ) case as introduced in Eq. (A.31). By introducing an full set of

## A. Appendices to Part I

energy eigenstates  $\hat{H}|n\rangle = E_n|n\rangle$ , explicit expression for Eqs. (A.35) are obtained to

$$C_\gamma^>(t, t') = -i \sum_{nl} e^{-(1-\gamma)E_n/k_B T - \gamma E_l/k_B T} e^{-i(E_l - E_n)(t-t')/\hbar} |\langle n|\hat{\varphi}|l\rangle|^2, \quad (\text{A.36a})$$

$$C_\gamma^<(t, t') = i\zeta \sum_{nl} (e^{-(1-\gamma)E_l/k_B T} + e^{-\gamma E_n/k_B T}) e^{-i(E_l - E_n)(t-t')/\hbar} |\langle n|\hat{\varphi}|l\rangle|^2. \quad (\text{A.36b})$$

By Fourier transform and by introducing the usual single-particle spectral density

$$A(\omega) \equiv C^A(\omega) - C^R(\omega) = C_0^> + \zeta C_1^> \quad (\text{A.37a})$$

$$= \frac{2\pi}{\text{tr}[e^{-\hat{H}/k_B T}]} \sum_{nl} \delta(\omega - E_l + E_n) (e^{-E_n/k_B T} + \zeta e^{-E_l/k_B T}) |\langle n|\hat{\varphi}|l\rangle|^2, \quad (\text{A.37b})$$

the interloop Keldysh components are found to

$$C_{ul,\gamma}^K(\omega) = 2i \frac{\zeta e^{\gamma\omega/k_B T}}{e^{\omega/k_B T} + \zeta} A(\omega) \quad \text{and} \quad C_{lu,\gamma}^K(\omega) = -2i \frac{e^{(1-\gamma)\omega/k_B T}}{e^{\omega/k_B T} + \zeta} A(\omega), \quad (\text{A.38a})$$

which yield for the fermionic and bosonic components, respectively, in the non-regularized case ( $\gamma = 0$ ),

$$G_{ul,0}^K(\omega) = \frac{2iA(\omega)}{e^{\omega/k_B T} + 1} = -e^{-\omega/k_B T} G_{lu,0}^K(\omega), \quad (\text{A.39a})$$

$$D_{ul,0}^K(\omega) = -\frac{2iA(\omega)}{e^{\omega/k_B T} - 1} = e^{-\omega/k_B T} D_{lu,0}^K(\omega), \quad (\text{A.39b})$$

and in the regularized case ( $\gamma = \frac{1}{2}$ ),

$$G_{ul,\frac{1}{2}}^K(\omega) = \frac{iA(\omega)}{\cosh\left(\frac{\omega}{2k_B T}\right)} = -G_{lu,\frac{1}{2}}^K(\omega), \quad (\text{A.40a})$$

$$D_{ul,\frac{1}{2}}^K(\omega) = -\frac{iA(\omega)}{\sinh\left(\frac{\omega}{2k_B T}\right)} = D_{lu,\frac{1}{2}}^K(\omega). \quad (\text{A.40b})$$

Hence, the regularized interloop Keldysh components are exponentially small for transferred energies  $|\omega| > k_B T$ . In contrast, the non-regularized components are exponentially small only for  $\omega > k_B T$  or  $\omega > -k_B T$ , otherwise of order of the spectral weight. This suggest that the out-time-order correlator and therefore the scrambling rate does depend on the regularization scheme. Whereas the regularized out-of-time order correlator probes excitations with excitation energies lying in a band of width  $2k_B T$ , the non-regularized out-of-time order correlator probes excitations with excitation energies up to an energy scale determined by  $A(\omega)$ .

## REFERENCES

A. Kamenev, *Field Theory of Non-Equilibrium Systems*, 1st ed. (Cambridge University Press, 2011).

#### A.4. HOMOGENEOUS BETHE-SALPETER EQUATION

In what follows, the expressions constituting the homogeneous part of the Bethe-Salpeter equation (2.42) discussed in Ch. 2 are given explicitly and the largest eigenvalue, which represents the scrambling rate, is determined. This Appendix is an extract of the Appendix of Ref. Klug *et al.* (2018) and is presented here for the sake of completeness..

Generally, it is assumed that the eigenfunctions are rotationally invariant, i.e.  $f = f(\omega; |\mathbf{k}|)$ . Thus, the angle integration over  $\theta_{\mathbf{k}, \mathbf{k}'}$  can be performed analytically mapping the two-dimensional homogeneous integral equation onto a one-dimensional problem. In the following, all momenta are expressed in terms of dimensionless variables, e.g.  $K = \frac{v_F |\mathbf{k}|}{2k_B T}$ . Furthermore, the angle integration is replaced by an auxiliary momentum integration. Hence, the homogeneous integral equation is rewritten to (Klug *et al.*, 2018)

$$\lambda f(\omega, K) = \frac{4}{N} \frac{2\pi k_B T}{\hbar} \int_0^\infty \frac{K' dK'}{2\pi} \mathcal{M}(K, K') f(\omega, K') \quad (\text{A.41})$$

with  $\mathcal{M} = \mathcal{M}_+ + \mathcal{M}_-$  denoting band preserving (+) and band changing (−) scattering processes. The one-rung contributions (superscript (1)) are given by

$$\mathcal{M}_+^{(1)}(K, K') = \frac{2}{KK'} \int_{|K-K'|}^{K+K'} \frac{Q dQ}{2\pi} \frac{\sqrt{(K+K')^2 - Q^2}}{\sqrt{Q^2 - (K-K')^2}} \frac{\text{Im} \mathcal{D}_{ul}^R(|K-K'|, Q)}{\sinh(|K-K'|)}, \quad (\text{A.42a})$$

$$\mathcal{M}_-^{(1)}(K, K') = \frac{2}{KK'} \int_{|K-K'|}^{K+K'} \frac{Q dQ}{2\pi} \frac{\sqrt{Q^2 - (K-K')^2}}{\sqrt{(K+K')^2 - Q^2}} \frac{\text{Im} \mathcal{D}_{ul}^R(K+K', Q)}{\sinh(K+K')}, \quad (\text{A.42b})$$

where the dimensionless imaginary part of the bosonic propagator dressed by particle-hole fluctuations is given by

$$\text{Im} \mathcal{D}_{ul}^R(x, y) = \frac{(\frac{\alpha}{2})^2 \mathcal{I}_F(x, y)}{[y + \frac{\alpha}{2} \mathcal{I}_G(x, y)]^2 + [\frac{\alpha}{2} \mathcal{I}_F(x, y)]^2}. \quad (\text{A.43})$$

The dimensionless functions  $\mathcal{I}_F$  and  $\mathcal{I}_G$  are defined via the real and imaginary part of the electronic polarization operator at finite temperatures whose derivation is standard (e.g. see Ref. Schütt *et al.* (2011)),  $\text{Im} \Pi^R(\omega, \mathbf{q}) = \frac{k_B T}{2\pi} \mathcal{I}_F(\frac{\omega}{2k_B T}, \frac{v_F |\mathbf{q}|}{2k_B T})$  and  $\text{Re} \Pi^R(\omega, \mathbf{q}) = \frac{k_B T}{2\pi} \mathcal{I}_G(\frac{\omega}{2k_B T}, \frac{v_F |\mathbf{q}|}{2k_B T})$ , respectively. Their explicit expressions are

$$\mathcal{I}_F(x, y) = \frac{\sinh x}{\sqrt{|x^2 - y^2|}} \begin{cases} \int_y^\infty d\xi \frac{\sqrt{\xi^2 - y^2}}{\cosh x + \cosh \xi} & \text{for } y > |x| \\ \int_0^y d\eta \frac{\sqrt{y^2 - \eta^2}}{\cosh x + \cosh \eta} & \text{for } |x| > y \end{cases}, \quad (\text{A.44a})$$

$$\mathcal{I}_G(x, y) = -\frac{2}{\pi} \int_y^\infty d\xi \int_0^y d\eta \left( \frac{\sqrt{\xi^2 - y^2}}{\sqrt{y^2 - \eta^2}} \frac{\eta}{x^2 - \eta^2} \frac{\sinh \eta}{\cosh \eta + \cosh \xi} + \frac{\sqrt{y^2 - \eta^2}}{\sqrt{\xi^2 - y^2}} \frac{\xi}{x^2 - \xi^2} \frac{\sinh \xi}{\cosh \eta + \cosh \xi} \right). \quad (\text{A.44b})$$

## A. Appendices to Part I

The two-rung contributions (superscript (2)) are given by

$$\begin{aligned} \mathcal{M}_+^{(2)}(K, K') &= \frac{4\pi}{KK'} \int \frac{\tilde{K} d\tilde{K}}{2\pi} \\ &\times \left( \int_{\max[|K-\tilde{K}|+K, |K'-\tilde{K}|+K']}^{\min[2K+\tilde{K}, 2K'+\tilde{K}]} \frac{dQ}{2\pi} \sqrt{\frac{\tilde{K}^2-(2K-Q)^2}{Q^2-\tilde{K}^2}} \sqrt{\frac{\tilde{K}^2-(2K'-Q)^2}{Q^2-\tilde{K}^2}} \frac{|\mathcal{D}(Q, \tilde{K})|^2}{\cosh(K-Q) \cosh(K'-Q)} \right. \\ &\left. + \int_{\max[|K-\tilde{K}|-K, |K'-\tilde{K}|-K']}^{\tilde{K}} \frac{dQ}{2\pi} \sqrt{\frac{(2K+Q)^2-\tilde{K}^2}{\tilde{K}^2-Q^2}} \sqrt{\frac{(2K'+Q)^2-\tilde{K}^2}{\tilde{K}^2-Q^2}} \frac{|\mathcal{D}(Q, \tilde{K})|^2}{\cosh(K+Q) \cosh(K'+Q)} \right) \end{aligned} \quad (\text{A.45})$$

and

$$\begin{aligned} \mathcal{M}_-^{(2)}(K, K') &= \frac{4\pi}{KK'} \int \frac{\tilde{K} d\tilde{K}}{2\pi} \\ &\times \int_{\min[|K-\tilde{K}|-K, K'-|K'-\tilde{K}|]}^{\tilde{K}} \frac{dQ}{2\pi} \sqrt{\frac{(2K+Q)^2-\tilde{K}^2}{\tilde{K}^2-Q^2}} \sqrt{\frac{(2K'-Q)^2-\tilde{K}^2}{\tilde{K}^2-Q^2}} \frac{|\mathcal{D}(Q, \tilde{K})|^2}{\cosh(K+Q) \cosh(K'-Q)}, \end{aligned} \quad (\text{A.46})$$

where

$$|\mathcal{D}(x, y)|^2 = \frac{\left(\frac{\alpha}{2}\right)^2}{\left[y + \frac{\alpha}{2}\mathcal{I}_G(x, y)\right]^2 + \left[\frac{\alpha}{2}\mathcal{I}_F(x, y)\right]^2}. \quad (\text{A.47})$$

For strong couplings  $\alpha \gg 1$ , the bosonic propagators are given by  $\text{Im}\mathcal{D}_{ul}^R(x, y)|_{\alpha \gg 1} = \frac{\mathcal{I}_F(x, y)}{\mathcal{I}_G^2(x, y)^2 + \mathcal{I}_F^2(x, y)^2}$  and  $|\mathcal{D}(Q, \tilde{K})|^2|_{\alpha \gg 1} = [\mathcal{I}_G^2(x, y) + \mathcal{I}_F^2(x, y)]^{-1}$  and are independent of the coupling strength  $\alpha$ . Thus for strong couplings, the  $\alpha$ -dependence of the integrands drop out completely and the scrambling rate is independent of  $\alpha$ . In contrast for weak couplings, the  $\alpha$ -dependence of the integrands is subtle and needs special consideration as discussed in Sec. 2.6.

The homogeneous integral equation (A.41) is solved numerically by discretizing the area of momentum integration. A homogeneous grid with up to  $2^9 \times 2^9$  grid points in  $K \times K'$ -space is used to diagonalize the obtained matrix. The results are compared to results obtained by solving the integral equation recursively for the one-rung  $\mathcal{M}_+^{(1)}$ -contribution only, where the kernel is evaluated analytically. In this case, the one-dimensional  $K$ -domain is discretized using  $10^4$  grid points. It turns out that this process contributes predominantly to the largest eigenvalue and serves as a lower bound on the scrambling rate for weak couplings.

## REFERENCES

- M. J. Klug, M. S. Scheurer, and J. Schmalian, *Hierarchy of information scrambling, thermalization, and hydrodynamic flow in graphene*, *Phys. Rev. B* **98**, 045102 (2018).
- M. Schütt, P. M. Ostrovsky, I. V. Gornyi, and A. D. Mirlin, *Coulomb interaction in graphene: Relaxation rates and transport*, *Phys. Rev. B* **83**, 155441 (2011).

### A.5. KINETIC EQUATION APPROACH

In this Appendix, a detailed derivation of the kinetic equation governing the dynamics of the out-of-time order correlator and the four-point correlator  $K(\mathbf{R}\mathbf{p}, \mathbf{R}'\mathbf{p}', t)$  introduced in Eq. (3.14) as discussed in Ch. (3) is presented. This Appendix is an extract of the Appendix of Ref. Klug and Syzranov (2019) and is presented here for the sake of completeness.

The presented derivation is similar to the derivation of the conventional kinetic equations for two-point correlation functions (e.g. see Refs. (Mahan, 2000; Kamenev, 2011)), which describe the evolution of single-particle distribution functions. Here, it is extended to four-point correlators, such as  $K(\mathbf{R}\mathbf{p}, \mathbf{R}'\mathbf{p}', t)$ , which determine the dynamics of out-of-time order correlators. The left-hand side of the kinetic equation Eq. (3.17) represents its kinetic part and describes the evolution of the correlator in the presence of the impurity potential  $U_{\text{imp}}$ . The right-hand side is given by the collision integral  $I_{\text{ph}}[K]$  and accounts for the effect of electron-phonon scattering.

The sequence of operators entering the correlation function  $K(\mathbf{R}\mathbf{p}, \mathbf{R}'\mathbf{p}', t)$  is not time ordered and its evaluation therefore requires the augmented Keldysh formalism introduced in Sec. 2.4. The two-loop Keldysh contour used in the following is depicted in Fig. A.2. The kinetic equation is determined for the operator averages

$$M_{(a,b),c}^{(\alpha,\beta),\gamma}(1, 2; 1', 2') = -\langle \hat{P}_z^c(0) \hat{\psi}^{\dagger b}(2') \hat{\psi}^a(1') \hat{P}_z^\gamma(0) \hat{\psi}^{\dagger\beta}(2) \hat{\psi}^\alpha(1) \rangle \quad (\text{A.48})$$

of single-particle operators placed on the four-branch Keldysh contour where  $i = (\mathbf{r}_i, t_i)$ . In the calculation below, *greek* letters  $\alpha, \beta, \gamma \in \{+1, -1\}$  are used for operators on the upper branch ( $i = 1$ ) of the Keldysh contour and *latin* letters  $a, b, c \in \{+2, -2\}$  for operators on the lower branch  $i = 2$  (see Fig. A.2). “ $+_i$ ” and “ $-_i$ ” mimic, respectively, propagation forwards and backwards in time on each loop  $i$ . Averages of the form Eq. (A.48) can be evaluated as path integral  $\langle \dots \rangle_{\mathcal{K}} = \int \mathcal{D}(\bar{\psi}, \psi, \phi) \dots e^{iS_{\mathcal{K}}}$  on the two-loop Keldysh contour, where  $\psi, \bar{\psi}$  are the Grassmann fields representing the electronic degrees of freedom and  $\phi$  are real-valued fields representing the bosons (phonons) degrees of freedom with the augmented Keldysh action  $S_{\mathcal{K}}$  as introduced in Sec. 2.4. To distinguish between different ways to order a pair of fermionic fields  $\psi$  and  $\bar{\psi}$  on each loop  $i$  in the correlator Eq. (A.48),

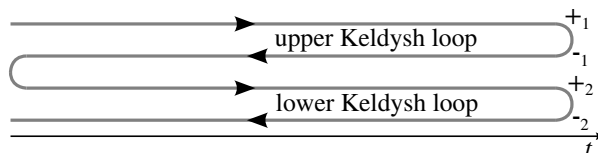


**Figure A.2.:** Two-loop Keldysh contour introduced in Sec. 2.4 used to compute out-of-time-order correlators. Branches marked with  $+_i$  and  $-_i$  mimic propagation forwards and backwards in time on each loop ( $i = 1$  and  $i = 2$ ) of the Keldysh contour. Reprinted figure with permission from [M.J. Klug, and S.V. Syzranov, Phys. Rev. B 100, 094304] Copyright (2019) by the American Physical Society. The original work is found under <https://dx.doi.org/10.1103/PhysRevB.100.094304>.



## A. Appendices to Part I

$$\begin{aligned}
M_{(a,b),c}^{(\alpha,\beta),\gamma}(1,2;1',2') &= M_{(a,b),c;0}^{(\alpha,\beta),\gamma}(1,2;1',2') \\
&+ g_{\text{el-ph}}^2 \left[ \sum_{\delta} \int_3 \Gamma^{(\alpha,\delta)}(3,2) M_{(a,b),c}^{(\delta,\beta),\gamma}(1,3;1',2') + i \sum_{\delta\epsilon} \delta\epsilon \int_{34} G^{(\alpha,\delta)}(1,3) D^{(\delta,\epsilon)}(3,4) G^{(\epsilon,\beta)}(4,2) M_{(a,b),c}^{(\delta,\epsilon),\gamma}(3,4;1',2') \right. \\
&+ \sum_d \int_3 \Gamma^{(a,d)}(3',2') M_{(d,b),c}^{(\alpha,\beta),\gamma}(1,2;1',3') + i \sum_{de} de \int_{34} G^{(a,d)}(1,3) D^{(d,e)}(3,4) G^{(e,b)}(4,2) M_{(d,e),c}^{(\alpha,\beta),\gamma}(1,2;3,4) \\
&\left. + i \sum_{\gamma c} d\delta \int_{33'} D'^{(\delta,d)}(3,3') G^{(d,b)}(3',2') G^{(\delta,\beta)}(3,2) M_{(a,d),c}^{(\alpha,\delta),\gamma}(1,3;1',3') \right]. \tag{A.54}
\end{aligned}$$

In contrast to fermionic propagators, bosonic propagators may be both intra- and inter-loop, i.e. with mixed greek and latin indices. As discussed in Sec. (2.4), there are only two distinct types of inter-loop bosonic propagators:  $D^{(\alpha,+2)} = D^{(\alpha,-2)} = D^{(\alpha,a)} \equiv D_I^<$  and  $D^{(a,\alpha)} \equiv D_I^>$ . Whereas these correlators enter the fourth line denoting scattering processes between the two Keldysh loops only, the second and third line of Eqs. (A.50) and (A.54) represent electron-phonon scattering processes acting within one Keldysh loop, respectively,

When introducing the Wigner transform of the four-point correlators with the center-of-mass coordinates  $t^{(l)} = \frac{t_1^{(l)} + t_2^{(l)}}{2}$  and  $\mathbf{R}^{(l)} = \frac{\mathbf{r}_1^{(l)} + \mathbf{r}_2^{(l)}}{2}$  and coordinate differences  $\tau^{(l)} = t_1^{(l)} - t_2^{(l)}$  and  $\mathbf{r}^{(l)} = \mathbf{r}_1^{(l)} - \mathbf{r}_2^{(l)}$ , intra-loop and the inter-loop processes on the two-loop contour in Fig. A.2 correspond to local processes, i.e. processes close to the locations  $\mathbf{R}$  or  $\mathbf{R}'$ , respectively, and to non-local processes which induce correlations between electrons at locations  $\mathbf{R}$  and  $\mathbf{R}'$ , as shown in Fig. A.3.

In the previous sections, self-energy contributions to four-point correlation functions Eq. (A.48) in form of Dyson equations were derived. Based on these equations, a kinetic equation for the four-point correlator  $K$  similarly to the derivation of the conventional kinetic equation for the distribution function  $f$  (see, e.g., Ref. Mahan (2000)) is derived. For this, the single-particle operator  $i\partial_t - \epsilon_{\hat{\mathbf{k}}} - U_{\text{imp}}(\mathbf{r})$  is acted on the Dyson equations (A.50) and (A.54), respectively, and the definition of the single-particle Green's function,  $[i\partial_{t_1} - \epsilon_{\hat{\mathbf{k}}_1} - U_{\text{imp}}(\mathbf{r}_1) - \Sigma^{a,b}(1,2)]G^{(a,b)}(1,2) = \mathbf{b} \delta(1-2) \delta_{a,b}$ , is used to simplify the result. By *subtracting* the obtained expressions and using  $M_{<}^R = M_{<}^T - M_{<}^>$  and  $M_R^< = M_T^< - M_{<}^>$  while introducing the Wigner representation of the correlator  $M$  (and, similarly,  $K$ ) at

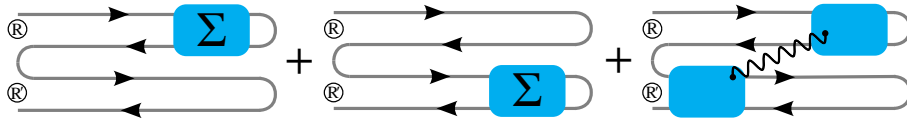


**Figure A.3.:** Leading-order interaction processes which contribute to self-energy corrections of the four-point correlators (A.48) used to determine the Dyson equations (A.50) and (A.54). The first two diagrams describe conventional self-energy contribution at location  $\mathbf{R}$  or  $\mathbf{R}'$ , respectively. The last diagram describes correlations between electrons at locations  $\mathbf{R}$  and  $\mathbf{R}'$ . Reprinted figure with permission from [M.J. Klug, and S.V. Syzranov, Phys. Rev. **B** 100, 094304] Copyright (2019) by the American Physical Society. The original work is found under <https://dx.doi.org/10.1103/PhysRevB.100.094304>.

## A. Appendices to Part I

coinciding centre-of-mass times  $t = t'$ ,

$$M_{(a,b),c}^{(\alpha,\beta),\gamma}(\mathbf{R}\mathbf{p}\omega, \mathbf{R}'\mathbf{p}'\omega, t) = \int_{\mathbf{r},\tau} \int_{\mathbf{r}',\tau'} e^{i\omega\tau - i\mathbf{p}\mathbf{r} + i\omega'\tau' - i\mathbf{p}'\mathbf{r}'} M_{(a,b),c}^{(\alpha,\beta),\gamma}(\mathbf{R}\mathbf{r}\tau, \mathbf{R}'\mathbf{r}'\tau', t), \quad (\text{A.55})$$

the renormalized retarded components of the correlators in the form

$$M_{<,c}^{R,\gamma}(\mathbf{R}\mathbf{p}\omega, \mathbf{R}'\mathbf{p}'\omega, t) = \frac{\mathcal{A}_{<,c}^{\gamma}(\mathbf{R}'\mathbf{p}'\omega, t)}{\omega - \epsilon_{\mathbf{p}} - \Sigma^R(\mathbf{p}, \omega)}, \quad (\text{A.56a})$$

$$M_{R,c}^{<,\gamma}(\mathbf{R}\mathbf{p}\omega, \mathbf{R}'\mathbf{p}'\omega, t) = \frac{\mathcal{A}_c^{<,\gamma}(\mathbf{R}\mathbf{p}\omega, t)}{\omega' - \epsilon_{\mathbf{p}'} - \Sigma^R(\mathbf{p}', \omega')}, \quad (\text{A.56b})$$

are obtained where  $\mathcal{A}_{(a,b),c}^{\gamma}(1, 2) = -\langle \hat{P}_z^c(0) \bar{\psi}^b(2) \psi^a(1) \hat{P}_z^{\gamma}(0) \rangle_{\mathcal{K}_0}$  and  $\mathcal{A}_c^{(\alpha,\beta),\gamma}(1, 2) = -\langle \hat{P}_z^c(0) \hat{P}_z^{\gamma}(0) \bar{\psi}^{\beta}(2) \psi^{\alpha}(1) \rangle_{\mathcal{K}_0}$ . On the other hand, by *adding* the two expressions, we obtain the quantum kinetic equation

$$iZ^{-1}(\partial_t + i\hat{L}_{\mathbf{R},\mathbf{p}} + i\hat{L}_{\mathbf{R}',\mathbf{p}'})M_{<,c}^{<,\gamma}(\mathbf{R}\mathbf{p}\omega, \mathbf{R}'\mathbf{p}'\omega, t) = I[M] \quad (\text{A.57})$$

where  $i\hat{L}_{\mathbf{R},\mathbf{p}} = \mathbf{v}_{\mathbf{p}} \cdot \nabla_{\mathbf{R}} - \nabla_{\mathbf{R}} U_{\text{imp}}(\mathbf{R}) \cdot \nabla_{\mathbf{p}}$  is the the Liouville operator introduced in Eq. (3.18) in the main text and with the renormalized velocity  $\mathbf{v}_{\mathbf{p}} = Z\nabla_{\mathbf{p}}(\epsilon_{\mathbf{p}} + \Sigma^R(\mathbf{p}, \omega))$ ;  $Z = (1 - \partial_{\omega}\Sigma^R(\mathbf{p}, \omega))^{-1}$  is the quasiparticle weight.  $I[M]$  is the collision integral, which accounts for the relaxation of the correlator due to electron-phonon scattering. In the weak-coupling limit, the renormalization of the quasiparticle parameters is negligible for small coupling, hence,  $\mathbf{v}_{\mathbf{p}} \approx v_F \frac{\mathbf{p}}{|\mathbf{p}|}$  and  $Z \approx 1$ . Furthermore, only leading order terms in the gradients of the center-of-mass coordinates of the correlators were kept when deriving Eqs. (A.56) and (A.57).

The collision integral is split up into three parts,

$$I[M] = I_1[M] + I_2[M] + I_3[M], \quad (\text{A.58})$$

where the first two terms represent local inelastic processes, i.e. occurring at the location  $\mathbf{R}$  or  $\mathbf{R}'$ , and the third term leads to correlations between quasiparticles at the location  $\mathbf{R}$  and those at the location  $\mathbf{R}'$ , as illustrated in Fig. A.3.  $I_1[M]$  involves correlators with external momenta  $\mathbf{p}$  and  $\mathbf{p}'$  and represents the processes of electron scattering from these momentum states to the states with other momenta:

$$\begin{aligned} I_1[M] = & -g_{\text{el-ph}}^2 \{ \Sigma^{<}(\mathbf{p}, \omega) (M_{<,c}^{R,\gamma} - M_{<,c}^{A,\gamma})(\mathbf{R}\mathbf{p}\omega, \mathbf{R}'\mathbf{p}'\omega, t) \\ & + \Sigma^{<}(\mathbf{p}', \omega) (M_{R,c}^{<,\gamma} - M_{A,c}^{<,\gamma})(\mathbf{R}\mathbf{p}\omega, \mathbf{R}'\mathbf{p}'\omega, t) \\ & - [(\Sigma^{>} - \Sigma^{<})(\mathbf{p}, \omega) + (\Sigma^{>} - \Sigma^{<})(\mathbf{p}', \omega')] M_{<,c}^{<,\gamma}(\mathbf{R}\mathbf{p}\omega, \mathbf{R}'\mathbf{p}'\omega, t) \}. \end{aligned} \quad (\text{A.59})$$

Conversely,  $I_2[M]$  contains correlators with internal momenta  $\mathbf{q} \neq \mathbf{p}$  (and identically  $\mathbf{q}' \neq$

$\mathbf{p}'$ ). It describes, therefore, processes where electrons scatter into the reference state and is given by

$$\begin{aligned}
 I_2[M] = & ig_{\text{el-ph}}^2 \int_{\mathbf{q}\nu} [D^>(\mathbf{p} - \mathbf{q}, \omega - \nu) G^<(\mathbf{R}\mathbf{p}\omega t) (M_{<,c}^{<,\gamma} + M_{<,c}^{R,\gamma} - M_{<,c}^{A,\gamma})(\mathbf{R}\mathbf{q}\nu, \mathbf{R}'\mathbf{p}'\omega', t) \\
 & - G^>(\mathbf{R}\mathbf{p}\omega t) D^<(\mathbf{p} - \mathbf{q}, \omega - \nu) M_{<,c}^{<,\gamma}(\mathbf{R}\mathbf{q}\nu, \mathbf{R}'\mathbf{p}'\omega', t)] \\
 & + ig^2 \int_{\mathbf{q}\nu} [D^>(\mathbf{p}' - \mathbf{q}, \omega' - \nu) G^<(\mathbf{R}'\mathbf{p}'\omega' t) (M_{<,c}^{<,\gamma} + M_{R,c}^{<,\gamma} - M_{A,c}^{<,\gamma})(\mathbf{R}\mathbf{p}\nu, \mathbf{R}'\mathbf{q}\omega', t) \\
 & - G^>(\mathbf{R}'\mathbf{p}'\omega' t) D^<(\mathbf{p}' - \mathbf{q}, \omega' - \nu) M_{<,c}^{<,\gamma}(\mathbf{R}\mathbf{p}\nu, \mathbf{q}\mathbf{R}'\omega', t)]. \tag{A.60}
 \end{aligned}$$

In contrast to these contributions accounting for the local processes around  $\mathbf{R}$  or  $\mathbf{R}'$ , the contribution  $I_3[M]$  represents processes of quasiparticle scattering between locations  $\mathbf{R}$  and  $\mathbf{R}'$  and vice versa. It is given by

$$\begin{aligned}
 I_3[M] = & ig_{\text{el-ph}}^2 \int_{\mathbf{q}\nu} e^{i\mathbf{q}(\mathbf{R}-\mathbf{R}')} [G^>(\mathbf{R}'\mathbf{p}' - \frac{\mathbf{q}}{2}\omega' - \frac{\nu}{2}t) D_I^<(\mathbf{q}, \nu) M_{<,c}^{<,\gamma}(\mathbf{R}\mathbf{p} - \frac{\mathbf{q}}{2}\omega - \frac{\nu}{2}, \mathbf{R}'\mathbf{p}' + \frac{\mathbf{q}}{2}\omega' + \frac{\nu}{2}, t) \\
 & - G^<(\mathbf{R}'\mathbf{p}' - \frac{\mathbf{q}}{2}\omega' - \frac{\nu}{2}t) D_I^<(\mathbf{q}, \nu) (M_{<,c}^{<,\gamma} + M_{<,c}^{R,\gamma} - M_{<,c}^{A,\gamma})(\mathbf{R}\mathbf{p} - \frac{\mathbf{q}}{2}\omega - \frac{\nu}{2}, \mathbf{R}'\mathbf{p}' + \frac{\mathbf{q}}{2}\omega' + \frac{\nu}{2}, t)] \\
 & + ig^2 \int_{\mathbf{q}\nu} e^{i\mathbf{q}(\mathbf{R}'-\mathbf{R})} [G^>(\mathbf{R}\mathbf{p} - \frac{\mathbf{q}}{2}\omega - \frac{\nu}{2}t) D_I^>(\mathbf{q}, \nu) M_{<,c}^{<,\gamma}(\mathbf{R}\mathbf{p} + \frac{\mathbf{q}}{2}\omega + \frac{\nu}{2}, \mathbf{R}'\mathbf{p}' - \frac{\mathbf{q}}{2}\omega' - \frac{\nu}{2}, t) \\
 & - G^<(\mathbf{R}\mathbf{p} - \frac{\mathbf{q}}{2}\omega - \frac{\nu}{2}t) D_I^>(\mathbf{q}, \nu) (M_{<,c}^{<,\gamma} + M_{R,c}^{<,\gamma} - M_{A,c}^{<,\gamma})(\mathbf{R}\mathbf{p} + \frac{\mathbf{q}}{2}\omega + \frac{\nu}{2}, \mathbf{R}'\mathbf{p}' - \frac{\mathbf{q}}{2}\omega' - \frac{\nu}{2}, t)], \tag{A.61}
 \end{aligned}$$

It is noted that the respective matrix element comes with a phase factor which oscillates rapidly as a function of the separation  $\mathbf{R} - \mathbf{R}'$ . At times  $t \gg t_{\text{ph}}$ , where phonon scattering is effectively short-ranged ( $|\mathbf{R} - \mathbf{R}'| \gg \xi_{\text{ph}}$ ), the contribution  $I_3$  to the collision integral  $I[M]$  is strongly suppressed and, thus, may be neglected.

In this work, electron dynamics in the regime known as the ‘‘quasiparticle regime’’ are considered, where the spectral function  $(G^R - G^A)$ , as well as  $(M_{<,c}^{R,\gamma} - M_{<,c}^{A,\gamma})$  and  $(M_{R,c}^{<,\gamma} - M_{A,c}^{<,\gamma})$ , see Eqs. (A.56), are sharply peaked at  $\omega \approx \epsilon_{\mathbf{p}}$  and contain a negligible incoherent background (Wölfle, 2018). It is therefore reasonable to describe the propagation of quasiparticles by the distribution function  $f(\mathbf{R}\mathbf{p}t) = -i \int_{\omega} G^<(\mathbf{R}\mathbf{p}\omega t)$ . Similarly, four-point out-of-time-order correlators are characterized conveniently by the function

$$K(\mathbf{R}\mathbf{p}, \mathbf{R}'\mathbf{p}', t) = - \sum_{c,\gamma=\pm} c_{\gamma} \int_{\omega\omega'} M_{<,c}^{<,\gamma}(\mathbf{R}\mathbf{p}\omega t, \mathbf{R}'\mathbf{p}'\omega' t) \tag{A.62}$$

introduced in Eq. (3.15). Thus, the collision integral contains also dynamical quasiparticle distribution functions  $f$  whose dynamics are governed by the conventional kinetic equation (Mahan, 2000; Kamenev, 2011). For practical applications, the distribution functions are expanded in small deviations from equilibrium,  $f(\mathbf{R}\mathbf{p}t) = f_0(\epsilon_{\mathbf{p}}) + g(\mathbf{R}\mathbf{p}t)$

## A. Appendices to Part I

with the Fermi distribution  $f_0(\omega) = [\exp(\omega/T) + 1]^{-1}$ , which takes into account that  $K(\mathbf{R}\mathbf{p}, \mathbf{R}'\mathbf{p}', t)$  vanishes in equilibrium. Eventually, this gives rise to the kinetic equation

$$\begin{aligned} (\partial_t + i\hat{L}_{\mathbf{R},\mathbf{p}} + i\hat{L}_{\mathbf{R}',\mathbf{p}'})K(\mathbf{R}\mathbf{p}, \mathbf{R}'\mathbf{p}', t) = & - \int_{\mathbf{q}} (\Gamma_{\mathbf{p}\rightarrow\mathbf{q}} + \Gamma_{\mathbf{p}'\rightarrow\mathbf{q}}) K(\mathbf{R}\mathbf{p}, \mathbf{R}'\mathbf{p}', t) \\ & + \int_{\mathbf{q}} \Gamma_{\mathbf{q}\rightarrow\mathbf{p}} K(\mathbf{R}\mathbf{q}, \mathbf{R}'\mathbf{p}', t) + \int_{\mathbf{q}} \Gamma_{\mathbf{q}\rightarrow\mathbf{p}'} K(\mathbf{R}\mathbf{p}, \mathbf{R}'\mathbf{q}, t), \end{aligned} \quad (\text{A.63})$$

where the scattering rates are given by

$$\Gamma_{\mathbf{p}\rightarrow\mathbf{q}} = ig^2 [D^{<}(\mathbf{p} - \mathbf{q}) f_0(\epsilon_{\mathbf{q}}) + D^{>}(\mathbf{p} - \mathbf{q}) (1 - f_0(\epsilon_{\mathbf{q}}))], \quad (\text{A.64})$$

with the greater and lesser boson propagators  $D^{<,>}(\mathbf{p} - \mathbf{q}) = D^{<,>}(\mathbf{p} - \mathbf{q}, \epsilon_{\mathbf{p}} - \epsilon_{\mathbf{q}})$ .

## REFERENCES

- A. Kamenev, *Field Theory of Non-Equilibrium Systems*, 1st ed. (Cambridge University Press, 2011).
- M. J. Klug and S. V. Syzranov, *Chaos and the dynamics of information in dissipative electronic systems*, *Phys. Rev. B* **100**, 094304 (2019).
- G. D. Mahan, *Many-particle physics*, 3rd ed., Physics of solids and liquids (Kluwer Acad./Plenum Publ., New York, NY, 2000).
- P. Wölfle, *Quasiparticles in condensed matter systems*, *Rep. Prog. Phys.* **81**, 032501 (2018).

### B.1. MOIRÉ BAND STRUCTURE

In the following, the electronic moiré band structure is obtained by considering a continuum model presented in Refs. [Bistritzer and MacDonald \(2011\)](#); [Weckbecker \*et al.\* \(2016\)](#), which assumes an approximate translational and point group symmetry of the superlattice as discussed in [Sec. 5.1](#), and is specified, apart from the properties inherited from the single-layer graphene systems such as the lattice constant  $a$  and Fermi velocity  $v_F$ , by the twist-angle  $\theta$  and the transition amplitude  $t_\perp$ . It is noted that this approach is applicable for commensurate and incommensurate but small twist-angles and is independent of the exact position of the center of rotation. An illustration of the single-layer graphene Brillouin zones and the emerging moiré Brillouin zone is depicted in [Fig. 5.1a](#).

Within this approach, electronic states of the two single-layer graphene systems with ultrarelativistic spectrum close to charge neutrality are considered. The characteristic Dirac cones are here centered at two, non-equivalent  $K$ -points of the hexagonal Brillouin zone. Because of their large separation in momentum space, states close to these “valleys” are assumed decoupled introducing an additional single-particle valley quantum number  $\xi = \pm$ .

The Hamilton operator describing Dirac electrons while neglecting spin orbit coupling is introduced as ([Castro Neto \*et al.\*, 2009](#))

$$H_0 = -v_F \sum_{\mathbf{k}\xi} \hat{\psi}_{\mathbf{k}\xi}^\dagger [\vec{\sigma} \cdot (\mathbf{k} - \mathbf{K}_\xi)] \hat{\psi}_{\mathbf{k}\xi}, \quad (\text{B.1})$$

with the two component operator  $\hat{\psi}_{\mathbf{k}\xi} = (\hat{\psi}_{\mathbf{k}\xi}^{(A)}, \hat{\psi}_{\mathbf{k}\xi}^{(B)})^T$  representing states assigned to the crystalline basis sites  $A$  and  $B$ , respectively, and possessing definite valley number. The Pauli matrices  $\boldsymbol{\sigma}_\xi = (\xi\sigma_x, \sigma_y)^T$  act in the crystalline basis space. The position of the considered Dirac cone is parametrized by  $\mathbf{K}_\xi$ , whereas the summation over crystal momenta is cut-off by  $|\mathbf{k} - \mathbf{K}_\xi| \leq \Lambda$ . The electron spin as well as the chemical potential is irrelevant to the present discussion and suppressed for the matter of representation.

The twisted bilayer system is obtained by rotating the two graphene systems, each one described by [Eq. \(B.1\)](#), and allowing for tunneling processes between them. The composite system is therefore described by

B. Appendices to Part II

$$\hat{H}_{\text{TBG}} = \hat{H}_{\theta/2} + \hat{H}_{-\theta/2} + \hat{H}_T, \quad (\text{B.2})$$

where  $\hat{H}_{\theta/2}^{(\text{I})}$  and  $\hat{H}_{-\theta/2}^{(\text{II})}$  represent the rotated graphene layers I and II with angles of rotations  $\pm\theta/2$ , respectively, and  $\hat{H}_T$  the interlayer tunneling operator. Rotation is performed by introducing the two-dimensional rotation matrix  $\mathcal{R}_\varphi$  with the angle of rotation  $\varphi$  and the axis of rotation pointing out-of-plane, yielding

$$\hat{H}_{\theta/2}^{(\text{I})} = -v_F \sum_{\mathbf{k}\xi} \hat{\psi}_{\mathbf{k}\xi}^{(\text{I})\dagger} [\vec{\sigma} \cdot \mathcal{R}_{\theta/2}^{-1}(\mathbf{k} - \mathcal{R}_{\theta/2}\mathbf{K}_\xi)] \hat{\psi}_{\mathbf{k}\xi}^{(\text{I})}, \quad (\text{B.3})$$

and  $\hat{H}_{-\theta/2}^{(\text{II})}$  accordingly.

$\hat{H}_T$  represents interlayer tunneling processes which couple states of different layers. Because of the large separation in momentum space, states  $\hat{\psi}_{\mathbf{k}\xi}^{(\text{I})}$  and  $\hat{\psi}_{\mathbf{k}'\xi'}^{(\text{II})}$  with  $\xi \neq \xi'$  are approximately decoupled for small angles (Bistritzer and MacDonald, 2011) and  $\hat{H}_T$  is therefore considered diagonal in the valley index. In the following, tunneling is considered a local process which suggests a real space representation of the respective matrix elements. The tunneling processes is introduced as

$$\hat{H}_{T,\xi} = \int d\mathbf{r}d\mathbf{r}' [\langle \mathbf{r} | \hat{t} | \mathbf{r}' \rangle \hat{\Psi}_\xi^{(1)\dagger}(\mathbf{r}) \hat{\Psi}_\xi^{(2)}(\mathbf{r}') + \text{h.c.}], \quad (\text{B.4})$$

with the field operator  $\hat{\Psi}_\xi^{(n)}(\mathbf{r}) = \sum_{i\alpha} \phi(\mathbf{r} - \mathbf{a}_i^{(n)} - \mathbf{u}_\alpha^{(n)}) \hat{\psi}_{i\alpha\xi}^{(n)}$  of single-layer graphene states with the layer index  $n$ , the unit cell index  $i$  and the crystalline basis index  $\alpha$ .  $\mathbf{a}_i^{(n)}$  denotes the lattice and  $\mathbf{u}_\alpha^{(n)}$  the crystalline basis vector of the  $n$ th-layer, whereas  $\phi(\mathbf{r})$  represents the wave function of the localized  $p_z$ -orbitals (Castro Neto *et al.*, 2009). The single-particle Wannier state is connected to the previously introduced Bloch states Eq. (B.3) by

$$\hat{\psi}_{\alpha i}^{(n)} = \frac{1}{\sqrt{N}} \sum_{\mathbf{k}} e^{-i\mathbf{k}(\mathbf{a}_i^{(n)} + \mathbf{u}_\alpha^{(n)})} \hat{\psi}_{\mathbf{k}\xi}^{(n,\alpha)}, \quad (\text{B.5})$$

with the number of graphene unit cells  $N$ . The tunneling matrix element  $t(|\mathbf{r} - \mathbf{r}'|) = \langle \mathbf{r} | \hat{t} | \mathbf{r}' \rangle$  associated with the tunneling operator  $\hat{t}$  is considered short-ranged and assumed to decay fast on length scales  $l_t$ .

In a next step, the tunneling operator Eq. (B.4) is expressed in terms of single-layer graphene Bloch states constituting the basis of  $\hat{H}_{\theta/2}$  and  $\hat{H}_{-\theta/2}$  using Eq. (B.5). One obtains as a result

$$\hat{H}_{T,\xi} = \frac{N}{V} \sum_m \sum_{\mathbf{k}\mathbf{k}'} \delta_{\mathbf{k} + \mathbf{G}_m, \mathbf{k}'} t(|\mathbf{k} - \mathbf{b}_m^{(\text{I})}|) \left[ \hat{\psi}_{\mathbf{k}\xi}^{(\text{I})\dagger} \begin{pmatrix} 1 & e^{-i\frac{2\pi}{3}(m_1+m_2)} \\ e^{i\frac{2\pi}{3}(m_1+m_2)} & 1 \end{pmatrix} \hat{\psi}_{\mathbf{k}'\xi}^{(\text{II})} + \text{h.c.} \right] \quad (\text{B.6})$$

with  $m_i \in \mathbb{Z}$  and where the Fourier transform of the tunneling matrix element was introduced to  $t(|\mathbf{r}|) = \int \frac{d^2q}{(2\pi)^2} e^{-i\mathbf{q}\mathbf{r}} t(|\mathbf{q}|)$  with  $t(q)$  decaying rapidly for  $q \gg 1/l_t$ . The reciprocal superlattice vector of the bilayer system  $\mathbf{G}_m = m_1\mathbf{G}_1 + m_2\mathbf{G}_2$  arises naturally with basis

## B. Appendices to Part II

vectors

$$\mathbf{G}_1 = \mathbf{b}_1^{(\text{II})} - \mathbf{b}_1^{(\text{I})}, \quad (\text{B.7a})$$

$$\mathbf{G}_2 = \mathbf{b}_2^{(\text{II})} - \mathbf{b}_2^{(\text{I})}, \quad (\text{B.7b})$$

where  $\mathbf{b}_1^{(n)}$  and  $\mathbf{b}_2^{(n)}$  represent the basis reciprocal lattice vectors of the  $n$ th layer taking the backfolding of electronic states into the reduced moiré Brillouin zone as illustrated in Fig. 5.1a into account.

Eq. (B.6) is further simplified by restricting the crystal momenta to the vicinity of the two rotated  $K$ -points of the graphene Brillouin zones, i.e.  $\mathbf{k} \approx \mathbf{k}' \approx \mathcal{R}_{\theta/2}\mathbf{K}_\xi \approx \mathcal{R}_{-\theta/2}\mathbf{K}_\xi$ . For  $m \neq 0$ , the electron has to scatter to another equivalent  $K$ -point, otherwise  $t(|\mathbf{k} - \mathbf{b}_m|)$  is small. Hence, there are in total three terms per  $\mathbf{k}$ -value, which contribute. One may also investigate processes which represent tunneling between non-equivalent  $K$ -points: As  $G_m$  must be large to connect  $\mathbf{K}_\xi$  and  $\mathbf{K}_{-\xi}$ ,  $t(|\mathbf{K}_\xi - \mathbf{b}_m^{(\text{I})}|) \ll t(|\mathbf{K}_\xi|)$  and these are safely neglected. Eventually, by approximating the tunneling matrix element for the typical momentum transfer by a constants,  $t(|\mathbf{k}|)|_{\mathbf{k} \approx \mathbf{K}_\xi} = t_\perp$ , the tunneling operator is given by

$$\hat{H}_{T,\xi} = \sum_{\mathbf{k}\mathbf{k}'} \left( \hat{\psi}_{\mathbf{k}\xi}^{(\text{I})\dagger} [\tilde{t}\delta_{\mathbf{k}-\xi\mathbf{G}_1,\mathbf{k}'} + \hat{t}\delta_{\mathbf{k},\mathbf{k}'} + \bar{t}\delta_{\mathbf{k}-\xi\mathbf{G}_1-\xi\mathbf{G}_2,\mathbf{k}'}] \hat{\psi}_{\mathbf{k}'\xi}^{(\text{II})} + \text{h.c.} \right), \quad (\text{B.8})$$

where the matrices in two-dimensional basis space are given by

$$\tilde{t} = t_\perp \begin{pmatrix} 1 & 1 \\ 1 & 1 \end{pmatrix}, \quad \hat{t} = t_\perp \begin{pmatrix} 1 & e^{i\xi\frac{2\pi}{3}} \\ e^{-i\xi\frac{2\pi}{3}} & 1 \end{pmatrix}, \quad \bar{t} = t_\perp \begin{pmatrix} 1 & e^{-i\xi\frac{2\pi}{3}} \\ e^{i\xi\frac{2\pi}{3}} & 1 \end{pmatrix}. \quad (\text{B.9})$$

Phenomenologically, it is also possible to consider lattice relaxation effects rendering the tunneling processes between sublattice sites of the same type (e.g.  $A \leftrightarrow A$ ) and different type ( $B \leftrightarrow A$ ) distinct. As the BA-stacking of lattice site is energetically favorable (Castro Neto *et al.*, 2009) and the distance between layers in BA-regions hence smaller, one may introduce  $t_{\perp,AA} < t_{\perp,AB}$  such that

$$\tilde{t} = \begin{pmatrix} t_{\perp,AA} & t_{\perp,AB} \\ t_{\perp,AB} & t_{\perp,AA} \end{pmatrix}, \quad \hat{t} = \begin{pmatrix} t_{\perp,AA} & t_{\perp,AB}e^{i\xi\frac{2\pi}{3}} \\ t_{\perp,AB}e^{-i\xi\frac{2\pi}{3}} & t_{\perp,AA} \end{pmatrix}, \quad \bar{t} = \begin{pmatrix} t_{\perp,AA} & t_{\perp,AB}e^{-i\xi\frac{2\pi}{3}} \\ t_{\perp,AB}e^{i\xi\frac{2\pi}{3}} & t_{\perp,AA} \end{pmatrix}, \quad (\text{B.10})$$

which enhances the band gaps between the moiré bands at charge neutrality and the continuum of bands at higher and lower energies (Koshino *et al.*, 2018).

The moiré bands are obtained by diagonalizing the Hamilton operator Eq. (B.2) and are identified as bands around charge neutrality. In principal, one reference state  $\mathbf{k}$  is coupled indirectly to (infinitely) many other states. However, as states with higher energy contribute less in the formation of moiré bands located at charge neutrality, the determined energies converge rapidly and the coupling  $t_\perp$  is set to zero when the cut-off  $\Lambda$  is reached.

As parameters, the Fermi velocity is chosen to  $v_F\hbar/a = 2.1354\text{eV}$ , whereas the interlayer

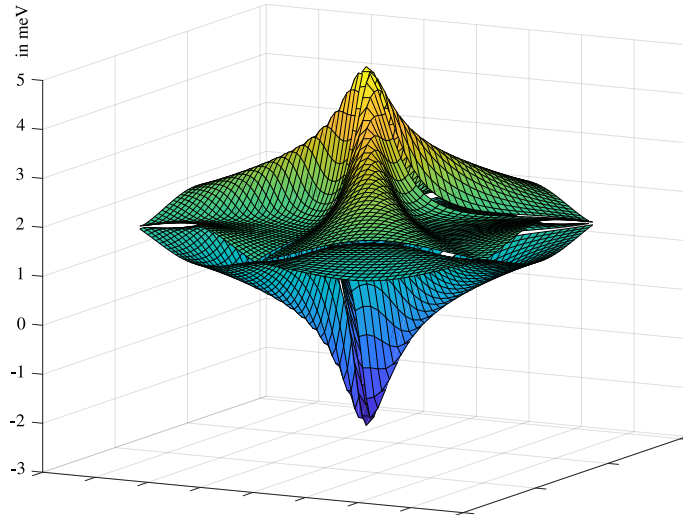


**Figure B.1.:** Moiré band structure in the moiré Brillouin zone for  $\xi = 1$  for the twist-angle  $\theta = 1.05$ .

tunneling amplitudes, which discriminate between intra- and inter-sublattice processes, to  $t_{\perp,AA} = t_{\perp,BB} = 79.7\text{meV}$  and  $t_{\perp,AB} = 97.5\text{meV}$  (Koshino *et al.*, 2018). The moiré bands in the hexagonal moiré Brillouin zone are plotted for  $\xi = 1$  in Fig. B.1, and are depicted as cuts along the high symmetry lines in Fig. 5.2.

## REFERENCES

- R. Bistritzer and A. H. MacDonald, *Moiré bands in twisted double-layer graphene*, *Proc. Natl. Acad. Sci.* **108**, 12233 (2011).
- A. H. Castro Neto, F. Guinea, N. M. R. Peres, K. S. Novoselov, and A. K. Geim, *The electronic properties of graphene*, *Rev. Mod. Phys.* **81**, 109 (2009).
- M. Koshino, N. F. Q. Yuan, T. Koretsune, M. Ochi, K. Kuroki, and L. Fu, *Maximally localized wannier orbitals and the extended hubbard model for twisted bilayer graphene*, *Phys. Rev. X* **8**, 031087 (2018).
- D. Weckbecker, S. Shallcross, M. Fleischmann, N. Ray, S. Sharma, and O. Pankratov, *Low-energy theory for the graphene twist bilayer*, *Phys. Rev. B* **93**, 035452 (2016).

## B.2. CONSTRUCTION OF THE WANNIER BASIS

The Wannier basis is constructed following the method of maximally localized Wannier functions (Marzari and Vanderbilt, 1997; Marzari *et al.*, 2012). In the case of twisted bilayer graphene, two orbitals centered at the AB- and BA-stacked regions of the superlattice are assumed which possess a definite valley quantum number as discussed in Sec. 5.3 and following the approach presented in Ref. (Koshino *et al.*, 2018). The indices for valley  $\xi$  and spin  $\sigma$  quantum numbers are dropped from the subsequent analysis because of the presence of corresponding symmetries as discussed in Sec. 5.1. The Wannier functions of the different valleys are connected by complex conjugation as they are connected by a mirror symmetry operation (Po *et al.*, 2018). This Appendix is an extract of the Appendix of Ref. Klug (2020) and is presented here for the sake of completeness.

The Bloch functions introduced in the construction of the moiré band structure presented in the Appendix B.1 are represented in real space by

$$\psi_{\lambda\mathbf{k}}(\mathbf{r}) = \psi_{\lambda\mathbf{k}}^{(I,A)}(\mathbf{r}) + \psi_{\lambda\mathbf{k}}^{(I,B)}(\mathbf{r}) + \psi_{\lambda\mathbf{k}}^{(II,A)}(\mathbf{r}) + \psi_{\lambda\mathbf{k}}^{(II,B)}(\mathbf{r}), \quad (\text{B.11})$$

with the crystal momentum  $\mathbf{k}$  which is an element of the moiré Brillouin zone. Their projection on the single-layer graphene layer  $j \in \{I, II\}$  and sublattice  $\gamma \in \{A, B\}$  is given by

$$\psi_{\lambda\mathbf{k}}^{(j,\gamma)}(\mathbf{r}) = \frac{1}{\sqrt{N}} \sum_{im} U_{jm}^{(\lambda)}(\mathbf{k}) e^{i(\mathbf{k} + \mathbf{G}_m) \cdot \mathbf{a}_i^{(j)}} \phi(\mathbf{r} - \mathbf{a}_i^{(j)} - \mathbf{u}_\gamma^{(j)}), \quad (\text{B.12})$$

where the unitary matrix  $U_{jm}^{(\lambda)}$  connects the microscopic two-layer graphene tight-binding basis and the moiré Bloch basis and was obtained in the construction of the moiré band structure by diagonalizing the Hamilton operator Eq. (B.2).  $\mathbf{G}_m$  denotes a reciprocal superlattice vector, and  $\mathbf{a}_i^{(j)}$  and  $\mathbf{u}_\gamma^{(j)}$  the single-layer graphene lattice and sublattice vector, respectively.  $\phi(\mathbf{r} - \mathbf{r}_0)$  represents the localized graphene  $p_z$ -orbital represented in real space and centered at  $\mathbf{r}_0$ .

The Wannier function located in the superlattice unit cell  $i$  and centered at the  $\alpha = \text{AB, BA}$ -stacked region is obtained as superposition of moiré Bloch functions Eq. (B.11) and is given by

$$\psi_{i\alpha}(\mathbf{r}) = \frac{1}{\sqrt{N_{SL}}} \sum_{\lambda\mathbf{k}} e^{-i\mathbf{k}\mathbf{A}_i} \mathcal{U}_{\lambda\mathbf{k}}^{(\alpha)} \psi_{\lambda\mathbf{k}}(\mathbf{r}), \quad (\text{B.13})$$

with the superlattice vector  $\mathbf{A}_i$ . The unitary matrix  $\mathcal{U}_{\lambda\mathbf{k}}^{(\alpha)}$  is chosen such that the spread functional

$$g[\mathcal{U}] = \int d^d r \psi_{i\alpha}^*(\mathbf{r}) (\mathbf{r} - \mathbf{r}_{i\alpha})^2 \psi_{i\alpha}(\mathbf{r}) \quad (\text{B.14})$$

is minimal (Marzari and Vanderbilt, 1997; Marzari *et al.*, 2012). Here,  $\mathbf{r}_{i\alpha}$  denotes the coordinate of the center of the Wannier function which is identified with the center of the

## B. Appendices to Part II

AB- or BA-stacked regions of the  $i$ th superlattice unit cell.

To obtain exponentially localized orbitals, the unitary matrix  $\mathcal{U}_{\lambda\mathbf{k}}^{(\alpha)}$  has to be determined in an optimization procedure. A first guess for parameters is obtained by demanding that  $\text{Im}\Psi_{i\alpha}(\mathbf{r}_{i\alpha}) = 0$  such that Bloch function interferes constructively around  $\mathbf{r}_{i\alpha}$ . The obtained orbitals are eventually checked for being exponentially localized. A set of Wannier functions obtained for a specific twist-angle configuration is depicted in Fig. 5.3.

The transition amplitudes entering the effective superlattice tight-binding model Eq. (5.11), which are, by construction, diagonal in valley number, are computed by evaluating

$$t_{i\alpha,j\beta} = \frac{1}{N_{SL}} \sum_{\mathbf{k}\lambda} e^{i\mathbf{k}(\mathbf{A}_i - \mathbf{A}_j)} \mathcal{U}_{\lambda\mathbf{k}}^{(\alpha)\dagger} \epsilon_{\lambda\mathbf{k}} \mathcal{U}_{\lambda\mathbf{k}}^{(\beta)}. \quad (\text{B.15})$$

It is observed that the amplitude of the transition amplitudes drops rather slowly with the distance: To recover the weakly dispersing moiré bands of the effective Hamiltonian introduced in Eq. (5.5), transition amplitudes between orbitals with a spatial separation of more than 10 superlattice unit cells have to be taken into account.

## REFERENCES

- M. J. Klug, *Charge order and mott insulating ground states in small-angle twisted bilayer graphene*, *New J. Phys.* (2020).
- M. Koshino, N. F. Q. Yuan, T. Koretsune, M. Ochi, K. Kuroki, and L. Fu, *Maximally localized wannier orbitals and the extended hubbard model for twisted bilayer graphene*, *Phys. Rev. X* **8**, 031087 (2018).
- N. Marzari and D. Vanderbilt, *Maximally localized generalized wannier functions for composite energy bands*, *Phys. Rev. B* **56**, 12847 (1997).
- N. Marzari, A. A. Mostofi, J. R. Yates, I. Souza, and D. Vanderbilt, *Maximally localized wannier functions: Theory and applications*, *Rev. Mod. Phys.* **84**, 1419 (2012).
- H. C. Po, L. Zou, A. Vishwanath, and T. Senthil, *Origin of mott insulating behavior and superconductivity in twisted bilayer graphene*, *Phys. Rev. X* **8**, 031089 (2018).

### B.3. UNRESTRICTED HARTREE-FOCK ANALYSIS

In this chapter, the unrestricted Hartree-Fock approach used to determine the electronic ground state in the weak-coupling limit Sec. 6.1 is presented. This Appendix is an extract of the Appendix of Ref. Klug (2020) and is presented here for the sake of completeness.

The ground state in the weak-coupling regime is obtained by minimizing an energy functional which derives from the mean field Hamiltonian obtained by applying the decoupling scheme introduced in Eq. (6.1), where the local mean fields are considered as variational parameters. The computation is conducted on a finite lattice of  $30 \times 30$  superlattice unit cells to capture the rather slowly decaying transition amplitudes  $\{t_{ab}\}$ . Mutually independent mean fields are introduced for a lattice of  $6 \times 6$  superlattice unit cells with imposed periodic boundary conditions.

The quadratic mean field Hamiltonian is given by

$$\hat{H}_{\text{MF}} = \sum_{ab} h_{ab,\sigma\sigma'} \hat{\psi}_{a\sigma}^\dagger \hat{\psi}_{b\sigma'}, \quad (\text{B.16})$$

where the mean field Hamiltonian contains the quadratic part of the effective Hamiltonian Eq. (5.11), which describes free moiré electrons, and the mean field terms, which are obtained by employing the mean field decoupling of interaction terms as introduced in Eq. (6.2). Eventually,  $h_{ab,\sigma\sigma'}$  is represented as hermitian  $d \times d$  matrix where  $d$  represents the dimensionality of the Hilbert space (here,  $d = 7200$ ). The energy functional is obtained as the thermal expectation value of the mean field Hamiltonian,

$$E[\langle \hat{\psi}^\dagger \hat{\psi} \rangle] = Z^{-1} \text{tr}[e^{-\hat{H}/k_B T} \hat{H}_{\text{MF}}], \quad (\text{B.17})$$

in the limit of zero temperature,  $T \rightarrow 0$ . To evaluate Eq. (B.17), correlations of type  $\langle \hat{\psi}_{a\sigma}^\dagger \hat{\psi}_{b\sigma'} \rangle$  have to be determined self-consistently. Therefore, the single-particle Green's function is computed first for a given initial mean field configuration by

$$G_{ab,\sigma\sigma'}^{R/A}(\omega) = [\omega - h \pm i0^+]_{ab,\sigma\sigma'}^{-1}. \quad (\text{B.18})$$

Consequently, the resulting correlations are obtained by

$$\langle \hat{\psi}_{a\sigma}^\dagger \hat{\psi}_{b\sigma'} \rangle = i \int_{-\infty}^{\mu} \frac{d\omega}{2\pi} [G_{ab,\sigma\sigma'}^R(\omega) - G_{ab,\sigma\sigma'}^A(\omega)]. \quad (\text{B.19})$$

Determining the inverse of a large matrix is very costly. To overcome this difficulty, the matrix inversion is locally approximated around a reference state  $a\sigma$  employing the Lanczos algorithm (Lanczos, 1950). This procedure is applicable as  $h$  possesses a local structure, i.e. the state  $a$  is locally coupled to only a handful of other states  $b$ . The dimensionality of the Lanczos space  $d_L$  is therefore much smaller than the original Hilbert space dimensionality  $d \gg d_L$  to accurately approximate  $G_{ab,\sigma\sigma'}^{R/A}(\omega)$ . Good results are obtained for  $d_L = 50$ . To approximate  $G_{ab,\sigma\sigma'}^{R/A}(\omega)$ , the Lanczos space is constructed using the reference state  $a\sigma$  as

## B. Appendices to Part II

initial state. The transformation is given by a  $d \times d_L$  unitary matrix  $u$  with  $u_{i1} = \delta_{ia}$ , which is provided by the Lanczos algorithm (Golub and Van Loan, 2013), such that  $\tilde{h} = u^\dagger h u$  represents a tridiagonal hermitian matrix. Because of its tridiagonal form and its reduced rank, the single-particle Green's function in Lanczos space is readily determined exactly to  $\tilde{G}^{R/A}(\omega) = [\omega - \tilde{h} \pm i0^+]^{-1}$  and the single-particle Green's function is eventually given by

$$G_{ab}^{R/A}(\omega) \approx [u \tilde{G}^{R/A}(\omega) u^\dagger]_{ab}. \quad (\text{B.20})$$

The mean fields  $\langle \hat{\psi}_{a\sigma}^\dagger \hat{\psi}_{b\sigma'} \rangle$  which obey Eq. (B.19) are determined recursively, where the stable fixed point coincides with the state with minimal total energy. Hence, a meaningful approximation of the electronic ground state and corresponding ground state energy is obtained.

### REFERENCES

- G. H. Golub and C. F. Van Loan, *Matrix Computations (4th Ed.)* (Johns Hopkins University Press, 2013).
- M. J. Klug, *Charge order and mott insulating ground states in small-angle twisted bilayer graphene*, *New J. Phys.* (2020).
- C. Lanczos, *An iteration method for the solution of the eigenvalue problem of linear differential and integral operators*, *J. Res. Natl. Bur. Stand. B* **45**, 255 (1950).

#### B.4. MEAN FIELD THEORY OF THE CHARGE DENSITY WAVE ORDER

In what follows, the mean field theory of the charge density wave order discussed as ground state candidate of the weak-coupling regime in Sec. 6.1 is specified. This Appendix is an extract of the Appendix of Ref. Klug (2020) and is presented here for the sake of completeness.

The charge order determined within the unrestricted Hartree-Fock approach breaks rotational and translational symmetry specified by the order parameter  $\Delta_{\mathbf{Q}}$  with the ordering vector  $\mathbf{Q}$  given in Eq. (6.4), but preserves spin and valley symmetry. Thus, only direct interaction channels including on-site, nearest neighbor- (NN), next-to-nearest neighbor- (NNN) and next-to-next-to-nearest neighbor (NNNN) interactions as discussed in Sec. 5.4 contribute to a formation of this particular order. In the following, two aspects will be discussed: The effective interaction strength in the charge density wave channel  $U_{\text{CDW}}$  and the corresponding susceptibility  $\chi_{\mathbf{Q}}$ . Both enter the usual criterion for the onset of order in mean field theories (see e.g. Fazekas (1999)),

$$1 + [U_{\text{CDW}}\chi_{\mathbf{Q}}^{(0)}(\mu)]|_{\text{cr}} = 0, \quad (\text{B.21})$$

which determines a critical interaction strength or doping level.

In the interaction part of the effective Hamiltonian Eq. (5.11) only direct channels are considered. It is given by

$$\hat{H}_{\text{int}} = \frac{1}{2} \sum_{\sigma\sigma'} \sum_{abcd \in \mathcal{O}} U_{abcd} \hat{\psi}_{a\sigma}^\dagger \hat{\psi}_{b\sigma'}^\dagger \hat{\psi}_{c\sigma'} \hat{\psi}_{d\sigma}, \quad (\text{B.22})$$

where  $a = (i, \alpha, \xi)$  with the unit cell index  $i$ , the basis index  $\alpha \in \{A, B\}$  the valley index  $\xi \in \{+, -\}$ , and the spin index  $\sigma$  specified the single-particle Wannier state. To determine the effective interaction strength, Eq. (B.22) is expressed in momentum space by using  $\hat{\psi}_{\mathbf{k}\alpha} = \frac{1}{\sqrt{N}} \sum_i e^{i\mathbf{R}_i \cdot \mathbf{k}} \hat{\psi}_{i\alpha}$  with the crystal momentum  $\mathbf{k}$ . In the following, the valley and spin indices are dropped for convenience but restored if necessary. By using  $U_{ab} = \sum_j \delta_{\mathbf{R}_a - \mathbf{R}_b, \mathbf{A}_j^{(i)}}$  where  $\{\mathbf{A}_j^{(i)}\}$  denotes the set of space vectors connecting the interacting lattice sites for density interactions of type  $i \in \{\text{on-site, NN, NNN, NNNN}\}$ , one obtains

$$\hat{H}_{\text{int}}^{(i)} = \frac{U_i}{2N} \sum_{\alpha\beta} \sum_{\mathbf{q}} \gamma_{\alpha\beta}^{(i)}(\mathbf{q}) \hat{\rho}_\alpha(\mathbf{q}) \hat{\rho}_\beta(-\mathbf{q}), \quad (\text{B.23})$$

where the density operator is given by  $\hat{\rho}_\alpha(\mathbf{q}) = \sum_{\xi\sigma} \hat{\rho}_{\alpha\xi\sigma}(\mathbf{q})$  with  $\hat{\rho}_{\alpha\xi\sigma}(\mathbf{q}) = \sum_{\mathbf{k}} \hat{\psi}_{\mathbf{k}+\mathbf{q}\alpha\xi\sigma}^\dagger \hat{\psi}_{\mathbf{k}\alpha\xi\sigma}$ . The vertex function is given by  $\gamma_{\alpha\beta}^{(i)}(\mathbf{q}) = \sum_j e^{i\mathbf{A}_j^{(i)} \cdot \mathbf{q}}$  which obeys  $[\gamma_{\alpha\beta}^{(i)}(\mathbf{q})]^* = \gamma_{\beta\alpha}^{(i)}(\mathbf{q}) = \gamma_{\alpha\beta}^{(i)}(-\mathbf{q})$ . For long-range interaction processes, the vertex functions are determined to

B. Appendices to Part II

$$\gamma_{AB}^{(NN)}(\mathbf{q}) = e^{-i\mathbf{u}_{AB}\mathbf{q}}(1 + e^{i\mathbf{q}\mathbf{A}_1} + e^{i\mathbf{q}\mathbf{A}_2}), \quad (\text{B.24a})$$

$$\gamma_{\alpha\alpha}^{(NNN)}(\mathbf{q}) = 2\{\cos[\mathbf{q}\mathbf{A}_1] + \cos[\mathbf{q}\mathbf{A}_2] + \cos[\mathbf{q}(\mathbf{A}_1 + \mathbf{A}_2)]\}, \quad (\text{B.24b})$$

$$\gamma_{AB}^{(NNNN)}(\mathbf{q}) = e^{-i\mathbf{u}_{AB}\mathbf{q}}[e^{i\mathbf{q}(\mathbf{A}_1+\mathbf{A}_2)} + e^{i\mathbf{q}(\mathbf{A}_1-\mathbf{A}_2)} + e^{-i\mathbf{q}(\mathbf{A}_1-\mathbf{A}_2)}], \quad (\text{B.24c})$$

with Bravais lattice vector  $\mathbf{A}_i$  and basis vector  $\mathbf{u}_{AB}$ , which connects the sublattice sites. For transferred momenta  $\mathbf{Q} \in \{\mathbf{G}_1/2, \mathbf{G}_2/2, (\mathbf{G}_1 + \mathbf{G}_2)/2\}$  and by dropping all other interaction channels, the interaction part reduces to

$$\begin{aligned} \hat{H}_{\text{int}} = \frac{1}{N}U_{\text{on-site}} & \left[ \sum_{\alpha\xi} \hat{\rho}_{\alpha\uparrow\xi}(\mathbf{Q})\hat{\rho}_{\alpha\downarrow\xi}(\mathbf{Q}) + \sum_{\alpha\sigma} \hat{\rho}_{\alpha\sigma+}(\mathbf{Q})\hat{\rho}_{\alpha\sigma-}(\mathbf{Q}) \right] \\ & + \frac{1}{2N} [U_{\text{NN}} - 3U_{\text{NNNN}}] \hat{\rho}_A(\mathbf{Q})\hat{\rho}_B(\mathbf{Q}) - U_{\text{NNN}} \sum_{\alpha} \hat{\rho}_{\alpha}(\mathbf{Q})\hat{\rho}_{\alpha}(\mathbf{Q}), \end{aligned} \quad (\text{B.25})$$

where the on-site interaction enters with a constant vertex function. Due to the finite momentum transfer, one finds negative interaction amplitudes for direct interactions of NNN- and NNNN-type. This is traced back to the fact that for a developed charge density wave order with ordering vector  $\mathbf{Q}$  contributions from these types of interaction are minimized which can be inferred from the representation of a possible order depicted in Fig. 6.1. Indeed,  $\gamma_{\alpha\alpha}^{(NNN)}(\mathbf{q})$  and  $\gamma_{AB}^{(NNNN)}(\mathbf{q})$  are minimal (and negative) for  $\mathbf{q} = \mathbf{Q}$ . Thus, matrix elements  $U_{\text{NNN}}$  and  $U_{\text{NNNN}}$  favor the a charge density wave order with ordering vector  $\mathbf{Q}$ , whereas  $U_{\text{on-site}}$  and  $U_{\text{NN}}$  act against it.

The mean field Hamiltonian is obtained by introducing mean fields  $\langle \hat{\rho}_{\alpha\sigma\xi}(\mathbf{Q}) \rangle = \Delta_{\mathbf{Q}}/8$  and by dropping constant terms yielding

$$\hat{H}_{\text{MF}} = \hat{H}_0 + \frac{\Delta_{\mathbf{Q}}}{4N}U_{\text{CDW}} \sum_{\alpha} \hat{\rho}_{\alpha}(\mathbf{Q}), \quad (\text{B.26})$$

where  $H_0$  denotes the quadratic part of Eq. (5.11) and the effective interaction strength in the charge density wave channel is given by

$$U_{\text{CDW}} = U_{\text{on-site}} + U_{\text{NN}} - 4U_{\text{NNN}} - 3U_{\text{NNNN}}. \quad (\text{B.27})$$

The effective interaction strength is complemented by the charge susceptibility with finite momentum and zero frequency transfer entering the criterion Eq. (B.21). By means of standard methods (see e.g. Ref. Fazekas (1999)) it is determined to

$$\chi_{\mathbf{Q}}(\mu) = -\frac{i}{4N} \sum_{\mathbf{k}} \int \frac{d\omega}{2\pi} f(\omega - \mu) \text{tr}_{\alpha\xi\sigma} [VG_{0,\mathbf{k}}^R(\omega)VG_{0,\mathbf{k}+\mathbf{Q}}^R(\omega) - VG_{0,\mathbf{k}}^A(\omega)VG_{0,\mathbf{k}+\mathbf{Q}}^A(\omega)], \quad (\text{B.28})$$

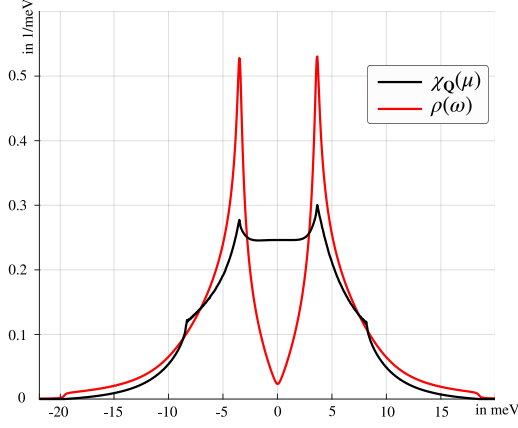


**Figure B.2.:** Charge susceptibility  $\chi_{\mathbf{Q}}(\mu)$  (black line) and single-particle density of states (red line)  $\rho(\omega) = -\frac{1}{\pi N} \sum_{\mathbf{k}} \text{Im} G_0^R(\omega, \mathbf{k})$  as function of doping level for a twist-angle representative for the weak-coupling regime.  $\chi_{\mathbf{Q}}$  is slightly peaked at the positions of the van Hove points (see the density of states in comparison), but has also finite weight at charge neutrality which is traced back to the finite momentum transfer  $\mathbf{Q}$  lying at the boundaries of the moiré Brillouin zone. Reprinted figure from Ref. Klug (2020). The original work is found under <https://dx.doi.org/10.1088/1367-2630/ab950c>.

where the free electronic Green's function is given by

$$G_{0,\alpha\beta}^R(\omega, \mathbf{k}) = ([\omega - h_0(\mathbf{k}) + i0^+]^{-1})_{\alpha\beta}, \quad (\text{B.29})$$

with the Fermi function  $f(\omega) = [e^{\omega/k_B T} + 1]^{-1}$ ,  $h_0$  obtained from the quadratic part of Eq. (5.11) by Fourier transform and  $V_{\alpha\beta} = \delta_{\alpha,\beta}$ . The two latter quantities are diagonal in spin and valley space and the corresponding indices are therefore suppressed from representation.

The charge susceptibility  $\chi_{\mathbf{Q}}$  is determined as function of doping level  $\mu$  and is depicted in Fig. B.2. It is slightly peaked at the positions of the van Hove points but does not diverge for any doping level because of the absence of nesting conditions connected with momentum transfer  $\mathbf{Q}$ . Substantial weight is observed at charge neutrality because of the finite momentum transfer with small extra weights at the van Hove points. Combined with an finite attractive interaction  $U_{\text{CDW}} < 0$  whose critical value is determined by Eq. (B.21), an onset of charge density wave order is expected for doping levels centered around charge neutrality as depicted in Fig. 4.2.

## REFERENCES

- P. Fazekas, *Lecture Notes on Electron Correlation and Magnetism* (World Scientific, 1999).  
 M. J. Klug, *Charge order and mott insulating ground states in small-angle twisted bilayer graphene*, *New J. Phys.* (2020).

### B.5. STRONG COUPLING ANALYSIS

In what follows, the numerical procedure is outlined to determine the electronic ground state in the strong coupling regime as function of band filling. This Appendix is an extract of the Appendix of Ref. Klug (2020) and is presented here for the sake of completeness.

For strong couplings, the electron dynamics is described by the Hamiltonian  $\hat{H}_{\text{SC}}$  introduced in Eq. (6.6) in Sec. 6.2. As  $[\hat{H}_{\text{SC}}, \hat{n}_{a\sigma}] = 0$ , the local densities represent conserved quantities rendering the model a classical model which can be solved by employing classical methods. Hence, the partition function is given by

$$Z = \prod_{i=1}^N \left( \sum_{n_i=0}^1 \right) e^{-\frac{E[n]}{k_B T}} \quad (\text{B.30})$$

where  $N$  specifies the total number of sites which are labeled by  $i = \{a, \sigma\}$  and  $n_i \in \{0, 1\}$  the local occupation number. The energy associated with the state  $n = \{n_1, \dots, n_N\}$  is given by

$$E[n] = \frac{1}{2} \sum_{\sigma\sigma'} \sum_{ab \in \square} (U_{ab} - J_{ab} \delta_{\sigma\sigma'}) (n_{a\sigma} - \frac{1}{2}) (n_{b\sigma'} - \frac{1}{2}). \quad (\text{B.31})$$

Accordingly, thermal expectation values are given by  $\langle \hat{O} \rangle = Z^{-1} \prod_{i=1}^N \left( \sum_{n_i=0}^1 \right) O_n e^{-\frac{E[n]}{k_B T}}$ , where  $O_n$  is the value of the observable for a particular state specified by the configuration  $n$ .

In what follows, one is interested in the ground state configuration  $n_{\text{GS}}$  which minimizes the energy functional  $E[n]$ , i.e.

$$E[n_{\text{GS}}] \equiv \min_n E[n], \quad (\text{B.32})$$

such that  $\langle \hat{H}_{\text{SC}} \rangle|_{T \rightarrow 0} = E[n_{\text{GS}}]$ . To determine  $n_{\text{GS}}$ , the simulated annealing algorithm (Kirkpatrick *et al.*, 1983) is employed. This Monte Carlo-based optimization algorithm is suited for high-dimensional problems and effectively scans the available state space. It is standard and can be found, e.g., in Ref. Laarhoven and Aarts (1987). The results for  $n_{\text{GS}}$  for various commensurate moiré band fillings are depicted in Fig. 6.2.

### REFERENCES

- S. Kirkpatrick, C. D. Gelatt, and M. P. Vecchi, *Optimization by simulated annealing*, *Science* **220**, 671 (1983).
- M. J. Klug, *Charge order and mott insulating ground states in small-angle twisted bilayer graphene*, *New J. Phys.* (2020).
- P. J. M. Laarhoven and E. H. L. Aarts, *Simulated Annealing: Theory and Applications* (Kluwer Academic Publishers, USA, 1987).